Investigation and management of residual stresses in selective laser melting of maraging steel

by

Lameck Mugwagwa

Dissertation presented in fulfilment of the requirements for the degree of Doctor of Philosophy in the Faculty of Engineering at Stellenbosch University

Supervisor: Prof. D. Dimitrov

Co-supervisors: Prof. S. Matope and Prof. I. Yadroitsau

April 2019

Declaration

By submitting this dissertation electronically, I declare that the entirety of the work contained therein is my own, original work, that I am the sole author thereof (save to the extent explicitly otherwise stated), that reproduction and publication thereof by Stellenbosch University will not infringe any third party rights and that I have not previously in its entirety or in part submitted it for obtaining any qualification.

April 2019

i

Abstract

Selective Laser Melting (SLM) is a leading metal additive manufacturing process that has gained a lot of traction since the turn of the new millennium. Despite many benefits associated with SLM, a major setback that continues to impede its wider application and uptake is the inherent phenomenon of residual stresses. Although post-processing methods such as heat treatment can significantly reduce the magnitude of generated residual stresses, these methods cannot reverse the cracking, delamination and warping distortions that occur during the process. This dissertation focuses on the investigation of residual stresses and explores effective ways through which these stresses can be managed in-situ.

An experimental study was conducted to establish the influence of input parameters on residual stresses and their accompanying effect on residual stresses. First, a study of the distribution of residual stresses was carried out on parts of different thickness. Secondly, scanning strategies and process parameters were studied through a structured experimental programme. Specimens were manufactured from maraging steel 300 powder on an M2 LaserCUSING as well as an EOSINT M280 machine. Residual stresses were measured using the neutron and X-ray diffraction methods whilst a coordinate measurement machine was used to measure distortions that arose from these stresses.

The results show that residual stresses increase as part thickness increases, and that these stresses are not uniform, even at the same depth of measurement. From the scanning strategy perspective, reducing the scan vector length lowered residual stress magnitudes, but increased porosity significantly. Whilst rescanning lowered tensile stresses and increased the magnitude of compressive stresses, it is also clear that maintaining the same laser parameters as the initial beam pass leads to overheating and a marginal rise in porosity. An improved scanning pattern, called the successive chessboard strategy, yielded up to 40 % reduction of residual stresses against the default island scanning strategy. The correlations between input parameters and process outcomes show that increasing laser power and scanning speed increases residual stresses and distortions for the range of parameters tested. On the other hand, increasing the layer thickness from 30 to 45 µm generally reduces residual stresses and distortions but promotes porosity. However, a satisfactory process parameter combination was found at 180 W and 600 mm/s for the 45 µm layer thickness. At this point, residual stresses and distortions were reduced by 31 % and 46 % respectively, relative to the 30 µm layer at the same laser power and scanning speed.

As original contribution, a method for evaluating and selecting residual stress management techniques was developed. Furthermore, new scanning sequences were developed, with the successive chessboard contributing to reduction of residual stresses and distortions. A process window was also devised for SLM of maraging steel 300. The process window demonstrates the porosity and residual stress state of final parts at different combinations of laser power and scanning speed. Finally, correlations were formulated between input parameters and the responses. This was extended to analysing the interdependencies between process outcomes, for example, residual stresses vs distortions and porosity vs distortions.

Opsomming

Selektiewe laserstraalsmelting (SLM) is 'n prominente byvoegingsverdaardigingsproses wat veel momentum begin gekry het sedert die nuwe millennium. Ten spyte van die voordele geassosieër met SLM, is 'n groot hindernis wat wyer topassing terug hou die inherente fenomeen van oorblywende spanning. Alhoewel na-bearbeidingsmetodes soos hittebehandeling gegenereerde oorblywende spanning noemenswaardig kan verminder, kan die metodes nie krake, delaminasie, en skeeftrekking wat tydens die proses voorkom omkeer nie. Hierdie proefskrif fokus op die ondersoek van oorblywende spanning en verken effektiewe maniere hoe hierdie spanning in-situ bestuur kan word.

'n eksperimentele studie was uitgevoer om die invloed van inset parameters op oorblywende spanning en hul gepaardgaande effekte van oorblywende spanning vas te stel. Eerstens, 'n studie van die verdeling van oorblywende spanning was uitgevoer op parte van verskillende dikte. Tweedens, skandeer strategieë en proses parameters was bestudeer deur 'n gestruktureerde ekperimentele program. Monsters was vervaardig van martensietverouderde staal 300 poeier op 'n M2 LaserCUSING sowel as 'n EOSINT M280 masjien. Oorblywende spanning was gemeet met neutron en x-straal diffraksie metodes terwyl 'n koördinaatmetingsmasjien gebruik was om die afwykings te meet wat onststaan het as gevolg van hierdie spanning.

Die resultate toon dat oorblywende spanning toeneem soos part dikte toeneem en dat hierdie spanning nie uniform is nie, selfs by dieselfde metingsdiepte. Van 'n skanderingsstrategie perspektief, vermindering van die skandeervektor lengte het die oorblywende spanninggrootte verlaag, maar die porositeit beduidend laat toeneem. Terwyl herskandering trekspanning verlaag en die grootte van drukspanning laat toeneem het, is dit ook duidelik dat deur dieselfde laserparameters as die oorsponklike straal pad te handhaaf tot oorverhitting en 'n marginale toename in porisiteit lei. 'n Verbeterde skanderingspatroon, genoem die skaakbordstrategie, het tot 'n 40 % verlaging van orblywende spanning in vergelyking met die standaard eiland skandeer strategie gelei. Die korrelasies tussen inset parameters en proses uitkoms toon dat verhoging van lasersterkte en skandeerspoed oorblywende spanning en afwykings verhoog vir die getoetsde gebied van parameters. Aan die ander kant, verhoging van die laagdikte van 30 na 45 µm verlaag normaalweg die oorblywende spanning en afwykings maar bevorder porositeit. Nietemin, 'n aanvarbare prosesparameterkombinasie was gevind by 180 W en 600 mm/s vir 'n laagdikte van 45 µm. By dié punt was die oorblywende spanning en afwykings

respektiewelik verminder met 31 % en 46 % relatief tot die van 'n 30 μm laagdikte by dieselfde lasersterkte en skandeerspoed.

As oorspronklike bydrae, 'n metode vir die evaluering en seleksie van oorblywendespanningbestuurstegnieke was ontwikkel. Verder, nuwe skandeervolgordes was ontwikkel, met die opvolgende skaakbord wat bygedra het tot die verlaging van oorblywende spanning en afwykings. 'n Prosesvenster was ook versin vir SLM van martensietverouderde staal 300. Die prosesvenster demonstreer die porositeit en oorblywende spanning toestand van finale parte by verskillende kombinasies van lasersterkte en skandeerspoed. Laastens, korrelasies was geformuleer tussen inset parameters en die reaksies. Dit was uitgebrei na die analise van onderlinge afhanklikhede tussen proses uitkomste, byvoorbeeld, oorblywende spanning teenoor afwykings en porositeit teenoor afwykings.

Acknowledgements

Table of Contents

List of Figures

xvii

List of Tables

Chapter 1:   Introduction

1.1   A background to additive manufacturing

The success of manufacturing processes in today's highly competitive global environment requires that manufacturers focus on developing high quality products rapidly, efficiently and cost effectively (Dimitrov *et al.*, 2016). Additive Manufacturing (AM), also widely known as 3D Printing, rapid prototyping/manufacturing, layer-wise manufacturing or solid free-form fabrication (Markl and Körner, 2016), is a key enabler for global competitiveness. AM is "a process of joining materials to make objects from 3D model data, usually layer upon layer, as opposed to subtractive manufacturing methodologies" (ASTM F2792-12a, 2013). Owing to the thin layer-by-layer style of consolidation, intricate and complex geometries can be built accurately (Bikas *et al.*, 2016). One key advantage of AM is that there is nearly no raw material loss as opposed to the conventional material removal processes. Furthermore, since parts are built directly from a CAD model, tooling is not a requirement. Thus, in comparison to conventional processes such as casting, AM reduces the product development cycle time.

AM evolved over the years from exclusive rapid prototyping in the late 1980s to gain more relevance in the low volume manufacturing of end-use components (Dimitrov *et al.*, 2006; Thompson *et al.*, 2016). AM is also applied in repair of components such as turbine blades and engine casings (Aggarangsi and Beuth, 2006). The turn of the new millennium has seen a shift of focus towards quality improvement and processing of metals and composites. The evolution of AM processes is shown in Figure 1.1.
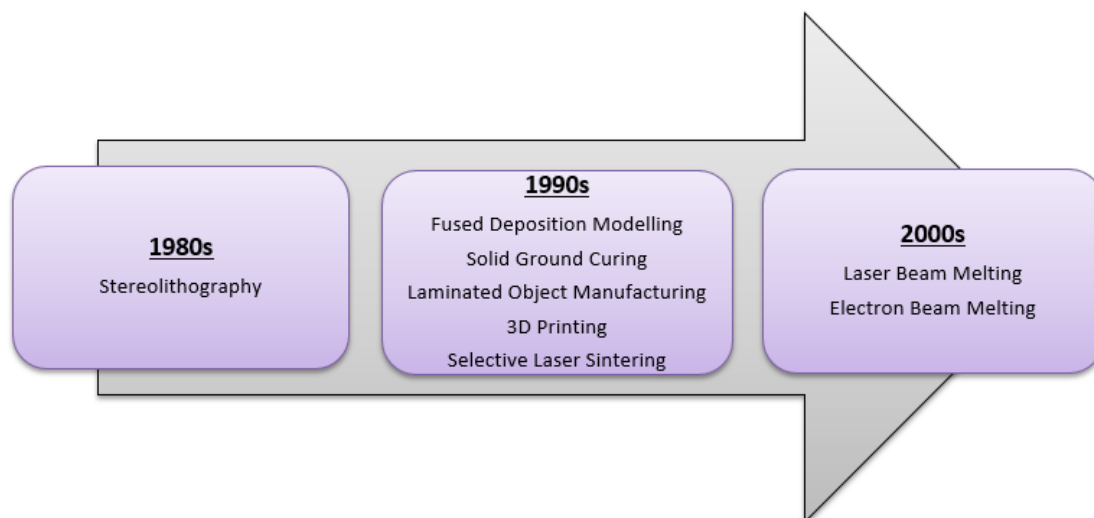
Figure 1.1: AM processes evolution (Adapted from Wohlers and Gornet, 2014; Thompson *et al.*, 2016)

1

Several AM techniques are available to process polymers, ceramics and metal alloys. Metal AM (MAM) has recorded enormous growth over the past few years as shown through a surge in MAM systems sales represented in Figure 1.2, with a huge 80 % leap being recorded for 2017 against 2016 machine sales.
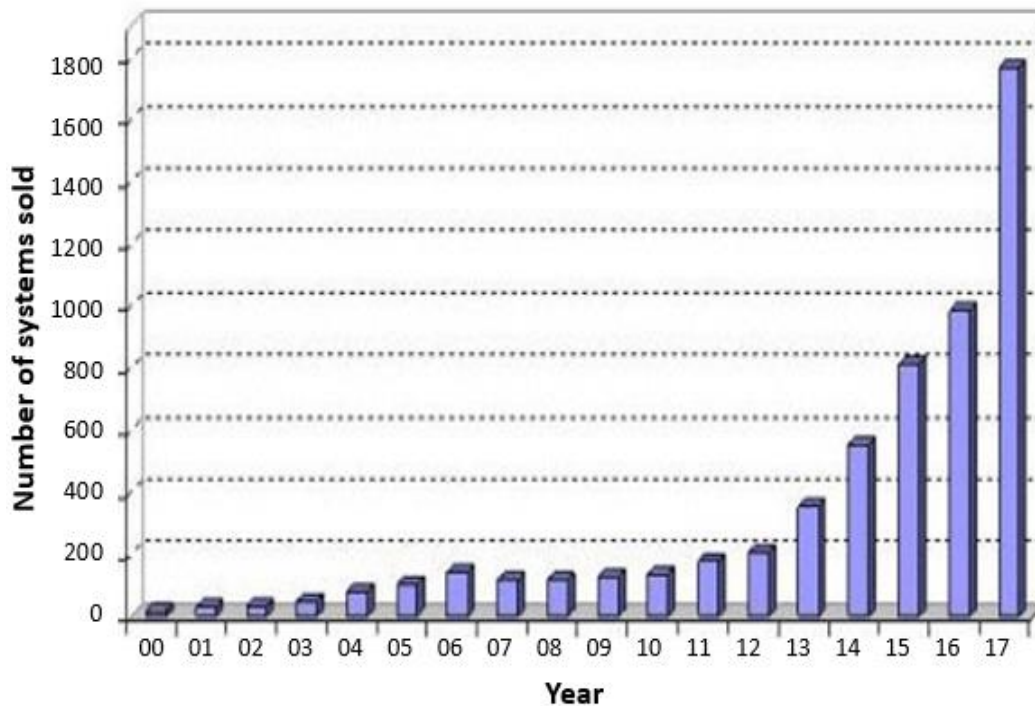
Figure 1.2: Rise in Metal AM machine sales between year 2000 and 2017 (Adapted from Wohlers, 2018)

Selective Laser Melting (SLM) is one of the AM methods that enjoy widespread use, and current research focuses on this process more than any other AM technology (Schmidt *et al.*, 2017). With SLM, it is possible to produce components which have static mechanical properties comparable to those achieved by conventional manufacturing methods (Kruth *et al.*, 2010; Zaeh and Branner, 2010; Król *et al.*, 2013). The high degree of geometric freedom associated with SLM makes the process suitable for manufacture of tooling inserts that have conformal cooling channels as well as topologically optimised aerospace parts and biomedical implants (Krauss and Zaeh, 2013; Thompson *et al.*, 2016).

Despite the progress and benefits presented by SLM, residual stresses remain a significant challenge that limit the wider uptake of the process for industrial applications. Residual stresses are those stresses that remain in a material after processing, when it has come to equilibrium with the ambient environment, in the absence of external loads and thermal gradients (Papadakis *et al.*, 2014). Although residual stresses develop during most manufacturing

2

processes such as forging, rolling, cutting and grinding, their impact and elusiveness is more profound in Laser Powder Bed Fusion (LPBF) processes such as SLM.

1.2 Problem statement

The localised heating and melting of powders during SLM, coupled with the short interaction of the laser beam with the powder bed, generates rapid heating and cooling cycles (Kruth *et al.*, 2012; van Belle *et al.*, 2013). This induces thermal stresses and, consequently, residual stresses in the part under consolidation. Literature analysis shows that residual stresses are a significant challenge in SLM and negatively affect the mechanical properties, surface integrity, shape and dimensional accuracy of finished as well as in-process parts. The major effects of residual stresses are shown in Figure 1.3. These setbacks restrict the practical application of the process, particularly for manufacture of components for the aerospace, medical and tooling industries where quality demands are stringent.

The subject of residual stresses in SLM is a very active research field due to its complex nature and the seriousness of the setbacks that these stresses pose to the capabilities of the SLM process. Previous studies on the subject of residual stresses have focused on post-process heat treatment for reduction of residual stresses. Whilst heat treatment is an effective and proven residual stress management technique, it cannot reverse effects of residual stresses such as shape distortions and thermal stress related cracking. Residual stress induced warping distortions that occur during the build process can impede the smooth movement of the coater blade and the process has to be terminated prematurely. Thus, the overall aim of this study is to investigate residual stresses in as-built parts and how these stresses and their effects on distortions can be reduced effectively *in-situ*.
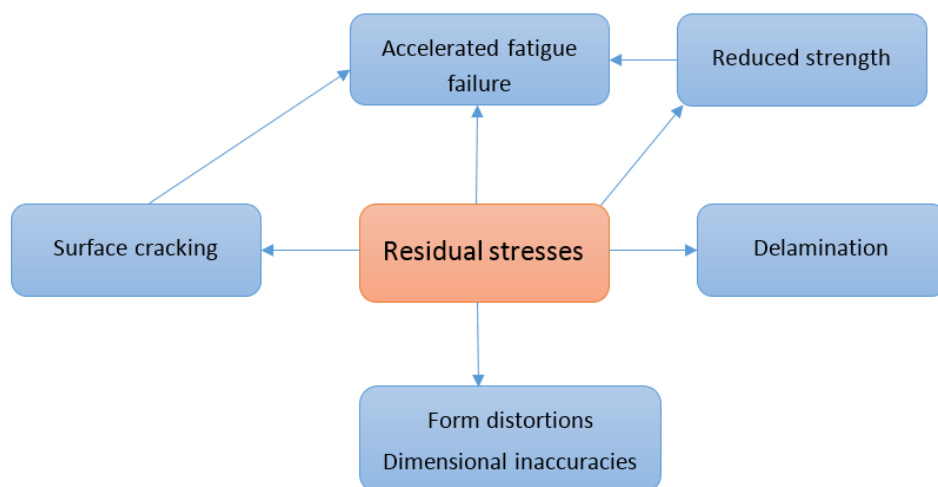
Figure 1.3: Summary of the major effects of residual stresses

3

1.3   Research questions

In line with the problem statement, the research questions are as follows:

(1) What are the current capabilities of the selective laser melting process with respect to form and dimensional accuracy?

(2) What are the effects of input parameters on residual stresses and form distortions in selective laser melting?

(3) What can be done to manage the effects of residual stresses on form accuracy of components produced by selective laser melting?

1.4   Research objectives

The main objective of the research is to study residual stresses in selective laser melting and their influence on form distortions of manufactured components, so as to manage these stresses.

The main research objective is broken down into specific objectives as follows:

(1) To study the current capabilities of the SLM process with regards to achievable form and dimensional accuracy

(2) To identify the major factors that govern the SLM process with respect to residual stresses

(3) To experimentally determine the effect of these major factors on residual stresses in components manufactured using SLM

(4) To model the interactions between residual stresses, porosity and distortions of final parts.

1.5   Research methodology

The research focuses on understanding the interactions between input parameters and the end-state outcome, namely residual stresses and form distortions of components manufactured by SLM. In this research, a quantitative experimental methodology is used to study residual stresses and explore ways in which these stresses can be effectively managed. The study begins with a structured literature analysis that leads to an informed approach of evaluating the methods for managing residual stresses. Based on the success stories reported in the literature, new scanning sequences are developed for investigation into their effect on residual stresses and accompanying distortions. Scanning strategies and processing parameters - identified as

critical in determining the residual stress state of finished parts - are investigated through a structured design of experiments. The experimental design involves both multi-factor and single factor experiments. For the multi-factor scenario, the full factorial design of experiments method is employed, with careful screening implemented in order to discard experiments that are not vital. The first phase of experimentation focuses on residual stresses whilst the second phase seeks to verify and validate the findings on residual stresses by investigating the correlations between these stresses and the distortions that arose from them. In order to propose the most appropriate interventions, the effect of input parameters on porosity is also studied. Cantilever geometries and thin titanium plates (1.8 mm thick) are utilised in this research to show that input factors that lead to lower residual stress magnitudes also lead to lower distortions. Therefore, parameters that lead to a reduction of both residual stresses and distortions can be confidently identified and implemented, as long as their effect on porosity is not dire. An overview of the study methodology followed is given in Figure 1.4.
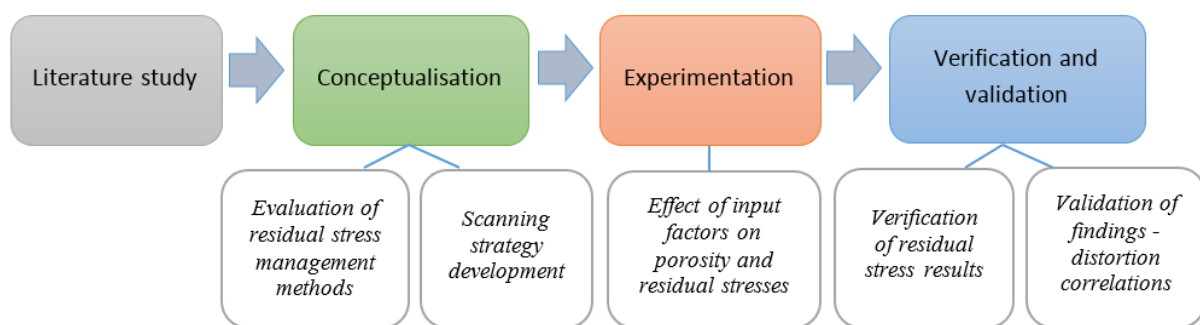
Figure 1.4: Major phases of the methodology

1.6   Dissertation outline

The dissertation is logically divided into seven chapters as shown in Figure 1.5. The current chapter (Chapter 1) introduces the research area, including problem statement, objectives and an overview of the research methodology. In Chapter 2, literature analysis is carried out on SLM capabilities and the factors that govern SLM, in particular their influence on residual stresses and form distortions. Focus is also placed on understanding the advances in the management of residual stresses and related effects. The residual stress measurement methods are also studied to establish the most appropriate method that can be used in this work. In Chapter 3, a conceptual framework for residual stress management is presented in which in-situ approaches for residual stress reduction are proposed. The methods for Design of Experiments (DoE) for this research are also discussed in Chapter 3 whilst Chapter 4 focuses

on the experimental set up from specimen preparation to residual stress, porosity and distortion measurement. In Chapter 5, experimental results are presented and discussed. From these results, empirical correlations are formulated between input parameters and residual stresses and porosity. The findings on residual stresses are verified and validated in Chapter 6 by inspecting the congruence between residual stresses and distortions. The research conclusions, contribution to knowledge and opportunities for further research, are summarised in Chapter 7.

1 • Introduction and background

2 • Literature study (SLM state of the art: a critical overview)

3 • Conceptualisation

4 • Experimental design and set-up

5 • Results and discussion

6 • Verification and validation of findings

7 • Conclusions and outlook
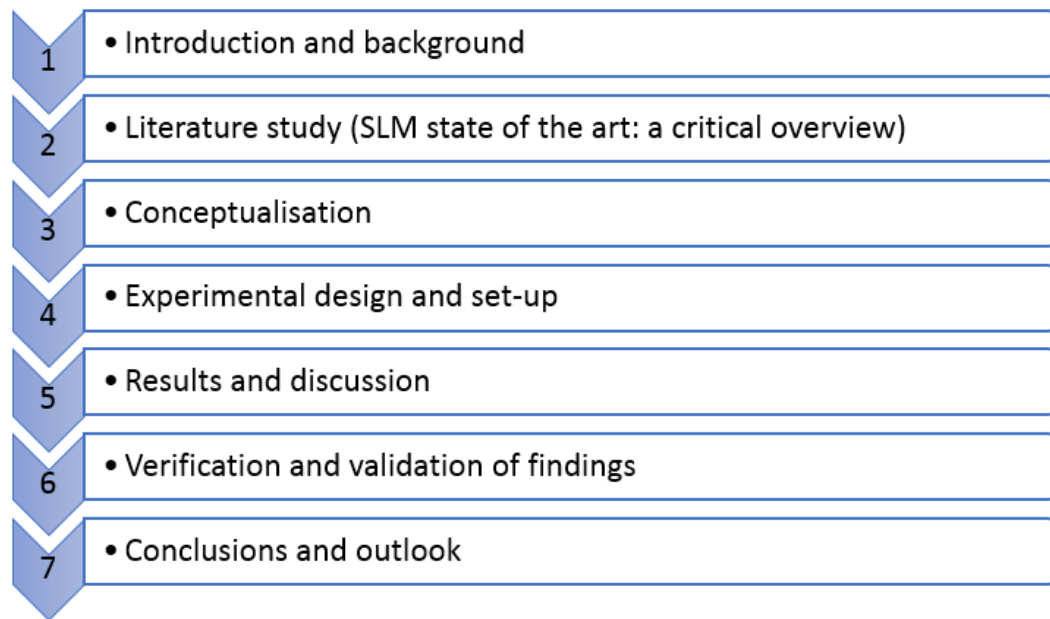
Figure 1.5: Dissertation outline

1.7 Summary

This Chapter presented a brief insight into the state of AM in general and SLM in particular, including current challenges that limit its wider application. A major setback for SLM is residual stresses and their effects on shape distortion, delamination and cracking. This challenge has prompted the need to investigate residual stresses further in order to understand and develop the most effective ways of managing these stresses. In order to understand the subject under study, a literature analysis is carried out in the next chapter.

Chapter 2: Selective laser melting state of the art: a critical overview

2.1 Introduction

This chapter covers a survey of literature on the subject of selective laser melting, with specific focus on residual stresses and their effects on finished parts. Firstly, an overview of metal additive manufacturing is given. Thereafter, a parametric investigation of the case study process - selective laser melting - is presented, along with the capabilities and limitations of this manufacturing process. Most importantly, this chapter details the subject of residual stresses and explores methods that effectively manage these stresses. A study of residual stress measurement techniques is also presented, leading to selection of the most suitable techniques for this study.

2.2 Classification of metal AM systems

AM techniques can be classified based on the state of the starting materials (solid, liquid, powder), or according to the type of material processed, that is, polymer additive manufacturing or metal additive manufacturing (MAM) methods. As extracted from Schmidt *et al*. (2017), MAM technologies are classified according to Figure 2.1 as per an ISO standard of 2014. Two broad classifications are evident - Powder Bed Fusion (PBF) and Directed Energy Deposition (DED) systems. A new category called "hybrid processes" can be added to this classification. Hybrid processes combine laser AM and CNC machining (Klocke *et al.*, 2017).
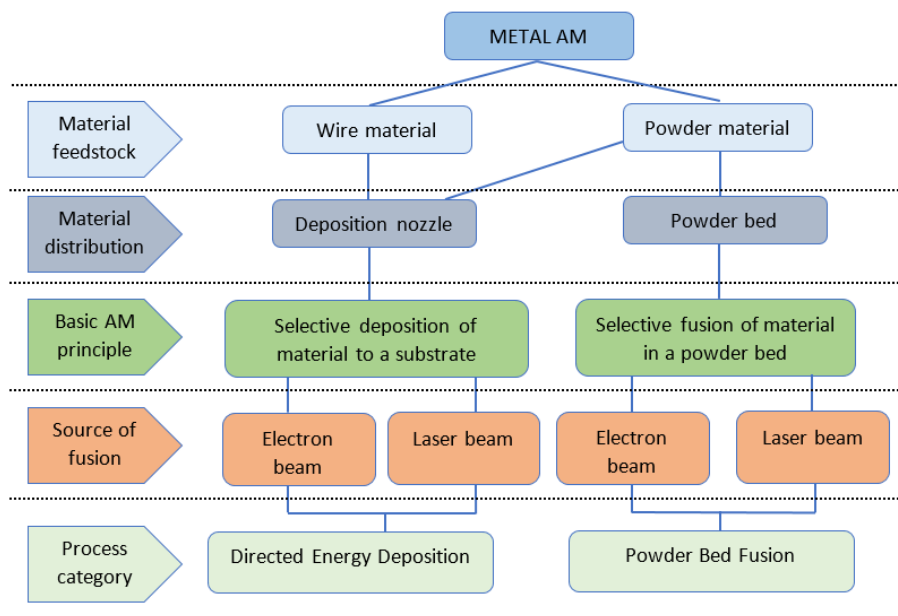
Figure 2.1: Classification of metal additive manufacturing processes (Adapted from Schmidt *et al.*, 2017)

2.2.1 Directed Energy Deposition techniques

In Directed Energy Deposition (DED) techniques, the material (powder or wire) is directed onto the building platform simultaneously with the laser or electron beam (Bourell *et al.*, 2017). Proprietary process names belonging to DED are Direct Metal Deposition (DMD), Laser Engineered Net Shaping (LENS) and Direct Light Fabrication (DLF). A unique feature of the DMD process that distinguishes it from LENS and DLF is the patented feedback system that provides for closed loop control of the process (Dutta *et al.*, 2011; Gu, 2015). Before powder is deposited in DED, a laser beam is used to melt the top surface of a metal substrate (baseplate) which acts as a building platform. This creates a small melt pool into which powders are injected. In some cases, multiple powder hoppers are used, thus permitting for the simultaneous deposition of two or more completely different powders at predetermined mixing compositions (Das *et al.*, 2013). The base plate is placed on a computer numerically controlled (CNC) table which can move in the X-Y directions, according to the generated tool path determined in the slicing step (Rangaswamy *et al.*, 2003; Das *et al.*, 2013). As the table is moved in the X-Y directions the thin (2D) melt layer solidifies, and the depositing head assembly moves upward (Z direction) by a specified layer thickness and another layer is deposited (Rangaswamy *et al.*, 2003; Das *et al.*, 2013). This sequence continues until the whole part is built. DED technology is used for building new components, repairing worn out metal surfaces as well as applying wear and corrosion resistant coatings to surfaces (Dutta *et al.*, 2011; Gu, 2015). The principle of both powder-fed and wire-fed DED systems is the same, except the nature of the feedstock.

An example of wire based DED process is Shaped Metal Deposition (SMD). The advantages of using wires are higher deposition rates and a cleaner building environment without the risk of powder contamination although the deposition process is sensitive to the position and orientation of the wire with respect to the melt pool and the deposition direction (Baufeld *et al.*, 2011; Heralić *et al.*, 2012).

2.2.2 Powder Bed Fusion (PBF) systems

In the powder bed fusion systems, a thin layer of metal powder is deposited onto the building platform. The powder layer thickness is usually between 20 and 80 µm for PBF systems. Subsequent to deposition, a high energy laser or electron beam is used to melt the powder. Thus, PBF can be classified into Laser Beam Melting (LBM) and Electron Beam Melting (EBM) techniques. LBM is also used to refer to other laser AM methods falling under DED systems. Laser based powder bed systems include Selective Laser Sintering (SLS) and

Selective Laser Melting (SLM). Currently, AM of metals is largely done using powder-bed fusion technologies (King *et al.*, 2015).

2.2.2.1   Electron Beam Melting

The EBM technique, sometimes called Selective Electron Beam Melting (SEBM) or electron beam manufacturing, employs a high energy electron beam to melt the powder. The process takes place in a vacuum chamber to avoid imperfections arising from oxidation of the metallic parts under build (Bikas *et al.*, 2016). The high vacuum environment is also necessary to avoid possible electron beam deflection as this can derail the process. The source of the electron beam is a heated tungsten filament, with a voltage of up to 60 kV to accelerate the electrons. Two electromagnetic lenses are used to control the electron beam, one for focusing and the other for deflecting the beam. The processing chamber consists of a building tank with an adjustable process platform, two powder dispensing hoppers, and a rake system for spreading the powders (Murr *et al.*, 2012; Wong and Hernandez, 2012; X. Gong *et al.*, 2014). In the building chamber, when the electrons reach the powder particles, their kinetic energy is converted to thermal energy. The EBM process is suitable for conductive metals, with the most common being Ti6Al4V, steel and cobalt-chromium alloys.

2.2.2.2   Selective Laser Sintering (SLS)

Selective Laser Sintering (SLS) is a process that is used to build metallic parts from powders by "sintering" the powder. Sintering involves heating the powder to a temperature that allows for fusing to take place without having to melt the powder fully. Heating is done with the aid of a laser beam. The common laser sources for laser based powder bed fusion systems are the lamp or diode-pumped Nd:YAG (Neodymium-doped Yttrium Aluminium Garnet), disk and fibre laser such as Yb:YAG (Ytterbium-doped Yttrium Aluminium Garnet), CO_2 laser, ionised argon laser and neon-helium (Ne-He) laser (Choi *et al.*, 2009; Savalani *et al.*, 2011; Song *et al.*, 2012). The SLS process was the first powder bed fusion process to be commercialised and was initially developed for making plastic prototypes. The process has two variations – direct and indirect SLS. Indirect SLS makes use of a polymer binder which can be in the form of a liquid or solid. When this polymer binder is melted by the laser, it bonds the metal particles together to create a *green* sintered part. To remove the polymer (de-binding), and thus create a direct metal-metal link, the sintered part is heated in an oven (Beal *et al.*, 2008; Campanelli *et al.*, 2010; Shahzad *et al.*, 2013; Deckers *et al.*, 2014). Direct SLS, on the other hand, makes use of a lower melting point metal rather than a polymeric binder. The lower melting point

powder particles melt first and act as a matrix for higher melting point powder particles. Typical binary systems are Ni-Cu and Fe-Cu in which copper melts first to create a matrix for nickel or iron powders respectively. Another option is to use two different powder particle sizes for the same material (Campanelli *et al.*, 2010). The smaller size particles will melt first and create a matrix for the larger powder particles. No de-binding is necessary for direct SLS.

2.2.2.3 Selective Laser Melting (SLM)

Selective Laser Melting (SLM®), Direct Metal Laser Sintering (DMLS) and Laser Cusing all refer to the same LBM process (with different proprietary names as used by the equipment suppliers – SLM Solutions GmbH, EOS and Concept Laser GmbH respectively). Selective Laser Melting (SLM) is the more widely used term and will be adhered to in this research when referring to these LBM processes. The SLM process developed from SLS, was driven by the need to produce fully dense parts and minimise post processing (Contuzzi *et al.*, 2011; Guo and Leu, 2013). SLM (and AM in general) is suitable for low volume manufacture of components since it is rather slow and expensive for high volume manufacturing. This technology is increasingly becoming popular for the manufacture of medical, aerospace and automotive parts and is now widely used in the die and mould making industry (Knowles *et al.*, 2012; Kempen *et al.*, 2013; Strano *et al.*, 2013). Complete melting of powder occurs in SLM rather than sintering or partial melting that characterises SLS and, therefore, SLM produces denser parts compared to SLS (Klocke *et al.*, 2017). The basic steps in SLM, which apply to AM in general, are shown in Figure 2.2.
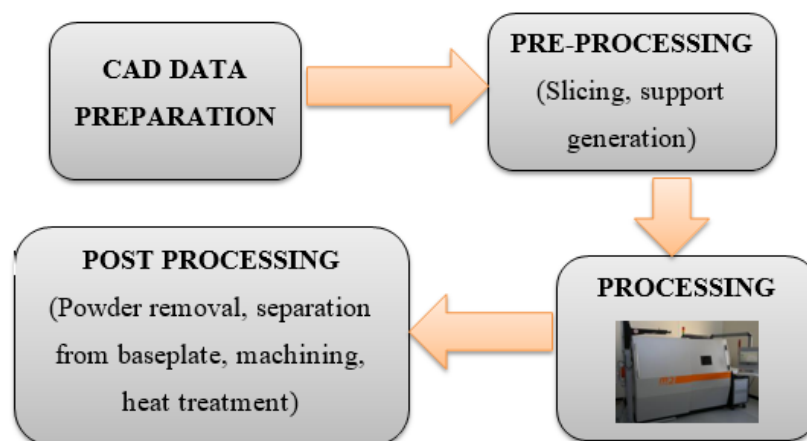
Figure 2.2: SLM basic steps

Like all AM processes, SLM relies on CAD data to build up parts layer by layer. The part to be made is developed using a three dimensional solid modeller. The CAD file is then converted into an STL (stereolithography) file in a process called tessellation or triangulation. In this step,

the closed external surfaces of the model are described using small triangles. The next step is pre-processing the data in AM software such as Magics®. This includes slicing of the model into thin layers (according to the preferred powder layer thickness), support structure generation (where necessary) and building orientations (Schmidt *et al.*, 2017). Once data preparation is complete, the process can commence. The SLM process is usually carried out in an inert environment to avoid reactions with oxygen which can lead to degradation of the final product (Ghany and Moustafa, 2006; Meier and Haberland, 2008). For highly reactive metals like titanium and aluminium, the process chamber is flooded with argon at an appropriate pressure. Less reactive metal alloys such as stainless steels can be built in nitrogen-filled chambers. Figure 2.3 shows the basic operating principle of SLM. A coater blade (also called re-coater) is used to distribute the metal powder across the powder bed as per the chosen layer thickness in the pre-processing step. The powder bed is melted selectively according to the input 3D CAD data by means of an irradiated laser beam which is guided by x/y-mirrors. Upon absorption of the laser radiation, the powder heats up and melts, hence consolidating the powder particles. Once scanning of the first layer is complete, the build platform is lowered through a distance equal to the layer thickness and another layer of powder is deposited, melted and solidified. The process is repeated until the object is completely built (Campanelli *et al.*, 2010; Mumtaz and Hopkinson, 2010; Carter *et al.*, 2014). Post processing operations that are carried out include removal of parts from the baseplate, removal of support structures and polishing or machining of the final parts (Kellens *et al.*, 2017). Powder that is not melted is removed upon process completion and can be recycled.
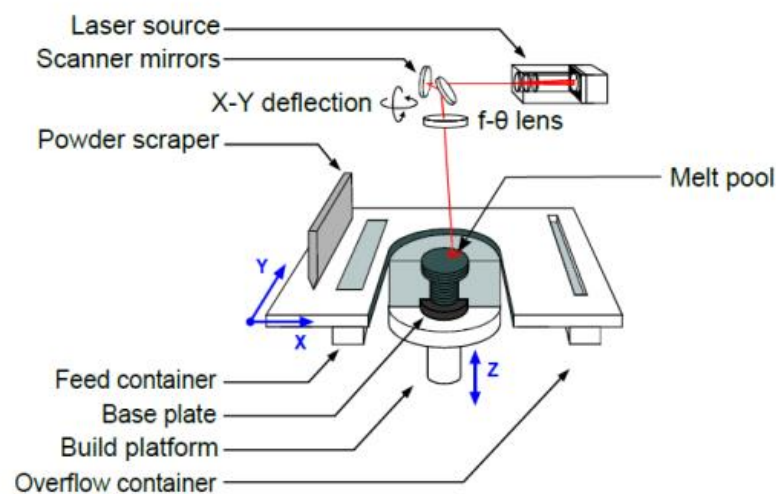
Figure 2.3: SLM process schematic (Source: Yasa and Kruth, 2011)

A range of weldable pure metals, compounds and metal alloys can be processed using SLM. Some commonly processed metal alloys include titanium, aluminium, nickel, chrome-cobalt and steel alloys (Schmidt *et al.*, 2017; Yusuf *et al.*, 2017). SLM is applicable for processing of alloys whose properties (such as hardness) make it difficult to process these alloys using conventional methods. An example is Ti6Al4V, which is a high-value alloy with excellent corrosion resistance, biocompatibility and strength-to-weight ratio. Ti6Al4V has common applications in the aerospace and biomedical fields (Ali *et al.*, 2017).

2.3 Selective laser melting capabilities

The SLM process is different in principle from conventional manufacturing processes and, therefore, the characteristics of products that the process can deliver is different to what is achievable using traditional processes. When discussing the capabilities of SLM, reference is usually made to how the process compares to conventional manufacturing process. In the following sections, the capabilities of SLM with respect to achievable microstructure, mechanical properties, surface integrity and dimensional and shape accuracy, are discussed.

2.3.1 Microstructure

The resultant microstructure in SLM depends on the starting powder material and the employed temperatures and building strategy. Each powder layer undergoes several phase changes in a short space of time and these changes determine the eventual microstructure and, thus, the associated mechanical properties that will result from the process (Fateri *et al.*, 2012). Investigations by authors such as Simonelli *et al.* (2012) and Vrancken *et al.* (2012), among others, have revealed a fine hexagonally packed martensite for Ti6Al4V parts built using SLM. According to Dadbakhsh and Hao (2014), the high cooling and solidification rates directly influence the martensitic structure. Typical SLM cooling rates range between 10^6 ^{o}C/s to 10^8 ^{o}C/s (Das *et al.*, 2010; Li and Gu, 2014a). Such cooling rates may impart hardness and some brittleness in the finished part. As a result of the layer by layer building strategy, the microstructure of SLM parts exhibit different morphology, depending on the direction or plane of viewing (Simonelli *et al.*, 2012; Wang *et al.*, 2016). The anisotropic microstructure leads to anisotropy of mechanical properties. It has been suggested that microstructural transformations have an influence on residual stress patterns and magnitudes in SLM-manufactured parts (Cottam *et al.*, 2014; Ali *et al.*, 2017; Yan *et al.*, 2017). Quite often, heat treatment processes such as annealing are performed on SLM manufactured parts to tailor/refine the grain structure and relieve thermal stresses (Vrancken *et al.*, 2012; Becker and Dimitrov, 2016).

2.3.2 Mechanical properties

SLM processes can achieve density almost equal to that of the bulk materials. As a result, SLM manufactured parts exhibit static mechanical strength which is comparable to parts manufactured using conventional methods (Kruth *et al.*, 2010; Zaeh and Branner, 2010). The achievement of high density is directly linked to full melting of metallic powders which takes place during SLM. Becker and Dimitrov (2016) recorded a 99.7 % relative density for maraging steel 300. Relative density as high as 99.8 % has also been recorded for tool steel (Kempen *et al.*, 2013). Despite these capabilities, little residual porosity is usually present in finished parts (Yasa and Kruth, 2011; Yusuf *et al.*, 2017). This porosity is not desirable in most applications. The main sources of porosity during SLM are insufficient melting, entrapment of gas, as well as *balling* (Bourell *et al.*, 2017; Demir and Previtali, 2017; Liverani *et al.*, 2017). During SLM, the molten material assumes a high surface tension difference with the underlying substrate. This brings about the "Marangoni" convection – a thermo-capillary flow of fluid within the melt pool from regions of low surface tension to high surface tension (Jhabvala *et al.*, 2010; Mumtaz and Hopkinson, 2010). The difference in the surface tension compromises the wetting properties of the molten material. This causes formation of isolated spheres (spheroidites) which then break away from the melt pool. This process is called balling or spheroidisation and results in unevenly layered or porous parts (Strano *et al.*, 2013; Campanelli *et al.*, 2014). Gu and Shen (2009) identified two types of balling: coarse and fine balling that are due to insufficient liquid (melt) formation and splashes from the melt respectively. Even though residual porosity is generally undesirable, it is also advantageous in some applications, for example in the biomedical field where this residual porosity in bone implants accelerates bonding between body tissue and the implant since the tissue can grow into and around the porous implant (Stamp *et al.*, 2009; Cardaropoli *et al.*, 2012).

According to Yang *et al.* (2012), SLM is capable of producing parts with higher hardness and ultimate tensile strength compared to wrought material, although ductility is compromised. Yasa *et al.* (2010) compared the mechanical properties of SLM built maraging steel to that of wrought maraging steel. Their findings show higher hardness of 40 HRC for SLM compared to 35 HRC for the wrought material. The ultimate tensile strength is also higher (1290 MPa) for SLM compared to the wrought material (1000 MPa). Yang *et al.* (2012) also present similar findings. Generally, studies show that SLM is capable of producing parts with mechanical properties that compare well with conventional manufacturing processes (Kruth *et al.*, 2010; Vrancken *et al.*, 2012). However, fatigue strength is compromised by existence of residual

stresses which quickens fatigue crack growth rates. Furthermore, the brittleness that SLM is associated with results in lower toughness of SLM built parts compared to those manufactured conventionally. According to a study by Kruth *et al*. (2010), the Charpy V-notch toughness of as built SLM specimens is lower than when conventional processes like casting are used. For example, the toughness of SLM built 316L stainless steel specimens was 59.2 J compared to 160 J for casting. A similar trend of results was also reported by Yasa *et al*. (2010). These challenges limit SLM in applications where the quality requirements are high and stringent (Craeghs *et al.*, 2011).

2.3.3 Surface quality

The achievable surface quality is one of the major challenges in SLM (Kruth *et al.*, 2010). Surface quality, particularly roughness, has significant influences on mechanical properties (particularly fatigue strength), heat transfer properties, optical properties as well as frictional properties (Pyka *et al.*, 2013). Surface roughness can lead to surface initiated cracking (due to nucleation of irregularities into crack and corrosion sites) and premature failure of components. A rough surface results in entrapment of gases when a successive layer is added, leading to porosity. High roughness peaks can interfere with the coater blade (Kruth *et al.*, 2010). In biomedical applications, surface roughness is important in determining the interaction between implant and bone tissue needed for healing (Campanelli *et al.*, 2014). More often than not, surface modification processes are required to improve the surface quality of final parts (Pyka *et al.*, 2013). Post-processing surface modification techniques that are usually employed for SLM processed parts are laser surface re-melting, sandblasting, ultrasonic filing (Kruth *et al.*, 2010; Strano *et al.*, 2013) and chemical etching (Pyka *et al.*, 2013). Re-melting the top surface of finished parts is a very effective method of reducing surface roughness as it has been reported to reduce roughness from 18.3 R_a to 8.6 R_a (Kempen *et al.*, 2013). Surface cracking can also occur due to tensile thermal stresses.

2.3.4 Thin walls and minute features

According to the work done by Krauss and Zaeh (2013), SLM cannot robustly manufacture walls of thickness 250 µm and below. Anything above this thickness is achievable, an indication that the process is generally capable of producing thin walls and "micro" objects (Yadroitsev and Smurov, 2011). It is likely that those walls thinner than 250 µm are actually scanned and melted during the build. However, they are probably removed by the coater blade as the process progresses due to the inability of these walls to resist forces associated with

deposition (Kruth *et al.*, 2005; Campanelli *et al.*, 2010). Cylindrical holes of less than 0.5 mm cannot be built using SLM because the enclosed powder is melted by the surrounding heat (Kruth *et al.*, 2005) to form a solid cylinder instead. However, careful control of the scanning strategy can easily counter this. Campanelli *et al.* (2010) concluded that building cylindrical extrusions of diameter less than or equal to 0.4 mm is practically impossible. As the nominal dimension approaches the laser spot diameter, SLM capabilities become limited.

A capability profile of the M2 Laser Cusing machine with regards to dimensional accuracy was carried out based on previous in-house studies (Dimitrov and Hugo, 2013). The benchmark part in Figure 2.4 was based on previous capability profile studies in the literature such as (Campanelli *et al.*, 2010). Parts used for assessing SLM capabilities of this nature should satisfy the following requirements:

- Thin walls in different directions
- Thin columns
- Small diameter holes with axes in different directions
- Overhangs
- Sharp edges
- Curved and sloping areas

From the study, it was concluded that thin walls larger than 0.5 mm can be manufactured on the M2 Laser Cusing machine. However, more recent in-house work has shown that even thinner walls of 0.3 mm thickness can be accurately manufactured on the same machine. Square holes of side less than 1 mm cannot be manufactured whilst horizontal square channels with sides larger than 1 mm need to be supported during the process in order to maintain form and dimensional accuracy. Horizontal round channels of diameters larger than 6mm require support structures to ensure form and dimensional accuracy. Square channels, with a side larger than 1mm, built at a 45° angle, can be produced with good quality. Sharp edges can be built to an accuracy of 1.6^o. As for the overhangs, it was concluded that features with angles below 40° to the horizontal require support structures in order to build properly. The surface quality at the bottom of these features progressively deteriorates with the reduction in build angle. Although special features such as sloping and curved edges, spheres and cones can be manufactured by the M2 Laser Cusing machine, the stair stepping effect negatively impacts on the surface quality. The stair stepping effect is intrinsic in layerwise manufacturing.

15
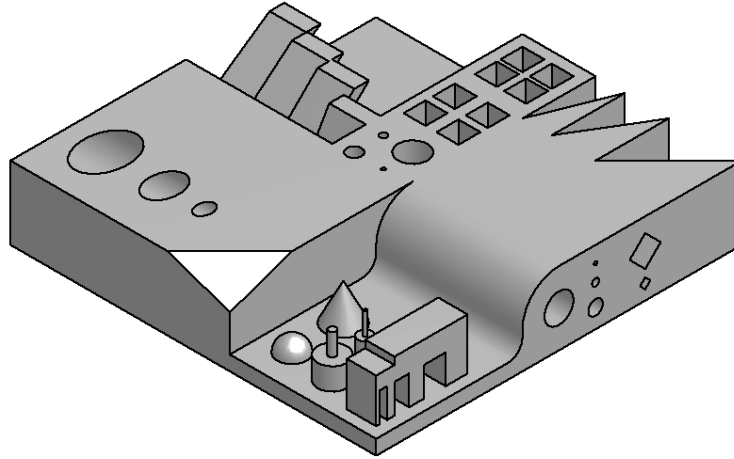
Figure 2.4: Benchmark part geometry for SLM capability profiling (Source: Dimitrov and Hugo, 2013)

2.3.5 Dimensional and shape accuracy

Neugebauer *et al*. (2014) observe that one of the main challenges of SLM is dimensional distortion when compared to the input CAD geometry. The thermal stresses that are set up during SLM and the material shrinkage that occurs during solidification could lead to shape distortion and dimensional inaccuracy. The occurrence of elevated edges or ridges at the ends of successive layers reduces both dimensional and shape accuracy (Yasa *et al.*, 2009). In the event that the elevated edges collide with the coater blade during powder deposition, the process can be derailed completely. A study by Yasa *et al*. (2009) revealed that elevated edges reduce the dimensional accuracy of the built parts by up to 150 µm.

Shape and dimensional distortions are largely due to the non-uniform heat transfer during solidification and the occurrence of residual stresses and many other factors such as scanning strategy, exposure strategy, process temperature, layer thickness and laser parameters (Toth-Tascau and Stoia, 2011). Qian (2012) consents to the seriousness of residual stresses and warping that can result from non-uniform cooling, leading to limited applicability of the SLM process. The experimental work done by Neugebauer *et al*. (2014) shows stress-induced warping distortions of up to 4.5 mm. Residual stress, as the name suggests, is the stress that remains locked up in the material after it has reached equilibrium with the ambient environment. The concept of residual stresses is discussed in greater detail in section 2.5. Evidence of warping of components during the build are shown in Figure 2.5 from previous in-house work on a titanium knuckle duster Figure 2.5 (a) and a hybrid tooling insert Figure 2.5 (b). The shape distortions shown are a result of thermal stresses. The injection moulding

16

hybrid tooling insert represents a severe case of the effects of residual stresses which can result in complete abandonment of the build process since the movement of the coater blade is impeded by the warpage.
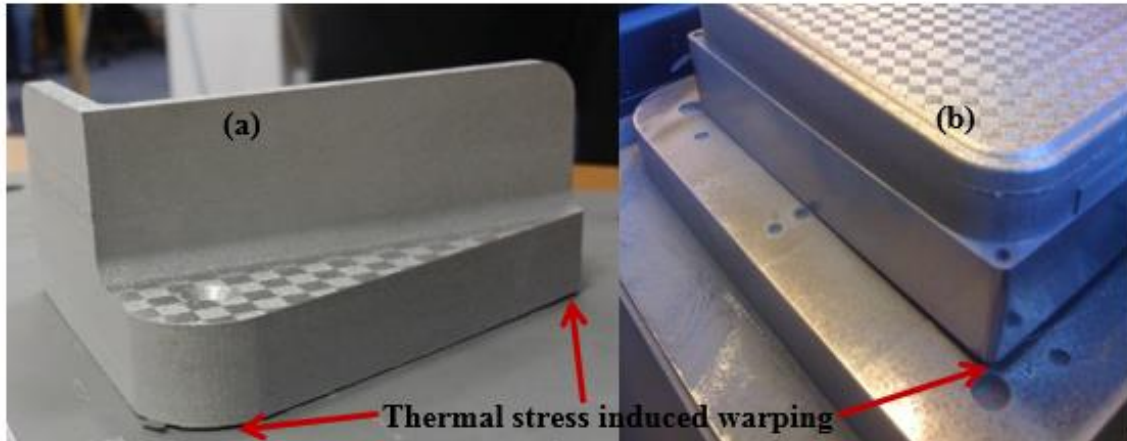
Figure 2.5: Delamination (and warping) of parts from the baseplate (in-house studies)

2.3.6 Summary

The overview has shown that thin walls of 0.3 mm and above can be manufactured using SLM, with overhanging features and horizontal channels requiring support structures to build accurately. Furthermore, SLM is capable of achieving mechanical/physical properties such as hardness and density that are comparable to those obtained through conventional manufacturing methods. Regardless, challenges arising from residual stresses still persist. These challenges include accelerated fatigue failure, cracking and delamination as well as shape distortions. The effects of such challenges may be catastrophic (in the case of fatigue failure) or lead to rejection of parts (if they are cracked or distorted). In order to understand the origins of these limitations, it is necessary to study the factors that govern the SLM processes.

2.4   Key parameters governing SLM

SLM is a complex thermal process with several input parameters that affect the outcome of the process. According to Averyanova *et al.* (2011), the parameters that govern SLM are over 130, but probably only 18 are crucial in determining final part properties (Ferrar *et al.*, 2012). Craeghs *et al.* (2011) summarised the several parameters that influence the selective laser melting process by classifying them into input parameters and boundary condition parameters. Input parameters are those parameters which can be controlled or tuned by the operator such as scanning parameters, powder deposition parameters and the atmosphere parameters.

Boundary conditions, on the other hand, are influenced by external requirements such as application, required geometry, material to be used and the type of machine available. It is more convenient to summarise SLM parameters based on an illustration by Mugwagwa *et al.* (2014), who grouped the factors into part geometry parameters, material parameters, environment parameters, laser and scanning parameters. A similar summarisation of SLM parameters was done by O'Regan *et al.* (2016) who listed 49 key factors. Coming up with standardised or optimised parameters for the SLM process is one of the major challenges faced by researchers (Pupo *et al.*, 2013). This is because the SLM process parameters are inter-related and should be carefully selected as adjusting one parameter without giving due attention to the interaction with other factors can completely derail the process. This interaction between the various process parameters and final part quality is not fully understood (Schmidt *et al.*, 2017).

Elsen *et al.* (2008) illustrate the dependency of the SLM outcome on various input parameters as follows:

$$y = f_1(x_1, x_2, \dots, x_n)$$

(2.1)

where x represents input parameters such as laser power, scanning speed and laser spot diameter and y is the output parameter such as part density, yield strength and residual stresses.

2.4.1 Part geometry parameters

The *size* and complexity of the part to be manufactured determines the accuracy achievable. Bigger part sizes are prone to greater dimensional error when compared to smaller parts (Toth-Tascau and Stoia, 2011). Part length and moment of inertia have also been reported to influence the magnitudes of residual stresses in final parts. Mercelis and Kruth (2006) studied the influence of part height on residual stresses by using three specimen heights – 10, 5 and 2.5 mm. The results show a reduction in residual stresses of approximately 75% when specimen height is reduced from 10 to 5 mm. A further decrease of about 50% is also recorded with a further decrease in specimen height from 5 mm to 2.5 mm. This trend was observed for both the longitudinal and transverse stress components. A study by Casavola *et al.* (2009) shows that generally residual stresses increase (from 97 MPa to 119 MPa) with increase in specimen thickness (from 3 mm to 11 mm). However, for the intermediate thicknesses (5 mm and 7 mm) these stresses actually decreased (to 84 MPa and 77 MPa respectively). The authors argue that thicker section require a greater number of laser beam passes since more layers are deposited when compared to thinner sections. With each laser beam pass, an action of post treatment is

introduced, thereby reducing residual stresses. These conclusions are at variance with findings of other authors such as Furumoto *et al*. (2010) and Mercelis and Kruth (2006). The study by Furumoto *et al*. (2010) shows that increasing the number of layers (which is basically increasing the specimen thickness) from 25 through to 400, is accompanied by a steady increase in deformation height from 5 µm through to 40 µm respectively. An accompanying residual stress increase from 200 MPa to 800 MPa is also observed. The likely reason for the general increase in the stresses as specimen thickness or number of layers is increased, is that bigger (thicker) parts cool down more rapidly than smaller (thinner) parts (Mercelis and Kruth, 2006; Casavola *et al.*, 2009; Toth-Tascau and Stoia, 2011). As far as the substrate (baseplate) geometry is concerned, studies show that the thickness (or height) of the baseplate has an influence on the development of residual stresses and distortions on both the part and the baseplate itself (Mercelis and Kruth, 2006; Furumoto *et al.*, 2010). Furumoto *et al*. (2010) report a general decrease in residual stresses from about 400 to 200, 150, 100 and 50 MPa when the baseplate thickness is increased from 5 to 10, 15, 20 and 30 mm respectively. The baseplate material itself should be carefully chosen for each material in order to manage residual stresses. Concept Laser, for example, has recommendations on what baseplate material to use for a given powder material. An example is hot work steel baseplate 1.2343 and 1.2709 for SLM of CL50WS.

Building orientations have been shown to have an influence on the mechanical strength of finished parts, particularly fatigue strength. Meier and Haberland (2008) observed lower tensile strength of 595 – 636 MPa for specimens built vertically as compared to those built horizontally which had tensile strength of 714 – 745 MPa. Vrancken *et al.* (2014) carried out a study in which they used different building orientations for SLM of Ti6Al4V and conclude that specimens built vertically, with notch cut along the building direction, have steeper fatigue crack growth rate due to effect of residual stresses which were oriented in the building direction. Similar results are reported by Yadollahi *et al*. (2017) for 17-4 PH stainless steel. Whilst the building orientation that results in the least building height is preferable, there could also be the need to consider orientations that take up the least surface area on the baseplate to allow for multiple parts to fit in one build. For some building orientations and part geometries, ***support structures*** are required to support overhangs as well as to remove heat from the part under consolidation. These support structures affect the heat transfer around the part under build and in turn influence the residual stresses magnitudes (Hussein *et al.*, 2013; Järvinen *et al.*, 2014; Nadammal *et al.*, 2018). A comparison of different support structure types has shown

that volume support structures are associated with higher residual stresses when compared to block and cone supports (Töppel *et al.*, 2016).

The ***building position*** on the baseplate has been studied to establish its effect on final part characteristics. Studies by Becker and Dimitrov (2016) as well as Ahuja *et al.* (2016) show that the chosen position on the baseplate has significant effect on the final part density. In the work by Ahuja *et al.* (2016) for SLM of stainless steel, the parts placed towards the centre exhibited about 99.80 to 99.95 % relative density whilst some specimens that were positioned closer to the borders of the baseplate recorded a relative density of as low as 99 %. The influence of building positions on residual stresses was studied by Casavola *et al.* (2009). The inert gas circulation system, positioning of the laser beam relative to the powder bed and errors in the deposition system, have been identified as the possible factors behind the differences in the residual stresses or relative density for different positions on the baseplate.

2.4.2 Material parameters

Important end-state information of the SLM process is dependent on the type of material and its state (powder or solid and grain size). Different materials and material states will respond differently, even when processed under the same conditions (Pupo *et al.*, 2013; Hodge *et al.*, 2014). Material parameters refer to metallurgical, physical, optical, rheological and thermal properties. For the same material, variation of powder particle size and morphology can result in distinct and specific microstructures (and accompanying mechanical properties) for each variation (Averyanova *et al.*, 2011). This shows that the initial powder (material) properties influence the final outcome during SLM, particularly in terms of microstructure and mechanical properties. As noted by Kovaleva *et al.* (2014), powder particle size affects the absorption of laser radiation, heat transfer, melting and agglomeration of particles. Compared to larger powders, smaller powder particles have larger surface area for laser absorption and heat up faster to melt before larger particles (Yadroitsev *et al.*, 2012; Ganeriwala and Zohdi, 2014). However, a study by Töppel *et al.* (2016) shows that powder particle size has no influence on development of residual stresses.

Materials with low thermal conductivity or thermal diffusivity retain heat in the component under build and this gives rise to residual stresses and effects such as warpage, shrinkage and reduced mechanical strength (Casavola *et al.*, 2008; Vrancken *et al.*, 2013). Vrancken *et al.* (2013) did a study on influence of material properties on residual stresses using nine different materials. Lower thermal conductivity materials such as Ti6Al4V (6.7 W/m/K), Inconel 718

(11.4 W/m/K), 18Ni300 maraging steel (15 W/m/K) and Hastelloy C-276 (19 W/m/K) generally exhibited the greatest maximum principal stress values of 406 MPa (tensile), 419 MPa (tensile), 263 MPa (compressive) and 358 MPa (tensile) respectively. Higher thermal conductivity materials like AlSi10Mg (113 W/m/K) and tungsten (173 W/m/K) had the least stress values of 64 MPa (tensile) and 34 MPa (compressive) respectively.

2.4.3 Build environment

The "build environment" refers to parameters such as the type of gas used and preheating conditions in the building chamber and the base-plate. Zhang *et al.* (2013) discovered that the gas used in the build chamber, and the mixture of gases, has an influence on the resultant density of 316L stainless steel parts built by SLM. Samples that were fabricated under argon or nitrogen had higher densities compared to samples that were fabricated in a helium or hydrogen environment. With respect to the influence of the build environment on residual stresses, previous studies have established that these stresses are directly proportional to the difference between the temperature of the melt pool and ambient temperature (Gusarov *et al.*, 2011). Thus, pre-heating the powder or baseplate reduces this temperature difference, resulting in a reduction of residual stresses.

2.4.4 Laser and scanning parameters

Laser power, scanning speed, hatch distance and layer thickness are interdependent and it is convenient to discuss them simultaneously. For example, when low *laser power* is selected, an accompanying decrease in the scanning speed is necessary to promote melting. The layer thickness should also be decreased in order to allow for sufficient penetration of the irradiating laser beam. For low laser spot diameters, the hatch spacing should be reduced in order to create sufficient overlaps between successive scan tracks. Due to this interdependence, a quantity called energy density is usually used when investigating the influence of laser/scanning parameters on the process. Among other things, the energy density directly influences part density and dimensional accuracy. The volumetric energy density *(VED)* is related to laser power *(P)*, scanning speed *(v)*, hatch distance *(h)* and layer thickness *(t)* as given in Equation ((2.2) (Król *et al.*, 2013; H. Gong *et al.*, 2014). To achieve full melting, high energy densities are necessary, for example 100 J/mm^3 for tool steel melting using the M2 LaserCUSING machine. However, when the energy density becomes too high, balling arises; and when it is too low, interlayer/track connection becomes very poor, and this leads to decrease in achievable density. These observations are evident from the work of Cherry *et al.* (2015).

21

$$VED = \frac{P}{v.h.t} \qquad \text{(2.2)}$$

Despite the interdependence, these factors (laser power P, scanning speed v, hatch distance h and layer thickness t), can also be discussed individually whereby only that factor under study is the variable. Kruth *et al*. (2010) studied the influence of **scanning speed** on final part density (Figure 2.6) and the results show that as the scanning speed is progressively increased from 150 mm/s to over 500 mm/s, the relative density decreases from 99% to 97%. This is because at higher scanning speed the powder bed is not sufficiently melted due to a decrease in the width of the melt pool (Rombouts *et al.*, 2009). Obviously, high scanning speeds increase the rate of production but may compromise the resulting quality of parts, particularly with respect to density and surface properties. Furthermore, the quick movement of the laser across the powder bed means that there is short laser-material interaction and therefore rapid solidification. This rapid solidification can modify microstructure of the material through microstructural refinement or solid solubility extension and can influence the setting up of thermal stress (Dadbakhsh and Hao, 2014). On the other hand, scanning at speeds lower than the optimum value(s) leads to over-melting and balling.
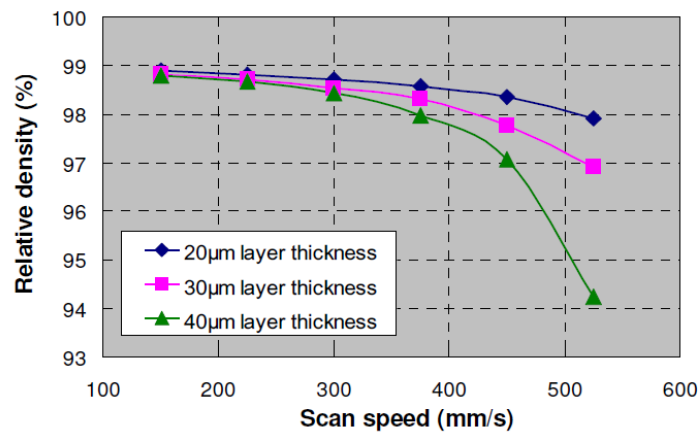
Figure 2.6: Influence of scanning speed on density (Source: Kruth *et al.*, 2010)**.**

Hatch distance is the distance or space between the centres of successive scan tracks/lines. A short hatch distance results in sufficient overlaps between adjacent scan tracks, promoting full melting and high achievable densities. Notably, short hatch distances decrease the amount of melted material, thus slowing down the build speed (Beal *et al.*, 2008; Yadroitsev and Smurov, 2011). Regardless of the laser power, small hatch distances promote sufficient overlaps and formation of homogenous layers. Heat from previous tracks is "carried over" to the next scan track, resulting in accumulation or amassing of heat (Pupo *et al.*, 2013). Furthermore, the bigger

the laser spot diameter, the wider the tracks and the greater percentage of overlapping between successive tracks. For the same hatch distance, bigger laser spot diameters will provide for better overlapping compared to smaller laser spot diameters. Narrow tracks result in isolation of the scan tracks, even at short hatch distances. As mentioned already, isolated tracks lead to many problems such as low density and poor surface integrity.

Increasing the powder *layer thickness* beyond the optimum value generally results in insufficient melting and weak interlayer bonding. This leads to porosity, reduced surface quality and delamination (Guan *et al.*, 2013; Savalani and Pizarro, 2016; Ali *et al.*, 2018). In order to avoid this, an increase in layer thickness should be accompanied by a reduction of the scanning speed. In this way, there is a prolonged interaction between the laser beam and the powder bed, resulting in full melting. Thinner layers are generally associated with higher dimensional and shape accuracy (Toth-Tascau and Stoia, 2011). In summary, it is important to strike a balance between laser parameters, particularly the laser power, scanning speed and layer thickness. This balance should be determined by the required part density and surface quality, among other desirable outcomes.

2.4.5 Scaling factors

During solidification in SLM and SLS, there is accompanying shrinkage, depending on part geometry, orientation and direction of laser scanning (Gupta and Kumar, 2014). It is necessary to scale up the size of the part in the CAD model using a compensation factor based on the material's properties. The shrinkage is more pronounced in the building direction (Z) compared to the in-plane directions (Singh *et al.*, 2012). The CAD model is scaled up accordingly in the X, Y, and Z directions to compensate for the inevitable shrinkage (Toth-Tascau and Stoia, 2011). The scaling factor is linearly related to the scan length and percentage shrinkage can be calculated and compensated for in the STL before build begins (Singh *et al.*, 2012). The scanning system itself may also result in errors to do with the sizes of segments to be scanned and these are also compensated for (Tang *et al.*, 2004). Therefore, scaling factors take care of the distortions that could arise from errors caused by shrinkage and errors due to the scanning system.

2.4.6 Scanning strategy

The manner or pattern in which the powder bed is scanned determines several outcomes such as residual stresses, mechanical properties, achievable density, microstructure and surface finish among other outcomes (Bo *et al.*, 2012; King *et al.*, 2015). Kruth *et al*. (2010) did a

comparison of three scanning patterns – uni-directional, bi-directional and alternating bi-directional. The alternating bi-directional pattern yielded the greatest density. This is because the uni-directional parallel scanning pattern gives rise to higher surface tension compared to the bi-directional scanning pattern. This surface tension results in the expelling of the melt pool (and balling), leading to occurrence of higher elevated edges (Yasa *et al.*, 2009). The scanning strategy also influences the orientation of grains and therefore the microstructure of the final part (Thijs *et al.*, 2010). Some scanning strategies such as the island strategy patented by Concept Laser, have been found to significantly reduce thermal stresses and deformations that arise from these stresses (Yasa *et al.*, 2009).

2.4.7 Summary

The research on part geometry, particularly thickness, only considers a maximum thickness of 11 mm. In practice, functional components may have thicknesses much greater than this. The range of thickness can be widened up to 20 mm and allow for investigation of a sufficient number of part thickness levels that can lead to the establishment of a valid trend of residual stresses and distortions within that range. Previously, the influence of laser scanning and deposition parameters has been approached from an energy density perspective. However, these studies have focused on achievable density, for example in Meier and Haberland (2008), Campanelli *et al.* (2010), Thijs *et al.* (2010) and Gu *et al*. (2013). Wu *et al.* (2014) carried out a qualitative investigation of the effect of laser parameters (grouped into energy density) on residual stress related distortion. A more quantitative approach is necessary. A previous study indicates that the most important parameters in SLM are (in order of importance) laser power, layer thickness and scanning speed (Yadroitsev *et al.*, 2012). Hanzl *et al*. (2015) also observed that laser power and scanning speed have the most significant effect on physical and mechanical properties of SLM manufactured parts. From a scanning strategy point of view, a lot of work still needs to be done in improving SLM capabilities, particularly with regards to residual stresses and their effects. In the next section, a detailed study of residual stresses and their effects is presented.

2.5   Residual stresses in SLM

Residual stresses are an inherent phenomenon of thermal manufacturing processes such as laser beam melting and welding (Gusarov *et al.*, 2011). These stresses cannot be avoided completely, but can be managed to reduce their effects on part quality and performance characteristics. Residual stresses can be classified as macro (Type I) or micro stresses (Type II and Type III).

Both types (macro and micro) can be present simultaneously in finished parts. Macro stresses extend over ranges that are much larger compared to the grain size (since they involve many grains in the material). On the other hand, the difference within the microstructure of a material due to presence of different phases or constituents in that material gives rise to micro stresses. Type II micro stresses (structural micro-stress) are generated at grain size level due to the anisotropic behaviour of each grain, whereas Type III stresses (intragranular stresses) develop at atomic size level due to imperfections in the material's structure (Kandil *et al.*, 2001; Cheng *et al.*, 2012). Kandil *et al.* (2001) further classified the origin of residual stress as mechanical, thermal or chemical. Mechanically generated stresses are a result of non-uniform plastic deformation during manufacturing processes such as shot peening, forging, wire drawing etc. – therefore, these stresses are based on the manufacturing process. Thermally generated stresses are a result of non-uniform heating and cooling and steep thermal gradients. Chemically generated stresses are a result of the volume changes due to chemical reaction and phase transformations arising from surface coating and heat treatment techniques such as nitriding and carburising.

2.5.1 Mechanism of residual stresses in SLM

During SLM, the laser beam and powder bed interaction time is very short, and the heating and melting of powders is highly localised. These scenarios lead to rapid heating and cooling cycles that induce steep thermal gradients. Consequently, thermal stresses are introduced in the part under consolidation (Kruth *et al.*, 2012; Song *et al.*, 2012; van Belle *et al.*, 2013; Mohanty and Hattel, 2014). These stresses remain in the material as residual stress after all the heat has eventually been removed from the part.

Mercelis and Kruth (2006) used two mechanisms to describe residual stresses. The first one is the Temperature Gradient Mechanism (TGM) in which during heating, the irradiated layer expands due to the high temperature in this layer. However, this expansion is partially restricted by the cold underlying substrate, resulting in a partially elastic and partially plastic compressive stress-strain condition being set up in the top layer of the irradiated zone. The compressive stresses may be so high that they exceed the yield strength of the material, resulting in plastic deformation of the top layers (Kempen *et al.*, 2013). Once deformations become plastic, residual stresses will remain in the material when it reaches equilibrium with ambient environment. It must be emphasised that as long as thermal strains are elastic, no residual stress will be set up (Kruth *et al.*, 2012). The second mechanism is the cool down mode in which,

25

when the irradiating laser beam is removed, the top surface tends to shrink. However, this shrinkage is restricted by the plastic deformation that developed during the heating cycle. Furthermore, the underlying solidified layers also hinder this contraction of the top layer. This leads to a residual tensile stress state being set up in the upper surface (irradiated zone) (Mercelis and Kruth, 2006; Kruth *et al.*, 2012; Kempen *et al.*, 2013). In other words, during cooling, an overall tensile state occurs in the irradiated region, while the surrounding material will be in an overall compressive state (Roberts, 2012). The TGM and cool down modes are shown in Figure 2.7 (where the symbols ε_{th}, ε_{pl}, σ_{tens} and σ_{comp} represent thermal strain, plastic strain, tensile stress and compressive stress respectively). If the rates of solidification can be reduced, thermal stresses are reduced as well. To further understand the development of residual stresses towards management of the same, an overview of the heat transfer mechanisms in SLM is undertaken.
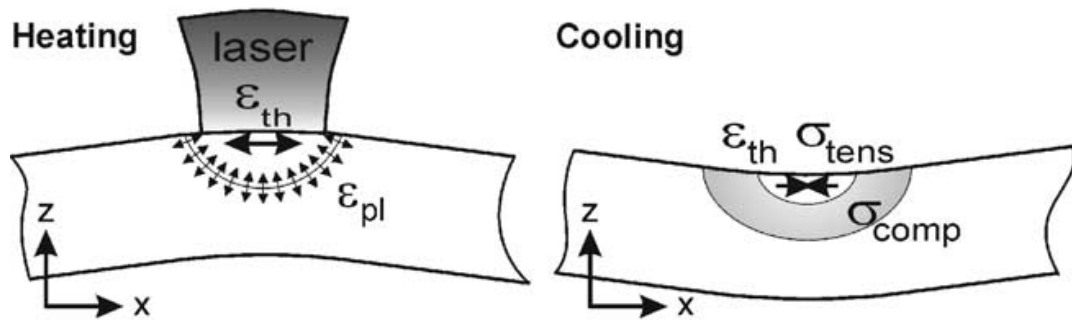
Figure 2.7: Development of residual stresses during SLM (Source: Mercelis and Kruth, 2006)

2.5.2 Heat transfer in SLM and implications for residual stresses

Krauss *et al.* (2012), point out that many process errors and product quality problems result from insufficient heat dissipation. The temperature evolution and distribution during SLM is influenced by various process parameters such as laser power, laser diameter, laser beam velocity and material properties. Rapid heating and solidification contribute the most significant part in development of thermal stresses during SLM. The evolution of powder to solid is characterised by volume shrinkage (Loh *et al.*, 2015) in which the irradiated powders melt and sink into the pores of the powder. The degree to which the volume shrinkage happens depends on temperature levels and distribution and/or heat transfer mechanisms at play during

the process. Non-uniform expansion and contraction (curling) is also responsible for warping during the building process (Campanelli *et al.*, 2010).

During SLM, heat is transferred via three mechanisms namely conduction, radiation and convection (Zeng *et al.*, 2012; Li and Gu, 2014b). Heat conduction occurs inside the powder bed and between the powder bed and substrate. Heat transfer through convection occurs between the powder bed and environment (Zeng *et al.*, 2012) as shown in Figure 2.8.
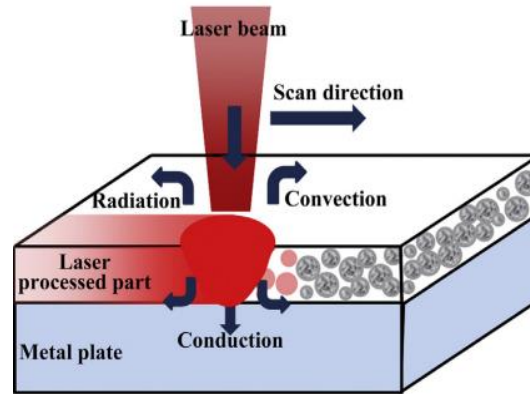
Figure 2.8: Heat Transfer during SLM (Source: Li and Gu, 2014a)

According to Roberts (2012), the bulk of the heat is transferred via conduction. The portions accounted for by convection and radiation are very small and usually neglected in thermal analysis without causing any significant errors. However, it is important to study the heat transfer through all three mechanisms. Zeng *et al.* (2012) cite Carslaw and Jaeger who, in 1959, proposed a solution to Fourier's governing equation and boundary condition equations for 3D heat conduction through a solid in a domain D. These equations have been used by other authors to model SLM temperature distributions, for example Ma and Bin (2007), as well as Li and Gu (2014a, 2014b).

$$\rho c \frac{\partial T}{\partial t} = k \left(\frac{\partial^2 T}{\partial x^2} + \frac{\partial^2 T}{\partial y^2} + \frac{\partial^2 T}{\partial z^2} \right) + Q \tag{2.3}$$

with initial condition:

$$\text{Initial temperature at time t=0:} \ T(x, y, z, t) = T_0 \tag{2.4}$$

Boundary conditions:

$$\text{Surface radiation and convection:} \ -\lambda \frac{\partial T}{\partial z} = \varepsilon_\theta \sigma (T^4 - T_0^4) + h(T - T_0) \tag{2.5}$$

where T is the final melt pool temperature, k the thermal conductivity coefficient, ρ the density, c the heat capacity coefficient, Q the internal heat, T_0 the powder bed initial temperature (ambient environment temperature), ε_θ the thermal radiation coefficient (or emmissivity), σ the Stefan-Boltzmann constant, and h the convection heat transfer coefficient. The internal heat energy Q represents laser heating or volumetric absorption of laser radiation (Gusarov *et al.*, 2007; Ma and Bin, 2007). A lot of other considerations have been put forward, and the governing equation has been modified to take into account the laser heat source, phase changes, enthalpy (Gusarov *et al.*, 2007), absorption, powder (volume) shrinkage, and evaporation (Verhaeghe *et al.*, 2009). When considering enthalpy (Gusarov *et al.*, 2007), the governing heat conduction equation is written as:

$$\frac{\partial H}{\partial t} - v \frac{\partial H}{\partial x} = k \left(\frac{\partial^2 T}{\partial x^2} + \frac{\partial^2 T}{\partial y^2} + \frac{\partial^2 T}{\partial z^2} \right) + Q \qquad \textbf{(2.6)}$$

where H is the volumetric enthalpy and v is the scanning velocity.

What is clear from the heat transfer equations is that steep cooling rates can be expected due to the localised heating and rapid movement of the laser beam as well as differences in the melt pool temperature T and the ambient temperature T_0. Furthermore, the linear thermal strain ε_{th} upon solidification is proportional to the difference between the powder bed temperature and final melt pool temperature as shown in Equation ((2.7) (Roberts, 2012). Thus, huge strains and corresponding stresses are expected to be present in solidified components.

$$\varepsilon_{th} = \int_{T_0}^{T} \propto dT \qquad \textbf{(2.7)}$$

where $\propto$ is the coefficient of thermal expansion.

2.5.3 Effects of residual stresses

Although residual stresses are reported to be a driving force for recrystallisation, they are generally undesirable (Sames *et al.*, 2016). The negative effects of residual stresses include cracking of parts and delamination from the baseplate, warping distortions and compromised mechanical strength (Y. Li *et al.*, 2018).

2.5.3.1   Cracking and delamination

The brittleness that is associated with SLM parts and the SLM process characteristics, especially occurrence of residual stresses, combine together to cause crack formation and delamination (Kempen *et al.*, 2013). Figure 2.9 shows an SLM manufactured part with cracks due to thermal stresses (Kruth *et al.*, 2012). Tensile residual stresses tend to open up cracks while the reverse is true for compressive residual stresses. Compressive residual stresses can therefore be desirable since they increase load resistance and slow down crack propagation rate. Unfortunately, residual stresses are largely tensile in nature, particularly near the free surface (Casavola *et al.*, 2008; Knowles *et al.*, 2012). As described earlier in section 2.5.1, it is evident that the upper layer is constrained from shrinking by the solidified layers underneath, and will retain net tensile stresses as explained by Merciles and Kruth (2006). Thermal stress related cracking and delamination has also been reported by Kempen *et al*. (2013).

<div align="center">(a)   (b)   (c)</div>
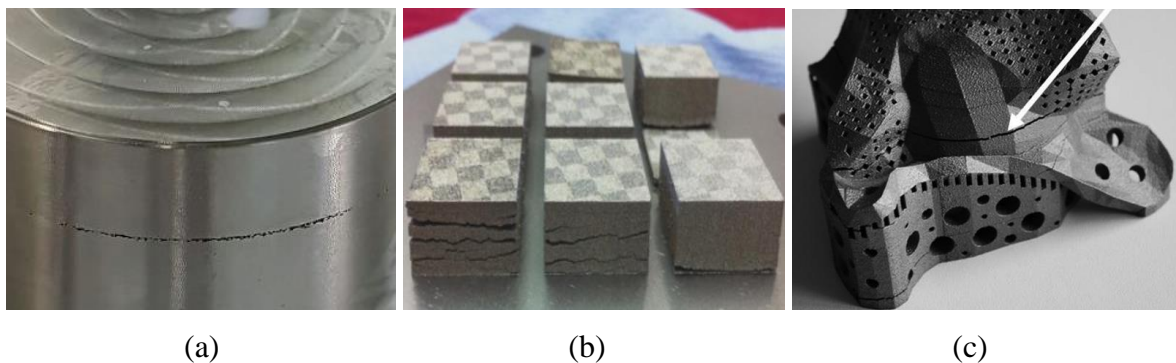
Figure 2.9: Stress induced cracking and delamination of SLM manufactured parts (a)
In-house work **(b)** (Kempen *et al.*, 2013) **(c)** (Kruth *et al.*, 2012)

2.5.3.2   Warping and dimensional distortions

Stress-induced distortion during consolidation is a major concern in SLM. The action of expansion of the top heated layer, which is also hindered by the colder, underlying substrate, leads to macroscopic curvature (warping) of the part under build when these stresses exceed the local yield stress of the material (Casavola *et al.*, 2008; Sames *et al.*, 2016). This phenomenon is well represented in Figure 2.7. Kruth *et al.* (2012) report that warping of SLM manufactured parts is a result of large and rapid temperature fluctuations experienced by the irradiated material. These large temperature fluctuations are likely to cause non-uniform cooling which may result in huge stresses and bending of the part's externals as explained by Zaeh and Branner (2010). Farrel and MacGregor (2010) also report that the magnitude of residual stresses has an influence on the degree of distortion of finished parts. These distortions

are of greater concern than stress-related premature failure (Aggarangsi and Beuth, 2006). According to King *et al*. (2015), AM processes can manufacture parts to required tolerances as long as parts are still attached to the baseplate. However, once the parts are removed from the baseplate, distortions may become noticeable due to residual stresses released upon separation.

2.5.3.3   Reduced mechanical strength

Since residual stresses impose a pre-loading stress condition, it means the load bearing capacity is reduced for components with residual stresses in them. Residual stresses are responsible for reduced yield strength of SLM-built parts (Kruth *et al.*, 2010; Zaeh and Branner, 2010). In some instances, residual stresses formed inside manufactured parts can come close to or even exceed the yield strength of the material. This results in reduced mechanical strength, leading to premature fracture of the component, even at low loads (Knowles *et al.*, 2012; Kruth *et al.*, 2012). Residual stresses may even cause failure of parts during the consolidation process (Jhabvala *et al.*, 2010). The fatigue strength of materials is greatly compromised by the presence of residual stresses since they increase fatigue crack growth rates (Leuders *et al.*, 2013; Vrancken *et al.*, 2014; Becker and Dimitrov, 2016).

2.6   Management of residual stresses

Common residual stress management methods include pre-heating, re-melting, heat treatment, and adjustment of scanning strategies. Residual stresses can also be managed by in-process monitoring, or pre-process thermal stress and/or distortion prediction. This allows for adjustment of process parameters before problems occur. A less common method is laser shock peening. This process introduces compressive stresses in SLM built parts. In an effort to address this, a new method of integrating laser shock peening and SLM has been recently described by Kalentics *et al.* (2017).

2.6.1 Thermal monitoring and numerical solutions for the SLM thermal problem

Experimental measurements of temperature during SLM are generally difficult to conduct due to rapid heating and cooling cycles that characterise the process (Li and Gu, 2014b). Novel methods such as thermography have been employed to investigate thermal behaviour during SLM. Infrared cameras have also been used as seen from research by Craeghs *et al*. (2011) and Krauss *et al.* (2012). However, poor resolution and cost implications work against use of cameras. Furthermore, experimental measurements alone are insufficient in providing information regarding thermal behaviour of the process and needs to be complimented with

Finite Element (FE) modelling (Dai and Gu, 2015). Finite Element Analysis (FEA) has been widely used to analyse thermal aspects of SLM and their influence on the overall process. A major limitation of FE for the SLM process is the long computational times which can take several hours or even days. To reduce the computational time, small models are used; these models usually range from 0.5 mm × 0.5 mm × 0.15 mm to 2 mm × 2 mm × 0.6 mm. The results are then mapped to obtain the behaviour at a macro or bigger scale but may not always be representative of the real physical environment because residual stresses depend on, and develop with part size. FE simulation lacks transferability of results due to many material specific assumptions and inadequate understanding of the physics of SLM (Schoinochoritis *et al.*, 2017).

2.6.2 Powder-bed, baseplate and chamber pre-heating

Some solutions have been suggested and implemented to reduce build-up of residual stresses and their effects on cracking and warping distortions. One of the most common intervention is pre-heating of the baseplate and/or powder bed (Campanelli *et al.*, 2010; Kempen *et al.*, 2014). The idea behind pre-heating of the powder bed is to reduce temperature gradients between consecutive layers since the new layer being introduced is already at an elevated temperature which compares to the temperature of the underlying layer (Casavola *et al.*, 2008). Gusarov *et al*. (2011) note that residual stresses are proportional to the difference between ambient and melting temperatures; hence by preheating powders, this difference is reduced. A study by Ali *et al* (2017) shows a general decline in residual stresses with increase in powder-bed (pre-heat) temperature. In that work, residual stresses were reduced from 214 MPa at standard powder bed temperature of 100°C to 1 MPa at a powder-bed temperature of 570°C. In another study, preheating the powder bed to 150°C improved the dimensional accuracy of 316L stainless steel tensile test specimens by 10 % (Zhang *et al.*, 2013). Preheating of the powder was also shown to significantly reduce residual stresses in SLM of AlSi10Mg (Wang *et al.*, 2018).

Pre-heating of the base plate has proven to reduce residual stresses significantly. Shiomi *et al*. (2004) posted a 40% decrease in residual stresses when the baseplate was preheated to 160°C compared to when no preheating was done. Kempen *et al*. (2013) used preheating temperatures of 90°C, 150°C and 200°C to demonstrate that increasing the preheating temperature of the baseplate progressively reduces stress related cracking and delamination in SLM of M2 HSS parts. Furumoto *et al*. (2010) studied the effect of baseplate preheating and the results showed reduction in residual stresses from around 1000 MPa (without baseplate preheating) to 200

MPa (with baseplate preheating). The results presented by Roberts (2012) for SLM of Ti6Al4V show that increasing the building chamber preheating temperature from 40ºC to 300ºC yields about 50 % reduction in residual stresses as shown in Figure 2.10. A corresponding reduction in deformation from 0.14 mm to 0.125 mm, was also recorded.
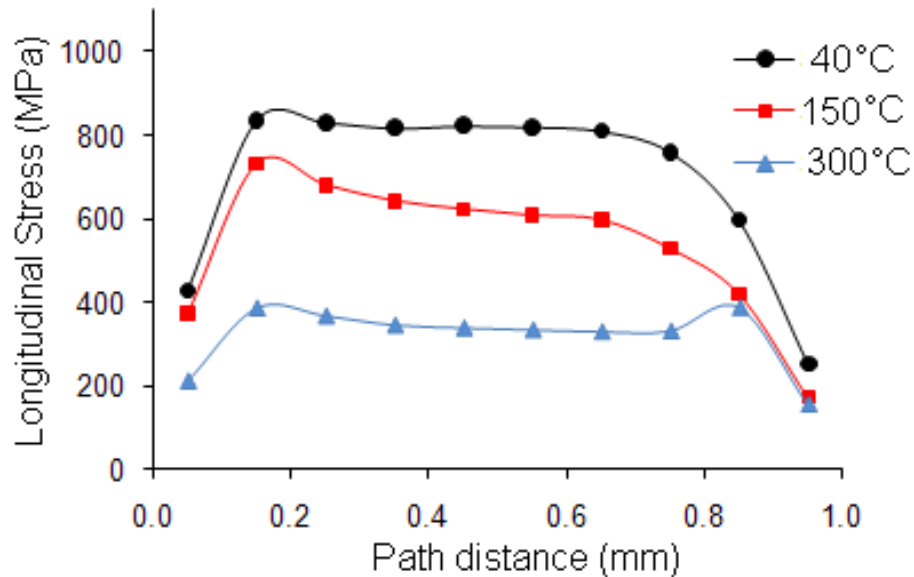
Figure 2.10: Effect of pre-heating the building chamber on residual stresses (Source: Roberts, 2012)

2.6.3 Re-scanning

Previous studies show that powder bed re-scanning significantly reduces residual stresses. In re-scanning, the laser beam moves a number of times over a single scan track, thus acting as a form of heat treatment to lower residual stress by relieving thermal stresses that could have been set up during the initial pass. For their study on effect of rescanning during SLM of chrome molybdenum steel powder mixed with copper phosphate and nickel powder, Shiomi *et al*. (2004) report that residual stresses were reduced by up to 55% by rescanning every layer. For SLM of 316L stainless steel, Mercelis and Kruth (2006) showed that re-scanning the powder bed at an energy density of 50% of the initial pass results in reduction of residual stresses in the range of 30% compared to when no re-scanning is performed. The apparent challenges that come with residual stress management methods such as pre-heating and re-scanning have to do with energy efficiency. It has been reported that up to 40 % of the energy used in SLM is associated with pre-heating (Papadakis *et al.*, 2018). Furthermore, re-scanning increases the building time (and total manufacturing cost).

2.6.4 Post-process heat treatment

Post-process heat treatment is also an effective way of reducing stresses in finished parts, but it cannot remove those stresses that led to warping and delamination during the build process (Meier and Haberland, 2008). Annealing is commonly used to negate the effects of residual stresses in finished parts, and this can be carried out whilst the built parts are still attached to the baseplate (Manfredi *et al.*, 2013; Pupo *et al.*, 2013; Sames *et al.*, 2016). Shiomi *et al.* (2004) investigated the effect of stress relief heat treatment by heating the finished parts in a muffle furnace for about one hour. Their results show that heat treatment at 600ºC for 1 hour reduced residual stresses by 70%.

2.6.5 Scanning strategy improvements

Scanning strategy refers to the pattern (or path) in which the laser is moved over the powder bed to effect melting. Scanning strategy adjustment is a solution to thermal stresses that can arise from inhomogeneous thermal shrinkage (Beal *et al.*, 2008; Jhabvala *et al.*, 2010). The common scanning strategies are discussed in the next sub-sections, with a special emphasis on their impact on residual stresses.

2.6.5.1   Parallel scanning strategy

According to Mohanty and Hattel (2014), the parallel scanning strategy, shown in Figure 2.11, is the most commonly used strategy in SLM. It has uni-directional and sometimes bi-directional scan lines that run parallel along the powder bed. The "sequential" variant of the parallel scanning strategy involves the scanning of neighbouring scan lines successively (Beal *et al.*, 2008). A variation to this is when the odd numbered scan lines are scanned successively before the even numbered lines, or vice-versa. Although this strategy is very easy to generate from a CAD file, it is associated with large temperature gradients especially at low scanning speeds. Increasing the scanning speed can reduce these temperature gradients but may result in other unfavourable phenomena such as partial melting of powders. Carter *et al.* (2014) call this strategy "a simple back and forth strategy".

The parallel strategy forms the basis of many other scanning strategies such as the paintbrush or stripe strategy (Jhabvala *et al.*, 2010; Yakout *et al.*, 2018) in which the scanning region is divided into strips that are then melted successively. The paint brush scanning strategy results in less overheating as compared to the typical parallel scanning strategy. However, this strategy results in poorly connected layers, leading to delamination (Jhabvala *et al.*, 2010).
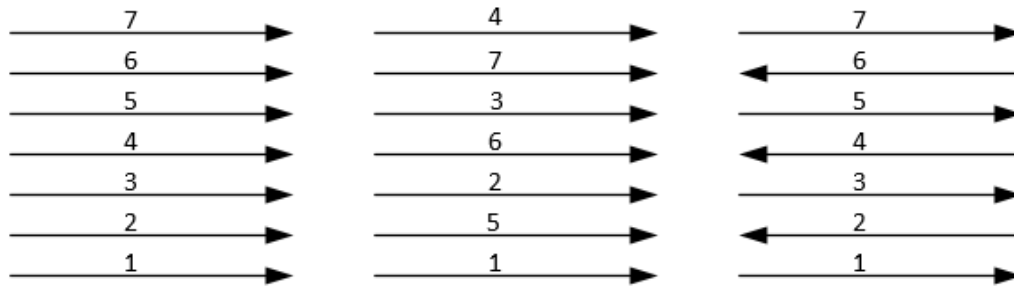
Figure 2.11: Parallel scanning strategy variants (Source: Beal *et al.*, 2008; Mohanty and Hattel, 2014)

2.6.5.2   Alternating x/y scanning strategy

The term "alternating x/y strategy" is used to describe the manner in which the succeeding layer is scanned relative to the previous layer. If the current layer is scanned along the x-direction, the hatches are turned through 90° for the next layer to scan along the y-direction as shown in Figure 2.12. This pattern continues for the rest of the build. In a way, this "scanning strategy" is the implementation strategy for the parallel scanning strategy through cross-hatched vectors (Beal *et al.*, 2008; Meier and Haberland, 2008). Kruth *et al.* (2004) described line X and line Y scanning strategies which can be considered two different strategies for implementing the parallel scanning strategy. In the line X strategy, the laser beam scans along the X direction only until the part is built. The same can be said of the line Y strategy. It appears that the apparent weaknesses of the line X and line Y strategies are overcome by implementing an alternating x/y strategy. This scanning strategy has a limitation in that the scan lines are too long in at least one direction, and therefore thermal distortions are likely to be very high (Zaeh and Branner, 2010).
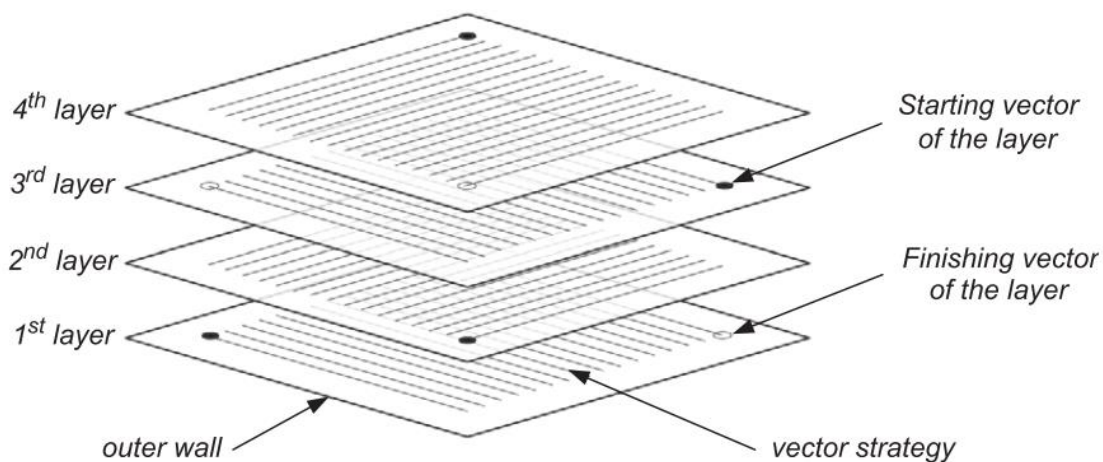
Figure 2.12: Alternating x/y scanning strategy (Source: Beal *et al.*, 2008)

2.6.5.3   Spiral scanning strategy

In this strategy, the laser beam moves continuously or progressively in a spiral manner. Although it eliminates overheating of surfaces perpendicular to the scanning direction, the spiral scanning strategy is associated with excessive overheating around the centre of the part (Jhabvala *et al.*, 2010). Fateri *et al.* (2012) reported that the spiral scanning strategy is associated with higher deformations and dimensional inaccuracies when compared to linear/parallel and random scanning strategies. Similar findings are posted by Cheng *et al.* (2016). Two variations of the spiral scanning strategy are available - the in-spiral and out-spiral strategies (Mohanty and Hattel, 2014). With in-spiral scanning, the laser beam scans from the borders towards the centre of the scanning area as shown in Figure 2.13. With the out-spiral strategy, the scanning begins at the centre of the scanning area towards the borders of this area. The spiral scanning strategy is similar to the so-called fractal scanning pattern. In separate studies on scanning strategies by Ma and Bin (2007) as well as Yu et *al*. (2011), the fractal strategy was shown to result in more uniform heat distribution and less distortion compared to strategies such as the spiral and the raster (parallel). The traditional spiral scanning strategies have recently been developed or improved into the "varying-helix island scan strategy" which utilises much shorter scan vectors (Hagedorn-Hansen *et al.*, 2017).
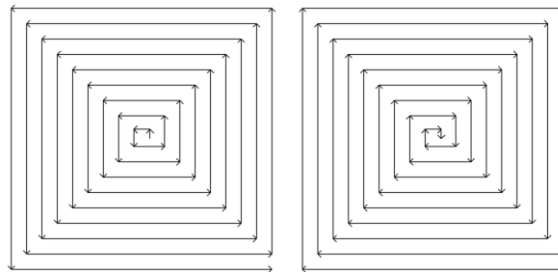
Figure 2.13: Spiral scanning strategy variants (Source: Jhabvala *et al.*, 2010; Mohanty and Hattel, 2014)

2.6.5.4   Chessboard scanning strategy

The chessboard scanning strategy is modified version of the parallel scanning strategy in which the area is divided into small squares. These squares are usually called sub-sectors. Successive squares can be scanned in alteranating scanning directions according to the parallel scanning pattern (Figure 2.14). This strategy lowers stresses resulting from thermal inhomogenity and is more or less the same as the "island" strategy by Concept Laser. The scanned areas are smaller compared to parallel and spiral strategies, therefore, thermal homogenity is easier to maintain (Jhabvala *et al.*, 2010; Wang *et al.*, 2018). The scan vectors can be oriented at various angles

at each layer as these will directly influence the vector lengths, thus also affecting temperature distributions.
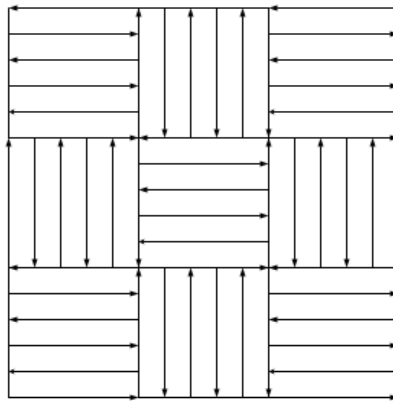
Figure 2.14: Chessboard scanning strategy (Source: Jhabvala *et al.*, 2010)**.**

2.6.5.5   Island scanning strategy

The "island" scanning strategy, patented by Concept Laser, is probably the leading strategy for reduction of residual stresses (Carter *et al.*, 2014). In the island scanning strategy, the large scanning zone is divided into several small scanning regions of usually 5 mm × 5 mm which are then scanned randomly (Yasa *et al.*, 2009; Kruth *et al.*, 2010, 2012; Carter *et al.*, 2014). A patent held by Concept Laser GmbH (DE 10 2006 059 851 B4) proposes that successive scan lines (labelled *a, b, c, d, e* ….. in Figure 2.15) should not lie next to each other. This ensures that no tension occurs between the current and previously irradiated segments. The spaces labelled A, B, C, D, E, …. are the "islands" to be scanned, with *a, b, c, d, e,* etc. showing the sequence of movement of the laser beam as it scans the powder bed.
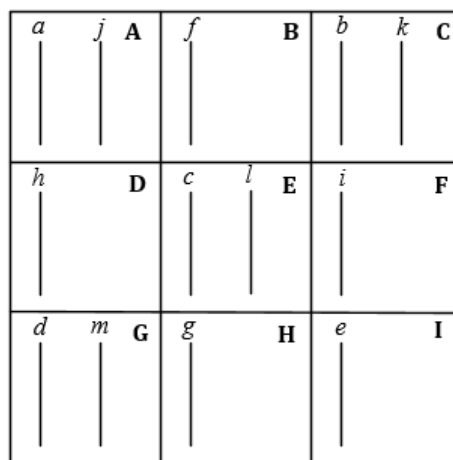
Figure 2.15: Scanning pattern as patented by Concept Laser (Adapted from Herzog, 2009)

2.6.5.6   Other variations of scanning strategies based on scanning order

Scanning strategies come with various scanning patterns which can be manipulated as needed. For example, a set of scanning parameters or patterns can be adopted when scanning the shell of a part whilst a different set of parameters will be chosen for the core. The sequence followed in scanning the powder bed has been used to further classify certain types of scanning patterns as suggested by Kruth *et al.* (2004) and Zhang *et al.* (2009). These strategies resemble the scanning strategies discussed earlier. For example the "sector 5" and "sector 2.5" (Figure 2.16) in Kruth *et al*. (2004) are simply the chessboard strategy utilising different sizes of scan sectors (5 mm and 2.5 mm square, respectively). The so-called sector 5 – LHI (Least Heat Input) and sector 2.5 – LHI are also a form of the island scanning strategy in which two neighbouring "islands" or sectors are not scanned successively.
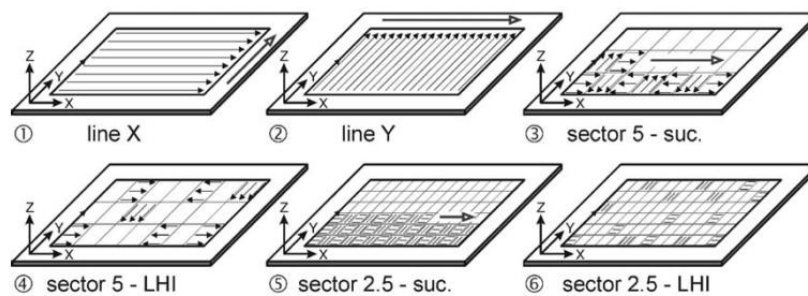
Figure 2.16: Variations of scanning strategies (Source: Kruth *et al.*, 2004)

2.6.6 Summary

A lot of progress in the management of residual stresses has been recorded, particularly by means of pre-heating (powder-bed, baseplate or build chamber), scanning strategy improvements, as well as post process heat treatment. From the comparative summary in Table 2.1, heat treatment seems to be the most effective method for reducing residual stresses but increases the cost and time of realising products considerably. Although stress induced warping that occurs after separation of parts from the baseplate can be effectively managed by heat treating whilst the parts are still attached to the plate, this method (heat treatment) fails to manage the in-situ problems arising from residual stresses such as warping and delamination. Residual stress management approaches that effectively deal with the in-situ effects of residual stresses on warping and cracking lie in pre-heating, scanning strategy and process parameter optimisation. Whilst pre-heating is effective, it is not cost and energy efficient, and is usually not available as for some LPBF systems.

When evaluating effect of scanning strategies on residual stresses, the effect on porosity should be considered because strategies that result in the least stresses could also be associated with porosity. This is one important consideration that has not been taken into account by previous researchers.

Table 2.1: Summary of residual stress management approaches

Strategy	References	Effectiveness
Powder pre-heating	(Shiomi *et al.*, 2004; Campanelli *et al.*, 2010)	40 %
Base-plate preheating	(Mercelis and Kruth, 2006; Furumoto *et al.*, 2010; Kruth *et al.*, 2012; Kempen *et al.*, 2013)	40 – 50 %
Rescanning	(Shiomi *et al.*, 2004; Mercelis and Kruth, 2006; Jhabvala *et al.*, 2010)	30 – 55 %
Scan vector length shortening	(Mercelis and Kruth, 2006; Zaeh and Branner, 2010; Kruth *et al.*, 2012; Vrancken *et al.*, 2014; Wu *et al.*, 2014; Li *et al.*, 2016)	40 %
Process parameter adjustment	(Vrancken, 2016)	*50 %
Heat treatment	(Shiomi *et al.*, 2004; Meier and Haberland, 2008; Furumoto *et al.*, 2010; Kruth *et al.*, 2012; Yadroitsava and Yadroitsev, 2015)	70 – 80 %

*- value inferred from stress induced curvature differences

This literature analysis has demonstrated that scanning strategies play a vital role in determining the form and dimensional distortions that usually arise from residual stresses. An evaluation of common scanning strategies is presented in Table 2.2 based on the discussions already presented. The scores allocated for each scanning strategy is consistent with discussions presented between sections 2.6.5.1 and 2.6.5.6. Strategies that employ short scan vectors show a lot of promise with respect to promoting thermal homogeneity and, thereby, reducing residual stresses. These scanning strategies (that utilise short scan vectors) can be used as a basis for further improvement by attempting to develop scan sequences that are more structured rather than random. From the independent results presented by Kruth *et al*. (2004) and Li *et al*. (2016), there is an opportunity to combine the LHI and the successive sector scanning strategies by getting the best out of each. Improved scanning strategies could attempt to evenly distribute heat throughout the scanned layer whilst benefitting from heat accumulation between successive scanning lines to manage thermal gradients.

Table 2.2: Scanning strategy evaluation

Scanning strategy	EVALUATION CRITERIA			
	Thermal homogeneity	Residual stress reduction	Effect on scanning time	Ease of implementation
Parallel	⊕	⊕	●	●
Alternating x/y	◑	◐	◕	◕
Spiral	⊕	⊕	◐	◕
Chessboard	◕	◕	◐	◐
Island	◕	◕	◐	◐

LEGEND

●	◕	◐	◑	⊕
Very good	Good	Average	Poor	Very poor

2.7 Measurement of residual stresses

Residual stress measurement methods are generally classified as destructive or non-destructive, although some of them *can* also be considered to be semi-destructive. Residual stress measurement techniques measure strain which is then converted to stress based on the material properties and the measurement principle. The choice of the measurement technique should be based on the type of stress to be measured. For example, material removal methods such as hole-drilling and layer removal techniques remove "large" volumes of materials; consequently, that Type II and Type III stresses cannot be measured (Kandil *et al.*, 2001).

2.7.1 Destructive techniques

All destructive methods of measuring residual stresses work on the same principle of inducing stress relaxation, followed by strain measurement. Thus, destructive techniques are also called relaxation methods (Schajer, 2010b). Stress relaxation can be achieved by cutting or removing some material from the specimen. Common destructive methods are the crack compliance, layer removal, contouring, sectioning and ring core drilling methods.

2.7.1.1 Layer removal

The layer removal method is a destructive technique that is used to measure residual stresses in flat plates. Removal of a layer of a flat plate results in an unbalance of stresses (if any) and the plate bends at the ends in order to achieve equilibrium, obeying the Euler–Bernoulli beam theory (Dreier and Denkena, 2014). The curvature formed depends on the magnitude and

distribution of the stress present in the layer that was removed and the elastic properties of the remainder of the plate. A series of layers are removed one after the other, with curvatures being measured each time to evaluate the strains (Kandil *et al.*, 2001; Dreier and Denkena, 2014). Other methods which use comparable principles are the crack compliance and sectioning methods.

2.7.1.2   Hole drilling (strain gauge) method (HDM)

The HDM method is standardised as per ASTM 837-08 (Knowles *et al.*, 2012). In this method, a small hole is drilled in the centre of a strain gauge rosette attached to the surface of the component to be measured. The hole that is drilled is usually repairable or tolerable since it does not cause significant damage to the specimen surface and thus HDM can also be viewed as non-destructive or semi-destructive (Micro-Measurements, 2010; Schajer, 2010a). The action of drilling the hole relieves locked-up stress; and this is accompanied by a change in the strain state, which can easily be measured using the strain gauge. The strain change is then used to compute the equivalent stress state through a series of equations as outlined in the theory of Kirsch (Casavola *et al.*, 2008; Knowles *et al.*, 2012). Strain gauge rosettes come in different types – 3-gauge, 4-gauge, 6-gauge, 9-gauge and 12-gauge rosettes. While increasing the number of gauges increases measurement accuracy, complexity of setting up is also greatly increased (Schajer, 2010a). For a 3-gauge strain gauge rosette, three strains associated with each of the three gauges can be measured. From these strains, the maximum and minimum principal stresses can be calculated from Equation ((2.8) (Ajovalasit *et al.*, 2010; Micro-Measurements, 2010).

$$\sigma_{max}, \sigma_{min} = \frac{\varepsilon_1 + \varepsilon_3}{4A} \pm \frac{\sqrt{(\varepsilon_3 - \varepsilon_1)^2 + (\varepsilon_3 + \varepsilon_1 - 2\varepsilon_2)^2}}{4B} \qquad (2.8)$$

where $\varepsilon_1, \varepsilon_2$ and ε_3 are the strains from gauge 1, 2 and 3 respectively. *A* and *B* are calibration constants.

2.7.1.3   Bridge curvature method

The principle of the bridge curvature method (BCM) is similar to the layer removal technique. A bridge shaped part is built on a baseplate and later cut off. After cutting off from the base plate, the bridge bends due to the residual tensile stresses at the top of the part, resulting in the planes at the bottom of the pillars deviating from their normal positions. The angle through which this deviation occurs is a semi-quantitative measure or indication of the residual stress

relieved (Kruth *et al.*, 2010, 2012; Vrancken *et al.*, 2013). Finite Element (FE) modelling is used to calculate the actual residual stresses corresponding to this measured curl up angle, α. The BCM method is illustrated in Figure 2.17.
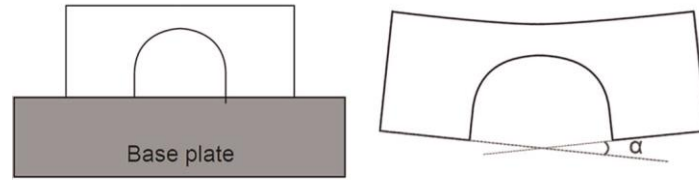
Figure 2.17: Bridge geometry before and after removal from baseplate (Source: Kruth *et al.*, 2012)

2.7.1.4   Contour method

In the contour method, the component under investigation is carefully cut into two using non-stress-inducing methods such as wire Electric Discharge Machining (wEDM). When the surface of the plane of interest is cut, residual stresses are relieved, causing deformations or deviations of the cut surfaces from the expected surface profile. These surface distortions can be measured using a touch probe of a coordinate measurement machine or a laser profilometer. The contour method is carried out by following three basic steps (A to C) as shown in Figure 2.18. The original stress state is determined by superimposing the partially relaxed stress state at B with the stress change at C (Pagliaro *et al.*, 2010; Prime and Dewald, 2013; Hosseinzadeh *et al.*, 2014).

$$\sigma^A(x, y, z) = \sigma^B(x, y, z) + \sigma^C(x, y, z) \tag{2.9}$$

where $\sigma^A, \sigma^B \ and \ \sigma^C$ represent the entire stress tensor (normal and shear). Since there is a zero stress state at B, the original stress at A is given by the change in stress at C only. The shear stress components are usually ignored since they are small (Pagliaro *et al.*, 2010).

$$\sigma_x^A(0, y, z) = \sigma_x^C(0, y, z) \tag{2.10}$$

The contour method only measures the stress component normal to the cut. Thus, multiple cuts are necessary to determine multi-axial stress components. Recently the multi-axial contour method has been developed to determine 3D stress maps by introducing multiple cuts along different planes (or axes) of interest to measure the stresses normal to the cut planes, for example by following steps A-B-D-E in Figure 2.18 (Pagliaro *et al.*, 2010). This method has

relied on FE modelling to calculate the stresses in components up until recently when Kartal (2013) developed the analytical solution which replaces the need for exclusive reliance on FE modelling.
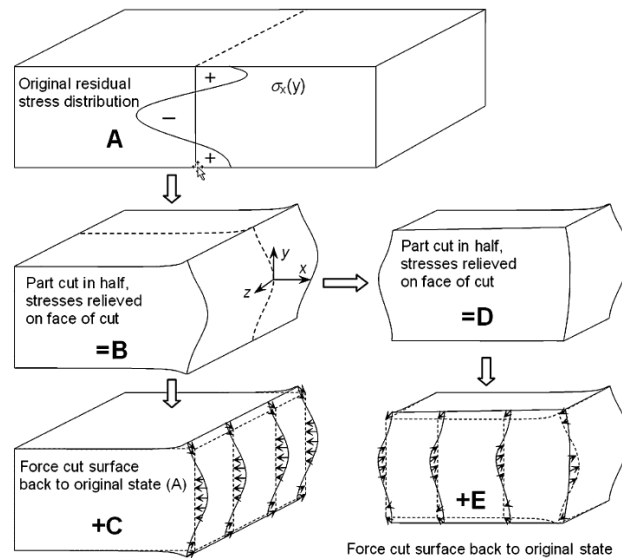
Figure 2.18: Contour method superposition principle (Source: Pagliaro *et al.*, 2010)

2.7.1.5   Digital image correlation (DIC)

Non-contact optical residual stress measurement methods do not involve use of strain gauges but can be accompanied by hole-drilling or sectioning (and any other displacement techniques). Examples of these methods are the Digital Image Correlation (DIC) technique, brittle and photo-elastic coatings, shearography as well as interferometry methods (electronic speckle-pattern interferometry and moiré interferometry) (Nelson, 2009). These optical techniques have the obvious advantage of reduced measurement cost by eliminating the need for strain gauges. Furthermore, as noted by Nelson (2009), optical methods combined with hole-drilling make it possible to take measurements at points that would ordinarily be difficult to mount strain gauges. DIC acquires strain data from images by comparing the location of a subset or block of pixels on a test piece before and after deformation (Lord *et al.*, 2008; Yang *et al.*, 2010). The image taken before deformation is the reference image and several other images can be taken at different stages of the deformation. Imaging can be done using a scanning electron microscope (SEM) (Nelson, 2009; Zhu *et al.*, 2014; Mansilla *et al.*, 2015) and other high speed cameras. DIC is simple to set up and provides for fast, accurate and non-contact acquisition of strain data during measurement (Yang *et al.*, 2010; Wu *et al.*, 2014). This method also requires very little surface preparation unlike the hole-drilling strain gauge method and XRD.

2.7.2 Non-destructive techniques

As the name suggests, the strain measurement principles and techniques applied in non-destructive methods do not lead to specimen damage. Non-destructive techniques for residual stress measurement include x-ray diffraction (XRD), neutron diffraction, ultrasonic and electromagnetic methods.

2.7.2.1 Neutron diffraction

Neutron diffraction measurement is a non-destructive technique for evaluating residual strain/stress through measuring the change in the spacing between the planes of the atomic lattice (crystallographic lattice spacing, d) and utilising Bragg's and Hooke's laws to measure subsurface tri-axial stress distributions (Cheng *et al.*, 2012). Effectively, this residual stress measurement method uses the inter-atomic d-spacing as a built-in strain gauge. Uncharged neutrons have a high penetrating power since they do not interact with and are not impeded by electrons in materials. With the ability to penetrate the specimen to depths up to 60 mm (and even 300 mm for aluminium), almost 1000 times X-rays (Suzuki *et al.*, 2011; Acevedo *et al.*, 2012; Cheng *et al.*, 2012), this technique is capable of measuring volumetric residual stress in thick specimens. The principle of this technique is that when a beam of neutrons is incident on the surface of a material, those atomic planes that are correctly orientated with respect to the measurement geometry will diffract the neutrons at a diffraction angle 2θ which is precisely measurable. The lattice plane spacing is calculated from this angle and the monochromatic wavelength of the neutrons used by employing Bragg's Law of constructive interference according to:

$$n\lambda = 2dsin\theta$$

<div align="right">(2.11)</div>

where n and λ represent the order and wavelength of the neutron radiation respectively. The residual strains can be calculated using Equation ((2.12) based on the change of lattice spacing before (d_0) and after (d) residual stress was introduced (Cheng *et al.*, 2012).

$$\varepsilon = \frac{d - d_0}{d_0}$$

<div align="right">(2.12)</div>

The strains are converted to stresses by applying Hooke's law with the incorporation of the appropriate elastic constants in Equation ((2.13) (Acevedo *et al.*, 2012; Cheng *et al.*, 2012).

$$\sigma_{x,y,z} = \frac{E}{1+v}\left[\varepsilon_{x,y,z} + \frac{v}{1-2v}(\varepsilon_x + \varepsilon_y + \varepsilon_z)\right] \qquad \textbf{(2.13)}$$

where E and v are the modulus of elasticity and Poisson's ratio for the material being tested. One limitation of the process is that large facilities in the form of nuclear reactors are needed as a source of neutrons and these are usually only available as central facilities for national governments.

2.7.2.2   X-ray diffraction

X-ray diffraction (XRD) is the most widely used non-destructive technique for analysing residual stresses and has a working principle similar to neutron diffraction, except that it employs x-rays rather than neutron to penetrate the material. The principle of this method is that when irradiated x-rays penetrate a material, the crystal planes of the material will diffract some of these rays. Using a detector, the angular positions of these diffracted rays are detected and their intensity at these positions is recorded. These positions are compared to the supposed original positions and, using Bragg's law, the new lattice spacing is calculated and the strains that resulted from the deformations, are also evaluated. This method is applicable for analysing surface stresses and are limited to shallow depths of below 50 µm (Farrel and MacGregor, 2010; Kuznetsov *et al.*, 2012; Wu *et al.*, 2014). Surfaces to be tested should be free from grease, coatings and roughness that might act as barriers to the x-ray beam, leading to many errors (Casavola *et al.*, 2009; Farrel and MacGregor, 2010). However, surface roughness reduction methods like polishing, may also induce stresses in the specimen. Therefore, as much as possible, specimens must be evaluated in the as-received condition. The cost per measurement using XRD is relatively lower compared to techniques that rely on strain gauges.

2.7.2.3   Ultrasonic Technique

The Ultrasonic (US) technique is a qualitative method that utilises the sensitivities of the velocity of ultrasound waves to the stress levels within the solid through which the wave is passing. Since the velocity of sound through the solid is directly affected by the magnitude and direction of stresses present (Kandil *et al.*, 2001), the variations of sound velocity in a stressed and non-stressed material can be used as the basis for evaluation of residual stresses using the ultrasonic technique (Belassel *et al.*, 2006) as given in Equation ((2.14).

$$v = v_0 + K\sigma$$

$$\textbf{(2.14)}$$

where v and v_0 denote the velocity of sound through stressed and non-stressed material respectively. K is the acoustoelastic constant, which is a function of the characteristic microstructure. The spatial resolution of this technique is very poor due to the presence of texture in the material (Kandil *et al.*, 2001).

2.7.3 Summary

Residual stress measurement methods are usually evaluated based on measurement cost, accuracy, and resolution among other considerations. The characteristics of the various residual stress measurement methods are given in Table 2.3 based on research by Huang *et al*. (2013), Prime (1999) and Belassel *et al*. (2006)

Table 2.3: Comparison of residual stress measurement methods

Method	Cost of equipment	Cost per measurement	Accuracy	Spatial resolution	Time per measurement	Maximum depth of measurement
LR	$100 000	> $60	±10 MPa	100 mm^2	Up to 5 hrs	½ specimen thickness
Contour	$100 000	< $20	±10 MPa	10 – 100 µm	Up to 5 hrs	Specimen thickness
BC	< $50 000	< $20	-	100 mm^2	1 – 3 hrs	-
HDM	≈ $40 000	> $60	±50 MPa	0.5 mm^2	1 hr	Up to 2 mm
DIC	> $50 000	< $10	±50 MPa	< 100 µm	Up to 5 hrs	Up to 2 mm (with HDM)
ND	> $150 000	< $10	±20 MPa	1 mm^3	Up to 2 hrs	Up to 50 mm in steel
XRD	≈ $150 000	< $10	±10 MPa	< 0.5 mm^2	10 min	5 – 50 µm
US	< $50 000	< $10	±20 MPa	0.1 – 30 mm^2	5 – 20 min	60 – 300 mm

The DIC technique combined with hole-drilling is limited to a few millimetres depth of measurement. The contour method, although destructive in nature, allows for analysing strains and stresses at various points along the length and depth of the cut surface. However, the method is prone to errors that can arise from rigid body motion and wire breakages. In terms of cost per measurement, methods that involve use of strain gauges are expensive and limit the number of measurement points. The cost per measurement for the non-destructive methods such as XRD and ND is low, whilst the measurement accuracy is high. However, XRD is limited to near surface measurements whereas ND is capable of deep penetration and is thus suitable for measuring depth-resolved stresses. The XRD and ND techniques are identified as ideal candidates for adoption in this research since they complement each other. These two methods are ranked first and second respectively by Belassel *et al.* (2006) based on a number of criteria, including repeatability and non-destructiveness.

2.8   Conclusion

Residual stresses setbacks still limit wider application of the SLM process as they negatively impact on the quality and performance of components. Residual stresses have been discussed widely in literature, but distribution of residual stresses in parts of varying size is poorly understood. Therefore, in order to manage residual stresses effectively, the distribution and magnitudes of these stresses must be investigated further. Some of the effects of residual stresses such as macro-cracking, delamination and warping, are non-reversible by post-processing methods. Therefore, managing residual stresses in-situ remains the most attractive option in dealing with this phenomenon. Opportunities to effectively manage these stresses in-situ lie in re-scanning, pre-heating, scanning strategy innovation and careful selection of process parameters. Re-scanning slows down the process and, therefore, its applicability should be evaluated taking into account the magnitude by which stresses are reduced against the loss in productivity and increase in manufacturing cost. Pre-heating methods are proven, and can be used together with other interventions such as process parameter optimisation and scanning strategy control. Unfortunately, pre-heating methods are not compatible with most SLM machines and in some instances powder-bed pre-heating may lead to degradation of metal powders. From a scanning strategy perspective, the most significant advances in reducing residual stresses have been brought about by reducing the scan vector length. However, the order of exposing the scanning area segments to the laser beam presents further opportunities for improving heat distribution and minimising residual stresses and their effects. Besides, researchers have not factored in the importance of considering the achievable part density in relation to residual stresses when comparing different scanning strategies. Careful selection of process parameters such as laser power, scanning speed and layer thickness, is a useful approach to minimising residual stresses and their effects, without negatively impacting on other important part outcome characteristics, in particular the part density. These parameters are highly interactive and are usually investigated simultaneously. Notably, optimised process parameters can only be as effective as the scanning strategy with which they are implemented.

Chapter 3: Conceptualisation

3.1 Introduction

In order to understand the effect of different process conditions on residual stresses and their accompanying effects on distortion, a quantitative experimental methodology is adopted for this research in line with the nature of the studies. The experimental investigation of residual stresses centres on the "gaps" and opportunities to understand and, effectively, manage these stresses and their effects. Firstly, an overview of the experimental methodology is given before proposing a method for evaluating residual stress management methods. The argument on how adjusting input parameters and scanning strategies can be used to improve end product characteristics, is presented. Scanning sequence variations are proposed based on the success stories discussed during literature analysis in the previous chapter. The methods for design of experiments used in this study, are also discussed.

3.2 Overview of the experimental investigation process

Foremost, a full understanding of residual stress distributions in SLM manufactured parts is necessary. To accomplish this, residual stresses are investigated for parts of different sizes (thickness). As a result, the major experimental investigations for the study revolve around part size, scanning strategies and process parameters as shown in Figure 3.1. The part geometry aspect is only investigated for thickness. Other geometric aspects such as features and part shape have already been investigated by Mugwagwa *et al*. (2016).
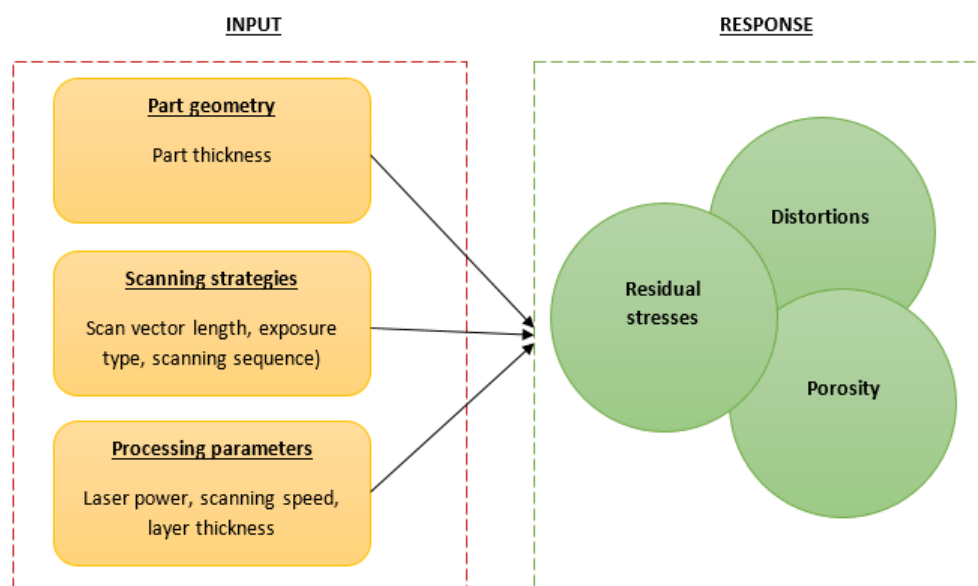
Figure 3.1: Major investigations of the research

The general experimental approach used in this study is shown in Figure 3.2. The primary aim is to experimentally investigate the influence of input parameters on residual stresses. The experimental investigations will further seek to establish the correlation between residual stress magnitudes and final part distortions. Secondarily, it is important to evaluate residual stresses and final part density together because if a part is residual stress-free but is porous, it is not good enough. Thus, as far as possible, porosity is investigated for all samples manufactured under various conditions. This study also makes it possible to analyse the interdependencies between process outcomes, namely, porosity, residual stresses and final part distortion.
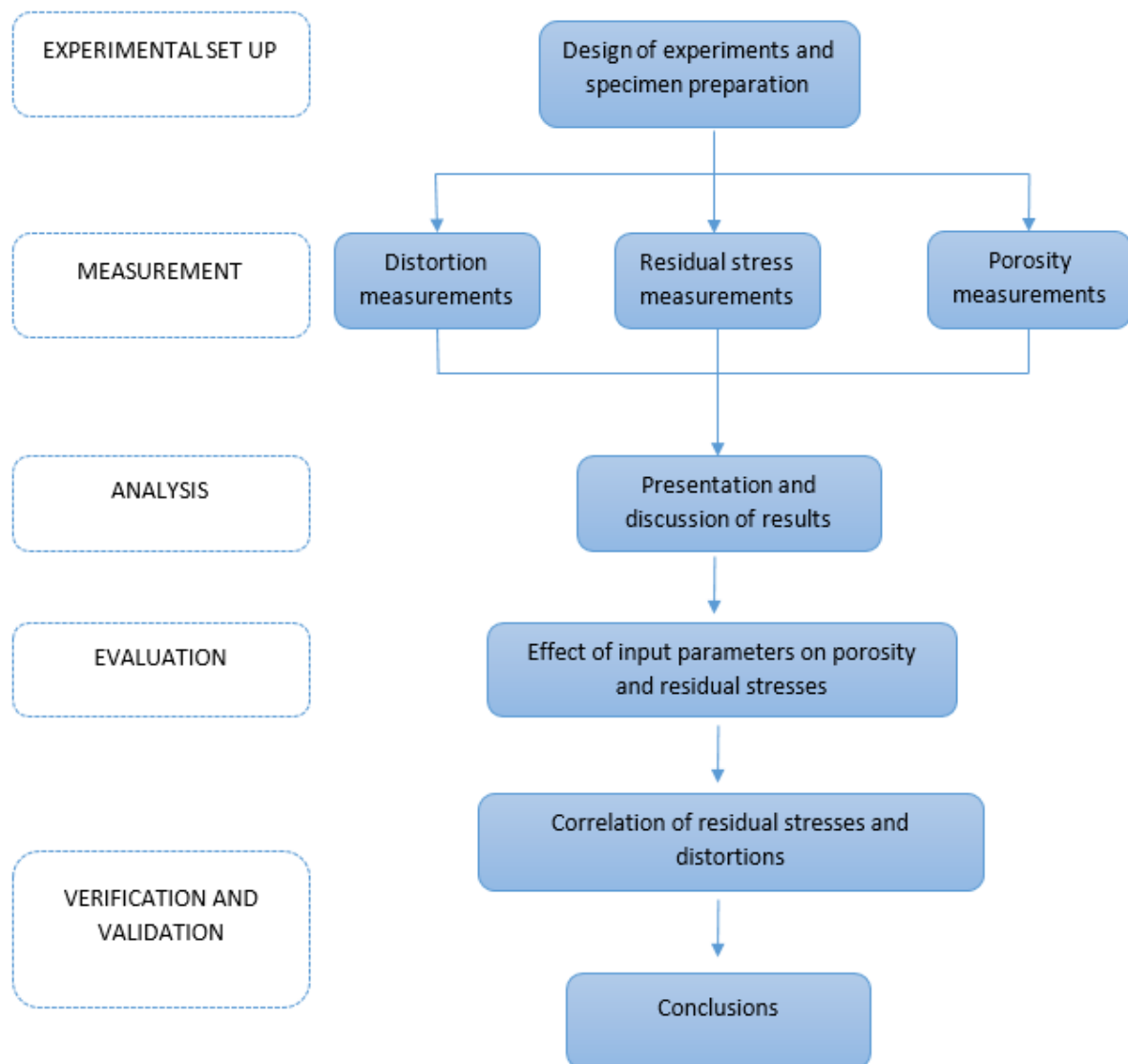
Figure 3.2: General experimental approach capturing the major phases of the methodology

3.3 A methodology for selection of residual stress management techniques

The main focus of this research is investigation and management of residual stresses. However, as identified in Chapter 2 and section 3.2, other outcomes such as porosity may need to be evaluated and discussed together with residual stress findings in order to fill the knowledge gap in the literature. In order to identify the most appropriate residual stress management technique, it is essential to take into consideration other related process outcomes that could be influenced by the method selected. A method that can be used to evaluate residual stress management techniques should primarily consider the effect of these methods on:

- Achievable part density

- Residual stresses and distortions

- Manufacturing time and cost

The above requirements are critical in most applications, but the priorities may vary from user to user or application to application. Therefore, a user-defined methodology for selecting effective and efficient residual stress management methods is proposed as shown in Figure 3.3. However, for tooling applications, the achieved density ought to be high (above 99 % relative density) in order to obtain sufficient part strength. In other applications, like biomedical implants, some porosity may be desirable. As for residual stresses, the yield strength of the material determines the maximum tolerable residual stress levels which will not lead to plastic deformation. However, these stress levels and their effect on deformation is also dependent on the geometry of the part. Therefore, as much as possible, residual stresses should be minimised. Residual stress management methods that do not negatively impact on the manufacturing time and total cost of building up parts are preferable, as long as they have positive impact on residual stress and part density outcome.
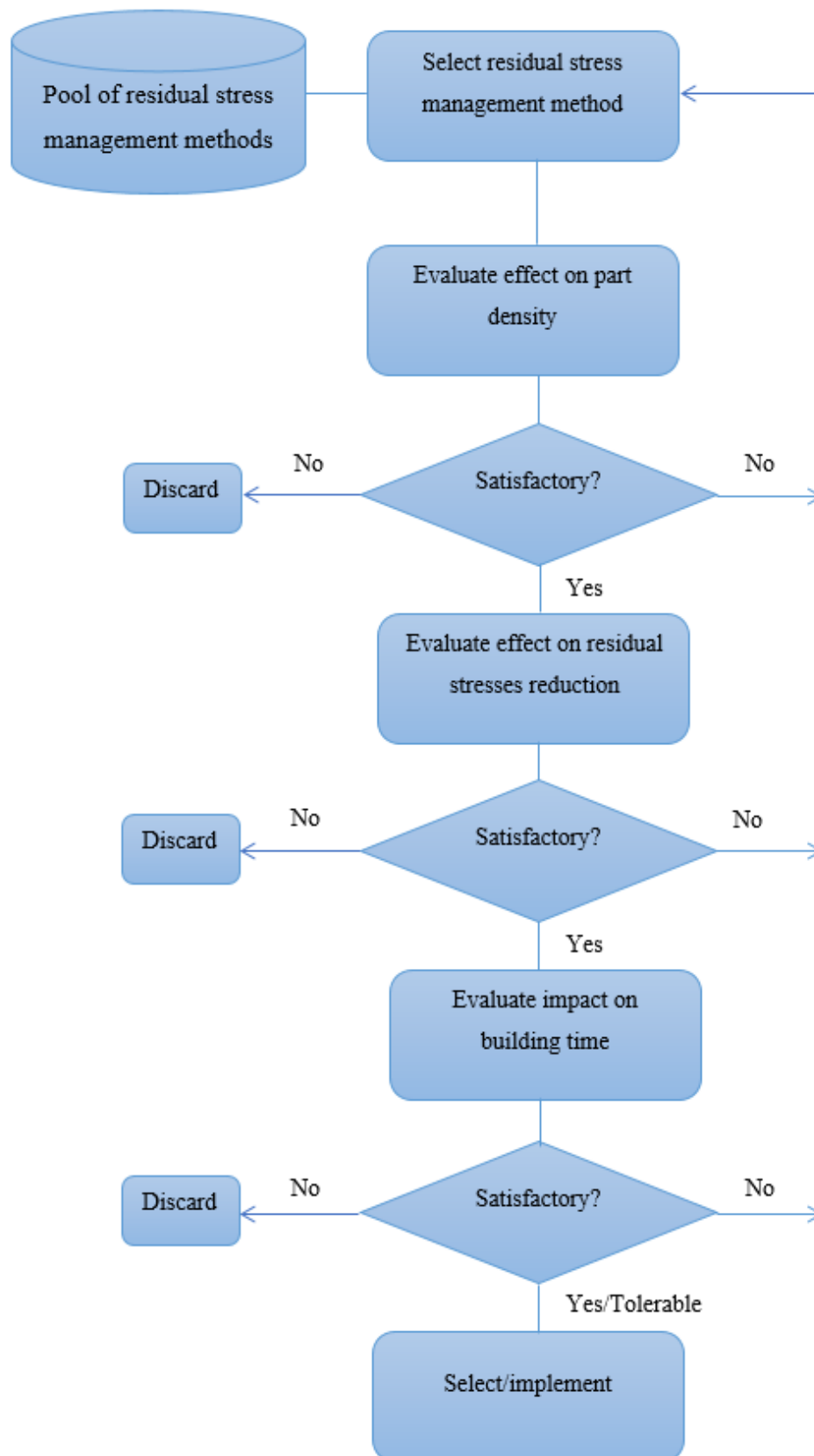
Figure 3.3: Proposed user-defined decision criterion for in-situ residual stress management methods

3.4 Experimental investigation mapping

The most common techniques for residual stress management are shown in Figure 3.4. These methods have different impacts with respect to residual stresses reduction, time and cost to realise parts. Scanning strategy options such as rescanning may increase the scanning time significantly, depending on the scanning speed chosen for the second laser beam pass. Adjustment of scan vector length, scanning sequence, layer thickness and scanning speed may also influence the manufacturing time and the corresponding cost. Despite having very little effect on building time, preheating methods increase the energy costs of the process. For quality stringent applications, the effectiveness of a residual stress management method usually takes precedence over time and cost. However, as already mentioned, a technique that can offer both effectiveness and time/cost efficiency is more attractive.

RESIDUAL STRESS MANAGEMENT OPTIONS
Stress relief heat treatment
Powder pre-heating
Baseplate pre-heating
Rescanning
Scanning strategy improvement
Process parameter adjustment
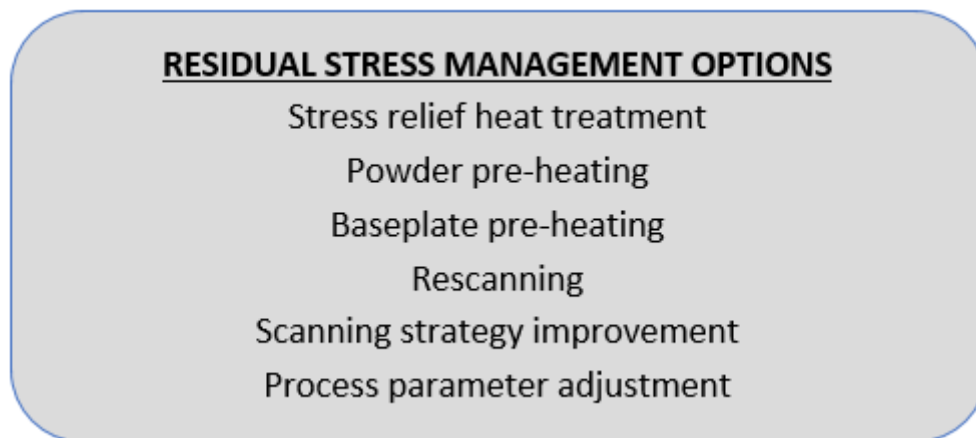
Figure 3.4: Options for residual stress management

In Figure 3.5, the residual stress management approaches are screened, leading to the final methodologies that were considered in this research. At the first screen, heat treatment is discarded because it cannot reverse the cracking/delamination and warping that occurs during the build. Base plate and powder bed pre-heating are dropped after the second screen since these are established in the literature and do not present opportunities for further research. Besides, these options are currently not available for most SLM machines and researchers have to improvise, usually with limited control over disturbances in the environment. For example, SLM systems that have no in-built baseplate or powder preheating units may rely on use of external units that are susceptible to contamination. Thus, the factors finally selected for experimental investigation are limited to rescanning, scanning strategies and process parameter adjustment.
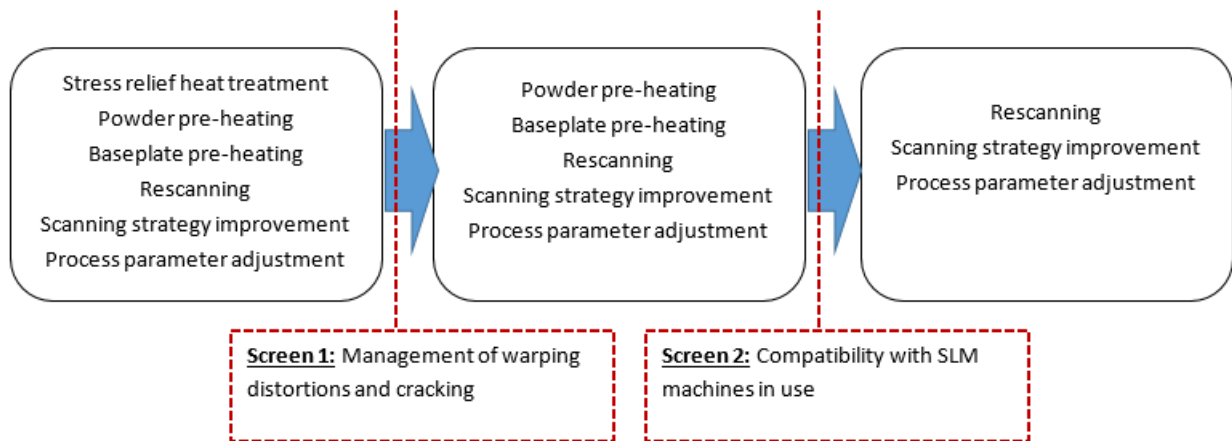
Figure 3.5: Screening process in identifying effective and applicable residual stress management techniques.

3.4.1 Rescanning

Whilst multiple exposures such as rescanning significantly delay the SLM process, such delays may be unimportant if control over key process outcomes such as density and residual stresses is enhanced. Rescanning works as a form of thermal treatment which cancels out previously induced thermal stresses during the initial laser beam pass. Despite the reported success in the few studies found on rescanning, this method's effect on residual stresses and achievable density is not sufficiently discussed. Rescanning with the same parameters as the initial laser beam pass can promote full melting, or inadvertently introduce over melting and balling. These "unknowns" must be adequately studied if rescanning is to be effectively applied.

3.4.2 Scan vector length adjustment

The birth of strategies such as the island and chessboard scanning strategies can be linked to the positive effect that shortening scan vector length has on residual stress magnitudes. In the island strategy, for example, the scanning area is divided into small segments of usually 5 mm × 5 mm. This means that short scan vectors are used (5 mm scan lines) and successive lines within an island can be scanned in a short space of time such that there will be amassing of heat between these successive lines. As a result, local temperature gradients are reduced, resulting in reduced thermal stresses. On the contrary, longer scan vectors promote cooling of the already scanned area because the laser beam travels a long distance along the scanning area. In this case, the high temperature differences between the scanned area and the new scan line results in greater thermal stresses (Mugwagwa *et al.*, 2016). Liu *et al*. (2016) compared scan

lengths of 42 mm, 32 mm and 18 mm and their results show a general decline of residual stresses with decrease in the scan length. Kruth *et al.* (2012) observed a 13 % reduction in the curl up angle for the bridge specimens when the scan vector length was reduced from 20 mm to 2 mm. Wu *et al*. (2014) reduced scan vector lengths from 5 mm to 3 mm and recorded an accompanying tensile residual stresses reduction from 760 to 560 MPa. At the same time, this scan vector length reduction resulted in slightly higher porosity (1.3 %) for the 3 mm vectors compared to that of the 5 mm vectors (1.2 %). From separate studies done by Parry *et al.* (2016) and Nadammal *et al.* (2017), it is also evident that residual stresses increase with increase in scan vector length. A study by Jhabvala *et al*. (2010), in which four scanning strategies (parallel, spiral, paintbrush and chessboard scanning strategies) were compared, it was concluded that the paintbrush and chessboard strategies result in better temperature homogeneity which can easily be maintained. The paintbrush and chessboard strategies have smaller scanning segments and, therefore, shorter vector lines are implemented compared to parallel and spiral strategies. On the contrary though, Töppel *et al*. (2016) observed a reduction in residual stresses (from approximately 125 MPa to 105 MPa) and distortions (from approximately 2.5 mm to 2.1 mm) by changing from 2.5 mm and 5mm square islands to a 10 mm square island respectively. This points to the possibility of overheating as a result of accumulation of heat for short scan vectors. In this research, it is hypothesised that the heat accumulation can lead to overheating and porosity due to the balling effect. The development of porosity can contribute to stress relief and, therefore, the generally lower stress magnitudes reported in the literature.

3.4.3 Scanning sequences

Based on previous success stories, the key consideration in developing/selecting scanning strategies is to subdivide the scanning area into smaller sub-regions. Thus, all the scanning strategies are essentially developed around the island scanning strategy with 5 mm × 5 mm sub-divisions or "islands". The actual sequence of scanning these islands is what distinguishes the scanning strategies studied. Firstly, the islands can be scanned successively as described by Li *et al*. (2016) as well as Kruth *et al*. (2004). Secondly, the traditional island scanning sequence can be followed in which the islands are scanned randomly. In this research, a more structured scanning sequence is proposed – the chessboard scanning strategy. The ***chessboard strategy*** proposed involves scanning the "white" islands before the "black" islands can be scanned, or vice versa. The scan vectors are rotated between neighbouring segments such that if the black segments are scanned in the horizontal direction, the white segments would all be scanned in

the vertical direction. Two variations of the chessboard strategies are proposed and investigated and these are named the ***successive chessboard*** and the ***Least Heat Input (LHI) chessboard*** strategies.

For the ***successive chessboard strategy***, the white segments are scanned successively before the black segments are scanned in the same manner. An illustration of a typical scanning order for this scanning strategy is given in Figure 3.6 (a). The other proposed scanning strategy – the LHI chessboard as shown in Figure 3.6 (b), is based on the patent held by Concept Laser (DE 10 2006 059 851 B4) and on the concept of net amassing of heat that is described by Kruth *et al*. (2004), Li *et al.* (2016) and Y Li *et al*. (2018). In principle, the proposed strategy is similar to the island strategy, but with a unique exposure sequence for the islands. The LHI chessboard scanning strategy has the following characteristic rules (in order of priority):

- White segments are scanned before black segments can be scanned or vice versa.
- Islands scanned one after the other (successively) should be as far apart as possible.
- The next segment to be scanned should not lie next to or side by side with an already scanned segment as much as possible.
- Choice of the first segment to be scanned should result in the least possible violation of the above rules (deterministic rather than random selection).
- Each segment is scanned completely before shifting to the furthest segment.

(a)   (b)
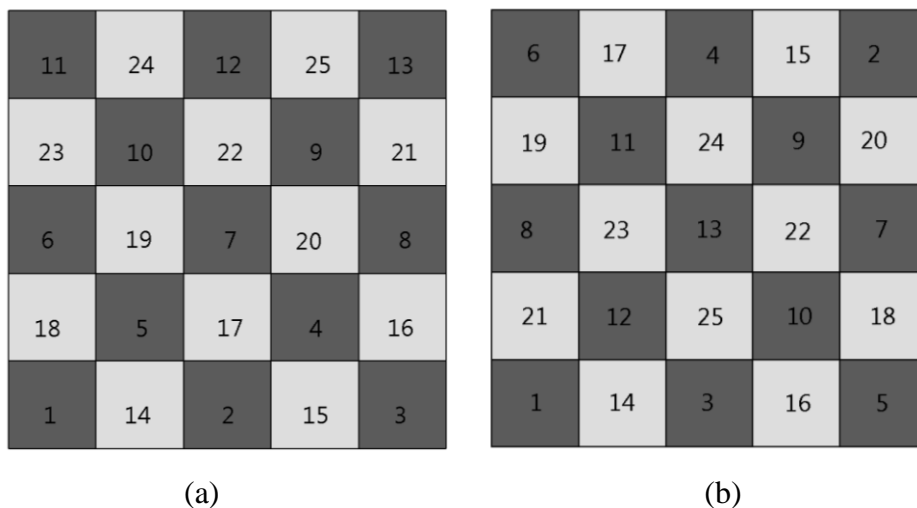
Figure 3.6: Illustration of the chessboard scanning sequences: (a) Successive chessboard (b) LHI chessboard

3.4.4 Process parameter adjustment

The balance between manufacturing time (and) cost and product quality is critical in SLM. Systems that enable use of high scanning speed and thicker powder layers have the potential to significantly reduce the total building time. Adjusting powder layer thickness upwards is usually limited by the available laser power available for efficient manufacture of non-porous parts. Where the layer thickness allows for sufficient connection between inter-layer melt pools, fully dense parts can be manufactured. At the same time, the heat input is reduced for thicker powder layers, and this has the potential to reduce thermal stresses when compared to thinner layers (provided the other quantities – scanning speed, hatch spacing and laser power – are held constant). As long as the heat input is sufficient to promote full melting and inter-layer bonding, thicker powder layers have the potential to reduce both part building time and residual stresses and associated defects.

3.5 Verification and validation approach

In order to verify the performance of the optimum operating parameters (i.e. laser power, scanning speed and layer thickness) with respect to residual stresses, a part that is susceptible to stress induced distortion is selected and built using these identified parameters (as well as the default/benchmark parameters). This serves as validation of the findings on residual stresses. Typical geometries for this purpose include cantilever beams (twin or single arm) as well as thin flat plates (up to 2 mm) that can easily warp on exposure to SLM parameters that induce residual stresses. Cantilever geometries have been used widely in residual stresses and distortion studies, for example by Töppel *et al.* (2016), Buchbinder *et al.* (2014), Papadakis *et al.* (2014), Neugebauer *et al.* (2014) as well as Yadroitsava and Yadroitsev (2015), among other research. L-shape and bridge geometries are also commonly used to check the effect of input parameters on residual stress induced distortions (Wu *et al.*, 2014; C. Li *et al.*, 2018). Thin titanium plates were used by Li *et al*. (2016) to test the effect of different scanning strategies on residual stress induced distortions. For the investigation of process parameters, rescanning and scan vector length, cantilever geometry is preferred since the current investigations include powder layer thickness as a studied input parameter. An illustration of cantilever distortion due to residual stresses is given in Figure 3.7. It is expected that parameters or strategies that lower residual stresses should also reduce the associated distortions.
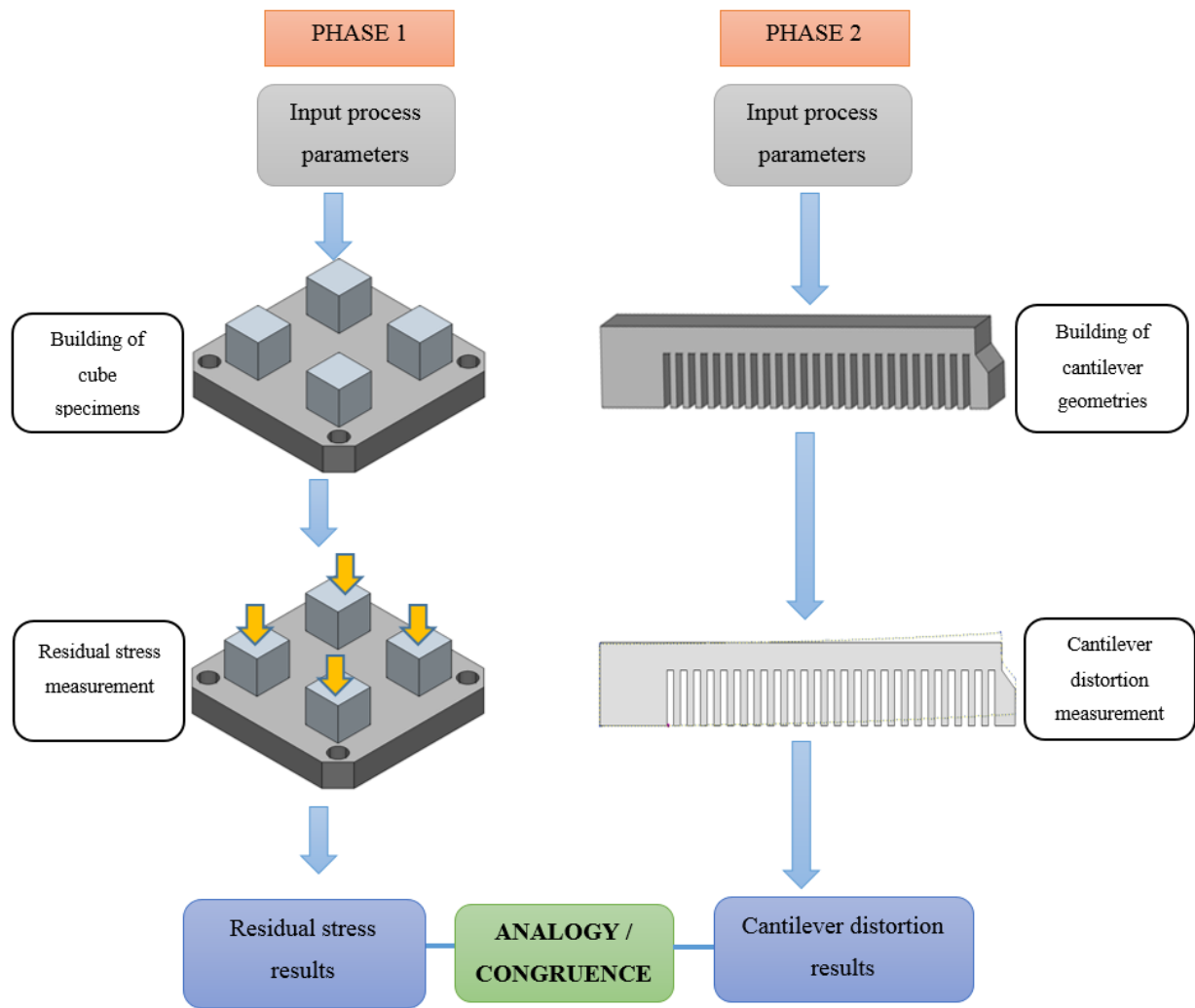
Figure 3.7: Validation methodology for the influence of process parameters

The effect of scanning strategies on residual stresses can be verified by extending the study to investigate how these scanning strategies influence residual stress-induced distortions. This can be achieved by utilising thin plates of a metal susceptible to warping distortion, for example Ti6Al4V. Single track experiments can be conducted by exposing the thin metal plate, acting as the substrate, to the laser beam with or without application of metal powder. Thin plates are easily susceptible to warping under thermal stress, making it possible to measure the warping distortion and correlating the same to the previously measured residual stresses as seen from a similar study by Li *et al*. (2016). This is an indirect but effective method of evaluating or modelling the effect of residual stresses on distortions. Figure 3.8 shows the sequence of experimentation for the scanning strategies.
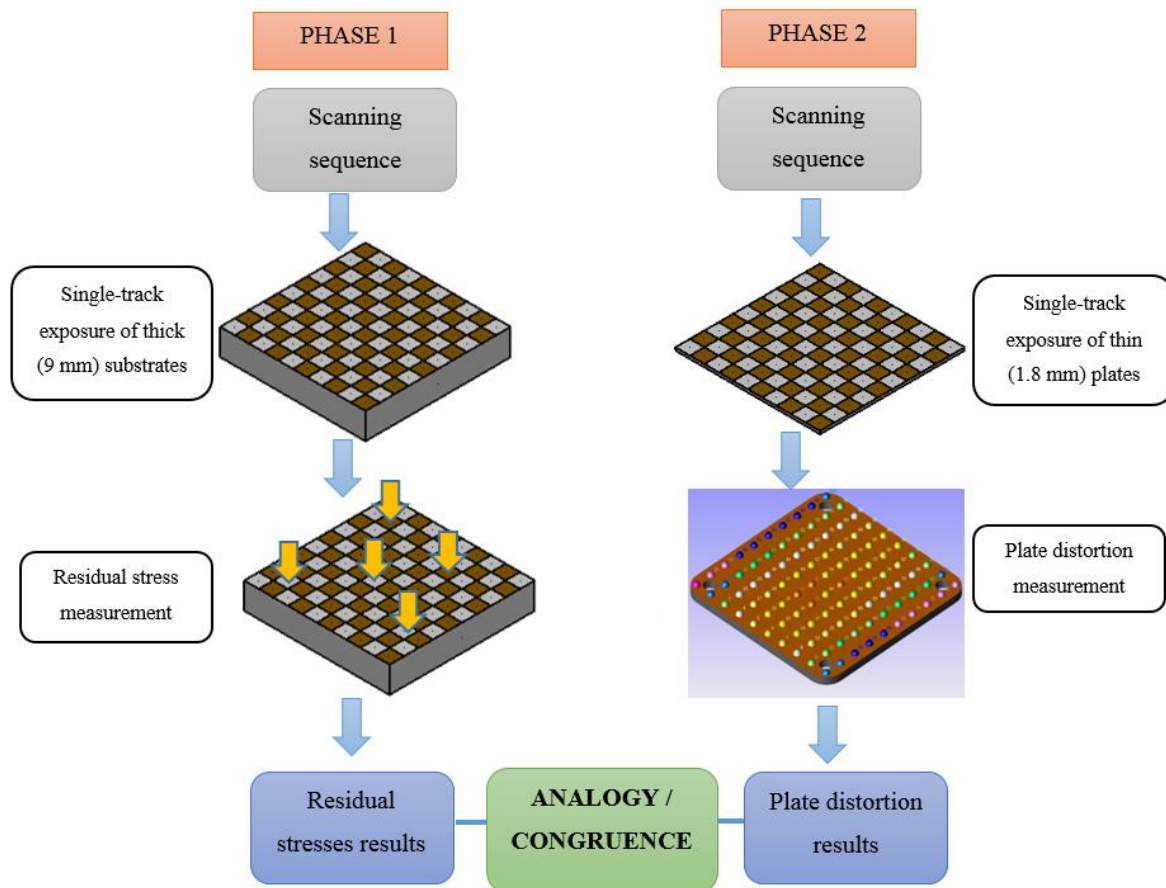
Figure 3.8: Validation methodology for the influence of scanning strategies

3.6 Design of experiments methodology

Properly designed and conducted experiments are a useful source of accurate data generation and collection for the drawing of accurate conclusions. Experimental design is an important tool for product/process design, development and improvement in the science and engineering fields (Montgomery, 2013). Design of Experiments (DoE), also called strategy for experimentation, refers to the "structured way of planning, designing, conducting and analysing of experiments" (Antony, 2003; Montgomery, 2013). The idea behind DoE is to investigate and understand and establish the relative importance and influence of parameters that govern a process on the outcome of the process, since all parameters cannot have the same effect on the process (Antony, 2003). In selective laser melting for example, researchers have identified over 150 parameters that govern the process, but only about 30 are critical. Even so, these "key" parameters are not equally important in determining the outcome of the process. Thus, in order to be able to have sufficient control over the SLM process, there is need to

establish the key parameters' relative interactions with each other and their relative importance to the process.

It is necessary at this point to understand the terms "factor" and "level(s)" as used in DoE. A factor is one of the variables/parameters (inputs) under investigation to establish how they influence the response (output). These factors can take up several of states or values, such as ON and OFF; or LOW, MEDIUM and HIGH; or 1, 2, and 3 etc. These states or values are known as the "levels" of the factors. Design of experiments does not only involve multiple factors as it is possible to have single factor experiments (Montgomery, 2013).

3.6.1 One-factor-at-a-time

Probably the most common experimental investigation method in daily practice is the One-Factor-at-a-Time (OFAT) approach (also called One-Variable-at-a-Time – OVAT). In this method, one factor is varied across its range (levels) whilst keeping the other factors at their entry level. This approach often leads to unsatisfactory and misleading results since each factor is not tested at the different levels of other factors, thus possibly skipping some important interactions between the factors (Antony, 2003; Montgomery, 2013)

3.6.2 Taguchi method

The Taguchi method has been used to investigate LBM processes by Dingal *et al*. (2008) and Raghunath and Pandey (2007). The Taguchi method eliminates the need to run a large number of costly experiments that take a lot of time to analyse by making use of orthogonal arrays (Bolboacă and Jäntschi, 2007). Apart from orthogonal arrays, another unique feature of the Taguchi method is the use of Signal to Noise (S/N) ratios. This ratio should be maximised such that the important and controllable factors (Signal) that affect a process are investigated while the uncontrollable factors (Noise) are minimised. Taguchi seeks to make a process robust by making it insensitive to uncontrollable or noise factors (Montgomery, 2013; Perec, 2016). Orthogonal arrays are particularly useful where the interaction between factors and accuracy of results is not critical. In this research, the accuracy of the results is critical and factors are highly interactive. Therefore, Taguchi cannot be used since it does not investigate all parameter combinations at all the different level combinations.

3.6.3 Full factorial design

In a full factorial design, factors are varied together and all possible combinations of factors at their various levels, are investigated. Casalino *et al*. (2015) used this method to optimise the

SLM of maraging steel. This approach is very important in investigating the effect of individual as well as combined or simultaneous variation of input parameters on the process outcome (Savalani *et al.*, 2012). The simplest and most common full factorial designs described in literature have factors with only two levels because of the complexity, time and cost constraints associated with the huge number of experiments required for a higher number of factors and levels. However, three or more factor levels are well explained by authors such as Montgomery (2013) and the SAS Institute (2014). The number of required runs or trials in a full factorial design is the product of the number of levels for each factor (Antony, 2003). Where the number of levels is the same across all the factors (parameters), then the required number of runs is simply:

$$Number\ of\ runs = l^k$$

where l is the number of levels and k represents the number of factors (parameters).

However, when the factors have different number of levels (such designs are termed mixed level factorials), then the product of these levels for the factors gives the required number of runs. For example for a 3 factor design, if factors 1 and 2 both have 3 levels and factor 3 has 2 levels; then:

$$Number\ of\ runs = 3\ \times 3 \times 2$$

Full factorial design is not recommended for factors above or equal to five. As the number of factors increases, the required number of experiments also increases, resulting in too many measurements and higher cost of running the experiments.

3.6.4 Fractional factorial

As seen from the full factorial approach, as the number of factors increases, more runs are required and this can be limiting with regards to cost of running the experiment. Suppose the number of factors is 8 for a 2-level design; a full factorial would require 2^8 runs, that is, 256 runs. In cases like this, a fractional factorial design should be considered in which only a subset of the full factorial runs is considered (Cavazzuti, 2013; Montgomery, 2013). A one half fraction (fractional factorial) of a 2^k design is given by 2^{k-1}. For example, half fractional factorial for a 2^8 design is 2^{8-1} or 128 runs (which is half of 256 for a full 2^8 design). Similarly, one-third fractional factorial for a 3^k design is given by 3^{k-1}. However, fractional factorials should only be conducted after **screening experiments** have been done to establish which

combination of parameters (runs) has negligible or the least effect on the experimental result. Such runs can then be dropped, resulting in only a fraction of the runs being conducted. Fractional factorial DoE has been adopted previously in the SLM research filed by Averyanova *et al.* (2012).

For this work, the full factorial method has been identified as the most suitable DoE approach for cases where interactions between factors under investigation exist. The full factorial method allows for a complete study of all the interactions between input parameters in relation to the process outcome. However, screening of the experiments is applied in order to remove experiments that are deemed unnecessary as discussed later in section 3.6.6. The full factorial design only applies to investigation on the influence of process parameters on residual stress, the other experiments are one factor type.

3.6.5 Randomisation, replication and blocking

The principles of randomisation, replication and blocking are observed in experimental design. *Randomisation* is whereby the order in which the experiments are run is selected randomly, usually using statistical software. This is done to eliminate any possible bias that may result from ordering the experiments in a certain preferred manner. Replication refers to repeating the same experiment at the same conditions for a stated number of times. *Replication* is very important to check consistency of the experimental results. The part geometry and scanning strategy experiments are replicated three times. Due to the large numbers of runs required for the investigation of the influence of process parameters (that is, laser power, scanning speed and layer thickness), only two replicates are used for these investigations. Besides replication, repeat measurements are performed for most of the experiments as much as economically feasible in order to check the repeatability of the measurements. When conducting experiments, one source of error or variability can stem from use of inhomogeneous conditions, known as nuisance factors. These nuisance factors are not part of the investigation and they should therefore be "blocked" so that no variability arises due to these factors. Only those experiments that are run from the same block can have their results compared against each other (Montgomery, 2013). A *block* is a group of experiments run under the same conditions (apparatus, materials etc.). In this research, the principles of randomisation, replication and blocking were followed.

3.6.6 Screening method

The experiments on investigation of process parameters on residual stresses are screened based on the practicality of the parameter combinations. The achievable part density at different parameter combinations is used as a basis to screen the experiments. Based on previous in-house studies on tool steel and general literature studies on influence of process parameters on final part density, volumetric energy density can be used as a *basis for initial screening* before specimen building. Too low volumetric energy densities (for example, below 50 J/mm^3) result in insufficient melting and porous parts. At the same time, excessive energy density (e.g. above 150 J/mm^3) results in the Marangoni effect, again leading to porosity. From in-house studies using the same SLM machine and material used in this research, an energy density of 95 J/mm^3 has been satisfactorily used. Therefore, it is prudent to keep the energy density within reasonable limits around this satisfactory energy density of 95 J/mm^3. However, since the effect of energy density on residual stresses or porosity is not very clear when input parameters vary simultaneously, the screening criterion used allows a relatively wide range of energy between 50 J/mm^3 and 150 J/mm^3 to be the upper and lower limits respectively.

3.7 Statistical analysis of results

Statistica^{TM} software is identified for designing the experiments, as well as for analysing results. One of the key goals of statistical analysis is the formulation of empirical relationships to correlate process input(s) to output(s). The threshold for statistical significance of correlations is set to 0.05 (5 %) in this study. Statistical significance value, usually called p-value, indicates the probability or risk of concluding that a factor contributes to observed variation when it actually does not. The risk should be kept as low as practically possible. Whilst the risk must be kept low, it should also be realistic and not be set to 0 % as it is nearly impossible to predict outcomes from empirical data with 100 % confidence.

3.8 Summary

This chapter presented the experimental methodology followed in this study. A methodology for evaluating or screening residual stress management methods has been presented. Furthermore, modified scanning sequences that can be investigated for residual stress performance were discussed. The proposed scanning strategies will be compared against the traditional scanning strategies such as the island (random exposure) scanning strategy and stripe hatch strategy which is implemented on EOS machines. While empirical data is usually

foolproof, it must still be verified by either performing additional experiments, or by implementing the findings for a related study. In this case, the verification and validation will be by way of conducting further experiments on a different machine, as well as implementing optimum results to build cantilever beams and thin plates. The distortion results can easily be used to either confirm or discredit the initial findings on residual stresses. To successfully conduct the intended work, a comprehensive experimental design and set up is presented in the succeeding chapter.

Chapter 4: Experimental design and set up

4.1 Introduction

It was established in the previous chapter that residual stress management methods should seek to minimise the detrimental effects of these stresses in-situ. Understanding the distribution of residual stresses in SLM parts is a pre-requisite if effective solutions are to be developed. For this reason, this research will consider an investigation of the influence of part thickness on residual stresses. Experimental designs for the investigation of scanning strategies and process parameters (laser power, scanning speed and layer thickness) are presented in detail, with the broad goal of establishing effective methods of managing residual stresses and their associated effects on distortion of final parts. In this chapter, the equipment used for specimen manufacture and evaluation is also described.

4.2 Sample preparation

The first step in specimen manufacture is CAD data preparation. The 3D CAD modelling was done in PowerSHAPE. Magics® software was used to slice the models into thin layers (according to the intended layer thickness), and export the CAD files into STL format which can be directly processed by the SLM machine. Process parameters such as the scan vector length and beam compensation were also specified in Magics® prior to the final building with the SLM machine. No support structure was used; all specimens were built directly from the baseplate. All specimens manufactured for the initial experimental study were built on the M2 LaserCUSING machine, shown in Figure 4.1. The advantage of using a single machine for all the builds is that it eliminates possible evaluation errors that may have to do with differences in the "environment". The M2 LaserCUSING machine, housed at Stellenbosch University's Department of Industrial Engineering, has a build envelope of 250 mm $\times$ 250 mm $\times$ 280 mm and is equipped with a single 200 W fibre laser operated under continuous mode. Laser melting machine properties such as laser power output can easily deteriorate with machine age, and it is necessary to check the actual power being delivered by the laser system against the selected power. A calibration exercise was conducted prior to building of specimens on the M2 LaserCUSING machine to ensure that the input parameter values are exactly what the machine is delivering. The details of the M2 LaserCUSING machine are given in Table 4.1. The island scanning strategy was adopted for the manufacture of all the specimens in this research except for some of the experiments listed in sections 4.5, 6.2 and 6.3.

Figure 4.1. The M2 LaserCUSING machine

Table 4.1: M2 Laser CUSING machine specifications

Parameter	Machine specifications
Layer thickness	20 – 50 μm
Scanning speed	Up to 7000 mm/s
Focus diameter	70 – 200 μm
Laser power	Up to 200 W
Coater blade	Rubber

4.3 Material

The material used in this study is maraging steel 300 (hot work steel 1.2709). Hot work tool steels are widely used for manufacture of tools, dies and moulds that are used in hot-forging, hot-stamping, hot-rolling, hot-extrusion and die casting operations (Klocke *et al.*, 2017). Currently, limited research has been done on residual stresses and distortions based on this material as most previous (and current) studies focus on stainless steel and Ti6Al4V and the other emerging high-value super alloys. Mazur *et al*. (2017) concur that the studies around the manufacturability and mechanical properties of tool steels via SLM are not thorough. The metal powders used in this research were supplied by Concept Laser and PraxAir. The chemical

64

composition specification of the powders is given in Table 4.2. According to Concept Laser material data sheets for CL50WS, this material has a yield strength of 950 MPa before application of heat treatment (Concept Laser, 2010). Becker and Dimitrov (2016) found yield strength of as-built CL50WS to be between 815 and 1080 MPa. Hot work steel has wide applications in the tooling industry due to its excellent fracture toughness. Baseplate material used for all builds is tool steel 1.2343. Concept Laser recommends use of tool steel grades 1.2343 or 1.2709 for the baseplate material for SLM of CL50WS.

Table 4.2: Maraging steel 300 specifications

Chemical composition	C	≤ 0.03
	Si	≤ 0.1 %
	Mn	≤ 0.15 %
	P	≤ 0.01 %
	S	≤ 0.01 %
	Cr	≤ 0.25 %
	Mo	4.5 - 5.2 %
	Ni	17 – 19 %
	Ti	0.8 – 1.2 %
	Co	8.5 – 10 %
	Fe	Balance
Yield strength (as-built)	950 MPa	
Density	8.1 g/cm^3	

4.4   Investigation of the influence of part geometry

To build on previous research as highlighted in Chapter 2, an investigation was conducted on the influence of part thickness on residual stresses. The thickness considered was 9 mm up to 21 mm in increments of 3 mm as shown in Figure 4.2. All specimens have the same length (50 mm) and width (15 mm). Lengths of 50 mm can easily be measured for deformation (if necessary) to determine the effect of such deformations on stress relief. The specimens were built using the default settings of the M2 LserCUSING machine for tool steel, that is, 185 W and 600 mm/s. In order to eliminate the possibility of variations arising from specific specimen placement on the baseplate, all the specimens were clustered on one end of the baseplate such that the effect of powder depletion across the baseplate width is minimised. Such powder depletion can lead to non-uniform energy density across the baseplate and differences in process outcomes for various positions on the baseplate as inferred from previous studies such as the one conducted by Casavola *et al*. (2009).
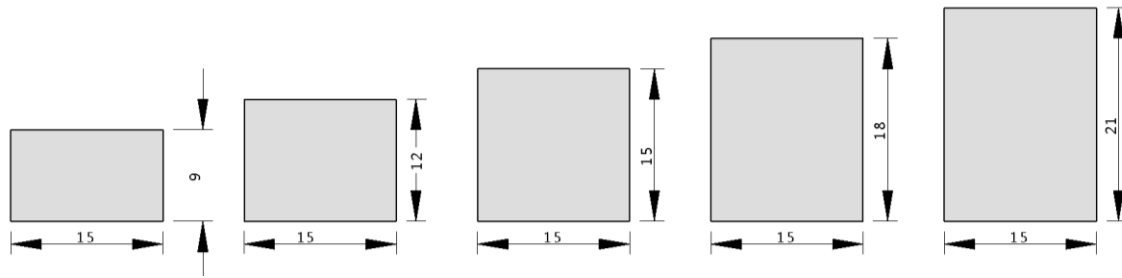
Figure 4.2: Part thicknesses under investigation (dimensions in mm).

4.5 Scanning strategies

The aim of this group of experiments is to investigate the influence that scanning strategies have on residual stress magnitudes in SLM. The term "scanning strategy" does not only refer to the pattern in which the laser beam is moved over the powder to effect melting, but also includes sub-parameters such as rotation angle between layers, hatch distance, scan vector lengths, and x-y shifts between successive layers. The rotation angle between layers is usually set to 90° as this gives the best results in terms of cancellation of stresses set up in the previous layer (Kempen, 2015). The impact of scan vector length and exposure sequence for strategies that subdivide the scanning regions are investigated further, with special attention given to residual stresses, achievable density and impact on scanning times.

4.5.1 Island sizes and double exposure

Keeping the scan vector short appears to be one of the widely acclaimed ways of residual stress management. From the research, separate studies conducted by Parry *et al.* (2016), Nadammal *et al.* (2017), Jhabvala *et al*. (2010) and Kruth *et al*. (2012) show that residual stresses decline with decrease in scan vector length. Regardless, little consideration has been given to the porosity that might arise from implementing these shorter vectors. It is not adequate to minimise residual stresses without ensuring that sufficient final part density is achieved. The results reported by previous researchers on the effect of island sizes on residual stresses do not take into account the possible porosity variations that could also contribute to the observed trends. Using the island scanning strategy already installed on the M2 LaserCUSING machine as a basis, different island sizes (scan vector lengths) were investigated as given in Table 4.3 to establish their influence on residual stresses and distortions in finished parts. In addition, re-scanning (double exposure) was also be compared to single exposure for the island scanning strategy. The study of the effect of re-scanning was conducted using only the default island size of 5 mm × 5 mm. Identical parameters were applied for the initial and second laser passes.

66

Table 4.3: Scanning strategy parameters investigated

Island size	Single exposure	Double exposure
3 mm × 3 mm	✓	
5 mm × 5 mm	✓	✓
7 mm × 7 mm	✓	

4.5.2 Scanning patterns

Whilst there is a general indication in the literature that sub-dividing the scanning area into smaller regions significantly reduces thermal stresses, the order in which the sub-regions are scanned and the impact that this has on heat distribution and eventual residual stresses, is a subject of interest. For this investigation, variations of scanning patterns based on the principle of sub-division were considered as follows:

- Island scanning strategy (random exposure sequence)
- Successive scanning strategy
- Successive chessboard scanning strategy
- Least Heat Input (LHI) chessboard scanning strategy

In the island scanning strategy, the total area is divided into segments (called islands) which are, in this case, 5 mm × 5 mm. These segments are then scanned randomly whilst rotating the scan vectors by 90º between neighbouring segments as shown in Figure 4.3. The orientation of the scan vectors in an island can be set to any angle, but maintaining equal vector lengths is beneficial as it reduces non-uniform heat input associated with heat amassing where the scan vector length progressively becomes shorter.
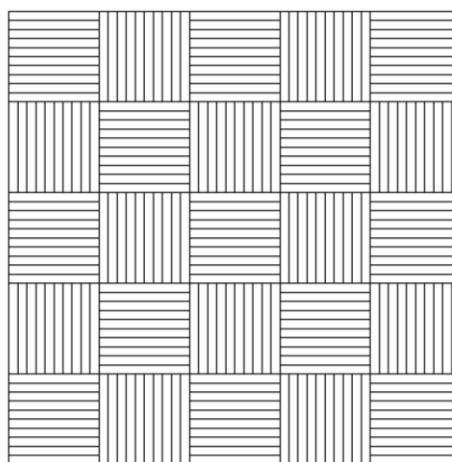
Figure 4.3: Orientation of scan vectors between neighbouring islands

The other three scanning strategies are variations of this island scanning strategy with respect to sequence of exposure of the segments. The so-called chessboard strategies (successive chessboard and LHI chessboard) were discussed in Chapter 3 under section 3.4.3. The successive scanning strategy involves scanning segments that lie next to each other successively as shown by the numbering sequence in Figure 4.4. However, the scan vectors are rotated by 90º between successive segments, similar to the island scanning strategy. In Figure 4.4, the black and white segments show alternating scan vector directions.
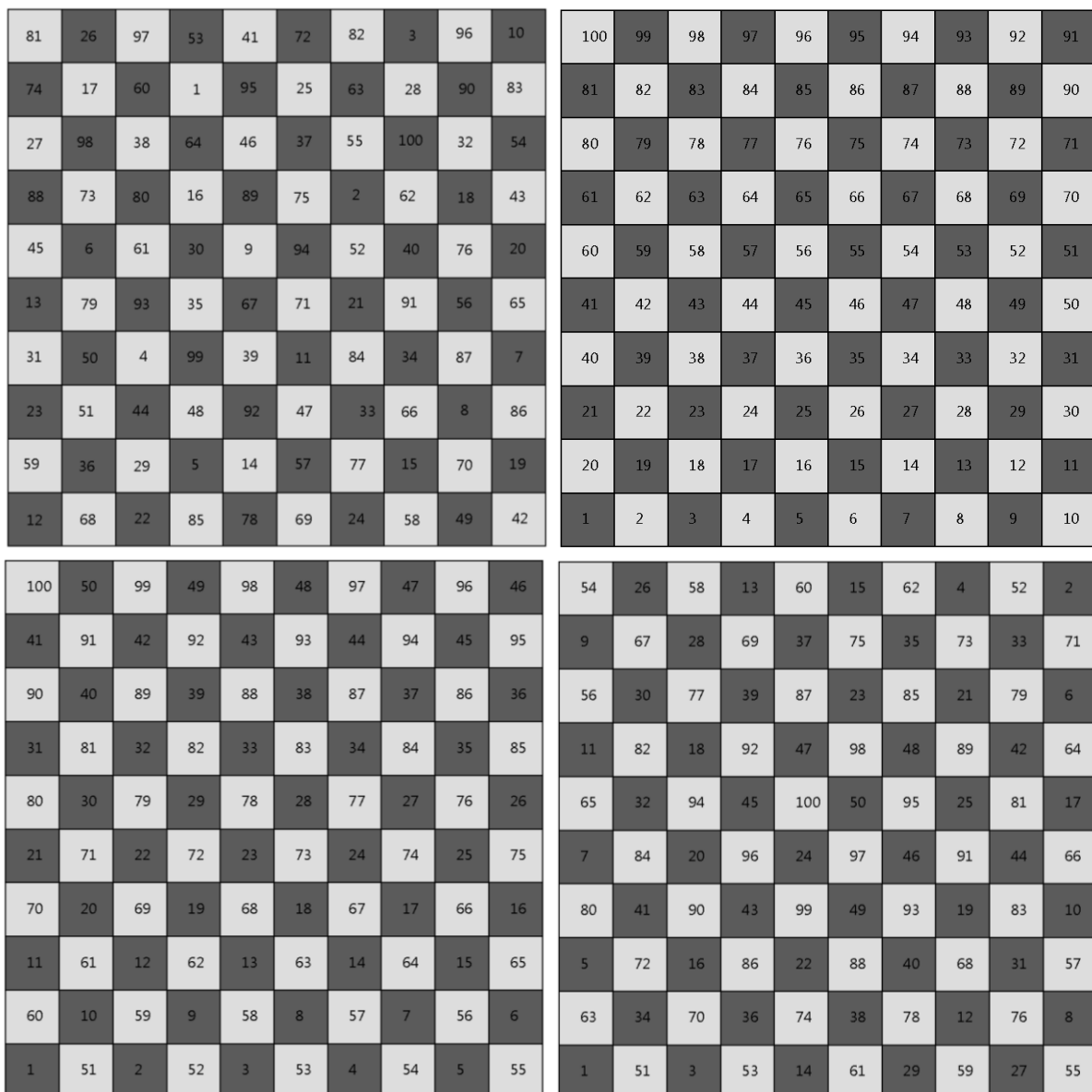
Figure 4.4: Scanning sequences for the studied strategies: Top left – Island scanning strategy approximation; Top right – Successive scanning sequence; Bottom left – Successive chessboard sequence; Bottom right – LHI sequence

The scanning strategies were investigated at the same parameters of hatch spacing, scanning speed, laser power and scan vector length. This means that the scanning sequence is the only variable to be investigated. Further to the effects of scanning strategies on residual stresses, the implications on building time were also studied. This approach results in a complete study in which residual stresses, density and productivity requirements are all investigated.

4.6 Influence of laser power, scanning speed and layer thickness

The aim of this investigation is to study the influence of laser power, scanning speed and layer thickness on residual stresses. This study paves way for establishing a stable process window within which laser power and scan speed can be varied without negatively impacting on the process outcome (density, residual stresses and accompanying distortions). A fixed hatch spacing of 100 µm was applied in this experimental study. Table 4.4 shows the parameters that were varied and the different levels at which they were investigated. The parameter ranges fall within the operating limits of the M2 LaserCUSING machine.

Table 4.4: Laser power and scanning speed values investigated

Factor/level	1	2	3	4	5	6	7	8	9
Laser Power (W)	80	100	120	140	160	180	-	-	-
Scan Speed (mm/)	200	300	400	500	600	700	800	900	1000
Layer thickness (µm)	30	45	-	-	-	-	-	-	-

For this study, the full factorial method was used to investigate the influence of scanning speed and laser power on porosity, residual stresses and distortions. A similar, but leaner experimental approach was used by Casalino *et al.* (2015) to test the effect of laser power and scanning speed on relative density, surface roughness, hardness and tensile properties of maraging steel 300. Since two layer thicknesses are considered – 30 µm and 45 µm – it is necessary to prepare specimens corresponding to the two different layer thicknesses in separate builds. Otherwise, if only one build was to be used, the parts built from thicker layers would gain more cooling time compared to those parts built from thinner powder layers, resulting in differences in residual stresses and distortions for the two scenarios due to differences in thermal gradients between layers (Denlinger *et al.*, 2015; Vrancken, 2016). For a full factorial, a total of 108 runs (before replication) would be required for the two layer thicknesses. However, only 42 base runs were deemed necessary after careful screening, based on the approach discussed in Chapter 3 (3.6.6). Only process parameter combinations for which the

energy density falls between 50 and 150 J/mm^3 were considered in order to avoid consolidating highly porous parts. Two replicates were used to give a total of 84 runs for residual stress analysis.

Table 4.5: Process parameters experiments at layer thickness 30 μm

Standard order	Run order	Laser power (W)	Scanning speed (mm/s)	Energy density (J/mm^3)
1	7	80	200	127
2	15	80	300	85
3	11	80	400	63
4	1	100	300	106
5	16	100	400	79
6	26	100	500	63
7	3	120	300	127
8	21	120	400	95
9	8	120	500	76
10	18	120	600	63
11	24	140	400	111
12	14	140	500	89
13	2	140	600	74
14	17	140	700	63
15	13	160	400	127
16	23	160	500	102
17	10	160	600	85
18	20	160	700	73
19	6	160	800	63
20	9	180	400	143
21	4	180	500	114
22	22	180	600	95
23	12	180	700	82
24	19	180	800	71
25	25	180	900	63
26	5	180	1000	57

The choice of part geometry should allow for ease of evaluation of porosity and residual stresses. For this requirement, cubes of 10 mm sides were satisfactory for density evaluation using Archimedes' density test method or CT scanning as well as for residual stress analysis

with XRD or neutron diffraction. Similar sample sizes have also been used by Vrancken (2016) in a related study. In Table 4.5, the parameter combinations that were studied at a layer thickness of 30 µm after screening, are listed. The "run order" shows that the experiments were *randomised*. This was done to remove any bias that might be associated with assigning a specific run order or building position for some of the experiments. In this way, any differences in observations can solely be attributed to the differences in the process parameters.

The experiments for powder layer thickness of 45 µm are given in Table 4.6. The number of base experiments (16) is considerably lower than that for the 30 µm layer. This is because the energy density becomes less and less as the layer thickness is increased, therefore, the number of experiments that would have to be discarded also increases.

Table 4.6: Process parameters experiments at layer thickness 45 µm

Standard order	Run order	Laser power (W)	Scanning speed (mm/s)	Energy density (J/mm^3)
1	2	80	200	85
2	6	100	200	106
3	12	100	300	71
4	7	120	200	127
5	15	120	300	85
6	4	120	400	63
7	5	140	300	99
8	8	140	400	74
9	9	140	500	59
10	3	160	300	113
11	14	160	400	85
12	10	160	500	68
13	11	180	300	127
14	1	180	400	95
15	13	180	500	76
16	16	180	600	63

4.7 Residual stress measurement

The Neutron Diffraction (ND) and X-ray Diffraction (XRD) methods were used in this research for residual stress measurements. These methods are established, accurate and applicable for this research. The ND method is preferred because of its depth resolved measurement capabilities. However, access to ND facilities is limited, therefore XRD will also be used to

complement the ND technique. Besides, the ND technique fails to accurately measure surface stresses, thus surface stresses were measured using XRD. All the residual stress measurements were done without any prior stress relief heat treatment on the samples.

The ND measurements in this research were performed with the MPISI neutron strain scanner instrument at the SAFARI-1 research reactor of the South African Nuclear Energy Corporation (NECSA). Tri-axial stresses – longitudinal (σ_L), transverse (σ_T) and normal (σ_N) – were calculated at each depth location of interest from the measured lattice plane spacing. Investigations were done along a cross sectional plane (shown as the red dotted surface) of the sample at the centre of the sample's length (X-axis) and a matrix over the width (Y-axis) and depth (Z-axis) as shown in Figure 4.5. The stress-free lattice plane spacing was determined from reference samples of sizes 5 x 5 x 5 mm^3 that were EDM extracted in the as-manufactured samples. Experimental conditions were: a gauge volume of 2 x 2 x 2 mm^3, neutron wavelength of 1.667 Å. Measurement positions were carefully selected to ensure full submerging of the neutron beam for the gauge volume of 2 mm $\times$ 2 mm $\times$ 2 mm. Only locations that lie at least 1.60 mm from the surfaces were considered.
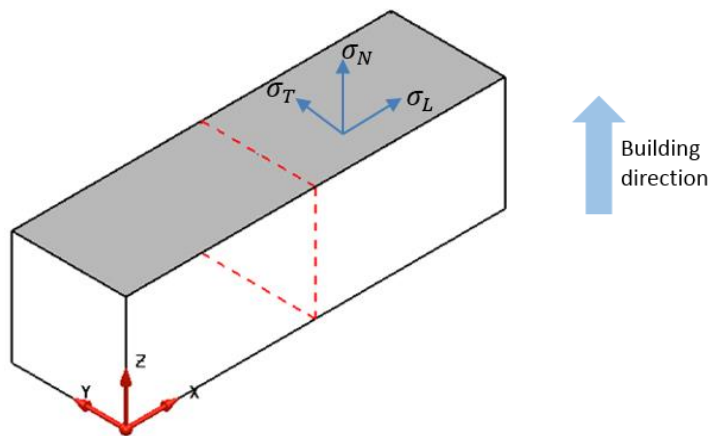
Figure 4.5: The measured residual stress components for neutron diffraction

XRD evaluation of surface residual stresses was conducted using facilities at Nelson Mandela University (NMU), Port Elizabeth, South Africa. A ProtoXRD machine (Figure 4.6), equipped with two detectors was utilised to determine the Fe-α {211} lattice deformations at 25 kV and 4 mA. The source of X-rays was a Cr K-α X-ray anode tube, at a wavelength of 2.291 Å. The rest of the parameters used for the XRD stress measurements are listed in Table 4.7 and were selected based on the guidelines in Cullity (1978) and Fitzpatrick *et al.* (2005). The sin^{2}ψ method was used to calculate the stress. This method, involves plotting a graph of *d-spacing*

against $sin^2\psi$ and using the gradient of this plot in calculating the residual stress using Equation ((4.1). Details of the derivation of the $\sin^2\psi$ method can be found in Fitzpatrick *et al.* (2005).

$$\sigma = \left(\frac{E}{1+v}\right) m \tag{4.1}$$

where E is the material's modulus of elasticity, v is the Poisson's ratio and m is the gradient of the plot. Recent studies on the mechanical properties of maraging steel 300 revealed modulus of elasticity to be between 181 and 194 GPa in the as-built state (Becker and Dimitrov, 2016).

Table 4.7: XRD parameters used

Parameter	Specification
Aperture diameter (Focus)	1 mm
Radiation	Cr K-α
Diffraction peak	Fe {211}
2θ (Bragg angle)	156.41º
ψ-tilt	-33º to 33º
Number of steps	9
S_1	-1.28×10^{-6} MPa^{-1}
½S_2	5.72×10^{-6} MPa^{-1}
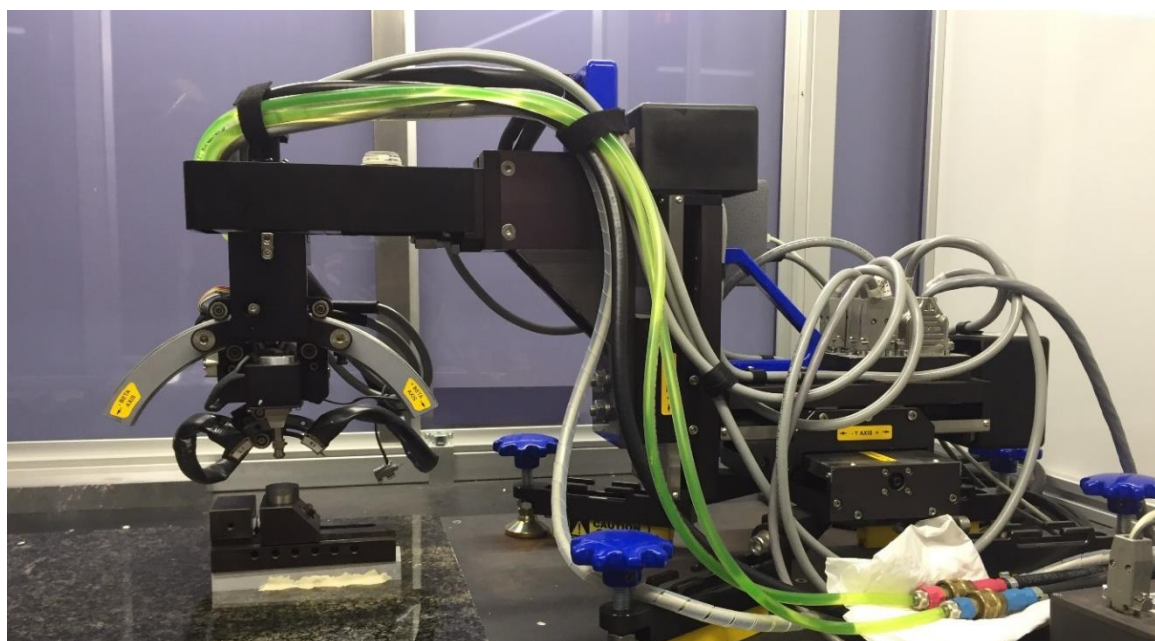
Figure 4.6: The ProtoXRD diffractometer used in this study

4.8   Porosity measurements

For porosity evaluation, three methods were used: the Archimedes' density test method, optical microscopy and CT scanning. The Archimedes' was used as the main measurement method whilst optical microscopy and CT scanning were used to check the consistency of the Archimedes' test findings. These methods are discussed in detail in the sections below.

4.8.1 Archimedes' density test method

The primary method for density measurement is the Archimedes' density test method. This method involves dividing the mass of a specimen in air, m_a, (dry weight) by the difference between dry weight and specimen's mass when immersed fully in a fluid. A precision scale with a readability of 0.1 mg was used to measure the mass of the specimens in air and when immersed in fluid - in this case distilled water with a density of 1 g/cm^3. The advantage of distilled water is that it is nearly bubble-free at room temperature. The specimen's density, ρ, is then calculated as follows:

$$\rho = \frac{m_a}{m_a - m_w} \rho_w \qquad \textbf{(4.2)}$$

where, m_w is the mass of sample when fully immersed in distilled water and ρ_w is the density of distilled water. Basically, the difference between m_a and m_w gives the mass of the displaced water. When this difference is divided by the density of the fluid, it equals the displaced water volume, which is exactly equal to the specimen volume. Relative density, which is a percentage ratio of the sample density to the theoretical density of the material, is usually used when reporting the density of components manufactured by AM. The theoretical density of the hot work steel material used in this study is taken as 8.1 g/cm^3 in line with related literature (Yasa *et al.*, 2010; Becker and Dimitrov, 2016). Porosity is simply the difference between 100 % (fully dense) and the specimen's measured relative density. The schematic representation of the Archimedes' density test method is shown in Figure 4.7. One of the weaknesses of the Archimedes' method is the associated errors in cases where water may penetrate specimens with cracks or open pores (Slotwinski *et al.*, 2014). For parts that have open cavities, air bubbles can be seen as the water penetrates these cavities. Such parts must be sealed to avoid incorrect measurements (Spierings *et al.*, 2011) In this research, no air bubbles were observed during immersion of parts into water, thus, sealing of the specimens was not required.
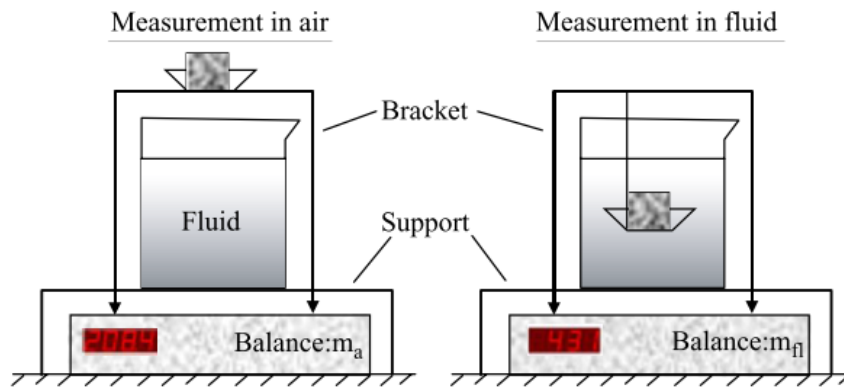
Figure 4.7: Measuring mass of specimen in air and in fluid (Source: Spierings *et al.*, 2011)

4.8.2 Optical microscopy and CT scanning

Archimedes' method does not provide information regarding the shape, size or position of pores (Ziółkowski *et al.*, 2014). Thus, optical microscopy and MicroCT scanning become necessary to check for distribution and size of pores as a way of validating the Archimedes test results. For optical microscopy, the samples were analysed for porosity along the XY and XZ planes as shown in Figure 4.8. The specimens were first cut using a precision cutter. Subsequent to this, the samples were polished, starting with coarse SiC paper of grit size 320, then medium (600) and fine (1000) and finally using diamond suspension of 9 µm, 6 µm, 3 µm and 0.04 µm. Each grinding or polishing step lasted five minutes. To reveal the exact location of pores, the as-polished specimens were etched in 2 % Nital.
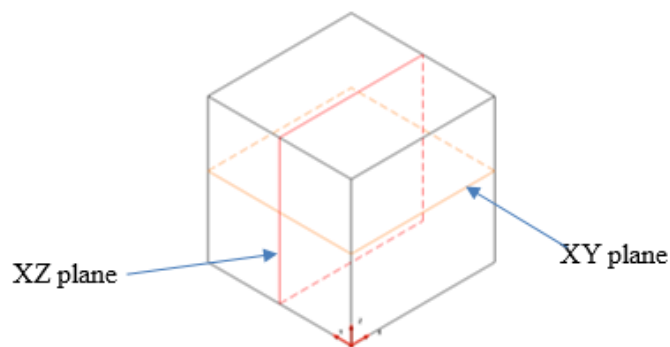
Figure 4.8: Cutting planes for optical microscopy

For MicroCT scanning, cubes of 15 mm sides were cut from the 50 mm lengths. The smaller the specimen, the higher the resolution that can be used, allowing for small pores to be analysed. A voxel size greater than the minimum feature to be measured is necessary for dimensional evaluation of the pores (Siddique *et al.*, 2015). A General Electric V|TomeX L240 system housed at the Central Analytical Facilities (CAF) at Stellenbosch University, was used

for this purpose. A voxel size of 15 µm was selected, allowing for pores above 45 µm to be easily detected for three voxels in one direction. X-ray settings were 220 kV, 200 µA and copper beam filtration of 1.5 mm. The images were reconstructed in Datos reconstruction software and Visualization and analysis was performed in Volume Graphics VGStudioMax 3.1.

4.9   Distortion measurement

Measurements of dimensional distortions for this research were done using a Cartesian 3-dimensional Coordinate Measurement Machine (CMM). The CMM is reported to be the best method for this purpose when compared to other options such as CT scanning. Furthermore, the geometries considered in this study are only measured on the outside surface, otherwise, CT scanning would be required for measurement of internal dimensions (Kruth *et al.*, 2011). Digital cameras such as the GOM would not be suitable for the small part sizes used in this research. In this research, therefore, a bridge type Mitutoyo Bright Apex 710 CMM (Figure 4.9) was utilised to measure the deviation of cantilevers and plate geometries from the original CAD model. In each case, the measurement speed was set at 5 mm/s to reduce the impact of collisions on the measurement process. A probe diameter of 2 mm was used to avoid the possibility of the probe getting stuck in between the "supports" of the cantilevers.

Figure 4.9: Mitutoyo Bright Apex 710 CMM machine used in this research

4.10 Summary

Appropriate selection of experimental methods and measurement or evaluation methods and equipment is critical for generation of dependable data. This chapter presented a comprehensive and systematic experimental set up for the research, from sample preparation to evaluation of the main responses under investigation. The experiments that were designed and discussed in this chapter focused on part geometry, scanning strategies and process parameters, namely, laser power, scanning speed and layer thickness. These focus areas are in line with the study objectives and present opportunities for unlocking new dimensions of knowledge in the subject of residual stresses and distortions in selective laser melting.

Chapter 5: Results and discussion

5.1 Introduction

The results from the experimental investigations are presented and discussed in this chapter. Firstly, the influence of part thickness on residual stresses is discussed in order to appreciate the magnitudes and distribution of residual stresses in different part sizes. Later, a discussion of the influence of scanning strategies on residual stresses, porosity and productivity, is presented. Lastly, the influence of process parameters (laser power, scanning speed and layer thickness) is analysed with respect to both porosity and residual stresses. These findings lead to the identification of the most applicable methods to reduce residual stresses and their effects on distortions.

5.2 Part size impact on residual stresses

The evaluation of residual stresses for the different part thicknesses was carried out using the neutron diffraction technique as discussed in Chapter 4. For all the specimens, the distribution of residual stresses shows that residual stresses vary for different locations even though these locations may be at the same distance below the specimen's surface or above the base of the specimen. In Figure 5.1, the symbols σ_N, σ_L and σ_T represent stresses in the normal, longitudinal and transverse directions respectively. The measurements were done along the red dotted cross sectional plane. It is important to note that positions lying on the surfaces or edges of the specimens were **not** evaluated for stresses using neutron diffraction.
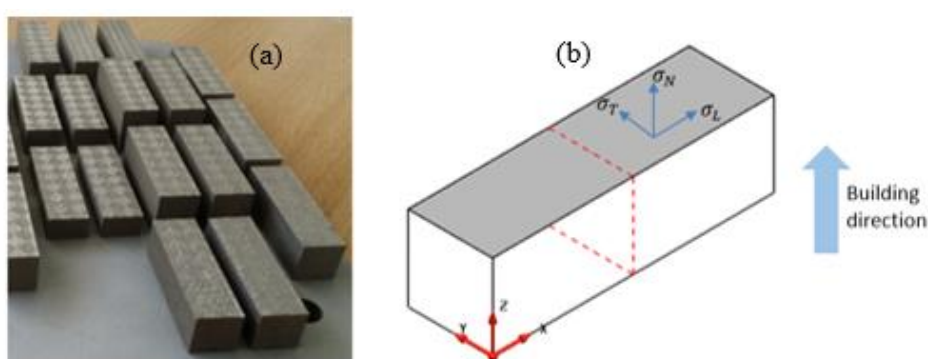
Figure 5.1: Finished parts attached to the baseplate (a), and residual stress components measured (b).

The results show that these stresses generaly decline with increase in height above the baseplate but increase again towards the specimens' surfaces. In general, the normal and longitudinal

stress components were much lower than the transverse component as shown in Figure 5.2 using results for an 18 mm thick sample at 6.3 mm across the width of the specimen.
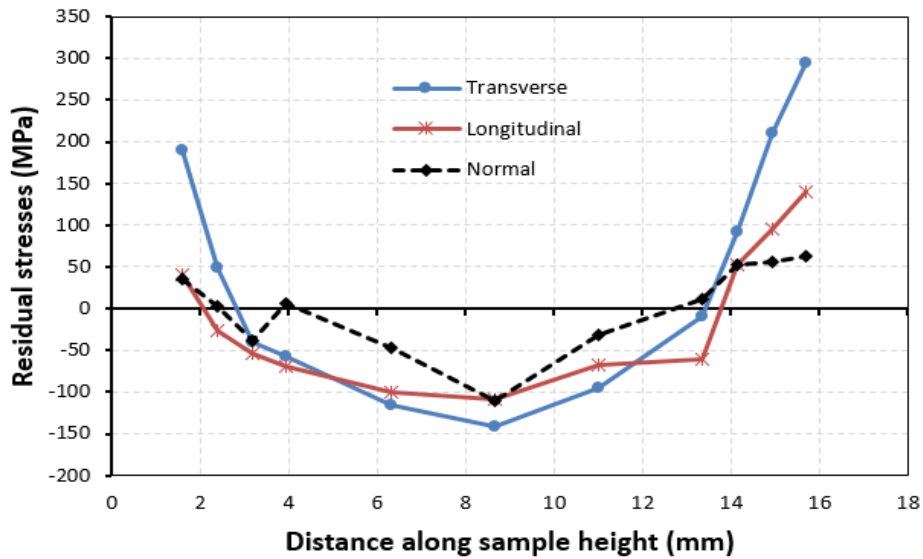
Figure 5.2: Stress components comparison for an 18 mm thick sample

5.2.1 Normal stresses

To make comparison of the stress magnitudes and distributions convenient, contour plots were utilised. The full stress data can be found in Addendum B. As shown in Figure 5.3, the bulk of the normal component of residual stresses lies between -100 and 100 MPa, which is relatively low against the yield stress of as-built maraging steel (950 MPa).

For the 9 mm specimen, the maximum tensile stress was 164 MPa which was found at about 2 mm above the wire-cut side of the specimen. The trend for the normal stress component of the 12 mm specimen was similar to that of the 9 mm thick specimen. The residual stresses for this part thickness ranged between -92 MPa and 147 MPa. Close to the baseplate, the maximum stress was 144 MPa and decreased to 28 MPa, 2 mm below the specimen surface. The 15 mm specimen showed less scatter of residual stresses for different widths at the same height of evaluation, but still falling largely in the same residual stress magnitude range of -100 MPa to 100 MPa as the 9 mm and 12 mm thick specimens. The stresses are generally compressive for the central regions of the 15 mm thick specimen's cross section, in sharp contrast to the observations for the 9 mm and 12 mm thick specimens. Approximately 2 mm from one of the edges of the 15 mm specimen, the normal stresses are much higher, reaching 268 MPa near the centre of the specimen's cross section. This trend was also observed for the 18 mm and 21 mm thick specimens. The normal stresses fluctuate between -110 MPa and 342 MPa for the 18 mm thick specimen. The high tensile stress of 342 MPa was measured at a width of 13.40 mm and

a height of 6.3 mm above the base of the specimen. Most of the compressive stresses were found between 6 mm and 12 mm above the baseplate whilst low tensile stresses of up to 100 MPa were concentrated close to the surface and base of the specimen. Similarly, a wide range of stresses from -165 MPa to 344 MPa was measured for the 21 mm thick specimen at a width of 13.40 mm. In summary, the magnitude of the normal stresses increased with part thickness.
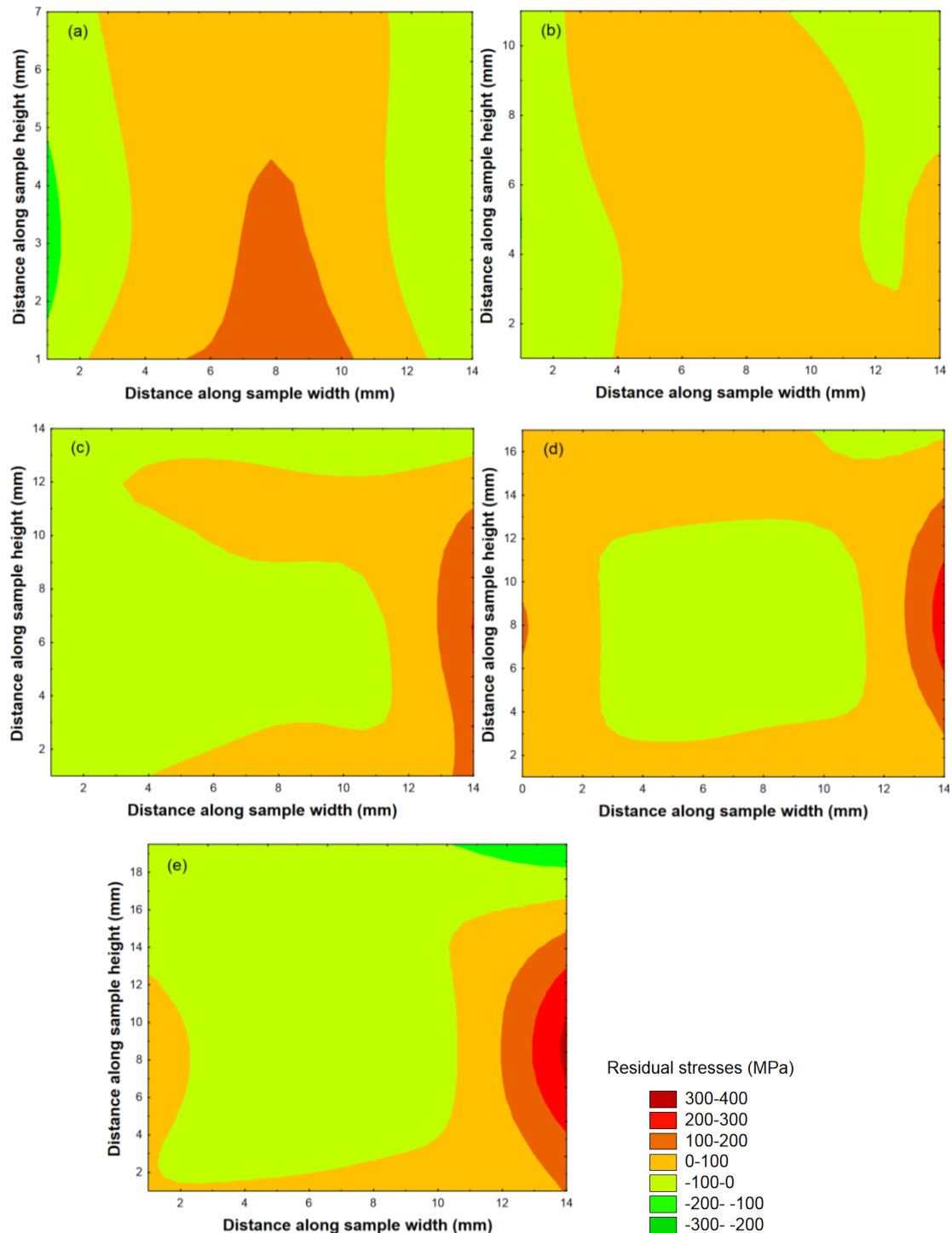
Figure 5.3: Normal stresses for parts of different thicknesses (a) 9 mm, (b) 12 mm, (c) 15 mm, (d) 18 mm and (e) 21 mm

5.2.2 Longitudinal stresses

The longitudinal stresses also generally ranged between -100 and 100 MPa. As shown in Figure 5.4, the samples were largely under compression around the central cross section regions. For regions approximately 2 mm from the top and bottom surfaces of the specimens, the stresses were mainly tensile.
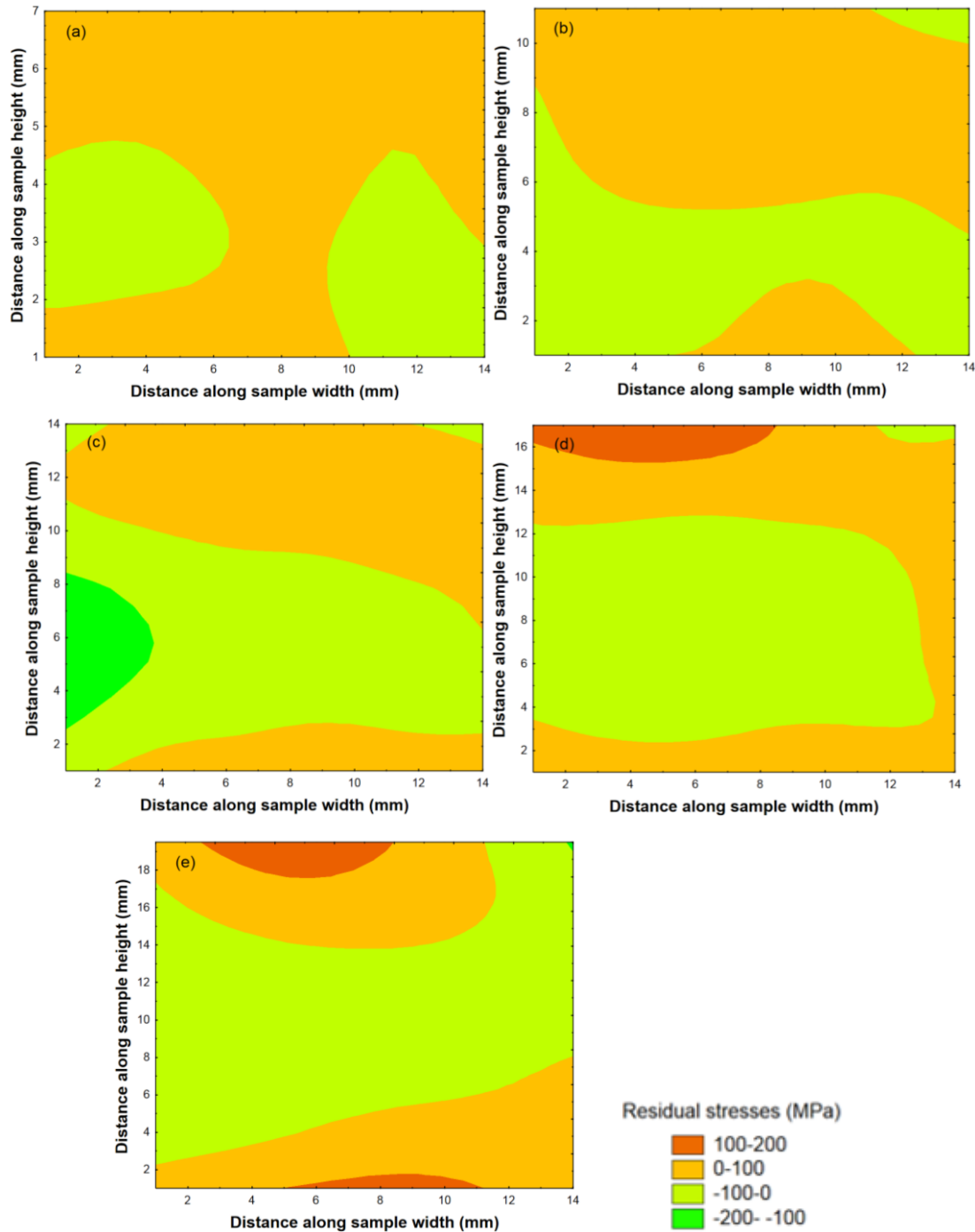
Figure 5.4: Longitudinal stresses for parts of different thicknesses (a) 9 mm, (b) 12 mm, (c) 15 mm, (d) 18 mm and (e) 21 mm

81

Despite an isolated maximum tensile stress of 198 MPa which was found at one position (at 4 mm and 13.4 mm along sample height and width respectively), the stresses in the 9 mm thick specimen were generally limited to 100 MPa and below. A similar trend was observed for the 12 mm specimen which had a peak stress of 114 MPa, as well as the 15 mm thick part whose maximum tensile stress was 152 MPa. The 18 mm and 21 mm thick parts have somewhat similar residual stress patterns and magnitudes that range from -108 MPa to 146 MPa. To summarise, longitudinal stresses are generally low relative to the material's yield strength. In terms of residual stress magnitudes, no significant difference was observed for the different part thicknesses except that the thicker specimens (18 mm and 21 mm) had slightly higher concentration of residual stresses greater than 100 MPa as inferred from Figure 5.4.

5.2.3 Transverse stresses

The transverse residual stresses are comparatively higher than the normal and longitudinal stresses. The results for this component are summarised in Figure 5.5. For all the evaluated width positions, the distribution of the transverse stresses shows a consistent pattern whereby the stresses relax from a tensile state near the baseplate into a more compressive state towards the centre of the specimen before increasing again closer to the surface of the specimen.

The 9 mm part experienced transverse residual stresses that ranged from -110 MPa to 174 MPa. In comparison, the 12 mm had higher stresses spanning between -150 MPa and 212 MPa. The stress magnitude increases further for the 15 mm thick part to vary from a minimum of -168 MPa to a maximum of 222 MPa. For the 18 mm thick specimen, the residual stress is much higher compared to the smaller part sizes already discussed. At about 2 mm above the wire-cut side of the specimen, the stress ranges from -6 MPa to 247 MPa. Further along the specimen's height, the stress falls into a nearly compressive state between heights of 4 mm and 13 mm, with the most compressive stress measured being -160 MPa. Near the top surface of the specimen, a maximum stress of 294 MPa was found. The highest stress magnitudes were measured for the 21 mm thick specimen. Near the bottom and top surface for this part thickness, the maximum stress was 394 MPa. Relatively high compressive stresses that reached a -343 MPa were also found for this thickness. There is strong evidence of a general increase of the magnitudes of the transverse stress component with increase in part thickness and this applies for both the tensile and compressive stresses.
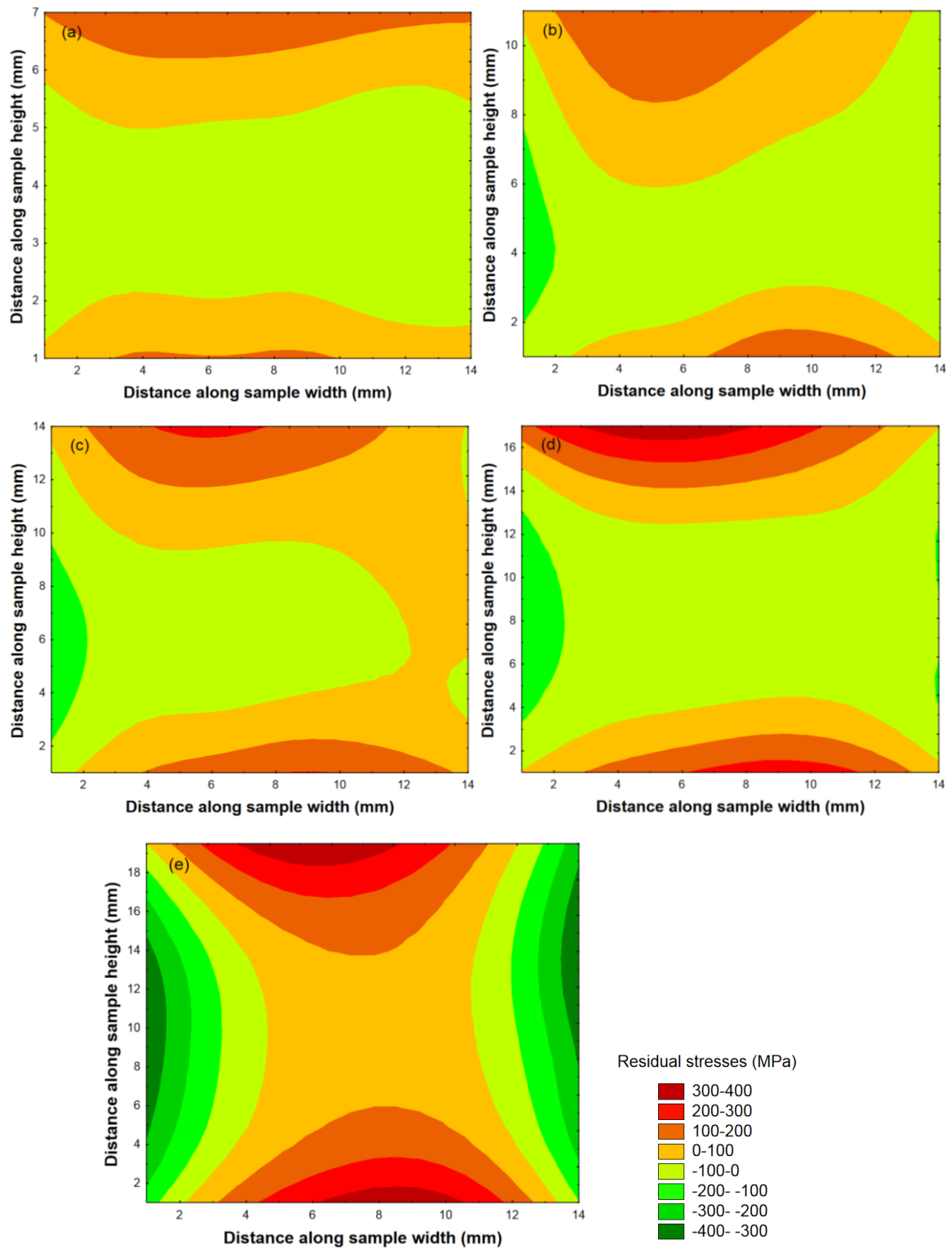
Figure 5.5: Transverse stress components for parts of different thicknesses (a) 9 mm, (b) 12 mm, (c) 15 mm, (d) 18 mm and (e) 21 mm

5.2.4 Summary

In order to come up with an appropriate comparison of the stress behaviour for different part thicknesses, similar measurement positions were chosen across all specimens – that is, just below the surface and just above the wire-cut side of the specimens. The comparative summary is given in Figure 5.6 where no specific trend is evident for the normal and longitudinal stress components, but it is clear that the stresses generally increase with increase in part thickness.
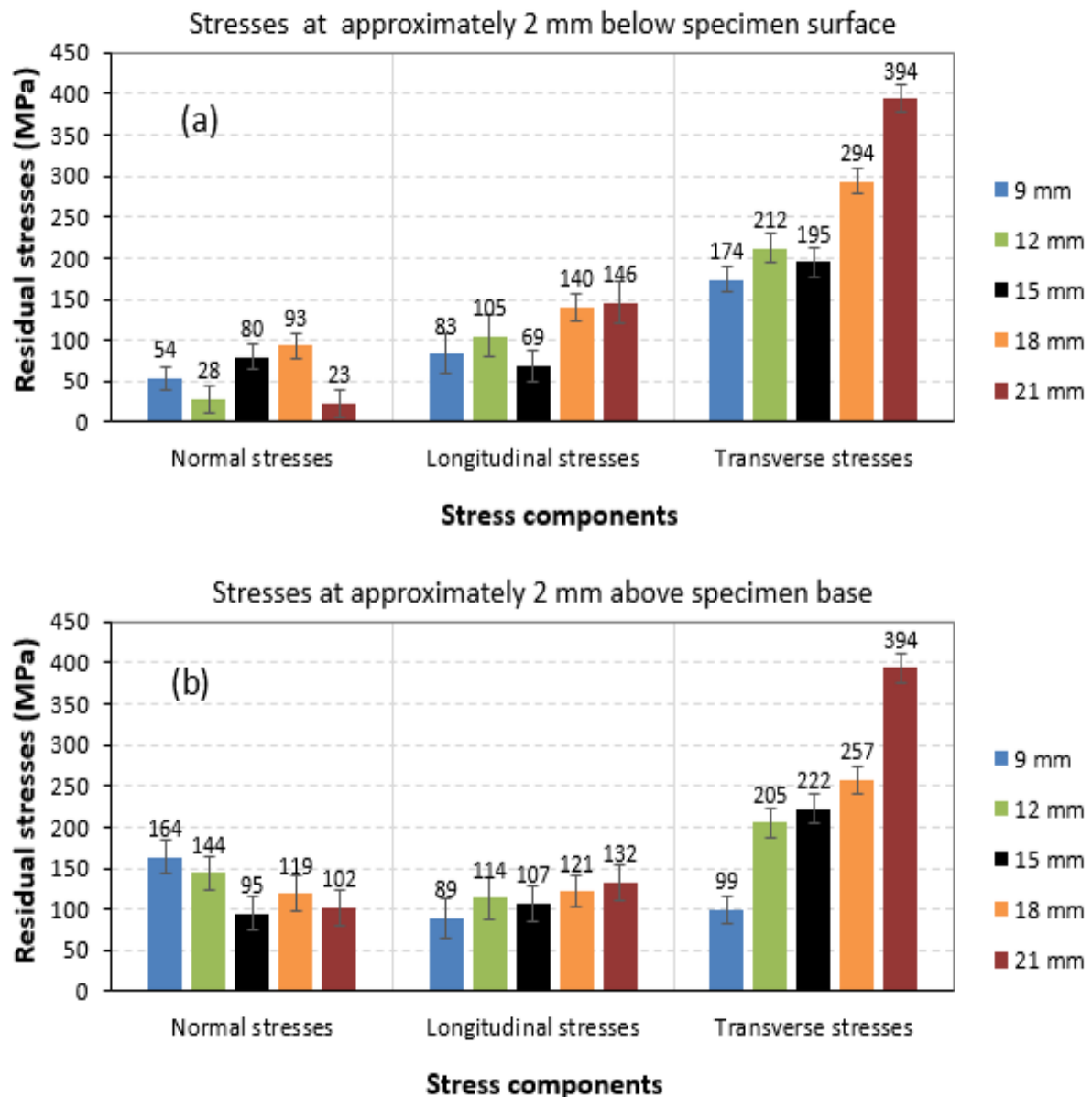
Figure 5.6: Maximum stresses for positions close to the top surface (a) and base of the specimen (b)

Overall, the highest residual stress magnitudes were measured along the transverse direction for all specimens. The longitudinal direction had relatively lower stresses. Similar observations relating to the differences in the stress magnitudes in these directions are reported by Nadammal *et al*. (2018). In this work, the wire (EDM) cutting was done along the length (X-axis) of the specimens and this could have directly impacted on stress relief in this longitudinal direction. Furthermore, the geometry of the specimens favours distortions in the longitudinal direction rather than in the transverse direction. The 21 mm thick part suffered the highest tensile residual stress of 394 MPa. Relative to the material's yield strength, stress levels in this range can be considered high. In comparison, the thinner specimens experienced lower maximum stresses as indicated in Figure 5.7 where it is clear that the magnitude of residual stresses experienced increases with increase in part thickness.
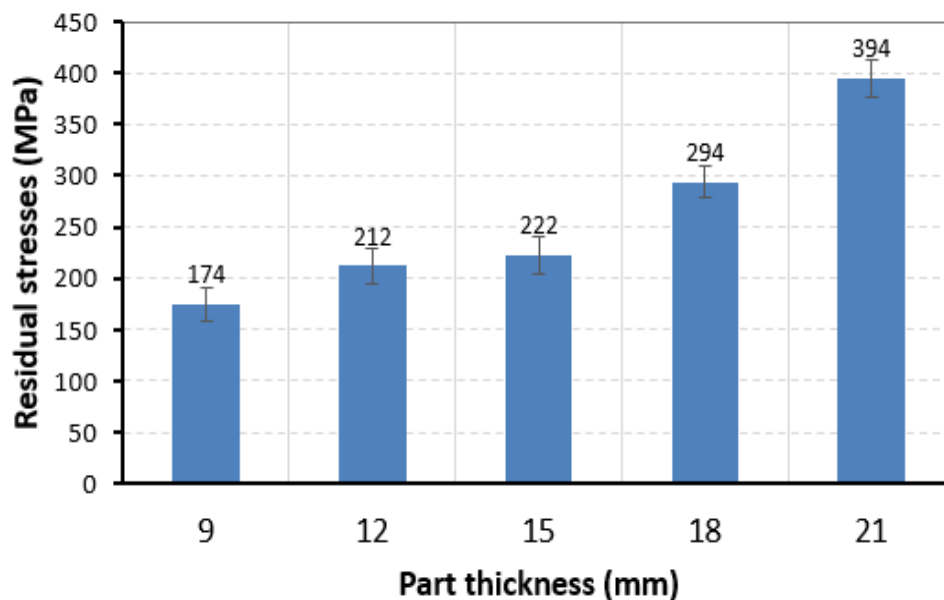
Figure 5.7: Maximum stresses for the different part thicknesses

Although no visible warping was observed for the finished components after removal from the baseplate, it is inevitable that some stress relief occurs after the separation and this can have an impact on residual stress measurement results. CMM measurements showed that the 9 mm and 12 mm specimens deformed slightly more than thicker specimens (15 mm, 18 mm and 21 mm) as shown in Figure 5.8. The distortion results in Figure 5.8 are based on averages for 3 specimens for each thickness investigated. The differences in the deformations, however small, can result in significant differences in the residual stresses. Thicker specimens, on the other hand, have higher stiffness, enabling them to easily resist deformation that would otherwise lead to stress relaxation and/or redistribution. Where possible, stress measurements should be

85

done whilst the specimens are still attached to the baseplate. Regardless, the thicker specimens (15 mm, 18 mm and 21 mm), which experienced almost identical deformations, still had different residual stress magnitudes which correlate to their thicknesses. The bulky material for the thick specimens (18 mm and 21 mm) contribute to faster cooling of these specimens that also leads to the observed higher residual stresses in comparison to 9 mm, 12 mm and 15 mm thick specimens.
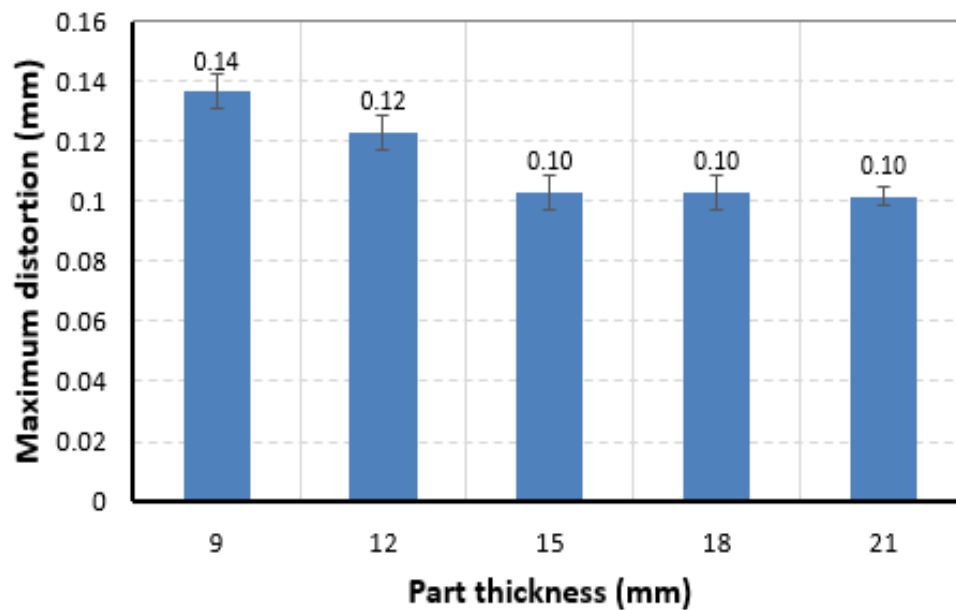
Figure 5.8: Distortion of specimens along the length

5.2.5 Preliminary conclusions

The results presented for influence of part thickness on residual stresses led to the following conclusions:

- Residual stresses are high closer to the specimen's top surface and near the base. However, in order to fully understand the distribution of residual stresses in the specimens, measurements can be taken at more positions along the specimen's length as well, and surface residual stresses need to be evaluated using X-ray diffraction method.

- Residual stress magnitudes are higher for thicker specimens as compared to their thinner counterparts. Whilst separation of the parts from the baseplate might have caused some redistribution of residual stresses, the trend of residual stresses is very consistent for the part thickness range studied.

- Tensile stresses are balanced by similar magnitudes and concentration of compressive stresses.

5.3 Influence of scanning strategies

The influence of island sizes, exposure type and scanning pattern are discussed in this section of the results. Firstly, an analysis of porosity for the different island sizes and exposure types is presented. Later, the effect of the scan vector length (island size) and scanning sequence on residual stresses and productivity is discussed. Residual stresses were measured using the neutron diffraction technique whilst XRD was also utilised to evaluate surface stresses.

5.3.1 Effect of island size on porosity

Square islands of 3 mm, 5 mm and 7 mm sides were adopted to consolidate parts of the same dimension, that is, a 50 mm × 15 mm × 15 mm geometry similar in length and width to the ones used in section 5.2. The images of the surfaces of the as-built specimens are given in Figure 5.9. The Archimedes' density test method was conducted on three 15 mm cubes extracted from each specimen, prior to CT scanning and optical microscopy.
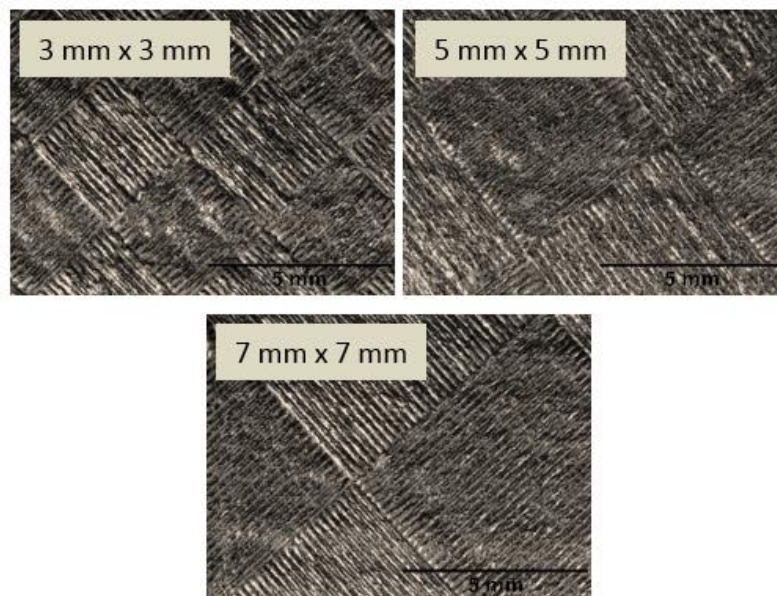
Figure 5.9: Images of the as-built surfaces for the 3 island sizes studied

The 3 mm × 3 mm islands resulted in the highest porosity of 1.32 % ± 0.35. A marginal difference was found between the porosities for 5 mm × 5 mm and 7 mm × 7 mm islands, standing at 0.66 % ± 0.18 and 0.63 % ± 0.22 respectively. Similar findings are reported by Lu *et al*. (2015) who observed high cracking and porosity tendencies with decreasing island size.

The CT scan results for parts manufactured using 3 mm × 3 mm and the 5 mm × 5 mm islands are shown in Figure 5.10. These results confirm the higher porosity that was calculated using

the Archimedes' technique for the 3 mm × 3 mm against that for 5 mm × 5 mm islands. The specimen built from 7 mm × 7 mm did not have any detectable pores for the 15 μm voxel size that was used. This does not mean that this specimen had completely no pores in it, but that there were no pores greater than 45 μm. The pores observed for the different islands were random across the planes of viewing. This indicates that the porosity was not a result of insufficient overlaps between tracks or islands, but a result of overheating. As the scan vector length is reduced, there is accumulation of heat within an island. This heat accumulation, when it becomes excessive, leads to balling and poor metallurgical bonding. In this research, there was sufficient overlap between islands and individual scan tracks. Therefore, the observed increase in porosity is due to balling that results from heat build-up and, thus, over-heating. In a related previous study, the work presented by Yasa *et al*. (2010) shows that higher porosity for smaller islands was a result of hatch spacing errors, which can easily be corrected.
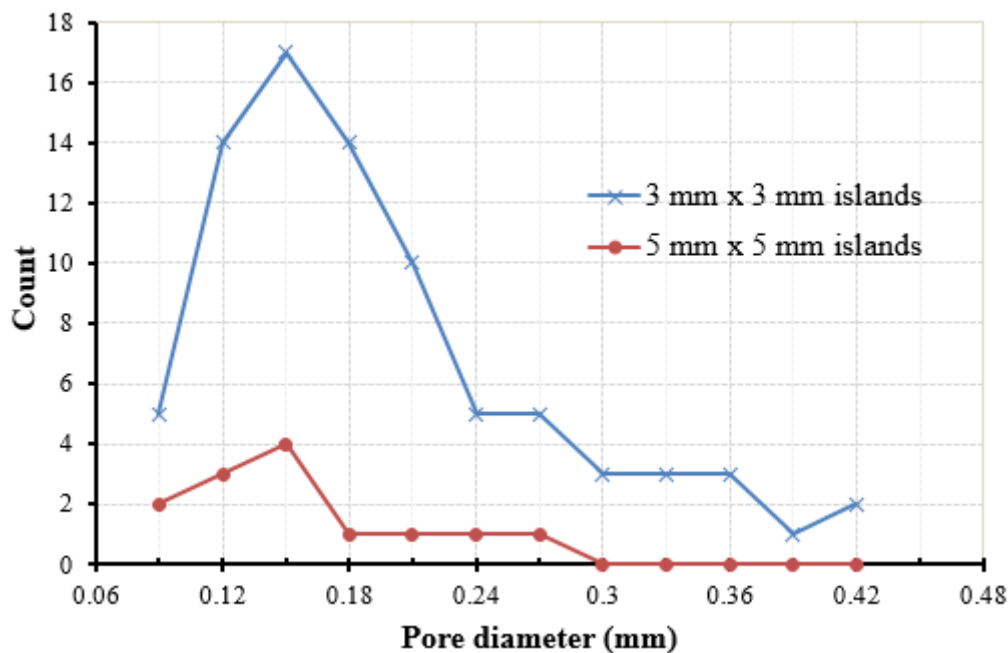
Figure 5.10: CT scan results - pore size distribution for parts built using 3 mm × 3 mm and 5 mm × 5 mm islands

Optical microscopy also showed a higher concentration of pores for the 3 mm × 3 mm islands compared to 5 mm × 5 mm and 7 mm × 7mm. Most of the pores for the 3 mm × 3 mm islands were irregularly shaped, particularly along the building direction as shown in Figure 5.11 where pores of greater than 100 μm length can be observed for this island size. The XZ plane is along the building direction whereas XY is the plane perpendicular to it. The images along the building direction clearly depict the layer-wise consolidation style. Along the building

88

direction (XZ plane), the pores are largely present around the overlapping track and layer regions where the heating effect is excessive. No notable differences were observed under the microscope for the 5 mm × 5 mm and 7 mm × 7 mm islands. This is in agreement with findings from the Archimedes' method. The size of pores that was picked by the CT scanner is generally bigger than that for optical microscopy. CT scanning is based on 3D measurements whereas in optical microscopy, there is a possibility of revealing only the tip of an otherwise huge pore. Regardless, the CT scan, optical microscopy and Archimedes' results correlate well.
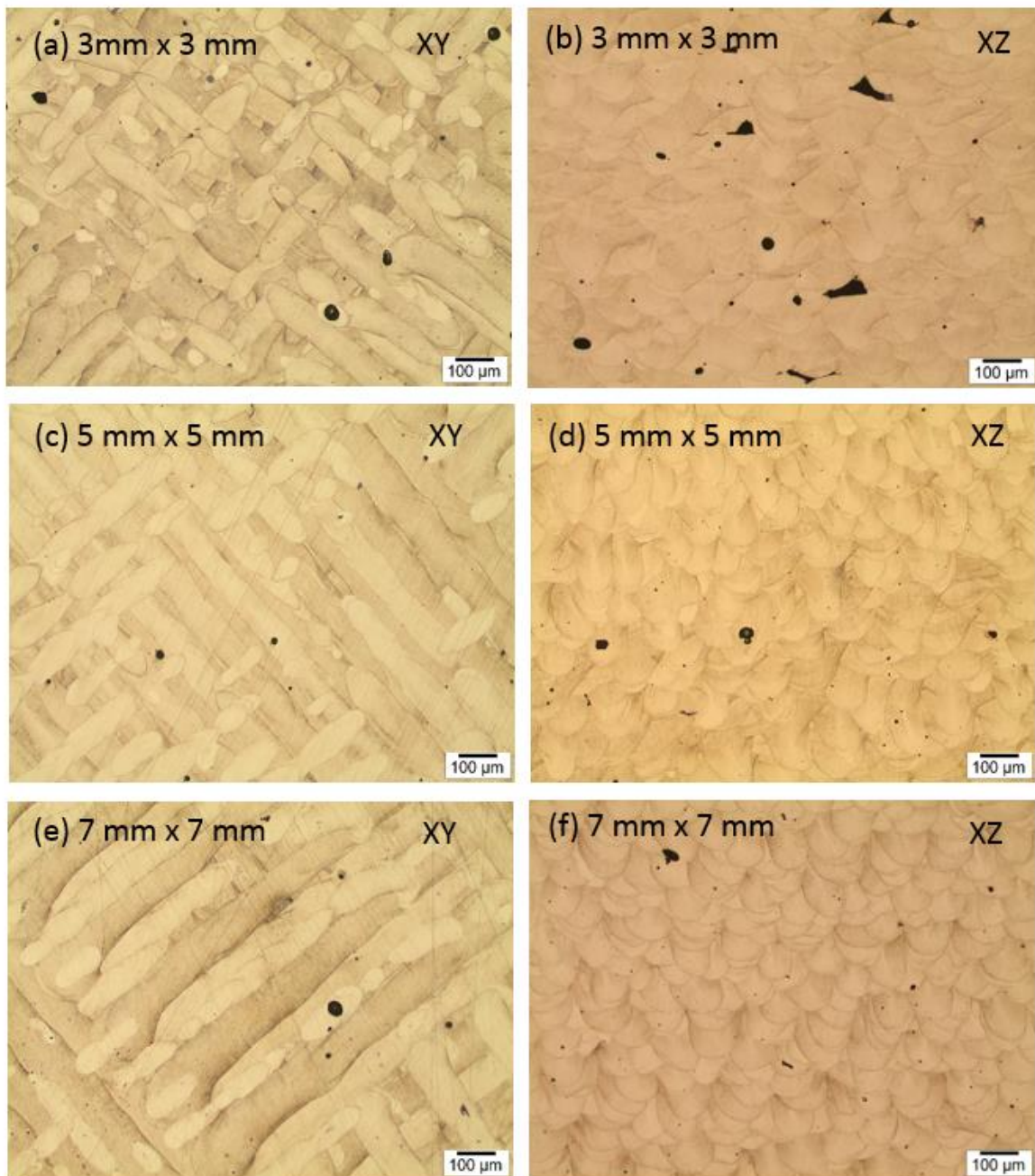
Figure 5.11: Microscope images of the etched samples

5.3.2 Effect of island size on residual stresses - ND results

For the neutron diffraction technique, residual stresses were evaluated in three directions, that is, normal, longitudinal and transverse directions in a similar fashion to the evaluation of stresses in parts of different thicknesses presented earlier in 5.2.
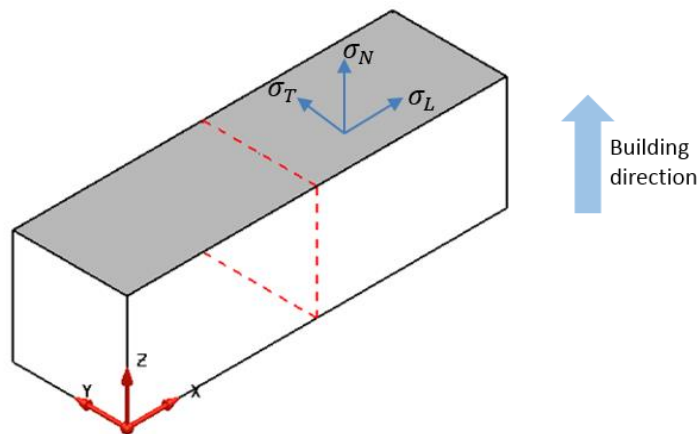
Figure 5.12: Components of residual stresses measured with neutron diffraction

5.3.2.1   Normal stresses

The influence of island size on the normal component of residual stresses is shown in Figure 5.13. For all the three island sizes, normal stresses are largely below 50 MPa, with small regions of the 3 mm × 3 mm as well as 5 mm × 5 mm islands falling into a compressive stress range between -150 and -200 MPa. Whilst there is generally no direct relationship between the nature/magnitude of the stresses and the positions within the specimen, these stresses become more tensile towards one of the edges along the width of the specimens. Maximum tensile stresses of 138, 268 and 280 MPa were found at 13.4 mm along the width direction for the 3 mm × 3 mm, 5 mm × 5 mm and 7 mm × 7 mm islands respectively. The distribution of normal stresses for 5 mm and 7 mm vectors is quite similar, except for the more tensile stresses present for 7 mm towards the top surface of the specimen.
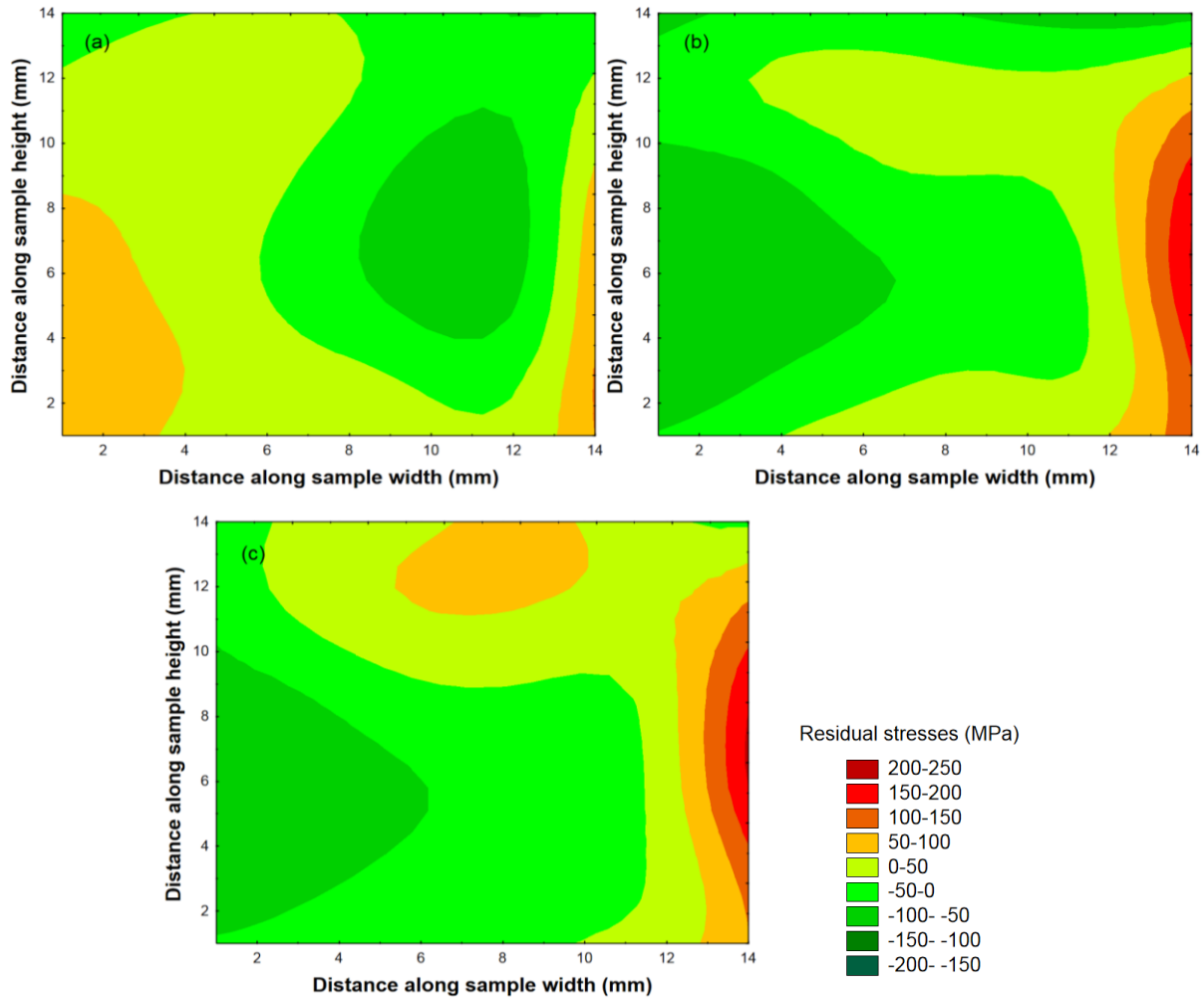
Figure 5.13: Normal stresses for the different island sizes: (a) 3 mm × 3 mm, (b) 5 mm × 5mm and (c) 7 mm × 7 mm

5.3.2.2   Longitudinal stresses

The longitudinal stresses illustrated in Figure 5.14 show less scatter compared to normal stresses described earlier. The specimen that was built using 3 mm × 3 mm islands had the highest magnitudes of both tensile and compressive stresses. Close to the surface, the stresses were purely tensile, ranging from 103 MPa and 195 MPa. Similarly, close to the wire cut side, tensile stresses between 48 and 131 MPa dominated. The compressive band of residual stresses at the centre of the specimen reached -215 MPa. On the other hand, the stresses were generally lower for the 5 mm × 5 mm islands compared to 3 mm × 3 mm islands. Residual stresses for this island size (5 mm × 5 mm) declined from a range between -55 MPa and 107 MPa near the baseplate to between -196 MPa and 36 MPa at 6 mm above the baseplate. Further above the baseplate, the residual stresses increase and reach top values of between 59 MPa and 152 MPa at height of 11 mm before declining to between -61 MPa and 69 MPa 2 mm below the specimen

surface. Relative to the material's yield strength, the 7 mm × 7 mm islands also exhibited generally low stresses that ranged from -166 MPa to 143 MPa. The longitudinal stresses for this island size are generally compressive above the wire-cut side of the specimen surface up to about 11 mm along the specimen's height. Thereafter, the stress becomes tensile, reaching a top value of between 72 MPa and 143 MPa at 2 mm below the top surface of the specimen.
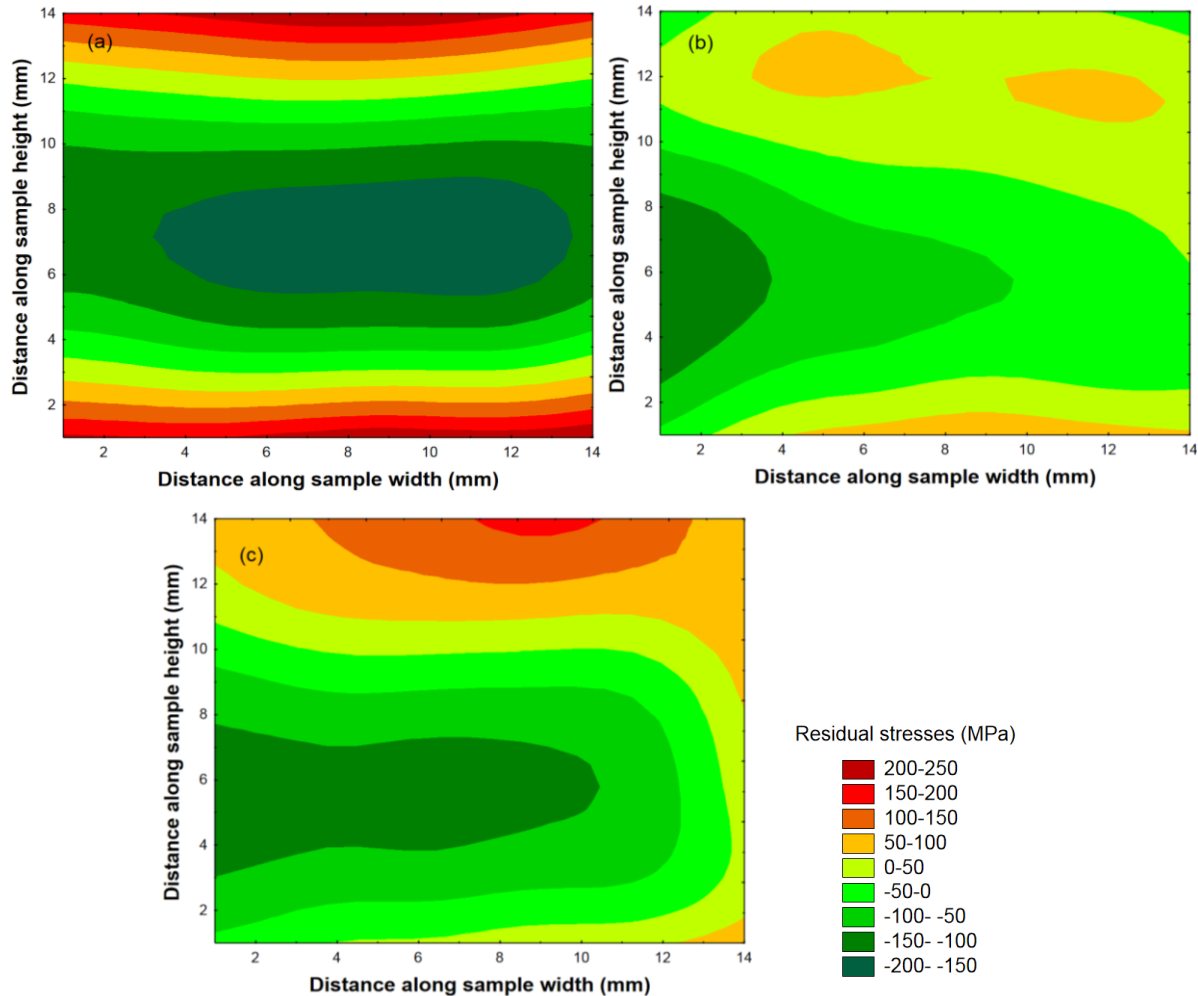
Figure 5.14: Longitudinal stresses for the different island sizes: (a) 3 mm × 3 mm, (b) 5 mm × 5mm and (c) 7 mm × 7 mm

5.3.2.3 Transverse stresses

For the transverse stress components, the general trend is that the stress is tensile near the specimens' bottom and top surfaces (Figure 5.15). Towards the centre of the specimens (between 3 mm and 9 mm along the height), the stress is almost purely compressive. The maximum stress measured for the 3 mm × 3 mm islands was 161 MPa, found at approximately 2 mm along the specimen's height and 9 mm along the width while the most compressive stress found was -112 MPa.

For the 5 mm × 5 mm islands, the maximum stress value was 222 MPa near the baseplate. All the other stresses found at this height were tensile, albeit low, except for a compressive stress of 58 MPa that was measured near the edge of the specimen. The lowest stress that was measured for this island size is -168 MPa. On the other hand, the highest stress value (250 MPa) was found close to the top surface of the specimen for the 7 mm × 7 mm islands. Other stress magnitudes for this island size ranged between 150 and 250 MPa. As for compressive stresses, the central region of the specimen reached -165 MPa around 6 mm along the height and width of the specimen.
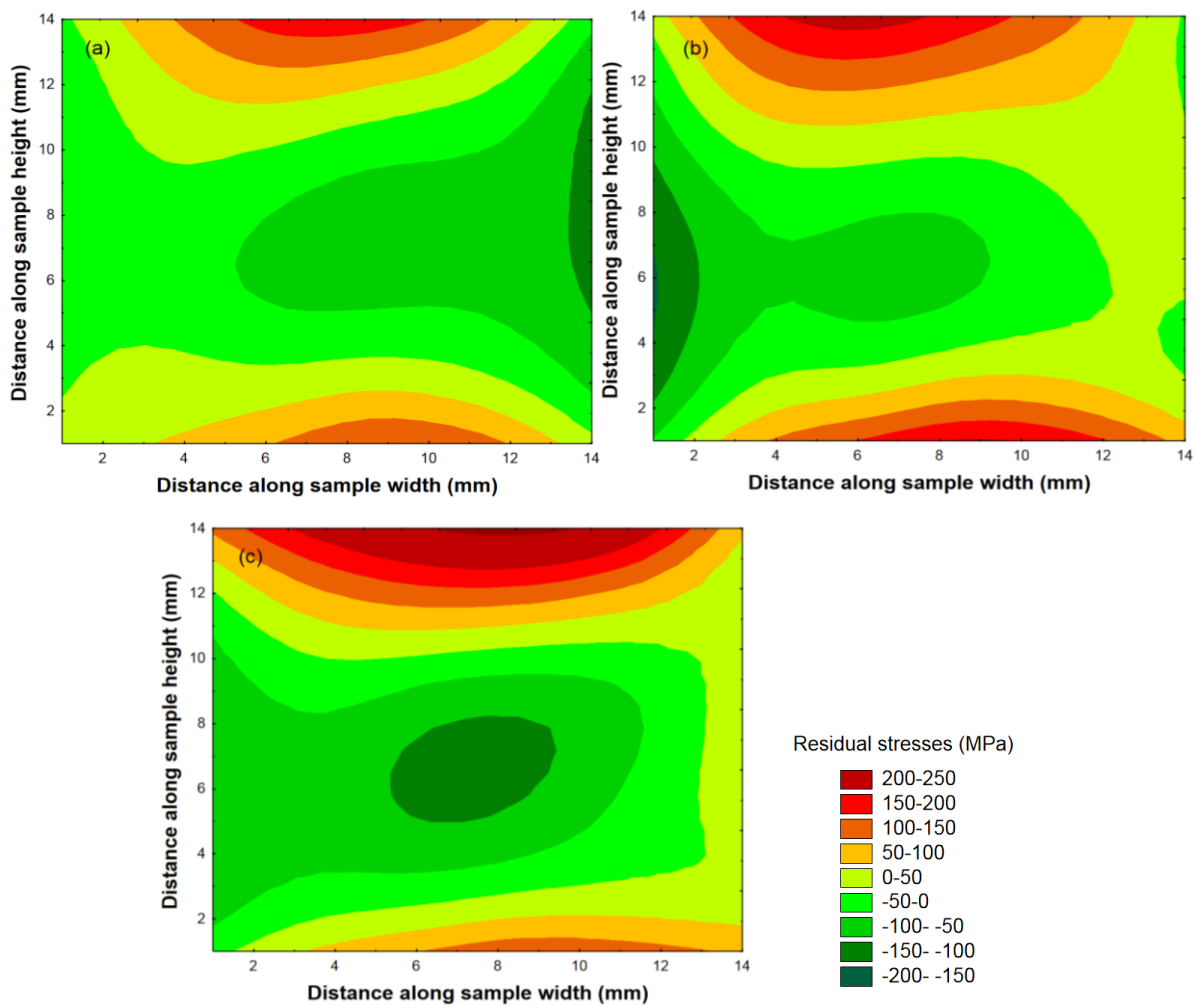
Figure 5.15: Transverse stresses for the different island sizes: (a) 3 mm × 3 mm, (b) 5 mm × 5mm and (c) 7 mm × 7 mm

5.3.3 Surface stresses – XRD measurements

Three positions were selected and evaluated for residual stresses as shown in Figure 5.16. The first and third positions were located at 10 mm from the ends of the specimen, along its length. The second point was at the centre of the specimen, that is, 25 mm along its length.
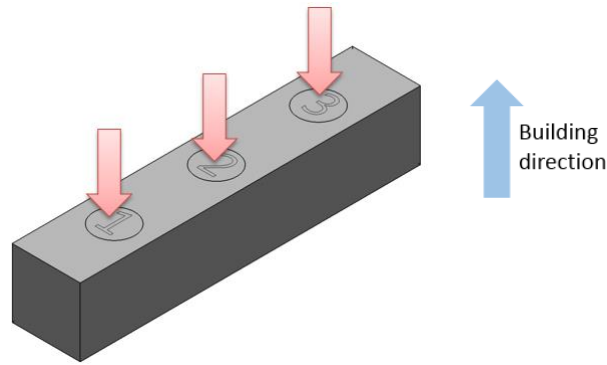
Figure 5.16: Measurement positions for XRD

All surface stresses evaluated by XRD were compressive. The least average residual stress magnitude of 204 MPa (compressive) was measured for an island size of 3 mm × 3 mm. The numerous pores associated with this island size as discussed in section 5.3.1 are responsible for the lower magnitude of residual stresses for this island size as compared to 5 mm × 5 mm and 7 mm × 7 mm islands. Dividing the scanning area into 7 mm × 7 mm segments yielded slightly lower compressive stresses compared to 5 mm × 5 mm as shown in Table 5.1. In agreement with ND findings, the residual stresses for the 5 mm × 5 mm and 7 mm × 7 mm islands are quite similar.

Table 5.1: Surface stress results for the different island sizes

Island size	Point 1 stress	Point 2 stress	Point 3 stress	Mean stress
3 mm × 3 mm	-155.1 ± 19.5 MPa	-268 ± 22.9 MPa	-187.4 ± 24.6 MPa	-204 ± 22 MPa
5 mm × 5 mm	-275.5 ± 37.8 MPa	-372.3 ± 15.7 MPa	-399.9 ± 35.2 MPa	-349 ± 30 MPa
7 mm × 7 mm	-324 ± 14.6 MPa	-314.1 ± 37.2 MPa	-342.6 ± 28.4 MPa	-326 ± 35 MPa

5.3.4 Discussion summary

The neutron diffraction measurement results show that normal and transverse residual stress magnitudes rose with increase in island size (or scan vector length), although no significant differences were observed between 5 mm and 7 mm vectors. Furthermore, shortening the scan vectors is accompanied by an increase in the total scanning time per layer. A quick scanning time analysis per layer was performed for a 50 mm × 50 mm scanning area from which the average scanning times were found to be 40, 41 and 42 seconds for the 7 mm, 5 mm and 3 mm scan vector lengths respectively. Reducing the island size increases the number of instances the laser beam should "jump" from one island to the other. Although changing the scan vector

94

length between 3 and 7 mm has an insignificant effect on scanning time per layer, it potentially becomes significant with increase in part(s) volume. Along the normal direction, the maximum tensile residual stress increased from 138 MPa for 3 mm × 3 mm islands to 268 MPa and 280 MPa when the island size was increased to 5 mm × 5 mm and 7 mm × 7 mm respectively. A similar pattern was observed for the transverse component for which the maximum tensile stress rose from 161 MPa to 222 MPa and 250 MPa for 3, 5 and 7 mm × 7 mm islands respectively. The magnitudes of compressive stresses were also similar for 5 mm and 7 mm vectors for the normal and transverse components. On the other hand, the longitudinal component shows an increase of both tensile stress and compressive stress magnitudes for 3 mm vectors compared to 5 mm and 7 mm. These results indicate the directional dependence of the effect of island size on residual stresses. The overheating that can arise from reducing island sizes could be responsible for the higher longitudinal stresses when the scan vector length is reduced. In agreement with the ND measurements, the XRD residual stress magnitudes for 5 mm × 5 mm and 7 mm × 7 mm islands are quite comparable. As mentioned, the increase in porosity with scan vector length reduction is a result of overheating. Additionally, the instances whereby the laser beam must make a turn are much higher for shorter scan vectors compared to longer vectors. As the laser makes this "u" turn, gas is entrapped, resulting in high porosity.

5.3.5 Effect of double exposure on residual stresses

In this research, rescanning was done using the same parameters as the first laser pass because the parameters could not be adjusted for the 2D laser system used. Whereas the porosity was 0.66 % for single exposure, scanning the powder bed twice resulted in an increase of porosity to 0.87 %. To qualitatively confirm these findings, the samples were cut and polished to reveal pores for optical microscopy. As per Figure 5.17, the pores were slightly more concentrated for double exposure compared to single scanning. The maximum size of pore was 50 μm for double exposure, whilst pores were generally below 25 μm for single exposure. These findings indicate that, for this material, rescanning using the same parameters as the initial laser beam pass does not increase density, but actually reduces it. This is possibly due to overheating and associated balling upon re-melting. From this perspective, and given the extra energy costs and increased manufacturing time, there is no motivation to use double exposure strategy at these parameters. However, a trade-off may be necessary depending on the impact of re-scanning on residual stresses.
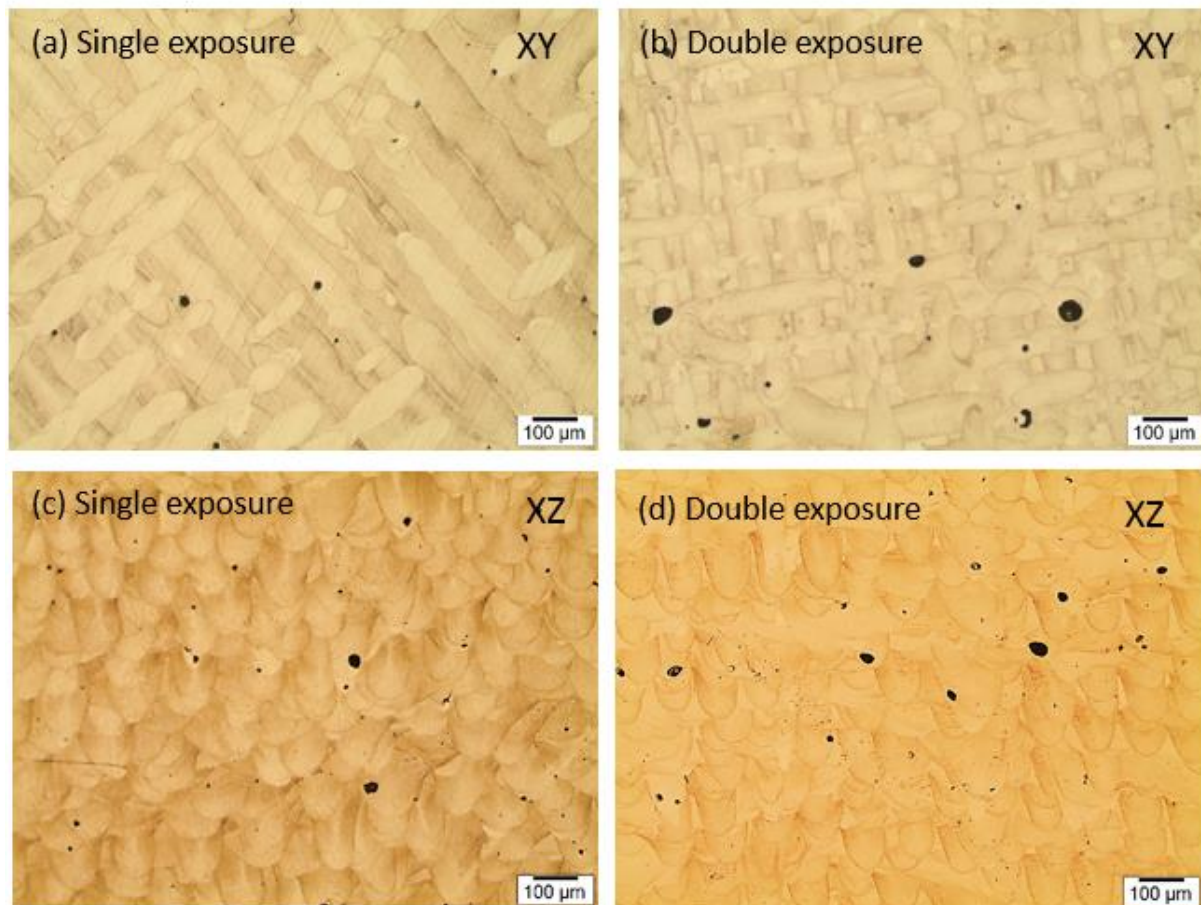
Figure 5.17: Microscope images for single and double exposure

Analysis of neutron diffraction results led to the conclusion that double exposure slightly reduces tensile stresses in all three directions by inducing compressive stresses, which cancel out the previously present tensile stresses. This phenomenon ultimately increases the magnitude of compressive stresses. The contour plots in Figure 5.18 show a bulk transformation from tensile to compressive stresses for all the components upon re-scanning, particularly for the longitudinal component. A maximum normal stress of 268 MPa that was found at 6 mm above the baseplate for single exposure decreased to 198 MPa when the powder bed was scanned twice. The maximum transverse stress for the single exposure strategy is 222 MPa whilst it is 189 MPa when double exposure is used. The stresses are generally more compressive for double scanning.
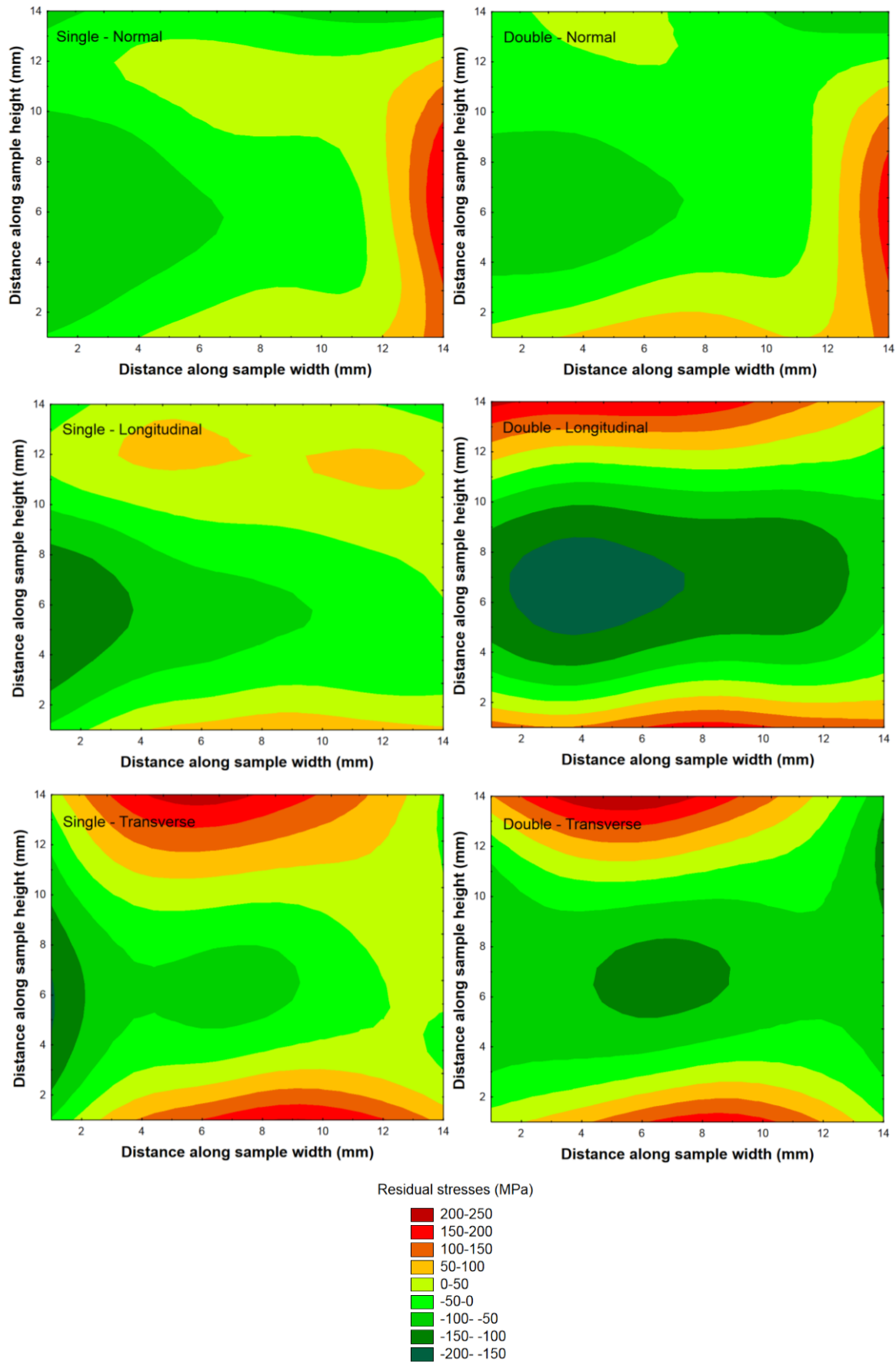
Figure 5.18: Residual stresses for single and double exposures

The XRD results show that the surface stresses become more compressive upon rescanning, averaging -478 MPa in comparison to -349 MPa for single exposure. This further confirms that compressive stresses are introduced during rescanning, a scenario which results in an increase of the magnitude of the already present compressive stresses that developed during the initial laser beam pass. Compressive surface stresses have the advantage of discouraging crack growth and are generally preferred as long as they do not result in warping distortion. However, if these stresses become very high, they can lead to deformations such as bulging. The full XRD stress readings are shown in Figure 5.19 for the measured points (Note: These stresses are all compressive).
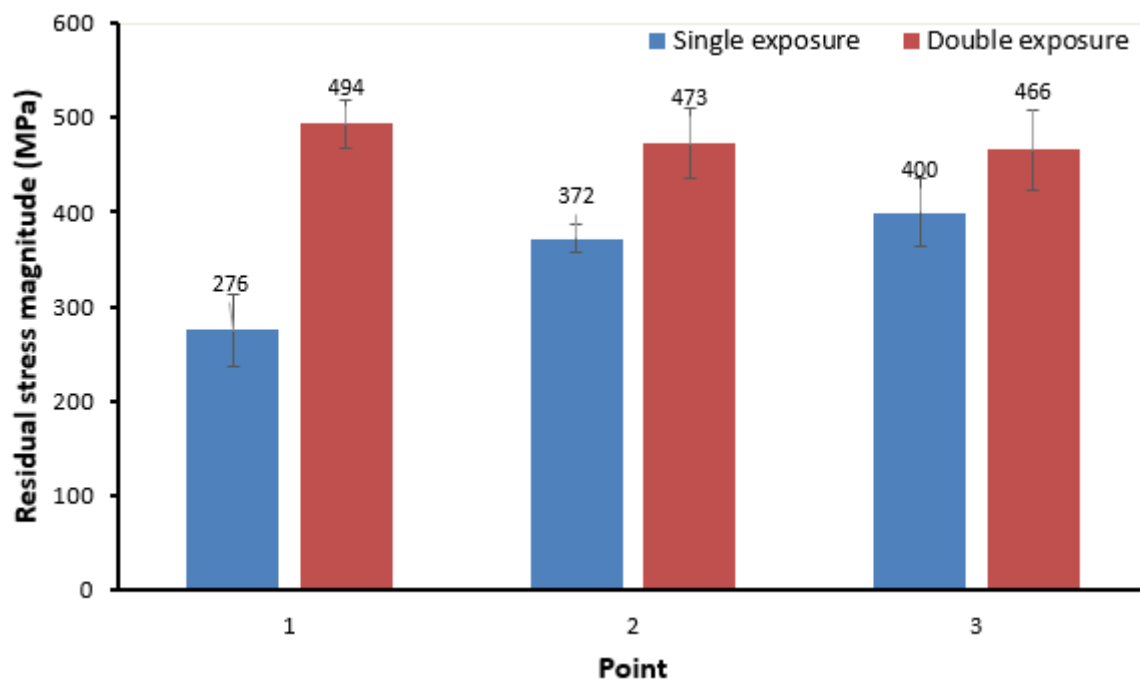
Figure 5.19: XRD residual stress results for single and double exposure

5.3.6 Influence of scanning sequence on residual stresses

To study the effect of scanning sequence on residual stresses, 9 mm thick AISI H13 hot work steel baseplates were exposed to the laser beam according to scanning sequences described in section 4.5.2, that is, the island strategy, successive strategy, successive chessboard and LHI chessboard strategies. The typical sequences for these scanning strategies are given in Figure 5.20.

98

(a) Island (approximation)   (b) Successive

(c) Successive chessboard   (d) LHI chessboard
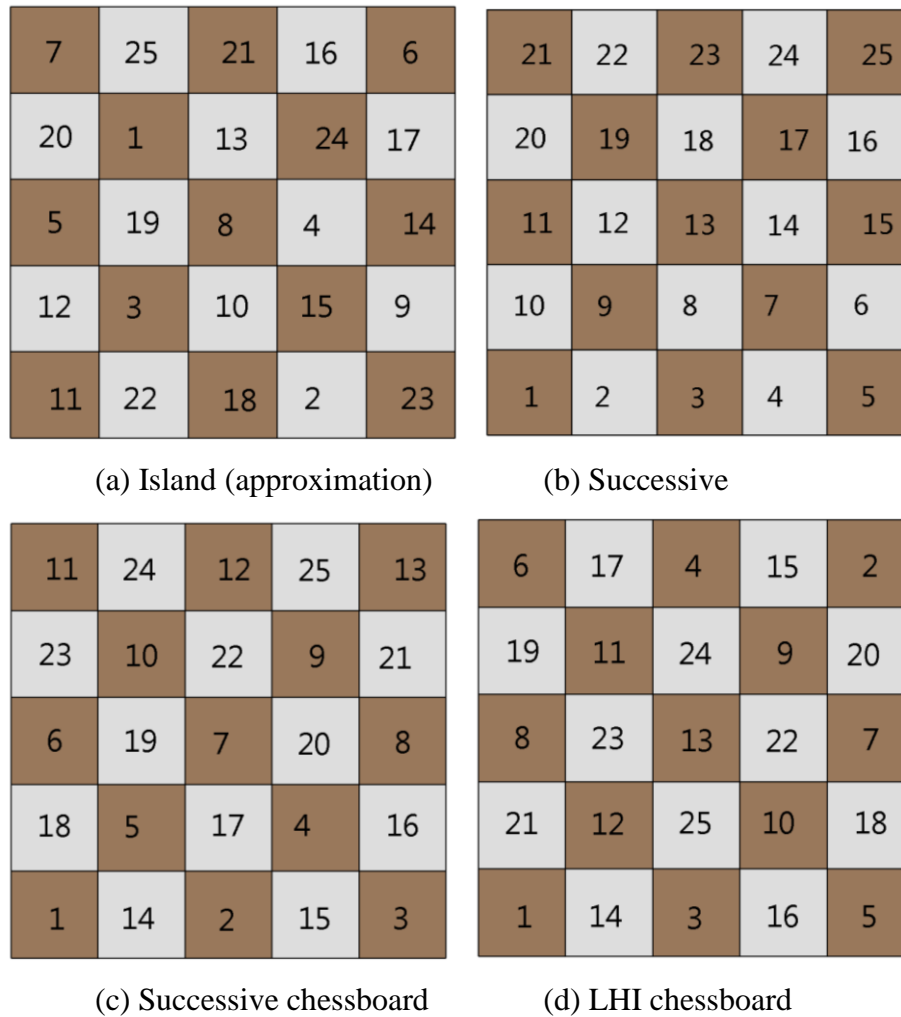
Figure 5.20: Typical sequences for the scanning strategies studied

Prior to laser beam melting, three random positions on the baseplate were analysed for residual stresses. The baseplate was observed to be under compressive residual stress prior to exposure to laser beam. This is due to previous manufacturing processes such as rolling and sandblasting which the baseplate was subjected to. Sandblasting is essential as it reduces the reflectivity of the pre-machined baseplate, thus improving laser absorption. The plot of the d-spacing, *d*, against $Sin^2\psi$ for one of the analysed points on the baseplate before melting is shown in Figure 5.21 where good consistency of measurement between the two detectors can be observed. A similar trend was found for the second evaluated point on the baseplate and indeed for the remainder of the measurements that were performed after exposure. The remainder of the plots can be found in Addendum C. From the stress calculations, the baseplate had an average compressive stress of -450 ± 11 MPa.
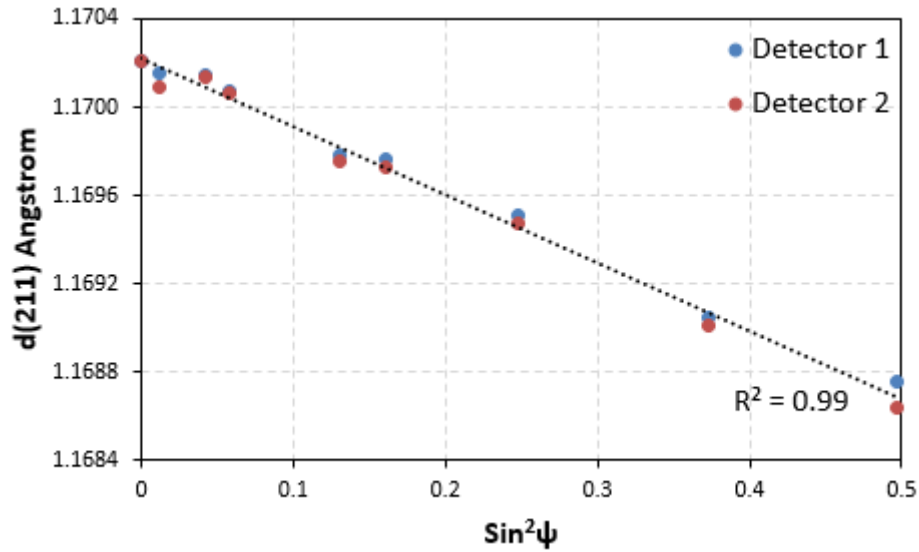
Figure 5.21: Plot of *d* against *sin²ψ* for the tool steel baseplate before laser exposure

Previous studies on residual stresses in SLM (Mugwagwa *et al.*, 2016) show that different positions at the same measurement depth can have different residual stress magnitudes. This has also been shown already in this research in sections 5.2, 5.3.2, as well as 5.3.4. Thus, it is essential to measure on more than one point on the surface in order to draw accurate conclusions. Five measurement positions on the melted surface were selected for residual stress evaluation as shown in Figure 5.22 (a). For each of the five points on the baseplate after exposure, measurements were done at the centre of each "island" along (longitudinal) and perpendicular (transverse) to the scanning direction.

(a)   (b)
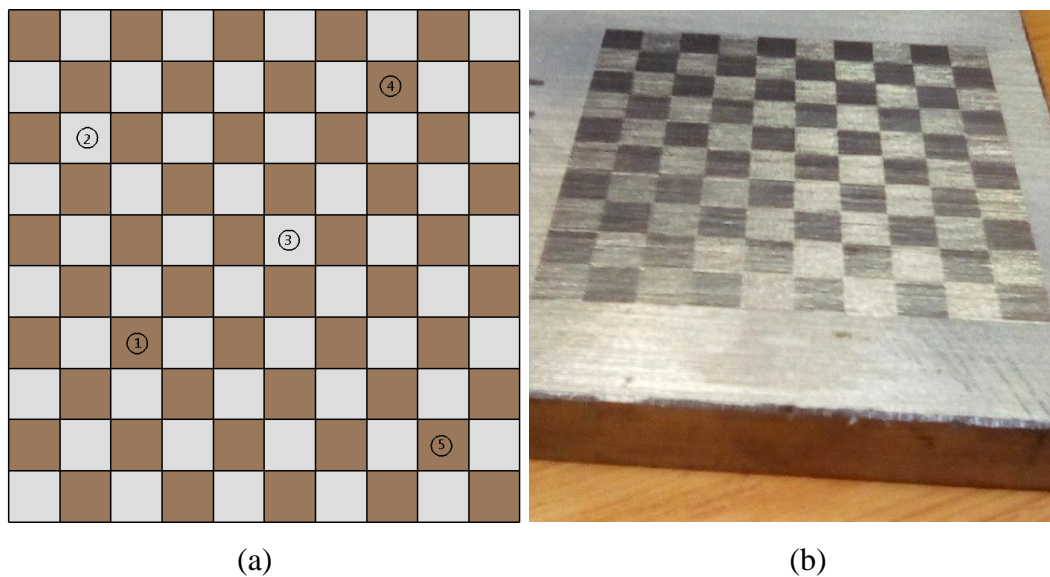
Figure 5.22: Illustration of the measurement positions (a) and image of a melted substrate (b).

After exposure of the baseplates to the laser beam, the measured residual stress magnitudes (for all cases) were much lower than initial stress state, ranging between -42 MPa and -299 MPa. This reduction in the compressive stress magnitude is an indication that exposure of the baseplates to the laser beam induced tensile residual stresses. The difference in the stress states before and after exposure was interpreted as the residual stress associated with the specific scanning strategy. The XRD results show that the successive chessboard scanning strategy contributes to the lowest residual stresses for all the measurement positions, that is, 281 MPa, 151 MPa and 202 MPa, 222 MPa and 188 MPa for points 1, 2, 3, 4 and 5 respectively as shown in Figure 5.23. These results correspond to measurements along the scanning direction only. The successive scanning strategy, on the other hand, contributed to the highest residual stresses. The island strategy (default on the M2 LaserCUSING system) and the LHI chessboard pattern yielded intermediate residual stress magnitudes which were similar for corresponding positions as shown in Figure 5.23.
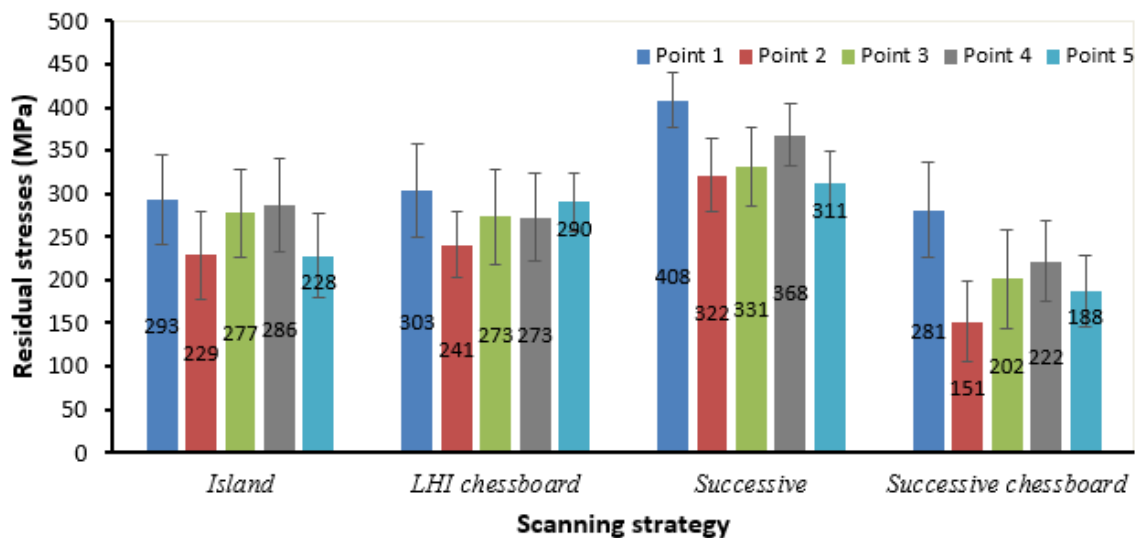
Figure 5.23: Residual stresses associated with the different scanning strategies.

In summary, the successive scanning strategy resulted in the highest mean residual stresses of 348 MPa. In comparison, the island and the LHI chessboard scanning strategies resulted in better distribution of heat and solidification across the powder bed; these strategies contributed to mean stresses of 263 MPa and 276 MPa respectively. Although the island and LHI scanning strategies are different in principle, observation during the actual scanning showed that the randomness of the island strategy in selecting the next island to scan is actually very similar to that of the LHI chessboard. This explains the similarities in the measured residual stress values

for the two scanning strategies. Of interest is the successive chessboard strategy, which contributed to the lowest average stress of 209 MPa as shown in Figure 5.24. The stress measurements in the transverse direction are all lower than the longitudinal direction, but both indicate a similar trend. The successive chessboard appears to have the best distribution of heat and more uniform solidification across the scanning area compared to the other strategies.
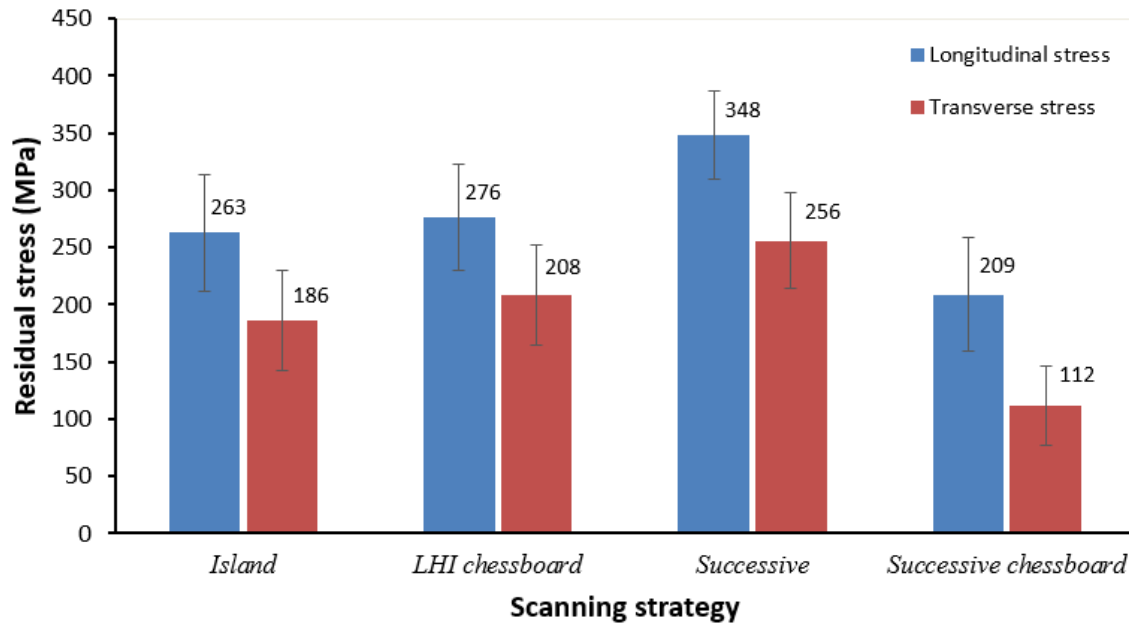
Figure 5.24: Mean stresses for the investigated scanning patterns

5.3.7 Implication of scanning strategies on productivity

Further to the most severe porosity problems, the 3 mm × 3 mm islands contributed to the highest scanning time of 41.77 seconds against 40.54 and 40.09 seconds for 5 mm × 5 mm and 7 mm × 7 mm islands respectively. With respect to the scanning sequence, the lowest scanning time of 40.04 seconds was recorded for the successive scanning strategy. This can be explained by the elimination of the laser beam "jump" time from sub-sector to sub-sector that is characteristic of all the other strategies. However, the successive scanning strategy yields the highest residual stresses as discussed earlier. On the other hand, the successive chessboard strategy is superior to the island and LHI chessboard strategies with respect to both residual stresses and scanning time. There is not much difference between the island and the LHI chessboard strategies for both residual stresses and scanning time since they, in practice, follow a very similar exposure sequence. The scanning times for the different scanning strategies are summarised in Table 5.2 for the 50 mm × 50 mm scanning area.

Table 5.2: Scanning times associated with the different scanning strategies

Scanning strategy	Mean scanning time (s)	Standard deviation (N=6)
Island	40.54	0.03
Successive	40.04	0.09
Successive chessboard	40.16	0.10
LHI chessboard	40.68	0.08

Although the differences in the scanning times for the different strategies are only fractions of a second, they still impact on total building time, especially with increase in consolidation height and for parts that cover a substantial area on the baseplate. For example, a building height of 45 mm translates to 1500 layers for a layer thickness of 30 µm. For the process settings used in this study, the corresponding scanning times for the different scanning strategies would be as given in Table 5.3. The time saving becomes apparent as the number or volume of parts consolidated increases. According to a study by Rickenbacher *et al.* (2013), the scanning time contributes about 77 % of the total time to build up parts. Furthermore, the cost of building is directly proportional to the building time as modelled in Equation ((5.1) (Rickenbacher *et al.*, 2013). Cutting on building time reduces the operational costs related to inert gas, energy and labour. In turn, this would result in reduction of the total manufacturing cost.

$$C_{Build}(P_i) = T_{Build}(P_i) * (C_{Machine} + C_{Inert\ gas}) + V(P_i) * C_{Material}$$

(5.1)

where C_{Build} is the cost of building the part, P_i is part with ith geometry; T_{Build} is the building time (hours); $V(P_i)$ is the volume of the part (mm^3); $C_{Machine}$, $C_{Inert\ gas}$ and $C_{Material}$ represent the machine cost (per hour), cost of inert gas consumption (per hour) and material cost (per kg) respectively (Rickenbacher *et al.*, 2013).

Table 5.3: Estimated scanning times for a 50 mm × 50 mm × 45 mm part

Scanning strategy	Mean scanning time per part (s)	Time savings (against island strategy) per part (s)
Island	60 810	-
Successive	60 060	+750
Successive chessboard	60 240	+570
LHI chessboard	61 020	-210

5.3.8 Preliminary conclusions

The following preliminary conclusions can be made with respect to scan vector length and scanning sequences:

- Reduction of island size leads to porosity increase. The pores observed in this research are randomly distributed across the viewing planes and are clearly not a result of hatching errors or insufficient overlaps between tracks and islands but rather a result of overheating that comes with heat build-up for the 3 mm × 3 mm islands. On the other hand, the porosity and residual stress results for 5 mm × 5 mm and 7 mm × 7 mm islands are very similar.

- Normal and transverse stresses generally decline with decrease in island size. Unfortunately, this is coupled with an increase in porosity. The observed porosity contributes to stress relief when using the 3 mm × 3 mm islands. On the other hand, the longitudinal stresses tend to increase with decrease in island size, an indication of a possibility of overheating due to heat accumulation for short vectors.

- In comparison to single exposure, rescanning generally introduces compressive stresses, thereby reducing tensile stresses by up to 26 %. The induced compressive stresses are generally desirable as they slow down crack initiation and growth. Regardless, double scanning has the obvious effect of increasing the building time. Furthermore, rescanning at the same parameters as the initial laser pass increases porosity.

- Scanning sub-sectors directly one after the other using the successive strategy results in the highest residual stresses. The default scanning strategy (island strategy) had very similar performance to the LHI chessboard with regards to residual stress magnitudes - both contributed to lower stresses due to better distribution of heat when compared to the successive strategy. The proposed successive chessboard had the least residual

stresses. In general, "chessboard" strategies promote more uniform heat distribution and solidification rates across the powder bed.

- There is a notable influence that both island size and scanning sequence have on total scanning time. Small island sizes yield the highest scanning time and vice versa. The successive scanning strategy takes the least time to complete scanning because the laser beam jumps are greatly minimised as opposed to the default and LHI chessboard strategies. There is negligible difference between the scanning times for the successive and the successive chessboard strategies.

5.4 Influence of process parameters

In this section, the influence of process parameters, namely, laser power, scanning speed and layer thickness on residual stresses are investigated. These investigations were carried out alongside porosity evaluations in order to establish the correlations between them. The influence of process parameters is very clear for all experimental results for components manufactured from 30 µm layer thickness as compared to 45 µm. For purposes of statistical analysis, only the 30 µm layer thickness experiments were considered since the porosity results for 45 µm layer thickness experiments do not seem to be significantly influenced by the other variables (laser power and scanning speed).

5.4.1 Influence of process parameters on porosity

The porosity that is associated with the different process parameters was evaluated using the Archimedes' density test method. The results, as illustrated in Figure 5.25, show that there is a very narrow window within which process parameters can be varied whilst yielding sufficient part density (of 99 % or above). Porosity decreases with increase in laser power. This is because generally more energy becomes available to sufficiently melt the powder bed as laser power is increased. In Figure 5.25, it can be seen that when scanning at a speed of 600 mm/s, the mean porosity decreases from 3.37 % at 120 W to 0.39 % at 180 W. It is also clear that for a scanning speed of 400 mm/s, the porosity initially declines from 10.41 % at 80 W to 3.32 % at 120 W. Thereafter, the porosity begins to increase. The increase in porosity either side of 120 W is due to a mismatch between the laser power and scanning speed, which leads to either insufficient melting and poor metallurgical bonding, or over-melting and balling. Both scenarios lead to undesirable porosity which reduces part strength (Kruth *et al.*, 2004; Mazur *et al.*, 2017). In all the experiments, the general trend is that the relative density increases as the scanning speed is gradually increased to an optimum value above which this relative density begins to decline.

The optimum scanning speeds coinciding with the least porosity is unique to the laser power being used. For example when scanning with 180 W, the optimum speed which results in the least porosity is 600 mm/s. Above or below this speed value, porosity tends to increase due to either insufficient or excessive energy density. However, for the tested range of speed, speeds lower than the optimum scanning speed contribute to significantly higher porosity than those above it. The discussion on the influence of laser power and scanning speed cannot be complete without looking at the effect of energy density on the process outcome. This is discussed later in section 6.6.
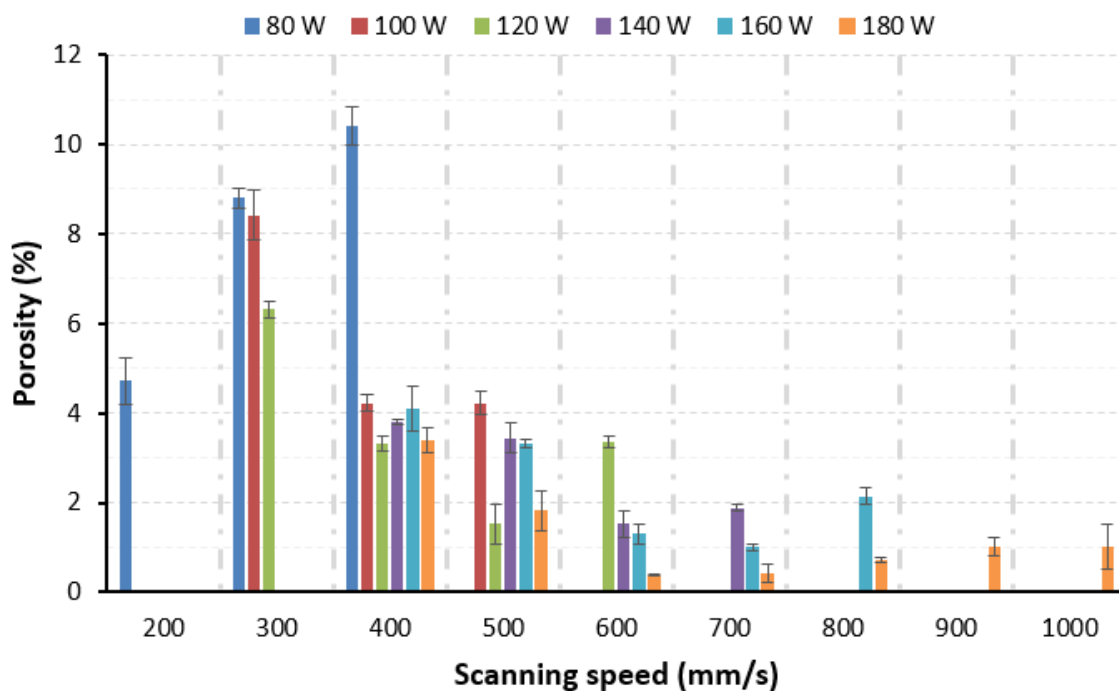
Figure 5.25: Results of porosity versus scanning speed at various laser power values

Good track connection is an important factor in determining the achievable relative density. If track connection or the metallurgical bonding is poor, porosity can be expected. The as-built surface images in Figure 5.26 (top) show poor and good track connection for more porous and less porous parts whilst in Figure 5.26 (bottom), the revealed internal pores are shown for a highly porous and a dense part. These images are consistent with the porosity results presented earlier.

106
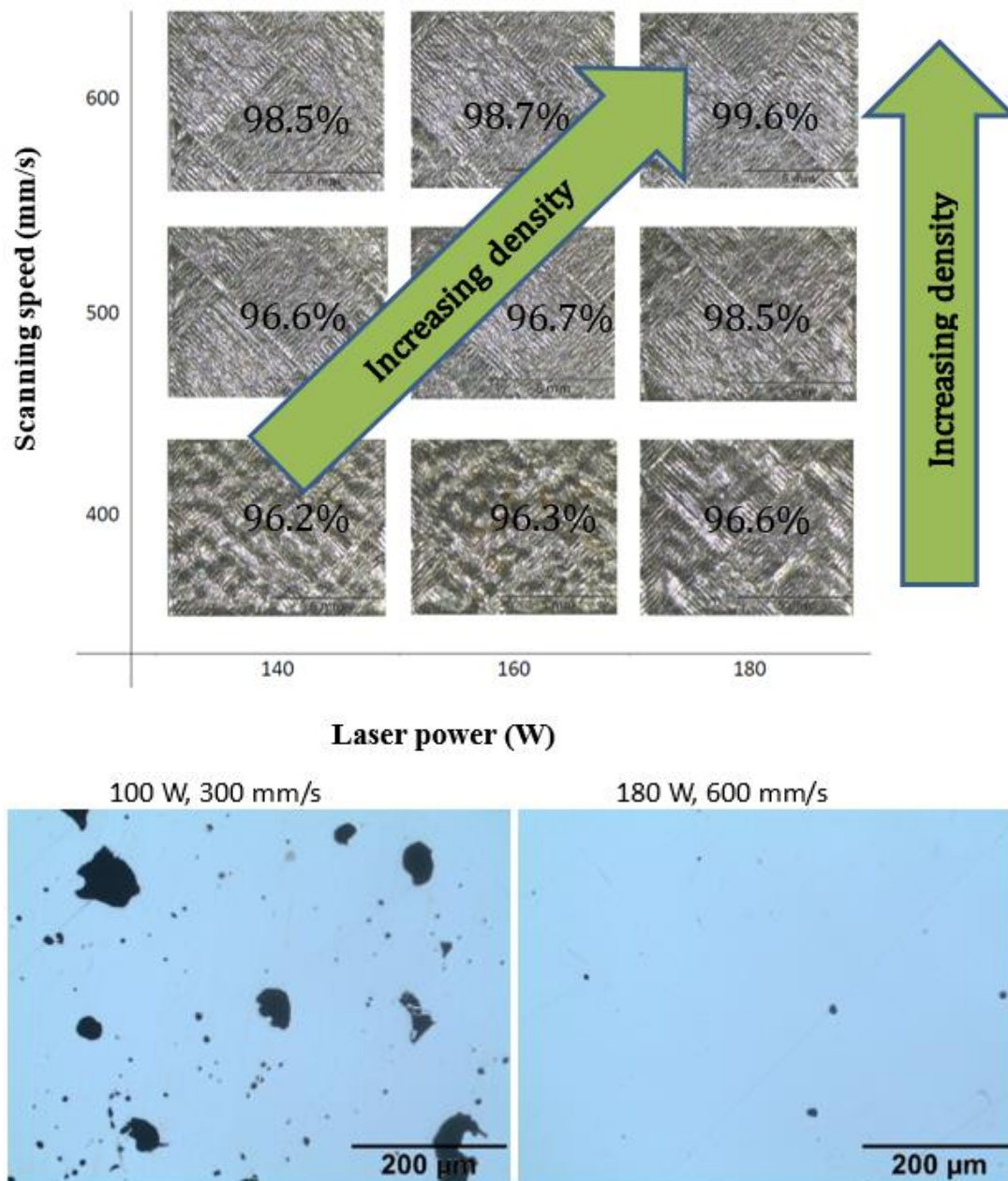
Figure 5.26: Surface images (top) and optical microscope images showing internal pores (bottom) for parts built at different parameter combinations

Statistical analysis shows that both laser power and scanning speed have a statistically significant effect on porosity and, from the experimental data obtained, the porosity, ϕ [%], is dependent on laser power, P [W], and scanning speed, v [mm/s], according to the relationship in Equation ((5.2) (applicable for maximum power of 180 W and scanning speed of 1000 mm/s).

$$\phi = 11.7371 - 0.0439P - 0.0043v$$

(5.2)

The summary statistics and regression summary for the relationship between laser power (in Watts), scanning speed (in mm/s) and porosity, is given in Table 5.4. The model has an overall p-value of less than 0.0001 which shows statistical significance at 95 % confidence level. The p-values for laser power and scanning speed in the regression summary also indicate statistical significance of both factors.

Table 5.4: Statistical summary - influence of laser power and scanning speed on porosity

SUMMARY					COMMENT on p-values (significance range is $0 \leq p \leq 0.05$)
Statistic		**Value**			
Multiple R		0.8199			
Multiple R²		0.6723			
Adjusted R²		0.6589			
F(2,49)		50.255			
p-value (of the whole model)		< 0.0001			*Significant*
Standard error of estimate		1.5542			
REGRESSION COEFFICIENTS					
	b	**Standard error of b**	**t(49)**	**p-value**	
Intercept	11.7371	0.9084	12.9203	0.0000	
Laser power [W]	-0.0439	0.0086	-5.0879	< 0.0001	*Significant*
Scanning speed [mm/s]	-0.0043	0.0015	-2.8333	0.0067	*Significant*

Most of the parts manufactured from 45 µm did not build well. The density results show severe porosity of more than 5 % for most of these parts as given in Addendum D. The maximum available power of the SLM equipment used cannot sufficiently melt this layer thickness, hence the comparatively higher porosities which were observed. The track connection is also poor for this layer thickness compared to 30 µm. The finish was so poor that most of the samples could not be considered for accurate residual stress evaluation with XRD. Some of the surface images for such parts are given in Figure 5.27.
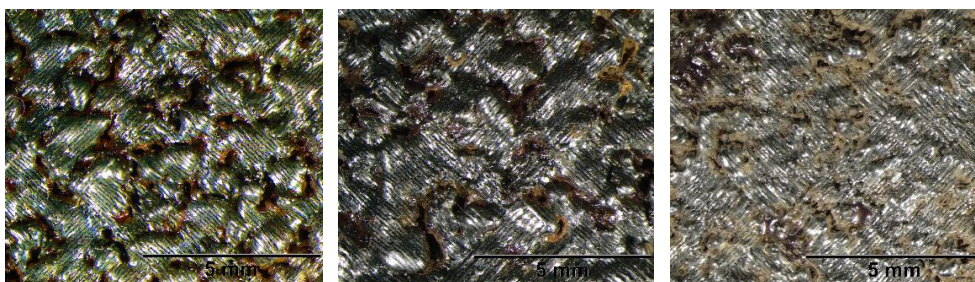
Figure 5.27: Surface images for some of the builds from the 45 µm layer experiments

However, the connection of tracks 180 W and 600 mm/s is very comparable for the two layer thicknesses investigated. The relative densities as calculated using the Archimedes method are also comparable for 30 and 45 µm layer thicknesses (at 99.6 and 99.4 % respectively). The microscope images in Figure 5.28 also show similar pore concentration and size. Plane XY is parallel to the powder bed while XZ is parallel to the building direction. At 180 W and 500 mm/s, the mean relative densities for parts manufactured using the two different layer thickness was also very similar (at 98.6 and 98.5 % respectively for 30 µm and 45 µm layer thicknesses).
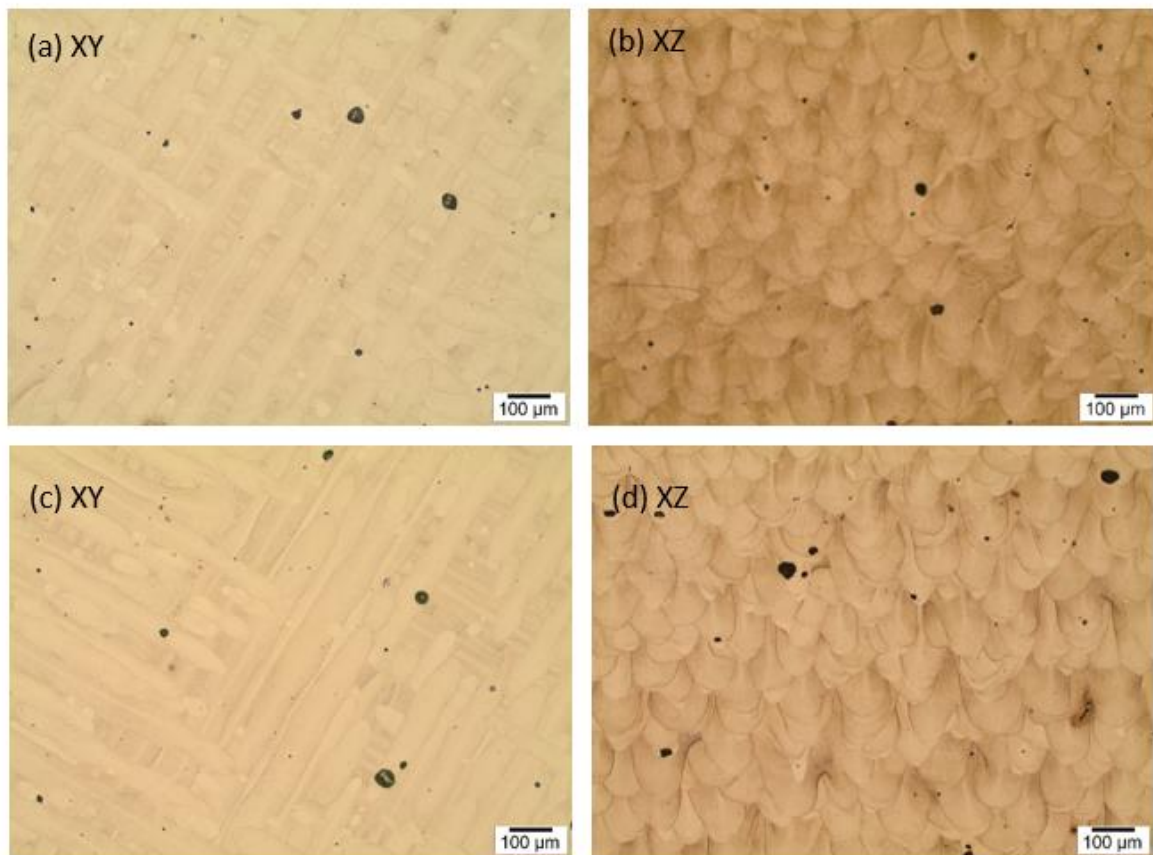
Figure 5.28: Microscope images for specimens built from (a-b) 30 µm and (c-d) 45 µm layers at 180 W and 600 mm/s.

5.4.2 Influence of process parameters on residual stresses (XRD measurements)

All the samples that were built from a 30 µm layer thickness were evaluated for residual stresses. However, only seven specimens from 45 µm were considered for residual stress evaluation because the rest had very poor surface finish that would distort accurate comparative measurement of residual stresses. Such specimens would require deeper grinding or machining, which is not recommended in XRD evaluation of residual stresses. Some examples of the

surfaces were shown earlier in Figure 5.27. Each sample was evaluated for residual stress at the centre of the top melted surface as shown in Figure 5.29.
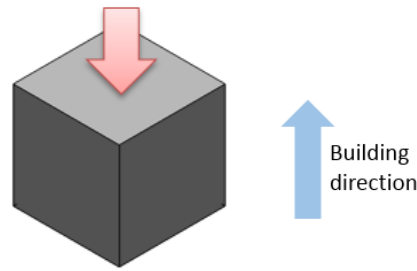
Figure 5.29: XRD measurement position for process parameter investigations

The measured residual stress was compressive at the surface for all the specimens that were considered. In other publications (Vrancken *et al.*, 2013; Cottam *et al.*, 2014; Mertens *et al.*, 2016; Yan *et al.*, 2017), tool steel materials have been found to exhibit compressive surface stresses as well. The compressive state of the stresses is due to the martensitic transformation and contraction that occurs during SLM of tool steel (Cottam *et al.*, 2014; Mertens *et al.*, 2016; Yan *et al.*, 2017). However, the existence of compressive residual stresses does not mean absence of tensile stresses in these specimens. In fact, the concept of residual stress is a "balancing act" in which tensile stresses are compensated by compressive stresses somewhere within the component (Safronov *et al.*, 2016). Compressive residual stresses between 23 MPa and 322 MPa were recorded for the various process parameter combinations that were studied.

The lowest residual stress magnitudes were measured for specimens fabricated from low laser power (80 W and 100 W) and low scanning speeds (200 mm/s and 300 mm/s). These stresses increase in magnitude as both laser power and scanning speed are increased into the intermediate and higher ranges as shown in Figure 5.30. High laser power contributes to steep thermal gradients, and high scanning speed increases the cooling rate – both scenarios lead to high thermal stresses. However, the effect of both extremes (*too low* or *too high* laser power or scanning speed) on porosity and, effectively, residual stresses, cannot be ignored since porosity could lead to stress relaxation. This interdependence is discussed later in section 6.5. for the 30 µm layer, the lowest combination of laser power (80 W) and scanning speed (200 mm/s) yielded a residual stress magnitude of 77 MPa while the highest laser power (180 W) and scanning speed (1000 mm/s), resulted in a much higher stress magnitude of 221 MPa. When scanning at 160 W, the residual stresses increase steadily from 158 MPa to 227 MPa when scanning speed is increased from 400 mm/s to 800 mm/s. For 180 W, residual stresses increase

from 179 MPa at 400 mm/s to a maximum value of 322 MPa at 600 mm/s before steadily declining to 221 MPa when scanning speed is increased to 1000 mm/s.
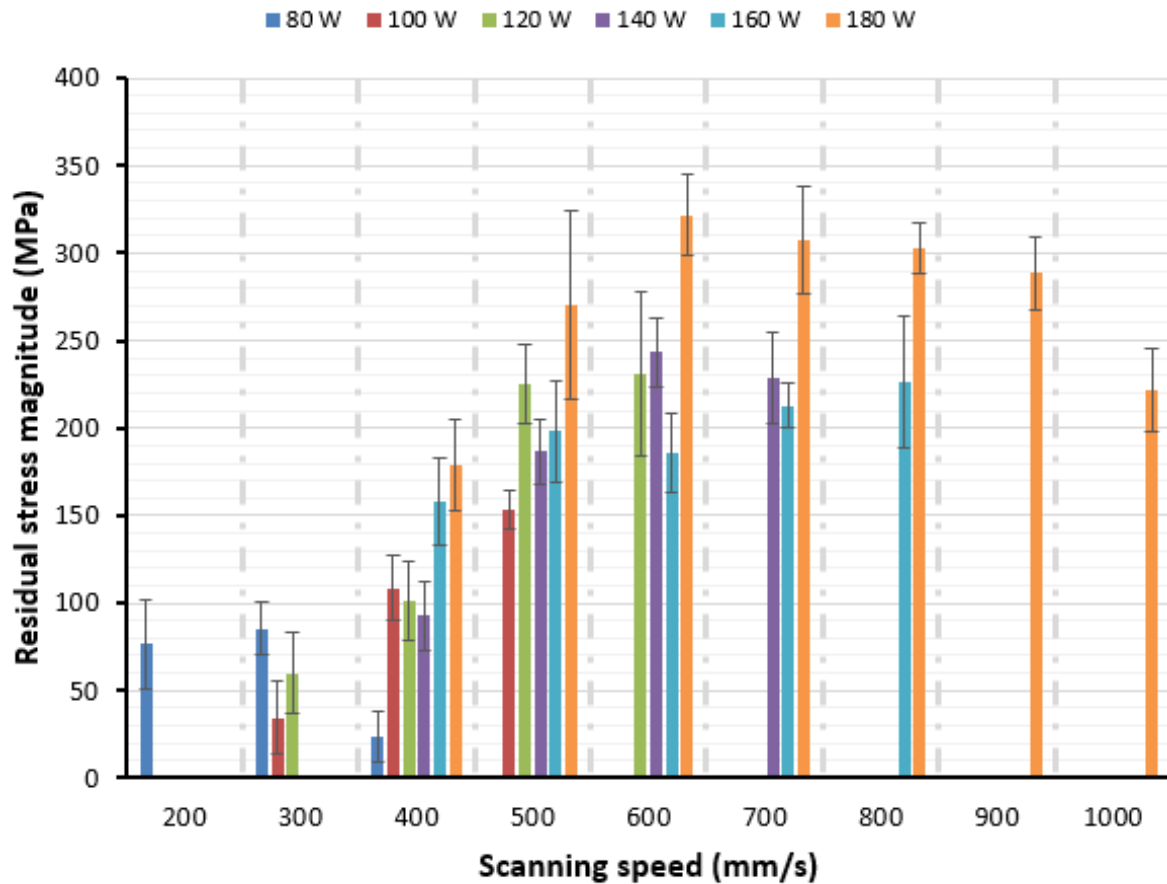
Figure 5.30: Variation of residual stress magnitude with laser power and scanning speed

5.4.2.1   Statistical influence of laser parameters on residual stresses

Both laser power and scanning speed have a statistically significant effect on residual stress magnitudes as shown from the p-values in Table 5.5. It must be noted that since only the magnitude (and not sense) of the stresses was considered, the stress values obtained from the models that could be generated from this statistical data must be treated as compressive.

$$\sigma = -93.4638 + 1.2819P + 0.1778v \tag{5.3}$$

Where residual stress magnitude σ is in MPa, laser power P in W and scanning speed v in mm/s.

Table 5.5: Statistical summary - influence of laser power and scanning speed on residual stresses

SUMMARY					COMMENT on p-values (significance range is $0 \leq p \leq 0.05$)
Statistic		**Value**			
Multiple R		0.8478			
Multiple R²		0.7188			
Adjusted R²		0.6943			
F(2,49)		29.3902			
p-value (of the whole model)		< 0.0001			*Significant*
Standard error of estimate		47.8818			
REGRESSION COEFFICIENTS					
	b	**Standard error of b**	**t(49)**	**p-value**	
Intercept	-93.4638	39.5785	-2.3615	0.0270	
Laser power (W)	1.2819	0.3760	3.4089	0.0024	*Significant*
Scanning speed (mm/s)	0.1778	0.0662	2.6866	0.0132	*Significant*

5.4.2.2 Effect of layer thickness on residual stresses

In order to formulate a relevant comparison, specimens that were manufactured using the same laser power and scanning speed (albeit at different layer thicknesses), were considered. A comparative summary of the residual stress values for the evaluated specimens for the two layer thicknesses is given in Table 5.6 where it can be seen that, generally, residual stress magnitudes decreased by increasing the powder layer thickness. For example, the maximum stress magnitude is 322 MPa for 30 µm at 180 W and 600 mm/s. This declines to 256 MPa at the same condition of laser power and scanning speed when the layer thickness is increased to 45 µm. The general decline in residual stress magnitudes can be attributed to reduced energy input. A study by Ali *et al*. (2018) shows that thicker layers reduce both temperature gradients and the cooling rates, resulting in an accompanying reduction in residual stresses. Moreover, fewer layers are deposited and scanned when a thicker layer is used, leading to a decrease in overall heat input. A similar trend of results for fewer layers (or thinner parts) was presented in section 5.2 as well as previous related research by Furumoto *et al*. (2010), Mercelis and Kruth (2006). Although it can be argued that the bulk of this reduction in stress magnitudes in this study was due to the high levels of porosity observed for the thicker (45 µm) powder layer, some parameter combinations such as 180 W/600 mm/s and 180 W/500 mm/s yielded similar porosity results for both layer thicknesses, with the thicker layer yielding superior results for residual stresses and distortions. The distortion results are discussed later in section 6.4.2.

Table 5.6: Summary of effect of layer thickness on residual stresses

Laser power (W)	Scanning speed (mm/s)	Residual stresses at 30 µm (MPa)	Residual stresses at 45 µm (MPa)
140	500	187	172
160	400	158	173
160	500	198	129
180	400	179	122
180	500	270	195
180	600	322	256

5.4.3 Process map - effect of process parameters on porosity and residual stresses

Based on the porosity and residual stresses results from the 30 µm layer thickness experiments, a process window was developed as shown in Figure 5.31. It is essential to identify regions that have specific characteristics of achievable part density and residual stresses. The identification of such regions or maps, can aid in process parameter selection based on specific applications or user requirements. In Figure 5.31, the regions labelled correspond to 30 µm layer thickness, laser power up to 200 W and scanning speeds up to 1000 mm/s. The map can be extended for higher laser power and scanning speeds (although such were not tested in this research).
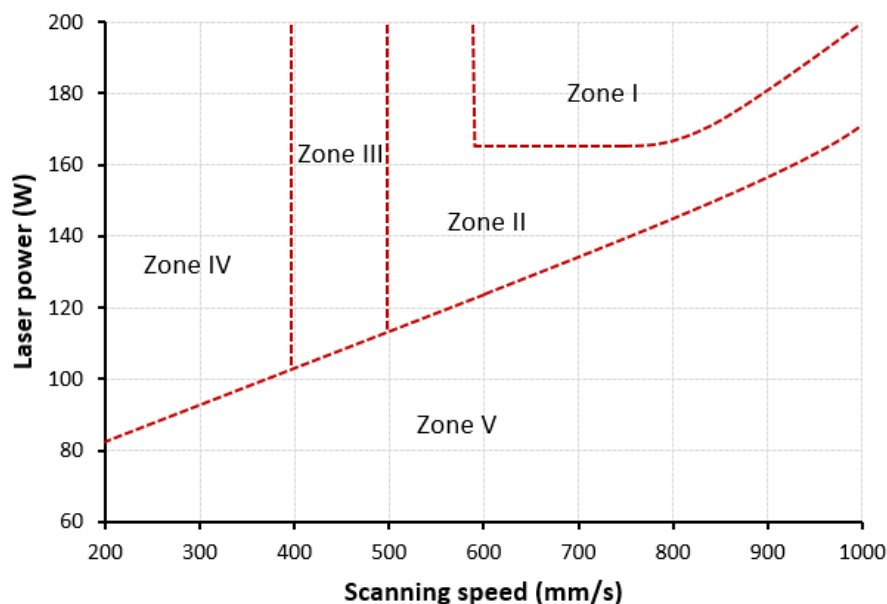
Zone	I	II	III	IV	V
Relative density	> 99 %	98 - 99 %	96 - 98 %	< 96 %	< 96 %
Residual stress magnitudes	High (> 300 MPa)	Moderate – high (200 – 300 MPa)	Moderate (100 – 200 MPa)	Low (< 100 MPa)	Low (< 100 MPa)

Figure 5.31: Process window for SLM of maraging steel on M2 LaserCUSING

113

Zone I represents laser power and scanning speed combinations that contribute to full melting, resulting in parts whose relative density is greater than 99 %. It can be seen that in this region, as the scanning speed is increased beyond 800 mm/s, the achievable density decreases because the interaction time between laser beam and powder bed is reduced and, therefore, the ability of the laser beam to fully melt the metal powder becomes compromised, especially at speeds lower than 180 W. In Zone II, the achievable relative density lies between 98 and 99 % which can easily be corrected by heat treatment methods if required. In this region (Zone II), lower part density is observed compared to Zone I because less laser power is available for melting the powder, or the scanning speed is too high for the selected laser power. Zone III is an intermediate region with relative density between 96 and 98 %. In Zone IV, there is overheating which leads to spattering and porosity, with the relative density generally falling below 96 %. This is due to the low scanning speeds and relatively high laser power being implemented for this region. Insufficient melting characterises Zone V because of the low laser power available, and relatively high scanning speeds that do not allow for sufficient laser beam and powder bed interaction. Of note, the parameters that led to full density also resulted in the highest residual stresses. It appears that porosity is *partly* responsible for the low residual stress magnitudes observed for some parameter combinations. Otherwise, high residual stress magnitudes are largely a result of steep thermal gradients, and vice-versa. It is important to note that different materials behave differently and, therefore, the porosity and residual stress magnitudes for other materials may not be identical to the proposed window. However, the general trend should apply for other materials, although the magnitudes of residual stress and porosity may differ significantly.

5.4.4 Preliminary conclusions

The discussion of results for the influence of process parameters led to the following preliminary conclusions:

- High scanning speeds and high laser power contribute to high residual stresses as both parameters contribute to high thermal gradients. The achievable part density also increases with increase in both laser power and scanning speed, but only until certain optimum values for each parameter combination.

- Increasing the layer thickness (from 30 to 45 µm) results in a decline in residual stresses but generally introduces severe porosity. However, at 180 W and 600 mm/s as well as 500 mm/s, no significant change in part density is observed for the two layer

thicknesses. This demonstrates that for tool steel material, the layer thickness can be increased to 45 µm in order to reduce residual stress magnitudes and to minimise on manufacturing time and related costs without severely impacting on achievable density.

5.5 Summary

Residual stresses and porosity have been discussed as a function of part size, scanning strategy and process parameters. The results presented show that residual stress magnitudes can be reduced by adjustment of the scanning strategy and process parameters. The developed successive chessboard strategy shows good potential in addressing the residual stresses challenge in SLM, while thicker layers lead to a decline of residual stress magnitudes. The residual stresses measured at the surface were compressive for the hot work steel material. These findings are in agreement with recent studies on maraging steel and other hot work tool steels, but contradict the general behaviour of residual stresses in most SLM manufactured metallic parts. The compressive nature of the surface stresses is probably due to the microstructural transformations in tool steels as discussed in the literature. The interdependence of process outcomes is presented in the next chapter, with a special focus on how residual stresses influence distortions in selective laser melting.

Chapter 6: Verification and validation of findings

6.1   Introduction

The purpose of this chapter is to validate the findings on residual stresses for different input parameters by investigating the effect of these input parameters on the residual stress induced distortions. The guiding principle is that factors that lead to higher residual stresses should also lead to higher residual stress induced distortions, and vice-versa. Firstly, the effect of the scanning sequences on distortions is analysed whereby the successive chessboard is further tested against the island (random exposure) strategy. Secondly, the residual stress results obtained for 30 and 45 µm layer thicknesses were verified by further investigating the most promising process parameter combinations identified in Chapter 5, namely, 180 W and 600 mm/s at both layer thicknesses. These investigations were conducted on a different selective laser melting machine in order to check consistency of results when different equipment is used. The initial findings on the effect of laser power, scanning speed and layer thickness are validated by demonstrating the effect of these input parameters on distortions. Furthermore, the correlation between the process outcomes, namely porosity, residual stresses and distortions, is also presented.

6.2   Effect of scanning sequences on distortions

After the evaluation of residual stresses for the different scanning strategies investigated (as presented in section 5.3.6), the island and the successive chessboard scanning strategies were further evaluated to establish their effect on distortions. Prior to laser beam exposure, the titanium plates were checked for flatness in order to ensure that any warping distortion observed after melting can be solely attributed to residual stress induced deformation. The plates were satisfactorily flat, showing no sign of warping or waviness of the surface, with an average initial distortion of 0.004 mm. Thereafter, an EOSINT M280 machine was utilised to melt the surfaces of 1.8 mm grade 5 titanium plates without any deposition of powder. As a control, the default scanning strategy on the EOS machines, the stripe hatch, was also evaluated. Laser power, scanning speed and hatch spacing were set to 170 W, 1200 mm/s and 100 µm respectively. Figure 6.1 shows the scanning patterns and the corresponding plates solidified according to these patterns.
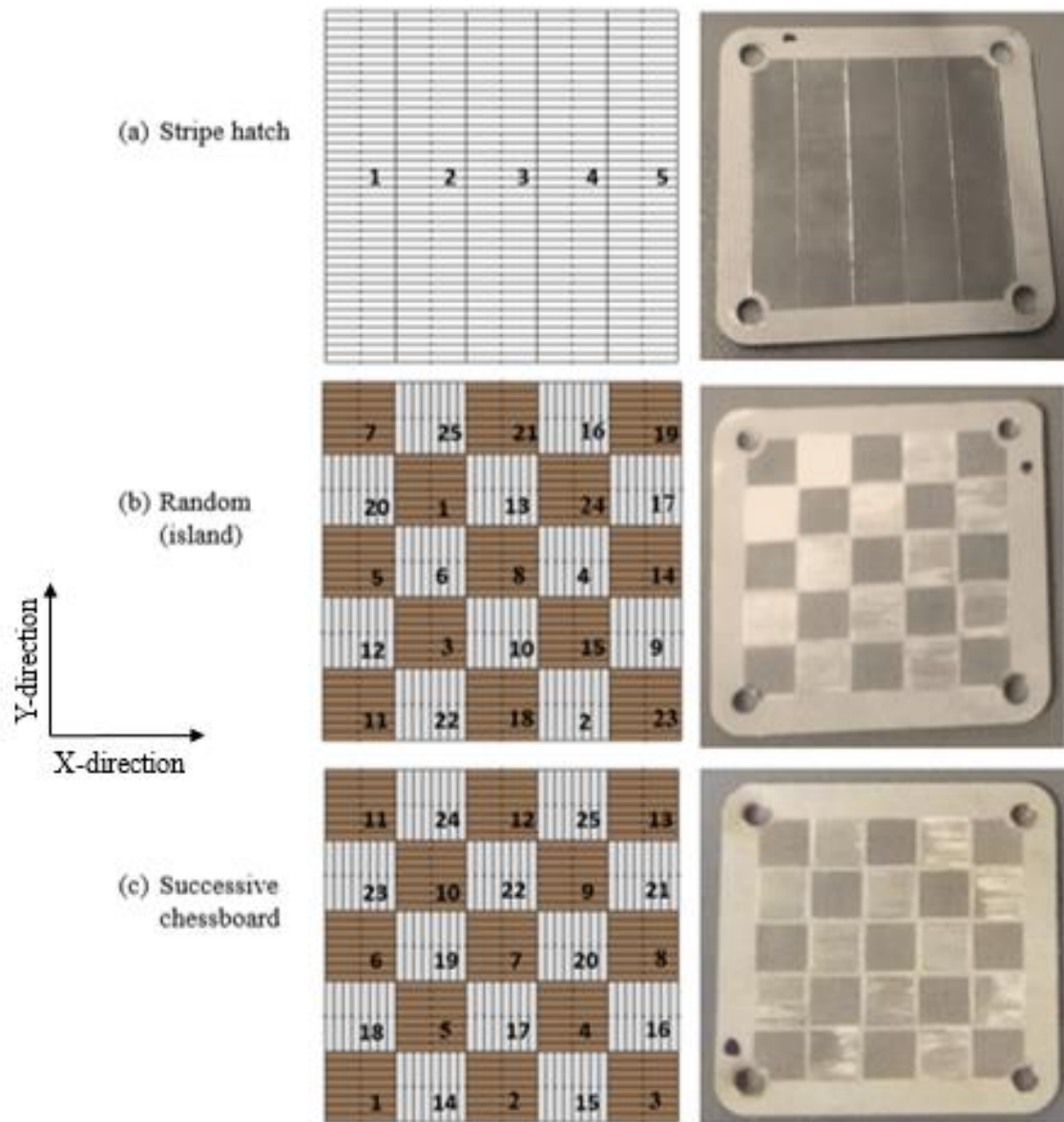
Figure 6.1: Illustration of the stripe hatch, random (island) and successive chessboard strategies with corresponding images of the solidified plate surfaces

After exposure to the laser beam, the thin plates warped slightly upwards along their edges and corners. The maximum distortion measured for the successive chessboard strategy was 0.18 mm while a maximum of 0.21 mm was found when the "islands" were scanned randomly. These results are consistent with the residual stress findings discussed earlier for these two strategies. On the other hand, the stripe hatch had the largest distortion, reaching a top value of 0.34 mm near the plate edges. This confirms that reducing short scan vectors indeed improves thermal homogeneity, thereby reducing the resulting stresses. On the contrary, stripe hatching tends to concentrate heat on the current strip being melted, resulting in less uniform heat

distribution across the scanned region's surface area. The differences in the distortion of the plates is illustrated in Figure 6.2. On average, the maximum distortions for the successive chessboard, random (island) and stripe hatch strategies were 0.17 mm, 0.20 mm and 0.28 mm respectively as shown in Figure 6.3. In summary, it has been demonstrated that a structured sequence of exposing the islands results in less residual stresses and associated distortions compared to randomly scanning the sub-divisions.
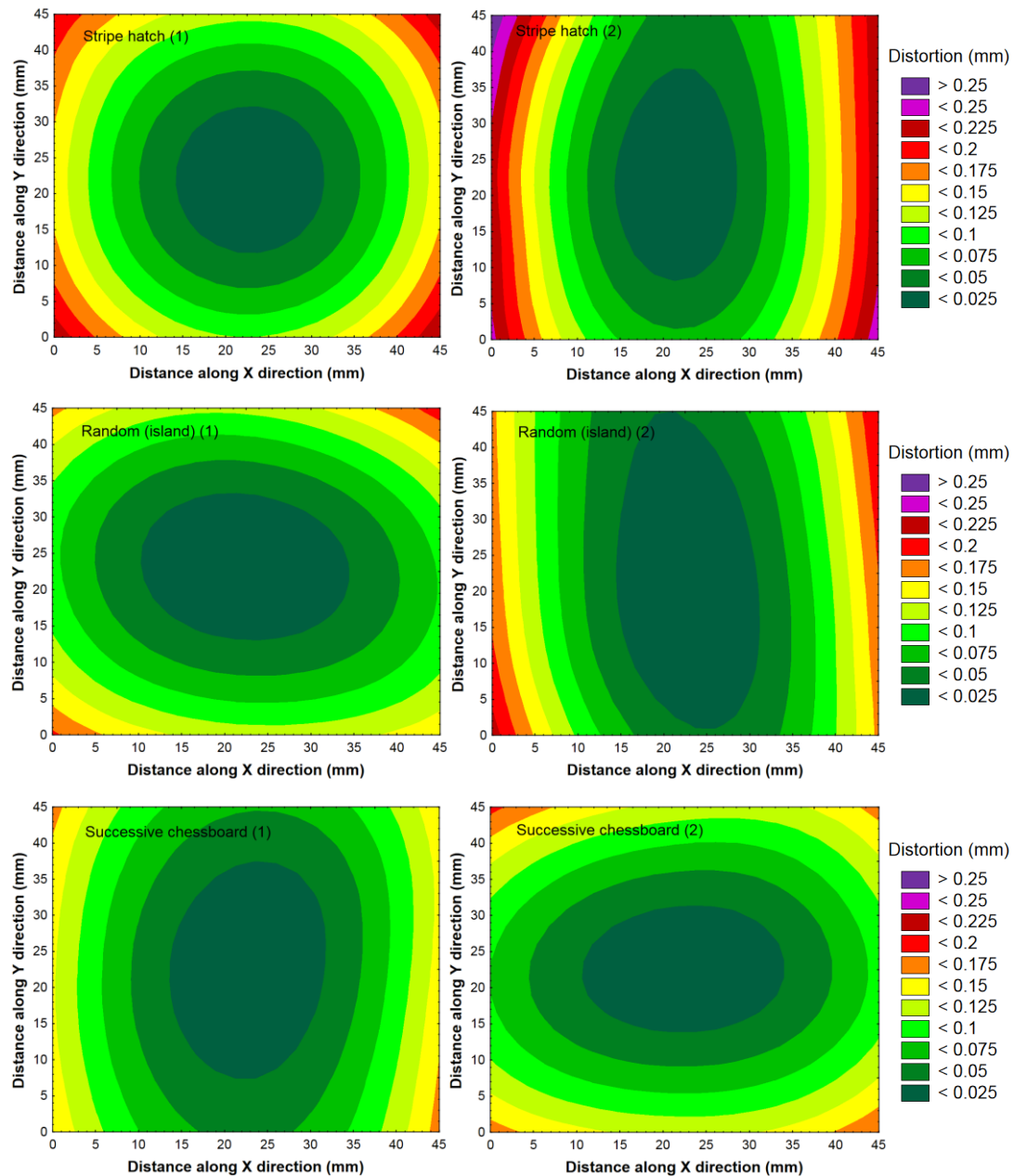
Figure 6.2: Distortion of the titanium plates for different strategies investigated
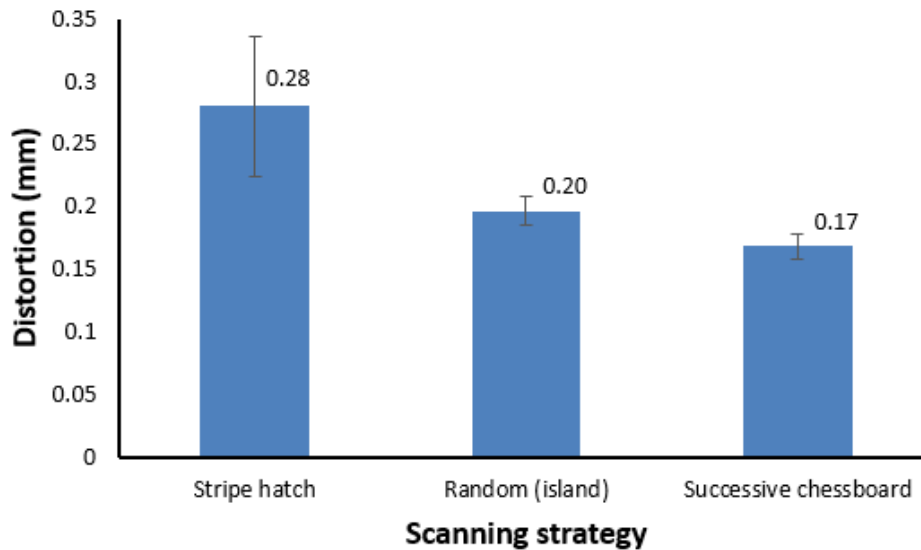
Figure 6.3: Mean maximum distortions for the scanning strategies studied

6.3   Verification of optimised process parameters

As identified from Chapter 5, there is an opportunity to produce maraging steel components with lower residual stresses and, expectedly, distortions by adopting 180 W and 45 μm layer thickness. At the same time, this thicker powder layer lowers the overall cost of manufacturing since fewer layers would have to be deposited, thereby reducing the total building time. To verify the initial findings, specimens were built from the same laser power and scanning speed (180 W and 600 mm/s respectively) but at two different layer thicknesses, namely, 30 μm and 45 μm as shown in Table 6.1. For this verification exercise, the parts were built on an EOSINT M280 machine at the Central University of Technology, Bloemfontein, South Africa. Four parts for each parameter combination were prepared and evaluated.

Table 6.1: Validation experiments for process parameter combinations

Laser power (W)	Scanning speed (mm/s)	Layer thickness (μm)	Number of samples
180	600	30	4
180	600	45	4

6.3.1 Residual stress results

Evaluation of the stresses was performed before the specimens were separated from the baseplates in order to avoid any possible relaxation and/or redistribution of residual stress

during wire cutting. The measurement set up before removal of the specimens from the baseplate is shown in Figure 6.4. The residual stresses, measured using the ProtoXRD machine, were found to be compressive at the surface, similar to the initial findings discussed earlier in section 5.4.2.

Figure 6.4: Measurement of residual stress with samples attached to the baseplate

As shown in Figure 6.5, the mean residual stress magnitude decreases from 376 MPa to 226 MPa when the layer thickness is increased from 30 to 45 μm at the same settings of laser power (180 W) and scanning speed (600 mm/s). These results compare well with those previously presented in Chapter 5 (321 MPa and 256 MPa for the respective layer thicknesses). After separation from the baseplate, the samples from the 30 μm were measured again and the mean stress was 378 MPa. This confirms that the geometry that was chosen for this study is good enough because it does not lead to significant changes in the residual stress magnitude at the surface before and after separation of the specimens from the baseplate. It can be concluded, therefore, that increasing the layer thickness from 30 to 45 μm reduces the residual stress magnitudes in maraging steel manufactured through SLM. This decline in the stress magnitude is expected to result in reduction of stress related distortions in SLM parts.
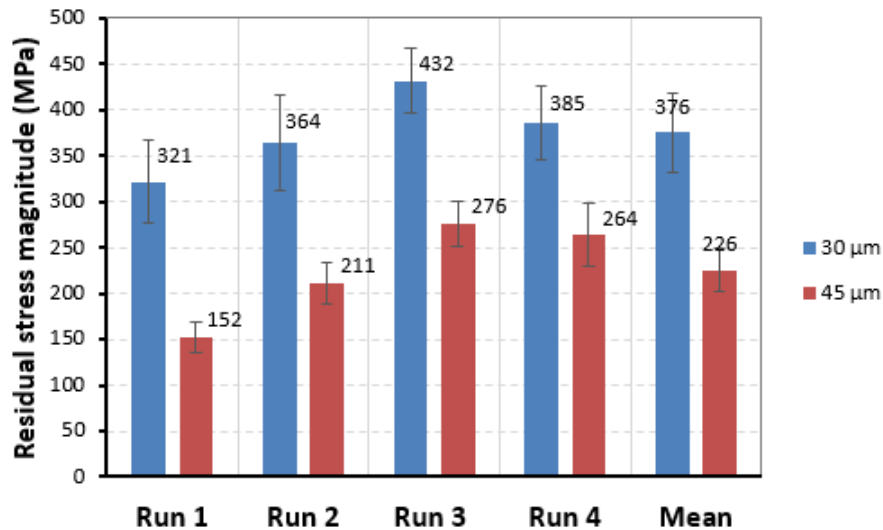
Figure 6.5: Residual stress magnitude comparison for 30 and 45 μm layer thicknesses

6.3.2 Implications for hardness

For tooling applications, it is essential to understand how the variation of process conditions affects the hardness of the final parts as this property also affects the wear resistance of the finished components. Micro hardness was evaluated for the XY plane (parallel to the scanning direction) and the XZ plane (parallel to the building direction). Five measurements were taken for each plane.
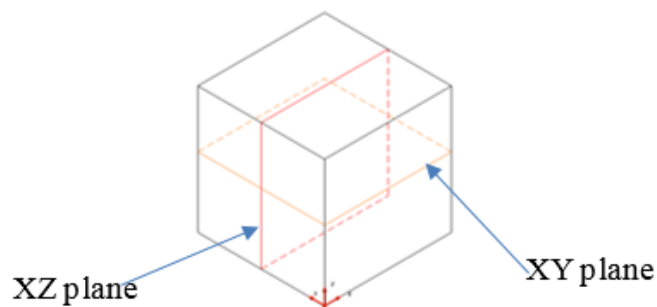
Figure 6.6: Hardness measurement planes

Results from the Vickers hardness tests are shown in Figure 6.7. From these results, hardness decreases slightly when the layer thickness is increased from 30 to 45 μm. However, the hardness is still within the range of 332 – 388 HV (35 – 40 HRC) which is the expected or standard hardness for as built maraging steel (Concept Laser, 2010). For practical industrial applications such as injection moulding, heat treatment is usually necessary to increase the hardness of components after SLM.

121
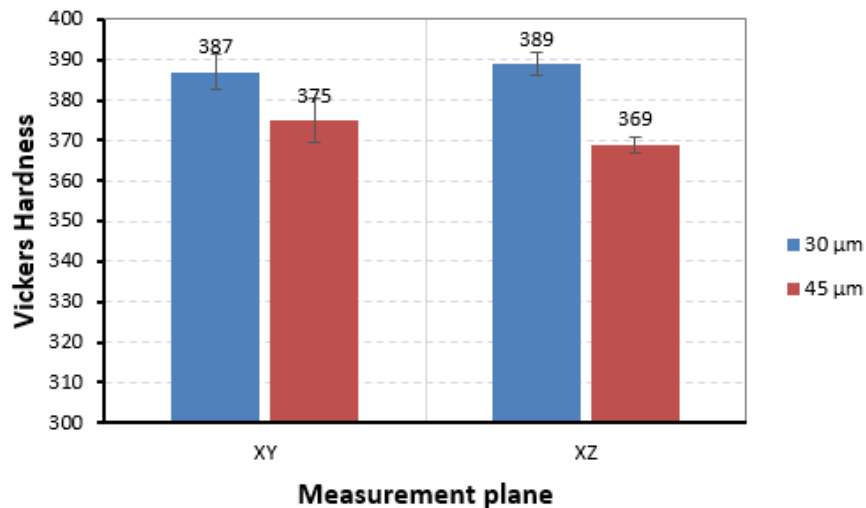
Figure 6.7: Hardness for the 30 and 45 μm samples

6.4 Influence of process parameters on distortions

To comprehensively check the effect of residual stresses on distortions, full process parameter combinations that were studied in section 5.4 were considered. It is expected that process parameter combinations that led to higher residual stress magnitudes would also contribute to higher distortions. For this purpose, cantilever geometries were selected as these have been successfully used in the literature for residual stress related distortion analysis in SLM in the work done by Töppel *et al.* (2016), Buchbinder *et al.* (2014), Papadakis *et al.* (2014) and Neugebauer *et al.* (2014) amongst others. A single arm cantilever geometry was selected for this research. The "free" end of the cantilever is supported by a prism block as shown in Figure 6.8 to improve accuracy of building. The "supports" are 1 mm wide and are separated by 1 mm.
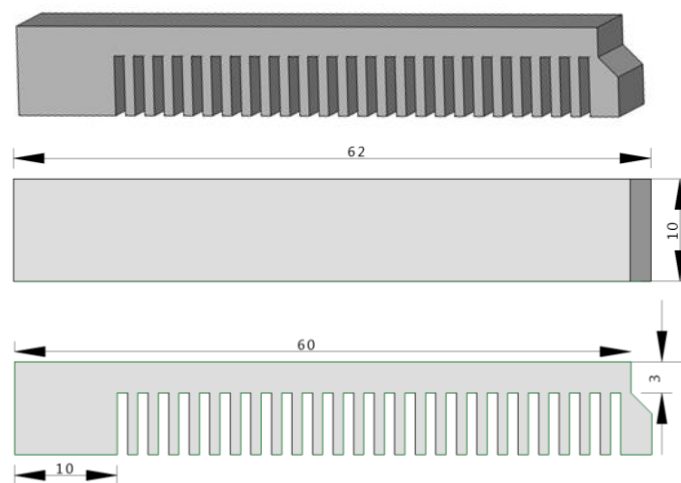
Figure 6.8: Cantilever geometry for distortion analysis (dimensions in mm)

After the cantilevers were built, they remained connected to the baseplate without deforming. There was no evidence of any surface cracking for any of the process parameter combinations. However, after separating the cantilevers from the baseplate, most of the cantilevers underwent noticeable warping distortion which increases with distance from the "rigid" base of the cantilevers. The actual distortion was measured based on the profile of the bottom (cut) surface of the specimens in order to negate the effects of the surface roughness of the top surface on the measurement accuracy. Cantilever geometries exhibit significant distortion variation along the geometry's length rather than across the width. Similar measurements by Safronov *et al*. (2016) show this trend. In this study, the measurement of distortion was done along the line of symmetry of the cantilevers.
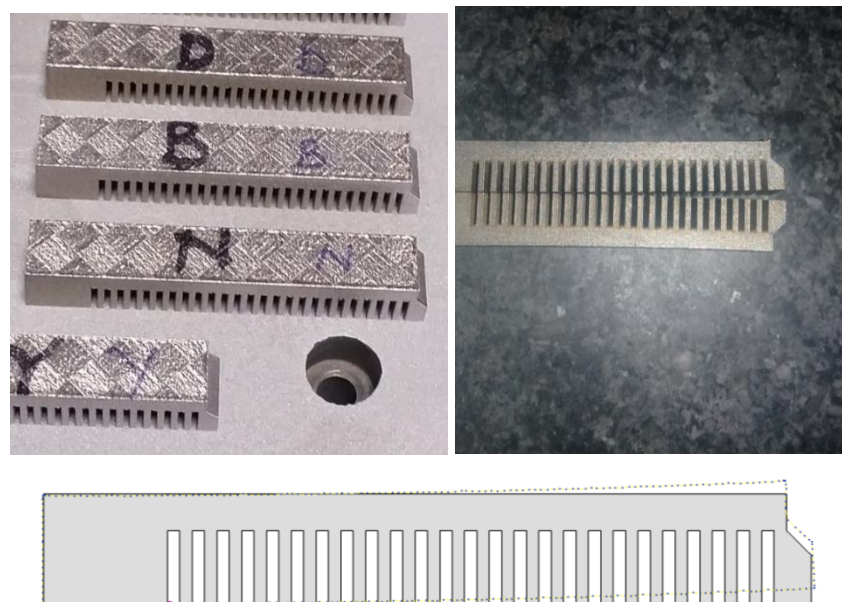
Figure 6.9: Undistorted parts before separation from baseplate (top left), distortion of parts relative to each other after separation from the baseplate (top right), and CMM profile showing deviation from original CAD profile (bottom).

Generally, distortion seems to increase as the scanning speed is increased. These trends can easily be seen from Figure 6.10 in which the distortion increases from 0.4 mm at 400 mm/s to 1.2 mm at 700 mm/s through to 1000 mm/s when scanning with 180 W. These trends can be attributed to the decrease in porosity that tends to increase residual stresses as scanning speed is increased for this range of parameters. The correlations between porosity, residual stresses and distortions are presented and discussed in detail in section 6.5.
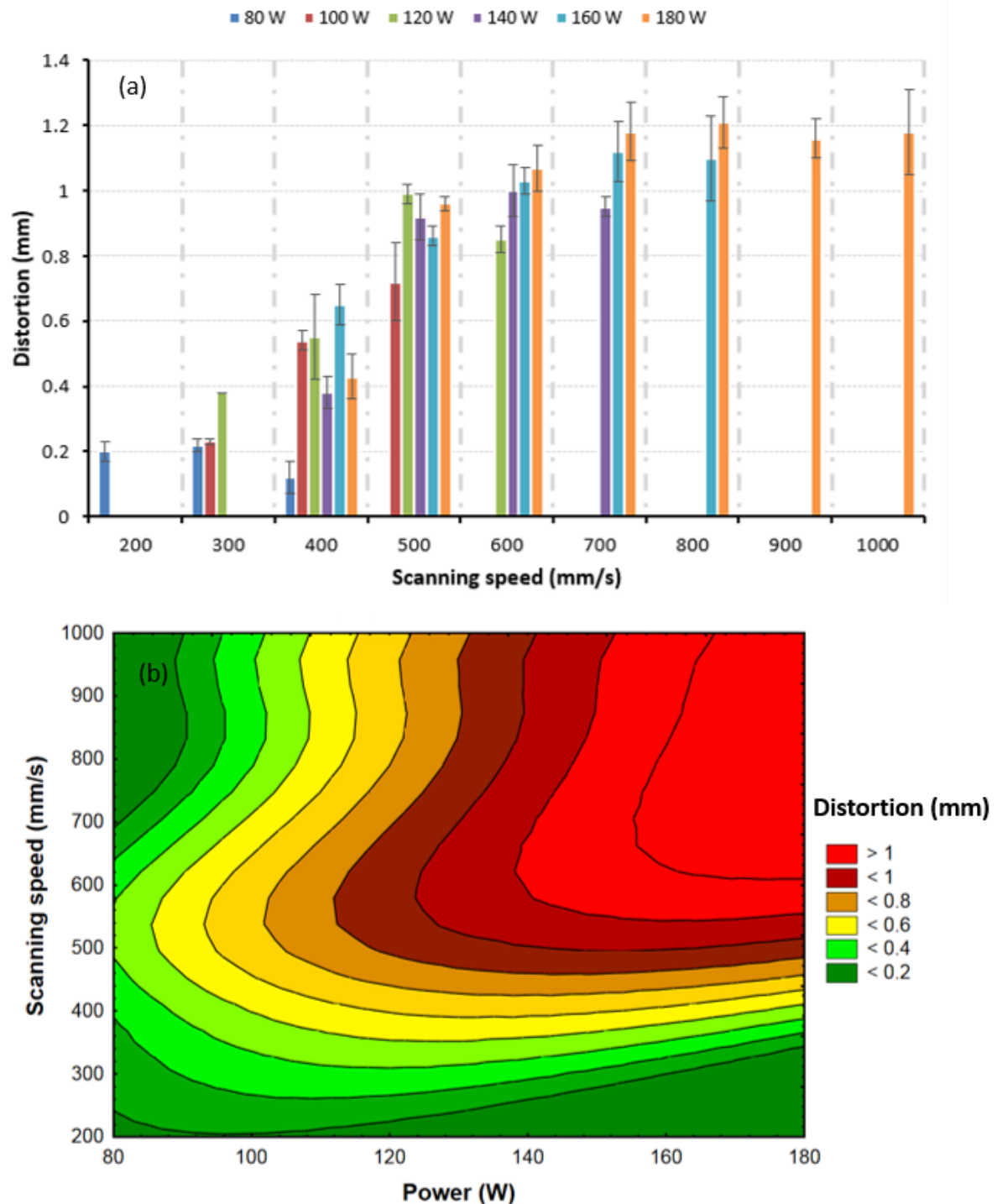
Figure 6.10: Results of distortions versus scanning speed at various laser power values (a), and contour plot of distortions against laser power and scanning speed (b)

However, as mentioned above, distortions do not infinitely increase with scanning speed. Similar to findings regarding porosity, distortions tend to slow down when the scanning speed becomes so high that it does not permit sufficient interaction of the powder bed with the laser. This increase in porosity is further expected to result in residual stress relaxation and an

124

accompanying decline in distortion. For every level of laser power, there is an accompanying optimum scanning speed that results in the highest density. Unfortunately, the achievement of high density is also accompanied by residual stresses and distortions. Although the effect of laser power on distortion is not as evident as that of scanning speed, it can generally be deduced that higher laser power contributes to greater distortions than lower laser power.

6.4.1 Statistical analysis of the effect of process parameters on distortions

It has been discussed already that distortions generally increased with increase in laser power and scanning speed for the range of parameters tested. For a 95 % confidence level, both parameters have a statistically significant effect on distortions. The results are summarised in where distortion y is in mm, laser power P in W and scanning speed v in mm/s.

Table 6.2 and can be represented using Equation (6.1).

$$y = -0.3087 + 0.0032P + 0.0012v$$

(6.1)

where distortion y is in mm, laser power P in W and scanning speed v in mm/s.

Table 6.2: Statistical summary of the influence of laser power and scanning speed on distortions

SUMMARY					COMMENT on p-values (significance range is $0 \leq p \leq 0.05$)
Statistic		**Value**			
Multiple R		0.88			
Multiple R²		0.77			
Adjusted R²		0.77			
F(2,49)		84.295			
p-value (of the whole model)		0.0000			*Significant*
Standard error of estimate		0.1737			
REGRESSION COEFFICIENTS					
	b	**Standard error of b**	**t(49)**	**p-value**	
Intercept	-0.3087	0.1015	-3.0409	0.0038	
Laser power	0.0032	0.0009	3.3115	0.0017	*Significant*
Scanning speed	0.0012	0.0002	6.9067	0.0000	*Significant*

6.4.2 Summary of influence of layer thickness on process outcomes

Increasing the layer thickness from 30 to 45 μm drastically reduces distortions to almost 0 mm for most of the investigated cases. However, increasing the layer thickness from 30 to 45 μm is accompanied by very high porosity of more than 5 % for the bulk of the parameter combinations considered (Addendum D). This increase in porosity also contributes to stress

relief and, hence, the observed reduction in residual stress induced distortions. In spite of this unwanted porosity, an optimum point was found at 180 W and 600 mm/s whereby the 45 μm layer thickness yields relative density (99.4 %) which is comparable to that obtained using a 30 μm powder layer thickness (99.6 %). This presents an opportunity for faster fabrication of tool steel parts on the SLM equipment used by shifting to a thicker powder layer (45 μm) from the default 30 μm, whilst, better still, reducing both residual stresses and distortion as summarised in Table 6.3. The reduced building time further results in manufacturing cost reduction without compromising on the product quality with regards to residual stresses, porosity and distortion. Shifting from 30 μm to 45 μm layer thickness reduces the number of slices by 33.3 % and a corresponding reduction in production time can be estimated in line with the production time and cost models found in Rickenbacher *et al*. (2013), Schröder *et al*. (2015) and Fera *et al.* (2017).

Table 6.3: Comparison of 30 and 45 μm layer thicknesses at laser power 180 W and scanning speed 600 mm/s.

Basis for comparison	30 μm layer thickness	45 μm layer thickness
Achievable relative density	99.6 %	99.4 %
Maximum residual stress magnitude	322 MPa	256 MPa
Average maximum distortion	1.07 mm	0.58 mm

6.5 Modelling the interdependence of porosity, residual stresses and distortions

Process parameters that contributed to high density also contributed to the greatest cantilever distortions. It is also readily clear that porous parts suffer less residual stresses compared to their less porous counterparts. To understand the correlations existing between these responses (porosity, residual stresses and distortions), three further interrelationships between the results were investigated, that is, *porosity vs residual stresses, porosity vs distortions* and *residual stresses vs distortions*.

6.5.1 Effect of porosity on residual stresses and distortions

The scatter plot in Figure 6.11 (a) shows that pores indeed have the effect of relaxing residual stresses. The highest residual stress magnitude of 322 MPa corresponds to the lowest porosity of 0.39 % whereas the highest porosity (10.42 %) is associated with the lowest residual stress of 23.4 MPa. The relationship between residual stresses, σ and porosity, ф, can be best approximated by applying Equation ((6.2). The R^2 value of 0.85 shows closeness between the

data and fitted regression. The residual stress relaxation effect of pores in turn results in diminished distortion. The higher the porosity, the less distortion the cantilevers experience. The influence of porosity on distortion is shown in Figure 6.11 (b) and can be estimated using Equation ((6.3).

$$\sigma = 329.88e^{-0.233\phi} \qquad \textbf{(6.2)}$$

$$y = 1.3718e^{-0.225\phi} \qquad \textbf{(6.3)}$$

where residual stress magnitude σ is in MPa, distortion y in mm, and porosity ϕ is expressed as a percentage (%)
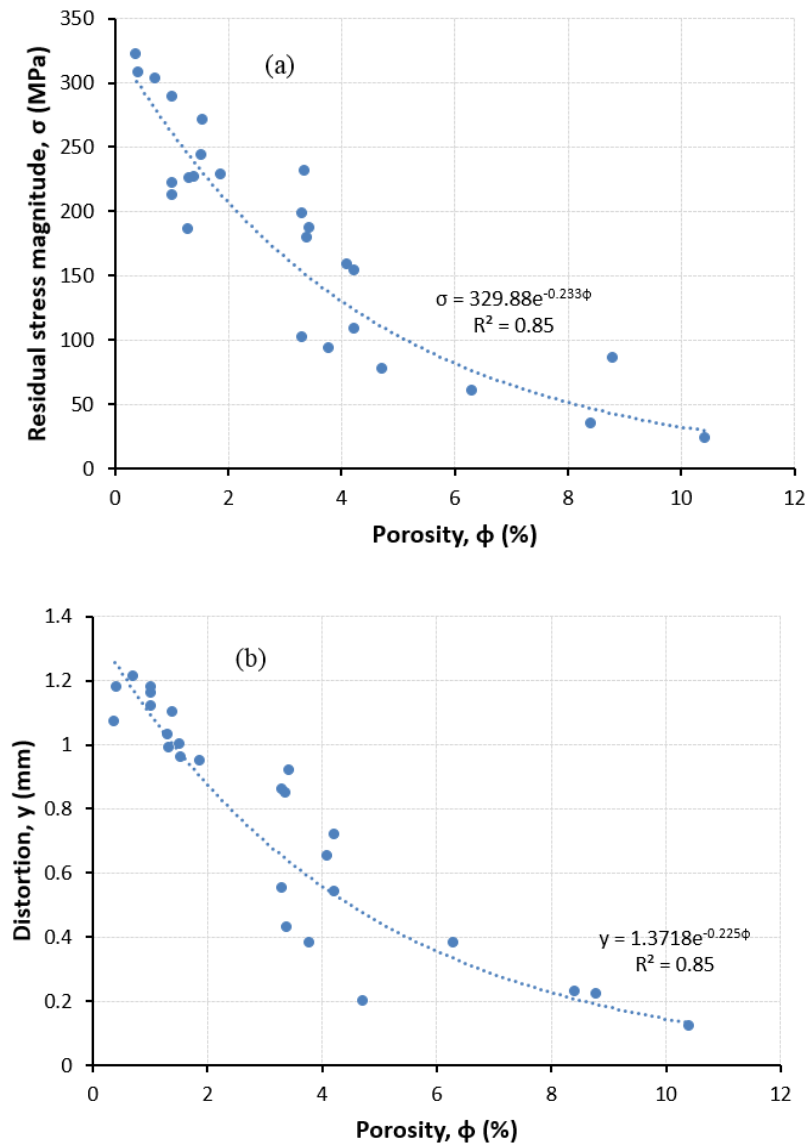
Figure 6.11: Effect of porosity on residual stresses and distortion

127

6.5.2 Effect of residual stresses on distortions

Process parameters that yielded low residual stresses resulted in cantilevers which showed very little distortions whereas parameters that contributed to higher residual stresses also, generally, contributed to higher cantilever distortions as shown in Figure 6.12. Within the 0.95 confidence interval, a very strong statistical correlation of 0.91 exists between residual stress and distortion magnitudes. A direct linear relationship exists between residual stresses and the distortions that arise from these stresses as shown in Equation ((6.4).

$$y = 0.0038\sigma + 0.0872 \qquad \textbf{(6.4)}$$

where the distortion y is in mm residual stress magnitude σ is in MPa.
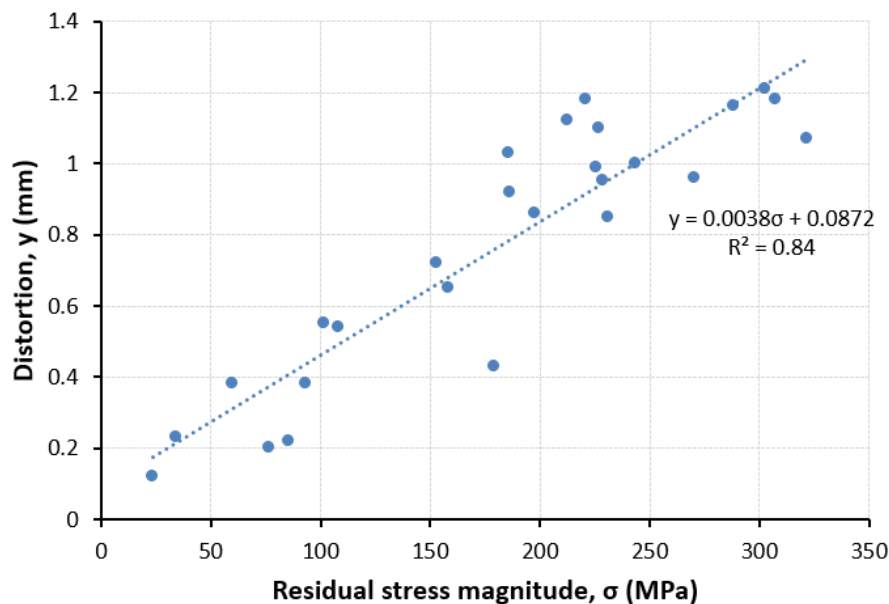
Figure 6.12: Variation of distortion with residual stress

It is clear that porosity lowers both residual stresses and distortions although the main reason for development of residual stresses is thermal gradients. Low laser power, which results in porosity due to insufficient melting, also results in reduced thermal gradient (and subsequently lower stresses) since the melt pool temperature is not as high as when using higher laser power. In summary, porosity does not cause residual stresses and distortions, but contributes to the magnitude of these stresses and distortion through stress relief. The target of SLM is to produce non-porous parts, except in some cases where porosity is required, especially in the manufacture of biomedical implants. Therefore, reduction of residual stresses in-situ, without compromising on the part density remains a challenge up to this day. Process conditions that minimise residual stresses during the SLM process also minimise the warping distortion of the

finished parts. Whereas residual stresses can be reduced by post process heat treatment processes like annealing, distortions that occur in-process cannot. An alternative could be to aim for slightly porous, distortion and residual stress free parts whose density would have to be increased by appropriate heat treatment.

There are strong inter-dependencies between the process outcomes. Therefore, optimisation of one or more of these process outcomes should be approached with care, bearing in mind the effect such optimisation could have on the other responses.

6.6 Process mapping – Residual stress reduction map validated through congruence between stress and distortion trends

Residual stresses were found to generally decrease when the layer thickness was increased from 30 μm to 45 μm (refer to Figure 6.13). For the same values of laser power and scanning speed, the 45 μm layer contributed to much lower residual stresses. At 180 W, the best part density was achieved for both layer thicknesses although the density was slightly higher for the 30 μm layer. As mentioned already, the objective of SLM is usually to manufacture dense parts, particularly for tooling applications. Therefore, only parameters that lead to full density are of interest as presented in Chapter 5 (Figure 5.31).
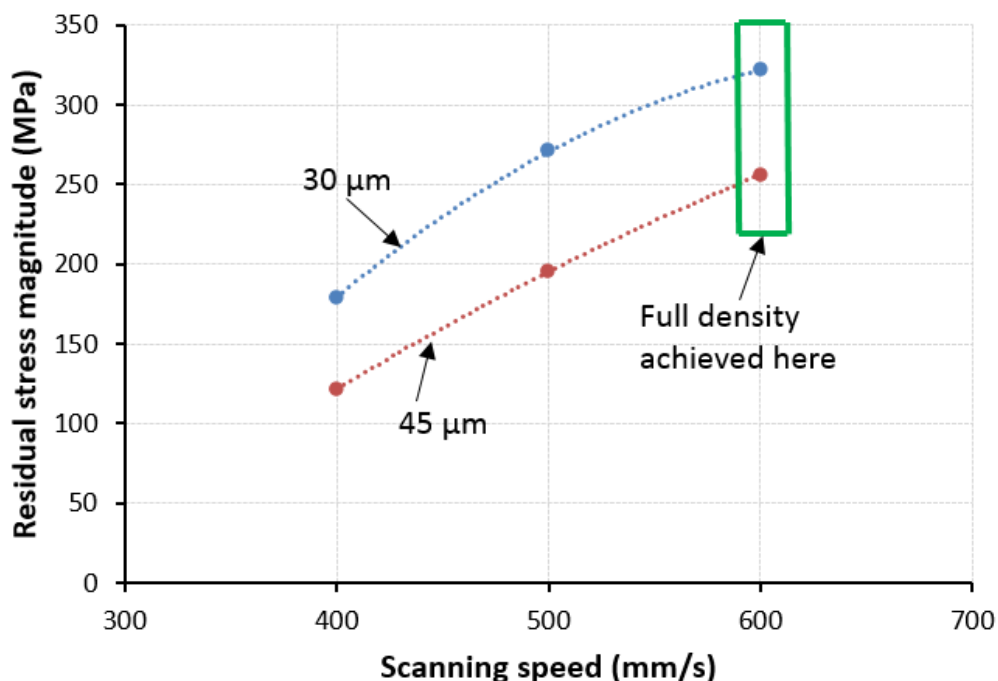
Figure 6.13: Comparison of residual stress magnitudes for 30 μm and 45 μm powder layer thicknesses at 180 W

The residual stress reduction map was validated for the two layer thicknesses at 180 W through establishing a congruence between the residual stresses and distortion trends. In Figure 6.14, the distortions increase with increase in scanning speed (at fixed power of 180 W). What is evident from the fitted trendlines is the lower distortions for the 45 μm layer compared to 30 μm for the same scanning speed values. This is in agreement with the residual stress trend shown earlier in Figure 6.13. Of interest is that distortion is 46 % lower at 600 mm/s for the 45 μm layer when compared to 30 μm. At this point, full density (greater than 99 %) is achieved for both layer thicknesses. The density boundaries were established based on the porosity results discussed in section 5.4.1. Conclusively, the 45 μm is more attractive as it reduces residual stresses and distortions without significant compromise on part density. Furthermore, using 45 μm layer thickness increases productivity as the number of layers required to build up a part is reduced by 33.3 % relative to the 30 μm layer thickness.
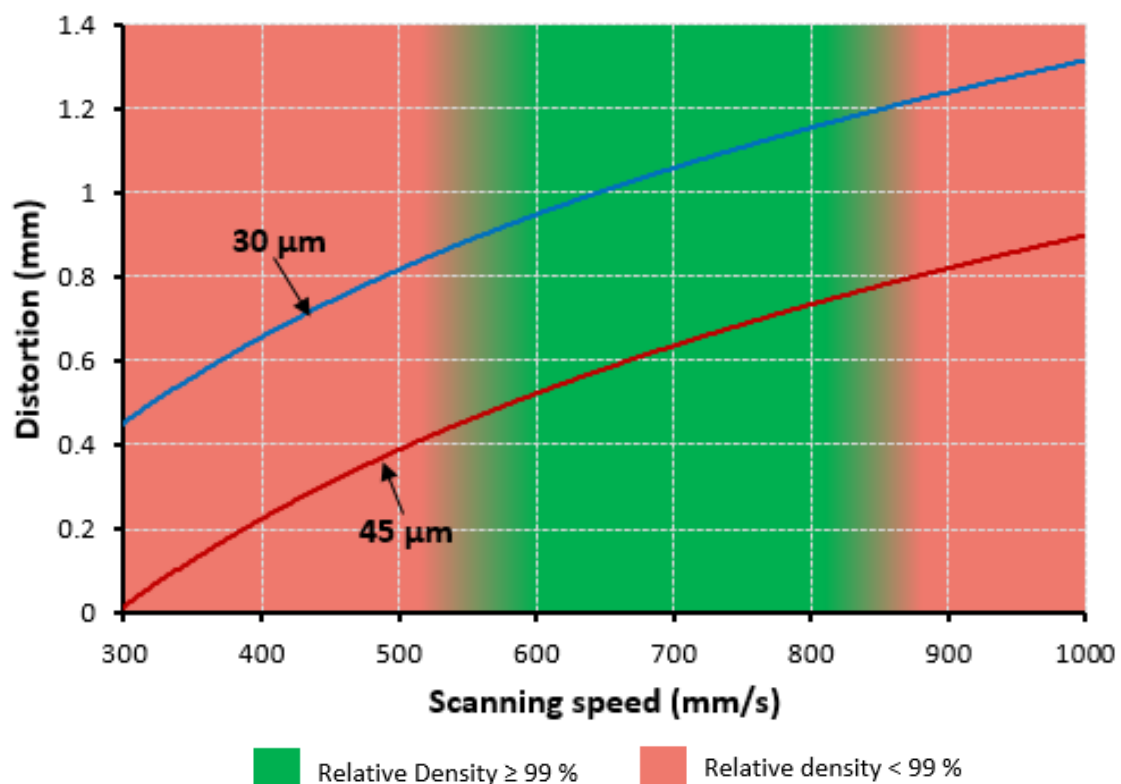
Figure 6.14: Distortion and porosity map for 30 μm and 45 μm layers at 180 W

6.7   Influence of energy density in SLM

When parameters are allowed to vary simultaneously, there is no observable influence of energy density on any of the responses (porosity, residual stresses and distortions). Thus, energy density cannot be used to explain or account for the differences in the observed process

outcomes. Table 6.4 shows two energy density levels (63 and 127 J/mm^3) for which completely different responses can be seen. This is because the two parameters do not have the same effect on the process as shown from the statistical analysis in the previous sub-sections. The effect of energy density when all parameters are varied is represented graphically in Figure 6.15.

Table 6.4: Variation of process outcomes at the same energy density levels

Laser power (W)	Scanning speed (mm/s)	Energy density (J/mm^3)	Mean porosity (%)	Residual stresses (MPa)	Mean distortion (mm)
80	400	63	10.42	23	0.12
100	500	63	4.23	153	0.72
120	600	63	3.37	231	0.85
140	700	63	1.88	229	0.95
160	800	63	1.4	227	1.10
180	900	63	1.02	289	1.16
80	200	127	4.73	77	0.20
120	300	127	6.31	60	0.38
160	400	127	3.70	158	0.65
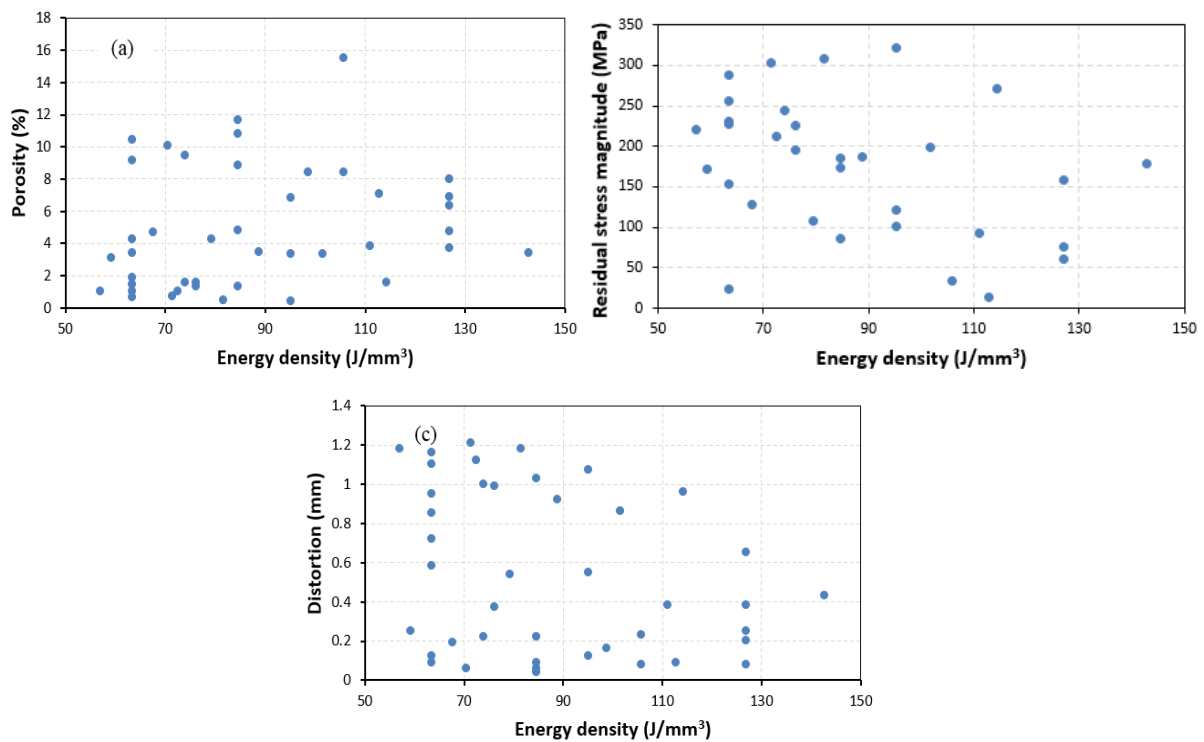
Figure 6.15: Scatter plots of the effect of energy density on (a) porosity, (b) residual stress magnitude and (c) distortions

131

Statistical analysis of all the experimental results shows that, indeed, energy density does not have a significant influence on porosity, residual stresses or distortions as shown. The summary of the ANOVA is presented in Table 6.5. Even though the p-value shows statistical significance of energy density on distortion (p = 0.001), the R-squared values are too weak, showing that the observed variation in distortions cannot be confidently attributed to energy density.

Table 6.5: Statistical analysis of the effect of energy density on SLM outcomes

Response	R^2 (%)	Adjusted R^2 (%)	Predicted R^2 (%)	p-value
Porosity	5.0	1.1	0.000	0.271
Residual stresses	11.5	7.8	0.000	0.090
Distortion	35.6	32.9	25.7	0.001

However, the energy density has a clear effect on process outcome when only one parameter is varied whilst the other(s) are held constant, for example varying laser speed at a fixed laser power of 180W and layer thickness 30 µm. The different energy density levels that correspond to the variation of scanning speed at these settings is shown in Table 6.6.

Table 6.6: Energy density values for various scanning speeds at fixed laser power and layer thickness

Laser power [W]	Scanning speed	Layer thickness (µm)	Energy density (J/mm^3)
180	400	30	143
180	500	30	114
180	600	30	95
180	700	30	82
180	800	30	71
180	900	30	63
180	1000	30	57

The effects of the different energy densities on porosity, residual stresses and distortions as listed in Table 6.6 are represented in Figure 6.16. At low energy density, there is insufficient energy to melt the powder, hence the porosity is higher than when the energy density is increased. For example, when energy density is 57 J/mm^3, a corresponding porosity value of 1.02 % is observed. The porosity gradually decreases to 0.72, 0.43 and 0.39 % when the energy density is increased to 71, 82 and 95 J/mm^3 respectively. Beyond 95 J/mm^3, porosity increases significantly to 1.55 % and 3.40 % for 114 and 143 J/mm^3 energy density values, respectively.

Excessive energy results in an unstable melt pool which gives birth to the balling phenomenon. As discussed already, balling promotes porosity.
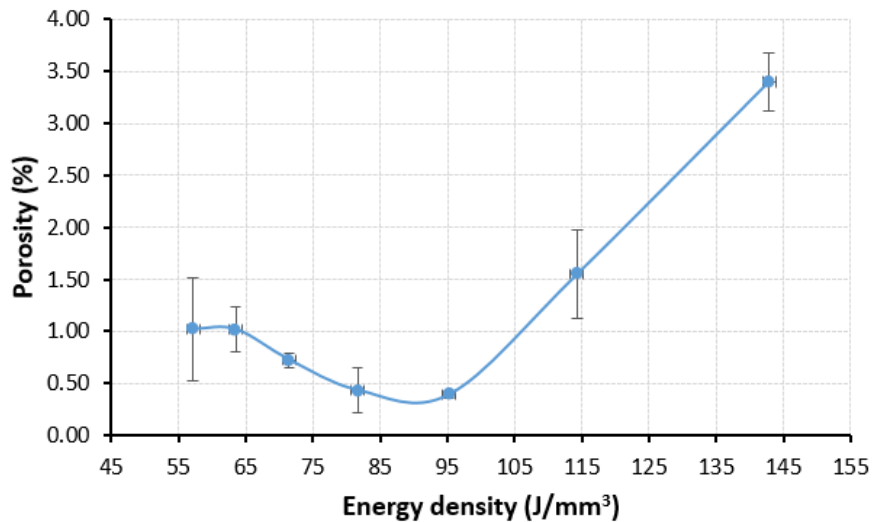
Figure 6.16: Effect of energy density on porosity at fixed laser power (180 W) and layer thickness (30 μm) while varying speed

The relationship between energy density and residual stresses where laser power and layer thickness are held constant is such that the residual stresses decrease either side of the optimum value for maximum density (95 J/mm^3). As shown in Figure 6.17, the maximum residual stress value is 322 MPa at 95 J/mm^3. The lowest energy density value (57 J/mm^3) contributes to 221 MPa whereas for the maximum energy density of 143 J/mm^3, 179 MPa residual stress value is observed. The reduction of the residual stresses when energy density is either too low or too high is attributed to the associated porosity which has the effect of relaxing residual stresses.
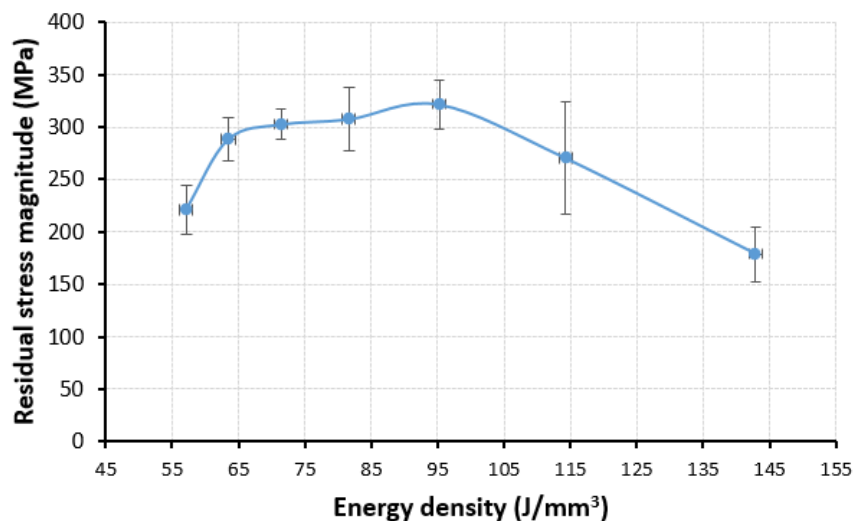
Figure 6.17: Effect of energy density on residual stresses at fixed laser power (180 W) and layer thickness (30 μm) while varying speed

133

6.8   Concluding summary

Based on the verification and validation results presented in this chapter, the following concluding remarks can be made:

- The results comparison between 30 and 45 µm were confirmed by building samples on a different machine (same technology) and evaluating the residual stresses. Increasing layer thickness from 30 to 45 µm indeed reduces residual stress magnitudes and the corresponding distortions. For the cantilever geometries used in this study, the distortions decreased from 1.07 mm to 0.58 mm which represents a 46 % reduction.

- Analysis of the interdependence between process responses (porosity, residual stresses and distortions) shows a direct linear relationship between residual stress and distortion. There is a strong correlation between porosity and residual stresses and corresponding distortion. The relaxation effect of porosity on residual stresses in turn results in reduction of warping distortions. It is noted, however, that high porosity is not the objective of SLM.

- As long as parameters vary simultaneously, energy density has no bearing at all on all process outcomes and cannot be used as a predictor of the outcome. However, the findings show that energy density can be used to demonstrate clear trend in the outcome if only one parameter is allowed to vary at a time.

Chapter 7: Conclusions and outlook

7.1 Introduction

This research focused on investigation and management of residual stresses in selective laser melting of maraging steel 300. The research successfully accomplished the broad aim and set objectives. Firstly, a study of the capabilities of SLM as well as the major parameters governing the process was done through detailed literature analysis and in-house case studies. Experimental investigation of the influence of these key parameters was completed and the major conclusions from the experimental study are summarised in this chapter. In-situ management of residual stresses and their effects can be effectively done by controlling the scanning strategy and processing parameters, namely laser power, scanning speed and layer thickness. The research significantly contributed to the existing studies on SLM of maraging steel, which is rather shallow in the literature, and led to original contribution of knowledge in the application of scanning strategy and process parameter adjustment for in-situ residual stress management. In the following section, the conclusions are discussed against the set objectives of the research.

7.2 SLM capabilities

In line with Objective 1 of the research, an investigation of the capabilities of SLM was conducted through literature analysis and in-house studies. The findings indicate that SLM is capable of accurately building complex geometries and walls as thin as 0.3 mm. Features such as holes, cylinders, sharp edges and sloping faces can be accurately built with good repeatability. Common dimensional and form inaccuracies relate to elevated edges. Residual stresses arising from steep thermal gradients, non-uniform heating and solidification also lead to shape and dimensional distortions. These stresses contribute to warping distortions that can result in macroscopic loss of form accuracy during the build or after separation of parts from the substrate. When warping distortions occur during the build, the smooth movement of the coater blade is often impeded and this results in process abandonment.

7.3 Identification of factors that govern SLM with respect to residual stresses

As per Objective 2, factors that govern SLM were identified and analysed. The factors are numerous, but only a few are critical with respect to residual stress occurrence. The major factors are material properties, part geometry, build environment, processing parameters (laser

power, scanning speed and layer thickness) as well as scanning strategies. Methods that can be used to manage residual stresses were analysed, leading to the development of an evaluation and selection method for residual stress management techniques. The criteria for evaluation of residual stress management methods should consider the effect of the methods on residual stresses, porosity and manufacturing time/cost. Unfortunately, form distortions resulting from residual stress-induced warping cannot be corrected using post process heat treatment or grinding and machining. For this reason, this study focused on in-situ management of residual stresses. Evaluation of the options for effectively managing residual stresses in-situ were identified as lying around scanning strategies and processing parameters as per sections 2.6.6 and 3.4. Analysis and evaluation of existing scanning strategies led to the development of the successive chessboard and LHI chessboard strategies in section 3.4.3, which formed part of the experimental investigations and contributed to management of residual stresses.

7.4 Experimental investigation of the effect of input factors on residual stresses

In order to fulfil Objective 3, experimental investigations were successfully conducted on the identified major opportunities for understanding and managing residual stresses in-situ. The experiments mainly involved specimen preparation (on M2 LaserCUSING or EOSINT M280 machines), measurements, analysis, evaluation and verification/validation.

7.4.1 Residual stress distributions within maraging steel produced by SLM

The surfaces of maraging steel components manufactured through SLM are under compressive residual stresses. This explains the non-susceptibility to surface cracking for this material. Throughout the 3D volume of the material, both tensile and compressive stresses are present, leading to a "balance of stresses". Furthermore, residual stresses in SLM parts vary for different positions, even at the same measurement depth. This demonstrates the non-uniform nature of SLM with respect to heating, cooling and solidification. This research also established that residual stress magnitudes increase with increase in part thickness. Thus, different part sizes (or geometries) require different management strategies, with bigger parts being more critical.

7.4.2 Scanning strategies

From the findings in section 5.3, it can be concluded that *scan vector length* has different impact on residual stresses in different evaluation directions. For normal and transverse stresses, the magnitude of residual stresses increased with increasing scan vector length. On the other hand, longitudinal stresses declined with increase in scan vector length, an indication

of a possibility of localised overheating due to heat accumulation for short vectors. Furthermore, the shortest island size investigated (3 mm × 3mm) led to high porosity, again possibly due to overheating. The residual stress results for 7 mm × 7 mm and 5 mm × 5 mm islands are quite similar. As such, it is more beneficial to use the 7 mm × 7 mm islands since they can substantially contribute to scanning time and porosity reduction without introducing significantly different residual stress magnitudes and distributions when compared to the 5 mm × 5 mm islands.

Rescanning induces compressive stresses that lead to cancellation or reduction of tensile stresses. In this research, up to 26 % tensile stress reduction was achieved (section 5.3.5). The induced compressive stresses are generally desirable as they slow down crack initiation and growth. Regardless, double scanning has the obvious effect of increasing the building time and, effectively, cost. Furthermore, rescanning **at the same parameters** as the initial laser pass **increases porosity**. The increase in porosity can be attributed to over-melting that brings with it the balling effect, more so for small specimens such as those used in this research where there is limited cooling and solidification time between the first laser beam and the rescan. However, this porosity decrease can easily be corrected by heat treatment.

Scanning patterns play an important part in determining residual stress magnitudes. Variations in the order of sub-sector scanning show that the highest residual stresses are obtained when subdivisions are scanned in direct succession. The successive chessboard strategy in which white islands are sequentially scanned before black segments (or vice-versa) yields the lowest residual stresses. The default island scanning strategy and the LHI chessboard strategy, which are very similar in implementation, result in similar stresses whose magnitudes are intermediate between those for the successive scanning strategy and the successive chessboard strategy.

A study of scanning strategies from the perspective of residual stresses and manufacturing time was conducted. The total scanning time is dependent on the number of times that the laser beam must jump from island to island. This is influenced by both scan vector length and scanning sequence. As a result, the successive chessboard strategy results in marginally lower scanning time compared to the island and LHI chessboard strategies. The same can be said for 3 mm × 3 mm islands when compared to 5 mm × 5 mm and 7 mm × 7 mm islands (section 5.3.7).

7.4.3 Process parameters (laser power, scanning speed and layer thickness)

Residual stresses and the accompanying distortions increase with an increase in laser power and scanning speed. The same can be said for achievable part density since by increasing laser

power, more energy becomes available to completely melt the metal powder. However, the relative density only increases until optimum values of laser power and scanning speed before declining due to insufficient melting or over-melting. Residual stress effects like distortions are irreversible, thus, these stresses must be managed during the build. Increasing the layer thickness is an effective way of managing residual stresses and their effects in-situ. This presents further opportunities to cut on the building time for every part built from 45 µm rather than the default 30 µm since the total number of layers is reduced by 33.3 %. Furthermore, an accompanying reduction in manufacturing cost and energy use can be expected when a thicker powder layer is adopted, directly contributing to sustainable manufacturing. Increasing the layer thickness to 45 µm whilst maintaining laser power and scanning speed at 180 W and 600 mm/s respectively led to a reduction of residual stress induced distortion of up to 46 %.

Further to the study on process parameters, the effect of energy density on residual stresses and distortions shows that this quantity can only be used as a comparison basis when only one parameter is varied (section 6.7) whilst the rest are held constant. Where parameters vary simultaneously, energy density does not have a clearly observable effect on process response. This indicates that the parameters that make up the energy density do not have the same weight or significance in determining the process outcome.

7.5   Effect of residual stresses on distortions - SLM correlations

In pursuance of Objective 4, empirical correlations were developed to demonstrate the dependency of process outcomes (porosity, residual stresses and distortions) on laser power and scanning speed. It was established that residual stresses and distortions increase with increase in both laser power and scanning speed. Furthermore, based on the interdependencies between the process outcomes, it was demonstrated that porosity relaxes residual stresses, this in turn leading to reduced stress-induced distortions. However, the goal of SLM is not to produce porous parts. It is critical, therefore, to always check and ensure that efforts to reduce residual stresses do not also lead to undesirable decrease in part density. Although it has been suggested that residual pores and imperfections relax residual stresses (Kruth *et al.*, 2012; Wu *et al.*, 2014; Yadroitsava and Yadroitsev, 2015), no actual corresponding study existed. This study established a verified argument to support this, thus contributing to the existing body of knowledge.

7.6   Original contribution

The original contribution of this research was in five areas as follows:

(a) Methodology for evaluation and selection of residual stress management techniques

A user-defined methodology for evaluation and selection of in-situ residual stress management options was developed (refer to Figure 3.3) The methodology is based on key process outcome considerations, namely achievable density, residual stresses and accompanying distortions as well as impact on productivity (rather than just considering influence of the techniques on residual stresses only). This methodology was also used in this work to evaluate or recommend the different methods that were investigated.

(b) Scanning strategies developed and evaluated

Two scanning strategies – the LHI chessboard and successive chessboard strategies were developed and tested experimentally as discussed in section 5.3.6. These strategies are based on the successes of the strategies that employ short scan vectors, but introduced structured approaches in the sequence in which sub-divisions of a large scanning area are actually exposed to the laser beam. As shown in results presented in Figure 5.24, the performance of the LHI chessboard was similar to that of the default island strategy used on the M2 LaserCUSING machine. The successive chessboard strategy, on the other hand, yielded lower residual stresses by 21 % (longitudinal direction) and 40 % (transverse direction) compared to the default island scanning strategy. Furthermore, the successive chessboard shows a lot of promise in reduction of scanning time since the "jump" distances are much shorter. Chessboard strategies are potentially useful for "large" area scanning in order to aid in uniform heat distribution.

(c) Process window for SLM of maraging steel 300

As shown in Figure 5.31, the research devised a process window for SLM of maraging steel 300. This can be extended to other machines with higher laser power and is useful during process planning for parameter selection based on application requirements. The window includes reasons for the observed porosity and residual stress states for the different zones and can, therefore, easily assist SLM users (regardless of material) to

adjust process parameters based on intended porosity outcome, with a clear view of the residual stress state to be expected within the different zones.

(d) *Process map for residual stress management*

Provided sufficient energy remains available to achieve full melting, residual stresses and distortions can be effectively reduced by increasing the layer thickness. Evaluation of both residual stresses and accompanying distortions led to the development of a process map (refer to Figure 6.14). Generally, the points along the thicker layer (45 μm) suffer less residual stresses and distortions, yet still result in comparable part density against the 30 μm layer. For this research, the satisfactory parameter combination was found at 180 W, 600 mm/s and 45 μm layer thickness which led to a reduction of residual stresses and distortion of 31 % and 46 % respectively.

(e) *Interdependencies between process responses*

SLM correlation studies have previously been limited to the relationships between input parameters (for example laser power, scanning speed and layer thickness) and output (for example residual stress, density and surface roughness). This research has gone a step further and investigated interdependencies between process outcomes, in this case porosity, residual stresses and distortions. A direct linear relationship was found between residual stress and distortion, while porosity contributed to an exponential decline of both residual stresses and distortions - refer to Equations ((6.2), ((6.3), and ((6.4).

7.7   Scope for future work

Considering volumetric energy density in experimental investigations can be a convenient way of clustering several process parameters into a single study. However, this research established that the SLM parameters that form an integral part of volumetric energy density (power, scanning speed and layer thickness) have different impact or significance on process outcomes. As such, a weighting methodology that can be incorporated into the formulae for energy density computations is necessary in order to render this quantity more "universally" applicable and acceptable.

In this research, scanning strategies were investigated using single layer experiments. Based on the promising residual results for the chessboard strategies, particularly the successive

chessboard, future focus is on testing these scanning strategies for multiple layer scenarios. The LHI chessboard, which exhibits similar residual stress results to the island strategy, can be developed further so that it becomes available to SLM users. The effect of scanning strategies may also be investigated for different geometries, such as for building of thin walls. The investigated chessboard strategies are beneficial to large area AM, but building of thin walls may require implementation of different strategies, such as the spiral scanning strategy. Furthermore, case studies for modelling the effect of scanning strategies and process parameters such as scanning speed, layer thickness and hatch spacing on actual cost and savings against achievable product quality are necessary in providing more insight when evaluating different options for residual stress management or for SLM production in general.

Finally, microstructure characterisation and micro-hardness investigations and their correlation to residual stresses have the potential to deepen the knowledge around the variation of residual stresses for different measurement positions. This can also open opportunities to fully understand the reasons for the compressive nature of surface stresses in maraging steel 300.

7.8   Research outputs

This PhD work led to the writing, submission and publication of research papers in both accredited journals and peer reviewed international conference proceedings. One journal paper has been published by Procedia Manufacturing whilst one more has already been accepted for publication in the International Journal of Advanced Manufacturing Technology. Two more journal articles have been submitted (as at December 2018). Four conference papers directly to do with this research were also written as listed below:

7.8.1 Journal articles

1. Mugwagwa, L., Dimitrov, D., Matope, S. and Yadroitsev, I. (2018). "Influence of process parameters on residual stress related distortions in selective laser melting", Procedia Manufacturing, 21, pp 92 – 99.

2. Mugwagwa, L., Dimitrov, D., Matope, S. and Yadroitsev, I. (2019). "Evaluation of the impact of scanning strategies on residual stresses in selective laser melting" – Int. Journal of Advanced Manufacturing Technology (Accepted).

3. Mugwagwa, L., Dimitrov, D., Matope, S. and Yadroitsev, I. "Residual stresses, distortions and density of hot work tool steel parts manufactured using selective laser melting" – Submitted to Additive Manufacturing Journal.

4. Mugwagwa, L., Dimitrov, D., Matope, S. and Yadroitsev, I. "Investigation of the effect of scan vector length on residual stresses in selective laser melting of maraging steel 300" – Submitted to South African Journal of Industrial Engineering.

7.8.2 Conference papers

1. Mugwagwa, L.*,* Dimitrov, D., Matope, S. and Venter, A.F. (2017). "Residual stress distributions within components manufactured using selective laser melting", Proceedings of the 18th Annual International RAPDASA Conference, 7 – 10 November 2017, Durban, South Africa, pp. 153 – 164

2. Mugwagwa, L.*,* Dimitrov, D., Matope, S. and Muvunzi, R. (2016). "Residual stresses and distortions in selective laser melting – a review", Proceedings of the 17th Annual International RAPDASA Conference, 2 – 4 November 2016, Vanderbijlpark, South Africa

3. Mugwagwa, L.*,* Dimitrov, D., Matope, S. and Becker, T. (2016). "A methodology to evaluate the influence of part geometry on residual stresses in selective laser melting", Proceedings of the International Conference on Competitive Manufacturing, 27 – 29 January 2016, Stellenbosch, South Africa, pp. 133 – 139

4. Mugwagwa, L.*,* Dimitrov, D. and Matope, S. (2014). "Exploring opportunities for improvement in selective laser melting", Proceedings of the 15th Annual International RAPDASA, Conference, 6 – 7 November 2014, Stellenbosch, South Africa, pp. 21 – 29

REFERENCES

Acevedo, C., Evans, A. and Nussbaumer, A. (2012) 'Neutron diffraction investigations on residual stresses contributing to the fatigue crack growth in ferritic steel tubular bridges', *International Journal of Pressure Vessels and Piping*, 95, pp. 31–38. Available at: http://dx.doi.org/10.1016/j.ijpvp.2012.05.004.

Aggarangsi, P. and Beuth, J. L. (2006) 'Localized preheating approaches for reducing residual stress in additive manufacturing', in *Solid Freeform Fabrication Symposium*. Austin, pp. 100–900.

Ahuja, B., Schaub, A., Junker, D., Karg, M., Tenner, F., Plettke, R., Merklein, M. and Schmidt, M. (2016) 'A round robin study for laser beam melting in a metal powder bed', *South African Journal of Industrial Engineering*, 27(2), pp. 30–42.

Ajovalasit, A., Scafidi, M., Zuccarello, B., Beghini, M., Bertini, L., Santus, C., Valentini, E., Benincasa, A. and Bertelli, L. (2010) 'The hole-drilling strain gauge method for the measurement of uniform or non-uniform residual stresses'. Florence: AIAS TR-01:2010, pp. 1–70.

Ali, H., Ghadbeigi, H. and Mumtaz, K. (2018) 'Processing parameter effects on residual stress and mechanical properties of selective laser melted Ti6Al4V', *Journal of Materials Engineering and Performance*, 27(8), pp. 4059–4068. Available at: https://doi.org/10.1007/s11665-018-3477-5.

Ali, H., Ma, L., Ghadbeigi, H. and Mumtaz, K. (2017) 'In-situ residual stress reduction, martensitic decomposition and mechanical properties enhancement through high temperature powder bed pre-heating of selective laser melted Ti6Al4V', *Materials Science and Engineering A*, 695, pp. 211–220.

Antony, J. (2003) 'Fundamentals of designing experiments', *Design of experiments for engineers and scientists*, pp. 6–16.

ASTM F2792-12a (2013) 'Standard terminology for additive manufacturing technologies'. West Conshohocken: ASTM International. Available at: http://www.ciri.org.nz/nzrma/technologies.html.

Averyanova, M., Bertrand, P. and Verquin, B. (2011) 'Studying the influence of initial powder characteristics on the properties of final parts manufactured by the selective laser melting technology', *Virtual and Physical Prototyping*, 6(4), pp. 215–223.

Averyanova, M., Cicala, E., Bertrand, P. and Grevey, D. (2012) 'Experimental design approach to optimize selective laser melting of martensitic 17-4 PH powder : part I – single laser tracks and first layer', *Rapid Prototyping Journal*, 18(1), pp. 28–37.

Baufeld, B., Brandl, E. and Van Der Biest, O. (2011) 'Wire based additive layer manufacturing: Comparison of microstructure and mechanical properties of Ti-6Al-4V components fabricated by laser-beam deposition and shaped metal deposition', *Journal of Materials Processing Technology*. Elsevier B.V., 211(6), pp. 1146–1158. Available at: http://dx.doi.org/10.1016/j.jmatprotec.2011.01.018.

Beal, V. E., Erasenthiran, P., Hopkinson, N., Dickens, P. and Ahrens, C. H. (2008) 'Scanning strategies and spacing effect on laser fusion of H13 tool steel powder using high power Nd:YAG pulsed laser', *International Journal of Production Research*, 46(1), pp. 217–232.

Becker, T. and Dimitrov, D. (2016) 'The achievable mechanical properties of SLM produced maraging steel 300 components', *Rapid Prototyping Journal*, 22(3), pp. 487–494.

Belassel, M., Pineault, J. and Brauss, M. E. (2006) 'Comparison and evaluation of residual stress measurement techniques, a technical and economical study', in *SEM Annual Conference and Exposition on Experimental and Applied Mechanics*. Saint Louis, pp. 756–762.

van Belle, L., Vansteenkiste, G. and Boyer, J. C. (2013) 'Investigation of residual stresses induced during the selective laser melting process', *Key Engineering Materials*, 554-557, pp. 1828–1834. Available at: http://www.scientific.net/KEM.554-557.1828.

Bikas, H., Stavropoulos, P. and Chryssolouris, G. (2016) 'Additive manufacturing methods and modelling approaches: a critical review', *The International Journal of Advanced Manufacturing Technology*, 83(1-4), pp. 389–405. Available at: http://link.springer.com/10.1007/s00170-015-7576-2.

Bo, Q., Yu-sheng, S., Qing-song, W. and Hai-bo, W. (2012) 'The helix scan strategy applied to the selective laser melting', *The International Journal of Advanced Manufacturing Technology*, 63(5-8), pp. 631–640. Available at: http://link.springer.com/10.1007/s00170-012-3922-9.

Bolboacă, S. D. and Jäntschi, L. (2007) 'Design of experiments: Useful orthogonal arrays for number of experiments from 4 to 16', *Entropy*, 9(4), pp. 198–232.

Bourell, D., Pierre, J.-P., Leu, M., Levy, G., Rosen, D., Beese, A. M. and Clare, A. (2017) 'Materials for additive manufacturing', *CIRP Annals - Manufacturing Technology*. CIRP, 66, pp. 659–681. Available at: http://dx.doi.org/10.1016/j.cirp.2017.05.009.

Buchbinder, D., Meiners, W., Pirch, N. and Schrage, K. W. (2014) 'Investigation on reducing distortion by preheating during manufacture of aluminum components using selective laser melting', *Journal of Laser Applications*, 26(1).

Campanelli, S. L., Contuzzi, N., Angelastro, A. and Ludovico, A. D. (2010) 'Capabilities and performances of the selective laser melting process', *New Trends in Technologies: Devices, Computer, Communication and Industrial Systems*, pp. 233–252.

Campanelli, S. L., Contuzzi, N., Ludovico, A. D., Caiazzo, F., Cardaropoli, F. and Sergi, V. (2014) 'Manufacturing and characterization of Ti6Al4V lattice components manufactured by selective laser melting', *Materials*, 7(6), pp. 4803–4822.

Cardaropoli, F., Alfieri, V., Caiazzo, F. and Sergi, V. (2012) 'Dimensional analysis for the definition of the influence of process parameters in selective laser melting of Ti-6Al-4V alloy', *Proceedings of the Institution of Mechanical Engineers, Part B: Journal of Engineering Manufacture*, 226(7), pp. 1136–1142. Available at: http://pib.sagepub.com/lookup/doi/10.1177/0954405412441885\nfile:///D:/Sorted Papers/Cardaropoli et al. - 2012 - Dimensional analysis for the definition of the influence of process parameters in selective laser melting of.pdf.

Carter, L. N., Martin, C., Withers, P. J. and Attallah, M. M. (2014) 'The influence of the laser scan strategy on grain structure and cracking behaviour in SLM powder-bed fabricated nickel superalloy', *Journal of Alloys and Compounds*, 615, pp. 338–347. Available at: http://dx.doi.org/10.1016/j.jallcom.2014.06.172.

Casalino, G., Campanelli, S. L., Contuzzi, N. and Ludovico, A. D. (2015) 'Experimental investigation and statistical optimisation of the selective laser melting process of a maraging steel', *Optics & Laser Technology*, 65, pp. 151–158.

Casavola, C., Campanelli, S. L. and Pappalettere, C. (2008) 'Experimental analysis of residual stresses in the selective laser melting process', in *XIth International Congress and Exposition*. Orlando.

Casavola, C., Campanelli, S. L. and Pappalettere, C. (2009) 'Preliminary investigation on distribution of residual stress generated by the selective laser melting process', *The Journal of Strain Analysis for Engineering Design*, 44(1), pp. 93–104. Available at: http://journals.pepublishing.com/openurl.asp?genre=article&id=doi:10.1243/03093247JSA46 4.

Cavazzuti, M. (2013) 'Design of experiments', in *Optimization methods: From theory to design*. Springer-Verlag, Heidelberg, pp. 13–42. Available at: http://link.springer.com/content/pdf/10.1007/978-3-642-31187-1.pdf\nhttp://link.springer.com/10.1007/978-3-642-31187-1.

Cheng, B., Shrestha, S. and Chou, K. (2016) 'Stress and deformation evaluations of scanning strategy effect in selective laser melting', *Additive Manufacturing*, 12, pp. 240–251. Available at: http://dx.doi.org/10.1016/j.addma.2016.05.007.

Cheng, X., Prask, H. J., Gnaeupel-Herold, T., Luzin, V. and Fisher, J. W. (2012) 'Neutron diffraction measurements for residual stresses in AL-6XN stainless steel welded beams', in Khidirov, I. (ed.) *Neutron Diffraction*. InTech, pp. 25–48.

Cherry, J. A., Davies, H. M., Mehmood, S., Lavery, N. P., Brown, S. G. R. and Sienz, J. (2015) 'Investigation into the effect of process parameters on microstructural and physical properties of 316L stainless steel parts by selective laser melting', *The International Journal of Advanced Manufacturing Technology*, 76(5-8), pp. 869–879. Available at: http://link.springer.com/10.1007/s00170-014-6297-2.

Choi, K. H., Kim, H. C., Doh, Y. H. and Kim, D. S. (2009) 'Novel scan path generation method based on area division for SFFS', *Journal of Mechanical Science and Technology*, 23(4), pp. 1102–1111.

Concept Laser (2010) *Heat treatment CL 50WS, M2 Cusing Manual - Serial number M2-2011-02-01*.

Contuzzi, N., Campanelli, S. L. and Ludovinco, A. D. (2011) '3D finite element analysis in the selective laser melting process', *International Journal of Simulation Modelling*, 10(3), pp. 113–121.

Cottam, R., Wang, J. and Luzin, V. (2014) 'Characterization of microstructure and residual stress in a 3D H13 tool steel component produced by additive manufacturing', *Journal of Materials Research*, 29(17), pp. 1978–1986. Available at:

http://www.journals.cambridge.org/abstract_S0884291414001903.

Craeghs, T., Clijster, S., Yasa, E. and Kruth, J.-P. (2011) 'Online quality control of selective laser melting', in *Solid Freeform Fabrication Symposium*. Austin, pp. 212–226.

Cullity, B. . (1978) *Elements of x-ray diffraction*. 2nd edn. Edited by M. Cohen. Reading, Massachusetts: Addison-Wesley.

Dadbakhsh, S. and Hao, L. (2014) 'Effect of layer thickness in selective laser melting on microstructure of Al/5 wt.%Fe2O3 powder consolidated parts', *The Scientific World Journal*, 2014, pp. 1–10. Available at: http://www.hindawi.com/journals/tswj/2014/106129/.

Dai, D. and Gu, D. (2015) 'Tailoring surface quality through mass and momentum transfer modeling using a volume of fluid method in selective laser melting of TiC/AlSi10Mg powder', *International Journal of Machine Tools and Manufacture*, 88, pp. 95–107. Available at: http://dx.doi.org/10.1016/j.ijmachtools.2014.09.010.

Das, M., Balla, V. K., Basu, D., Bose, S. and Bandyopadhyay, A. (2010) 'Laser processing of SiC-particle-reinforced coating on titanium', *Scripta Materialia*, 63(4), pp. 438–441. Available at: http://dx.doi.org/10.1016/j.scriptamat.2010.04.044.

Das, M., Balla, V. K., Kumar, T. S. S. and Manna, I. (2013) 'Fabrication of biomedical implants using laser engineered net shaping (LENS^{TM})', *Transactions of the Indian Ceramic Society*, 72(3), pp. 169–174. Available at: http://www.tandfonline.com/doi/abs/10.1080/0371750X.2013.851619.

Deckers, J., Meyers, S., Kruth, J. P. and Vleugels, J. (2014) 'Direct selective laser sintering / melting of high density alumina powder layers at elevated temperatures', *Physics Procedia*, 56, pp. 117–124.

Demir, A. G. and Previtali, B. (2017) 'Investigation of remelting and preheating in SLM of 18Ni300 maraging steel as corrective and preventive measures for porosity reduction', *The International Journal of Advanced Manufacturing Technology*. The International Journal of Advanced Manufacturing Technology, 93(5-8), pp. 2697–2709. Available at: http://link.springer.com/10.1007/s00170-017-0697-z.

Denlinger, E. R., Heigel, J. C., Michaleris, P. and Palmer, T. A. (2015) 'Effect of inter-layer dwell time on distortion and residual stress in additive manufacturing of titanium and nickel alloys', *Journal of Materials Processing Technology*, 215, pp. 123–131. Available at: https://linkinghub.elsevier.com/retrieve/pii/S0924013614002891.

Dimitrov, D., Becker, T. H., Yadroitsev, I. and Booysen, G. (2016) 'On the impact of different system strategies on the material performance of selective laser melting-manufactured Ti-6Al-4V components', *South African Journal of Industrial Engineering*, 27, pp. 184–191.

Dimitrov, D. and Hugo, P. (2013) 'Building capability profile of LaserCusing', in *14th Annual International Conference of the Rapid Product Developmement Association of South Africa*. Bloemfontein, pp. 1–15.

Dimitrov, D., Schreve, K. and de Beer, N. (2006) 'Advances in three dimensional printing – state of the art and future perspectives', *Rapid Prototyping Journal*, 12(3), pp. 136–147.

Dingal, S., Pradhan, T. R., Sundar, J. K. S., Choudhury, A. R. and Roy, S. K. (2008) 'The application of Taguchi's method in the experimental investigation of the laser sintering process', *The International Journal of Advanced Manufacturing Technology*, 38(9-10), pp. 904–914. Available at: http://link.springer.com/10.1007/s00170-007-1154-1.

Dreier, S. and Denkena, B. (2014) 'Determination of residual stresses in plate material by layer removal with machine-integrated measurement', *Procedia CIRP*, 24, pp. 103–107. Available at: http://linkinghub.elsevier.com/retrieve/pii/S2212827114009524.

Dutta, B., Palaniswamy, S., Choi, J., Song, L. J. and Mazumder, J. (2011) 'Additive manufacturing by direct metal deposition', *Advanced Materials & Processes*, 169(5), pp. 33 – 36.

Elsen, M. Van, Al-bender, F. and Kruth, J.-P. (2008) 'Application of dimensional analysis to selective laser melting', *Rapid Prototyping Journal*, 14(1), pp. 15–22.

Farrel, S. P. and MacGregor, L. . (2010) 'Application of X-ray diffraction for residual stress analysis on canadian naval platforms', in *Denver X-ray conference on Applications of X-ray Analysis*. Denver, pp. 164–171.

Fateri, M., Hötter, J.-S. and Gebhardt, A. (2012) 'Experimental and theoretical investigation of buckling deformation of fabricated objects by selective laser melting', *Physics Procedia*, 39, pp. 464–470. Available at: http://www.sciencedirect.com/science/article/pii/S1875389212025898.

Fera, M., Fruggiero, F., Costabile, G., Lambiase, A. and Pham, D. T. (2017) 'A new mixed production cost allocation model for additive manufacturing (MiProCAMAM)', *The International Journal of Advanced Manufacturing Technology*, 92(9-12), pp. 4275–4291. Available at: http://link.springer.com/10.1007/s00170-017-0492-x.

Ferrar, B., Mullen, L., Jones, E., Stamp, R. and Sutcliffe, C. J. (2012) 'Gas flow effects on selective laser melting (SLM) manufacturing performance', *Journal of Materials Processing Technology*, 212(2), pp. 355–364.

Fitzpatrick, M. E., Fry, A. T., Holdway, P., Kandil, F. A., Shackleton, J. and Suominen, L. (2005) 'Determination of residual stresses by X-ray diffraction', *Measurement Good Practice Guide*. National Physical Laboratory, Teddington, 52(2), pp. 1–68.

Furumoto, T., Ueda, T., Abdul Aziz, M., Hosokawa, A. and Tanaka, R. (2010) 'Study on reduction of residual stress induced during rapid tooling process: Influence of heating conditions on residual Stress', *Key Engineering Materials*, 447-448, pp. 785–789.

Ganeriwala, R. and Zohdi, T. I. (2014) 'Multiphysics modeling and simulation of selective laser sintering manufacturing processes', *Procedia CIRP*, 14, pp. 299–304. Available at: http://dx.doi.org/10.1016/j.procir.2014.03.015.

Ghany, K. A. and Moustafa, S. F. (2006) 'Comparison between the products of four RPM systems for metals', *Rapid Prototyping Journal*, 12(2), pp. 86–94.

Gong, H., Rafi, K., Gu, H., Starr, T. and Stucker, B. (2014) 'Analysis of defect generation in Ti-6Al-4V parts made using powder bed fusion additive manufacturing processes', *Additive Manufacturing*, 1, pp. 87–98. Available at: http://dx.doi.org/10.1016/j.addma.2014.08.002.

Gong, X., Anderson, T. and Chou, K. (2014) 'Review on powder-based electron beam additive manufacturing technology', *Manufacturing Review*, 1(2), pp. 1–12. Available at: http://mfr.edp-open.org/10.1051/mfreview/2014001.

Gu, D. (2015) *Laser additive manufacturing of high-performance materials*. Springer. Available at: http://link.springer.com/10.1007/978-3-662-46089-4.

Gu, D. and Shen, Y. (2009) 'Balling phenomena in direct laser sintering of stainless steel powder : Metallurgical mechanisms and control methods', *Materials and Design*, 30, pp. 2903–2910.

Gu, H., Gong, H., Pal, D., Rafi, K., Starr, T. and Stucker, B. (2013) 'Influences of energy density on porosity and microstructure of selective laser melted 17- 4PH stainless steel', in *Solid Freeform Fabrication*. Austin, pp. 474–479.

Guan, K., Wang, Z., Gao, M., Li, X. and Zeng, X. (2013) 'Effects of processing parameters on tensile properties of selective laser melted 304 stainless steel', *Materials & Design*, 50, pp. 581–586. Available at: http://linkinghub.elsevier.com/retrieve/pii/S0261306913002562.

Guo, N. and Leu, M. C. (2013) 'Additive manufacturing: Technology, applications and research needs', *Frontiers of Mechanical Engineering*, 8(3), pp. 215–243.

Gupta, A. and Kumar, S. (2014) 'Optimization of scale factors in shrinkage compensations in SLS using pattern search tool and genetic algorithm', *International Journal of Technical Research and Applications*, 2(2), pp. 11–13.

Gusarov, A. V., Pavlov, M. and Smurov, I. (2011) 'Residual stresses at laser surface remelting and additive manufacturing', *Physics Procedia*, 12(PART 1), pp. 248–254. Available at: http://dx.doi.org/10.1016/j.phpro.2011.03.032.

Gusarov, A. V., Yadroitsev, I., Bertrand, P. and Smurov, I. (2007) 'Heat transfer modelling and stability analysis of selective laser melting', *Applied Surface Science*, 254(4), pp. 975–979. Available at: http://linkinghub.elsevier.com/retrieve/pii/S0169433207011907.

Hagedorn-Hansen, D., Bezuidenhout, M., Dimitrov, D. and Oosthuizen, G. A. (2017) 'The effects of selective laser melting scan strategies on deviation of hybrid parts', *South African Journal of Industrial Engineering*, 28(3), pp. 200–212. Available at: http://sajie.journals.ac.za/pub/article/view/1862.

Hanzl, P., Zetek, M., Bakša, T. and Kroupa, T. (2015) 'The influence of processing parameters on the mechanical properties of SLM parts', *Procedia Engineering*, 100, pp. 1405–1413.

Heralić, A., Christiansson, A.-K. and Lennartson, B. (2012) 'Height control of laser metal-wire deposition based on iterative learning control and 3D scanning', *Optics and Lasers in Engineering*, 50(9), pp. 1230–1241.

Herzog, F. C. (2009) 'Procedure for the production of a three-dimensional component'. Germany: German Patent and Trademark Office.

Hodge, N. E., Ferencz, R. M. and Solberg, J. M. (2014) 'Implementation of a thermomechanical model for the simulation of selective laser melting', *Computational Mechanics*, (33-51), pp. 33–51.

Hosseinzadeh, F., Kowal, J. and Bouchard, P. J. (2014) 'Towards good practice guidelines for the contour method of residual stress measurement', *The Journal of Engineering*, 2014(8), pp. 453–468. Available at: http://digital-library.theiet.org/content/journals/10.1049/joe.2014.0134.

Huang, X., Liu, Z. and Xie, H. (2013) 'Recent progress in residual stress measurement techniques', *Acta Mechanica Solida Sinica*, 26(6), pp. 570–583. Available at: http://dx.doi.org/10.1016/S0894-9166(14)60002-1.

Hussein, A., Hao, L., Yan, C., Everson, R. and Young, P. (2013) 'Advanced lattice support structures for metal additive manufacturing', *Journal of Materials Processing Technology*, 213(7), pp. 1019–1026. Available at: http://dx.doi.org/10.1016/j.jmatprotec.2013.01.020.

Järvinen, J., Matilainen, V., Li, X., Piili, H. and Salminen, A. (2014) 'Characterization of effect of support structures in laser additive manufacturing of stainless steel', *Physics Procedia*, 56, pp. 72–81. Available at: http://dx.doi.org/10.1016/j.phpro.2014.08.099.

Jhabvala, J., Boillat, E., Antignac, T. and Glardon, R. (2010) 'On the effect of scanning strategies in the selective laser melting process', *Virtual and Physical Prototyping*, 5(2), pp. 99–109. Available at: http://www.tandfonline.com/doi/abs/10.1080/17452751003688368\nhttp://dx.doi.org/10.108 0/17452751003688368.

Kalentics, N., Boillat, E., Peyre, P., Gorny, C., Kenel, C., Leinenbach, C., Jhabvala, J. and Logé, R. E. (2017) '3D laser shock peening – A new method for the 3D control of residual stresses in selective laser melting', *Materials & Design*, 130, pp. 350–356. Available at: https://linkinghub.elsevier.com/retrieve/pii/S0264127517305658.

Kandil, F. A., Lord, J. D., Fry, A. T. and Grant, P. V. (2001) *A review of residual stress measurement methods - A guide to technical selection*. NPL Report MATC (A) 4.

Kartal, M. E. (2013) 'Analytical solutions for determining residual stresses in two-dimensional domains using the contour method', *Proceedings of the Royal Society A*. Royal Society, 469(2159), pp. 1–20. Available at: http://www.ncbi.nlm.nih.gov/pubmed/24204187.

Kellens, K., Mertens, R., Paraskevas, D., Dewulf, W. and Duflou, J. R. (2017) 'Environmental impact of additive manufacturing processes: Does AM contribute to a more sustainable way of part manufacturing?', *Procedia CIRP*, 61, pp. 582–587. Available at: http://dx.doi.org/10.1016/j.procir.2016.11.153.

Kempen, K. (2015) *Expanding the materials palette for selective laser melting of metals*. PhD Thesis, KU Leuven.

Kempen, K., Thijs, L., Vrancken, B., Buls, S., Van Humbeek, J. and Kruth, J.-P. (2013) 'Lowering thermal gradients in selective laser melting by pre-heating the baseplate', in *Solid Freeform Fabrication Symposium*. Austin.

Kempen, K., Vrancken, B., Buls, S., Thijs, L., Van Humbeeck, J. and Kruth, J.-P. (2014) 'Selective laser melting of crack-free high density M2 high speed steel parts by baseplate preheating', *Journal of Manufacturing Science and Engineering*, 136(6), pp. 1–6. Available at: http://manufacturingscience.asmedigitalcollection.asme.org/article.aspx?doi=10.1115/1.4028 513.

King, W. E., Anderson, A. T., Ferencz, R. M., Hodge, N. E., Kamath, C., Khairalla, S. A. and Rubenchik, A. M. (2015) 'Laser powder bed fusion additive manufacturing of metals; physics, computational, and materials challenges', *Applied Physics Reviews*, 2(4), p. 041304. Available at: http://dx.doi.org/10.1063/1.4937809.

Klocke, F., Arntz, K., Teli, M., Winands, K., Wegener, M. and Oliari, S. (2017) 'State-of-the-art laser additive manufacturing for hot-work tool steels', *Procedia CIRP*, 63, pp. 58–63.

Knowles, C., Becker, T. and Tait, R. (2012) 'Residual stress measurements and structural integrity implications for selective laser melted Ti-6Al-4V', *South African Journal of Industrial Engineering*, 23(3), pp. 119–129. Available at: http://sajie.journals.ac.za/pub/article/view/515.

Kovaleva, I., Kovalev, O. and Smurov, I. (2014) 'Model of heat and mass transfer in random packing layer of powder particles in selective laser melting', *Physics Procedia*, 56, pp. 400–410. Available at: http://dx.doi.org/10.1016/j.phpro.2014.08.143.

Krauss, H., Eschey, C. and Zaeh, M. F. (2012) 'Thermography for monitoring the selective laser melting process', in *Solid Freeform Fabrication Symposium*. Auckland, pp. 999–1014.

Krauss, H. and Zaeh, M. F. (2013) 'Investigations on manufacturability and process reliability of selective laser melting', *Physics Procedia*, 41, pp. 815–822. Available at: http://dx.doi.org/10.1016/j.phpro.2013.03.153.

Król, M., Dobrzański, L. and Reimann, I. (2013) 'Surface quality in selective laser melting of metal powders', *Archives of Materials Science*, 60(2), pp. 87–92.

Kruth, J., Badrossamay, M., Yasa, E., Deckers, J., Thijs, L. and Humbeeck, J. Van (2010) 'Part and material properties in selective laser melting of metals', in *16th International Symposium on Electromachining*, pp. 1–12.

Kruth, J. P., Bartscher, M., Carmignato, S., Schmitt, R., De Chiffre, L. and Weckenmann, A. (2011) 'Computed tomography for dimensional metrology', *CIRP Annals - Manufacturing Technology*, 60(2), pp. 821–842. Available at: http://dx.doi.org/10.1016/j.cirp.2011.05.006.

Kruth, J. P., Froyen, L., Van Vaerenbergh, J., Mercelis, P., Rombouts, M. and Lauwers, B. (2004) 'Selective laser melting of iron-based powder', *Journal of Materials Processing Technology*, 149(1-3), pp. 616–622.

Kruth, J.-P., Deckers, J., Yasa, E. and Wauthle, R. (2012) 'Assessing and comparing influencing factors of residual stresses in selective laser melting using a novel analysis method', *Proceedings of the Institution of Mechanical Engineers, Part B: Journal of Engineering Manufacture*, 226(6), pp. 980–991.

Kruth, J.-P., Vandenbroucke, B., Vaerenbergh, J. and Mercelis, P. (2005) 'Benchmarking of different SLS/SLM processes as rapid manufacturing techniques', in *International Conference Polymers & Moulds Innovations (PMI)*. Gent, pp. 1–7.

Kuznetsov, A. Y., Neves, R. S., Linares, L. P., Oliveira, T. L., Gravina, E. G., Hirsch, T. K. and Achete, C. A. (2012) 'X-ray diffraction using conventional Ψ or Ω geometries', in *15th International Conference on Experimental Mechanics*. Porto, pp. 1–12.

Leuders, S., Thöne, M., Riemer, A., Niendorf, T., Tröster, T., Richard, H. A. and Maier, H. J. (2013) 'On the mechanical behaviour of titanium alloy TiAl6V4 manufactured by selective laser melting: Fatigue resistance and crack growth performance', *International Journal of Fatigue*, 48, pp. 300–307. Available at: http://dx.doi.org/10.1016/j.ijfatigue.2012.11.011.

Li, C., Fu, C. H., Guo, Y. B. and Fang, F. Z. (2016) 'A multiscale modeling approach for fast prediction of part distortion in selective laser melting', *Journal of Materials Processing Technology*, 229, pp. 703–712. Available at: http://linkinghub.elsevier.com/retrieve/pii/S0924013615301746.

Li, C., Guo, Y., Fang, X. and Fang, F. (2018) 'A scalable predictive model and validation for residual stress and distortion in selective laser melting', *CIRP Annals - Manufacturing Technology*, 67, pp. 249–252.

Li, Y. and Gu, D. (2014a) 'Parametric analysis of thermal behavior during selective laser melting additive manufacturing of aluminum alloy powder', *Materials & Design*, 63, pp. 856–867. Available at: http://dx.doi.org/10.1016/j.matdes.2014.07.006.

Li, Y. and Gu, D. (2014b) 'Thermal behavior during selective laser melting of commercially pure titanium powder: Numerical simulation and experimental study', *Additive Manufacturing*, 1-4, pp. 99–109. Available at: http://dx.doi.org/10.1016/j.addma.2014.09.001.

Li, Y., Zhou, K., Tan, P., Tor, S., Kai, C. and Fai, K. (2018) 'Modeling temperature and residual stress fields in selective laser melting', *International Journal of Mechanical Sciences*, 136, pp. 24–35. Available at: https://doi.org/10.1016/j.ijmecsci.2017.12.001.

Liu, Y., Yang, Y. and Wang, D. (2016) 'A study on the residual stress during selective laser melting (SLM) of metallic powder', *The International Journal of Advanced Manufacturing Technology*, 87(1-4), pp. 647–656. Available at: http://dx.doi.org/10.1007/s00170-016-8466-y.

Liverani, E., Toschi, S., Ceschini, L. and Fortunato, A. (2017) 'Effect of selective laser melting (SLM) process parameters on microstructure and mechanical properties of 316L austenitic stainless steel', *Journal of Materials Processing Technology*, 249, pp. 255–263. Available at: http://dx.doi.org/10.1016/j.jmatprotec.2017.05.042.

Loh, L.-E., Chua, C., Yeong, W., Song, J., Mapar, M., Sing, S., Liu, Z. and Zhang, D. (2015) 'Numerical investigation and an effective modelling on the Selective Laser Melting (SLM) process with aluminium alloy 6061', *International Journal of Heat and Mass Transfer*, 80, pp. 288–300. Available at: http://dx.doi.org/10.1016/j.ijheatmasstransfer.2014.09.014.

Lord, J. D., Penn, D. and Whitehead, P. (2008) 'The application of digital image correlation for measuring residual stress by incremental hole drilling', *Applied Mechanics and Materials*, 13-14, pp. 65–73. Available at: http://www.scientific.net/AMM.13-14.65.

Lu, Y., Wu, S., Gan, Y., Huang, T., Yang, C., Junjie, L. and Lin, J. (2015) 'Study on the microstructure, mechanical property and residual stress of SLM Inconel-718 alloy manufactured by differing island scanning strategy', *Optics and Laser Technology*, 75, pp. 197–206. Available at: http://dx.doi.org/10.1016/j.optlastec.2015.07.009.

Ma, L. and Bin, H. (2007) 'Temperature and stress analysis and simulation in fractal scanning-based laser sintering', *The International Journal of Advanced Manufacturing Technology*,

34(9-10), pp. 898–903. Available at: http://link.springer.com/10.1007/s00170-006-0665-5.

Manfredi, D., Calignano, F., Krishnan, M., Canali, R., Ambrosio, E. and Atzeni, E. (2013) 'From powders to dense metal parts: Characterization of a commercial AlSiMg alloy processed through direct metal laser sintering', *Materials*, 6(3), pp. 856–869. Available at: http://www.mdpi.com/1996-1944/6/3/856.

Mansilla, C., Martínez-Martínez, D., Ocelík, V. and De Hosson, J. T. M. (2015) 'On the determination of local residual stress gradients by the slit milling method', *Journal of Materials Science*, 50(10), pp. 3646–3655. Available at: http://link.springer.com/10.1007/s10853-015-8927-y.

Markl, M. and Körner, C. (2016) 'Multi-scale modeling of powder-bed-based additive manufacturing', *Annual Review of Materials Research*, 46, pp. 1–34. Available at: http://arxiv.org/abs/1708.01312.

Mazur, M., Brincat, P., Leary, M. and Brandt, M. (2017) 'Numerical and experimental evaluation of a conformally cooled H13 steel injection mould manufactured with selective laser melting', *The International Journal of Advanced Manufacturing Technology*. The International Journal of Advanced Manufacturing Technology, 93(1-4), pp. 881–900. Available at: http://link.springer.com/10.1007/s00170-017-0426-7.

Meier, H. and Haberland, C. (2008) 'Experimental studies on selective laser melting of metallic parts', *Materialwissenschaft und Werkstofftechnik*, 39(9), pp. 665–670. Available at: http://dx.doi.org/10.1002/mawe.200800327.

Mercelis, P. and Kruth, J. (2006) 'Residual stresses in selective laser sintering and selective laser melting', *Rapid Prototyping Journal*, 12(5), pp. 254–265. Available at: http://www.scopus.com/inward/record.url?eid=2-s2.0-33750146493&partnerID=40&md5=7eebf030e96fa24df272aff5aea8f2cc.

Mertens, R., Vrancken, B., Holmstock, N., Kinds, Y., Kruth, J. P. and Van Humbeeck, J. (2016) 'Influence of powder bed preheating on microstructure and mechanical properties of H13 tool steel SLM parts', *Physics Procedia*, 83, pp. 882–890.

Micro-Measurements (2010) 'Measurement of residual stresses by the hole drilling strain gage method'. Vishay Precision Group, pp. 19–33.

Mohanty, S. and Hattel, J. (2014) 'Cellular scanning strategy for selective laser melting: Capturing thermal trends with a low-fidelity, pseudo-analytical model', *Mathematical Problems in Engineering*, pp. 1–14.

Montgomery, D. C. (2013) *Design and analysis of experiments*. 8th edn. John Wiley & Sons.

Mugwagwa, L., Dimitrov, D. and Matope, S. (2014) 'Exploring opportunities for improvement in selective laser melting', in *15th International Conference of the Rapid Product Development Association of South Africa*. Stellenbosch, pp. 21–29.

Mugwagwa, L., Dimitrov, D., Matope, S. and Becker, T. (2016) 'A methodology to evaluate the influence of part geometry on residual stresses in selective laser melting', in *International Conference on Competitive Manufacturing*. Stellenbosch, pp. 133 – 139.

Mumtaz, K. A. and Hopkinson, N. (2010) 'Selective laser melting of thin wall parts using pulse shaping', *Journal of Materials Processing Technology*, 210(2), pp. 279–287.

Murr, L. E., Gaytan, S. M., Ramirez, D. A., Martinez, E., Hernandez, J., Amato, K. N., Shindo, P. W., Medina, F. R. and Wicker, R. B. (2012) 'Metal fabrication by additive manufacturing using laser and electron beam melting technologies', *Journal of Materials Science & Technology*, 28(1), pp. 1–14. Available at: http://dx.doi.org/10.1016/S1005-0302(12)60016-4.

Nadammal, N., Cabeza, S., Mishurova, T., Thiede, T., Kromm, A., Seyfert, C., Farahbod, L., Haberland, C., Schneider, J. A., Portella, P. D. and Bruno, G. (2017) 'Effect of hatch length on the development of microstructure, texture and residual stresses in selective laser melted superalloy Inconel 718', *Materials & Design*, 134, pp. 139–150. Available at: https://doi.org/10.1016/j.matdes.2017.08.049.

Nadammal, N., Kromm, A., Saliwan-Neumann, R., Farahbod, L., Haberland, C. and Portella, P. D. (2018) 'Influence of support configurations on the characteristics of selective laser-melted Inconel 718', *JOM*, 70(3), pp. 343–348. Available at: https://doi.org/10.1007/s11837-017-2703-1.

Nelson, D. V (2009) 'Residual stress determination with hole drilling and optical methods', in *SEM Annual Conference*. New Mexico: Society for Experimental Mechanics.

Neugebauer, F., Keller, N., Ploshikhin, V., Feuerhahn, F. and Köhler, H. (2014) 'Multi scale FEM simulation for distortion calculation in additive manufacturing of hardening stainless steel', in *International Workshop on Thermal forming and welding distortion*. Bremen, pp. 1–11.

O'Regan, P., Prickett, P., Setchi, R., Hankins, G. and Jones, N. (2016) 'Metal based additive layer manufacturing: Variations, correlations and process control', *Procedia Computer Science*. Elsevier Masson SAS, 96, pp. 216–224.

Pagliaro, P., Prime, M. B., Swenson, H. and Zuccarello, B. (2010) 'Measuring multiple residual-stress components using the contour method and multiple cuts', *Experimental Mechanics*, 50(2), pp. 187–194.

Papadakis, L., Chantzis, D. and Salonitis, K. (2018) 'On the energy efficiency of pre-heating methods in SLM/SLS processes', *The International Journal of Advanced Manufacturing Technology*. The International Journal of Advanced Manufacturing Technology, 95(1-4), pp. 1325–1338. Available at: http://link.springer.com/10.1007/s00170-017-1287-9.

Papadakis, L., Loizou, A., Risse, J., Bremen, S. and Schrage, J. (2014) 'A computational reduction model for appraising structural effects in selective laser melting manufacturing', *Virtual and Physical Prototyping*, 9(1), pp. 17–25. Available at: http://www.tandfonline.com/doi/abs/10.1080/17452759.2013.868005.

Parry, L., Ashcroft, I. A. and Wildman, R. D. (2016) 'Understanding the effect of laser scan strategy on residual stress in selective laser melting through thermo-mechanical simulation', *Additive Manufacturing*, 12, pp. 1–15. Available at: http://dx.doi.org/10.1016/j.addma.2016.05.014.

Perec, A. (2016) 'Abrasive suspension water jet cutting optimization using orthogonal array design', *Procedia Engineering*, 149, pp. 366–373. Available at:

http://dx.doi.org/10.1016/j.proeng.2016.06.680.

Prime, M. B. (1999) 'Residual stress measurement by successive extension of a slot: The crack compliance method', *Applied Mechanics Reviews*, 52(2), pp. 75–96.

Prime, M. B. and Dewald, A. T. (2013) 'The contour method', in Schajer, G. S. (ed.) *Practical residual stress measurement methods*. Wiley-Blackwell, pp. 109–138.

Pupo, Y., Delgado, J., Serenó, L. and Ciurana, J. (2013) 'Scanning space analysis in selective laser melting for CoCrMo powder', in *5th Manufacturing Engineering Society International Conference*. Zaragoza, pp. 370–378.

Pyka, G., Kerckhofs, G., Papantoniou, I., Speirs, M., Schrooten, J. and Wevers, M. (2013) 'Surface roughness and morphology customization of additive manufactured open porous Ti6Al4V structures', *Materials*, 6(10), pp. 4737–4757.

Raghunath, N. and Pandey, P. M. (2007) 'Improving accuracy through shrinkage modelling by using Taguchi method in selective laser sintering', *International Journal of Machine Tools and Manufacture*, 47(6), pp. 985–995.

Rangaswamy, P., Holden, T. M., Rogge, R. B. and Griffith, M. L. (2003) 'Residual stresses in components formed by the laser-engineered net shaping (LENS) process', *The Journal of Strain Analysis for Engineering Design*, 38(6), pp. 519–527. Available at: http://sdj.sagepub.com/lookup/doi/10.1243/030932403770735881\nhttp://sdj.sagepub.com/content/38/6/519.abstract.

Rickenbacher, L., Spierings, A. and Wegener, K. (2013) 'An integrated cost-model for selective laser melting (SLM)', *Rapid Prototyping Journal*, 19(3), pp. 208–214. Available at: http://www.emeraldinsight.com/10.1108/13552541311312201.

Roberts, I. A. (2012) *Investigation of residual stresses in the laser melting of metal powders in additive layer manufacturing*. PhD Thesis, University of Wolverhampton.

Rombouts, M., Kruth, J.-P. and Froyen, L. (2009) 'Impact of physical phenomena during selective laser melting of iron powders', *Fabrication, Materials, Processing and Properties*, 1, pp. 397–404.

Safronov, V. A., Khmyrov, R. S., Kotoban, D. V. and Gusarov, A. V. (2016) 'Distortions and residual stresses at layer-by-layer additive manufacturing by fusion', *Journal of Manufacturing Science and Engineering*, 139(3), p. 031017. Available at: http://manufacturingscience.asmedigitalcollection.asme.org/article.aspx?doi=10.1115/1.4034714.

Sames, W. J., List, F. A., Pannala, S., Dehoff, R. R. and Babu, S. S. (2016) 'The metallurgy and processing science of metal additive manufacturing', *International Materials Review*, pp. 1–46.

SAS Institute Inc. (2014) *Design of Experiments*. Available at: http://www.scai.fraunhofer.de/fileadmin/ArbeitsgruppeTrottenberg/WS0809/seminar/Kapitza.pdf.

Savalani, M. M., Chung, C. C., Poon, C. and Yeung, W. (2011) 'Selective laser melting of

aluminum and its alloys', in *NZ Rapid Product Development Conference*. Auckland, pp. 1–5.

Savalani, M. M., Hao, L., Dickens, P. M., Zhang, Y., Tanner, K. E. and Harris, R. A. (2012) 'The effects and interactions of fabrication parameters on the properties of selective laser sintered hydroxyapatite polyamide composite biomaterials', *Rapid Prototyping Journal*, 18(1), pp. 16–27.

Savalani, M. M. and Pizarro, J. M. (2016) 'Effect of preheat and layer thickness on selective laser melting (SLM) of magnesium', *Rapid Prototyping Journal*, 22(1), pp. 115–122.

Schajer, G. S. (2010a) 'Advances in hole-drilling residual stress measurements', *Experimental Mechanics*, 50(2), pp. 159–168.

Schajer, G. S. (2010b) 'Relaxation methods for measuring residual stresses: Techniques and opportunities', *Experimental Mechanics*, 50(8), pp. 1117–1127.

Schmidt, M., Merklein, M., Bourell, D., Dimitrov, D., Hausotte, T., Wegener, K., Overmeyer, L., Vollertsen, F. and Levy, G. N. (2017) 'Laser based additive manufacturing in industry and academia', *CIRP Annals - Manufacturing Technology*, 66(2), pp. 561–583. Available at: http://dx.doi.org/10.1016/j.cirp.2017.05.011.

Schoinochoritis, B., Chantzis, D. and Salonitis, K. (2017) 'Simulation of metallic powder bed additive manufacturing processes with the finite element method : A critical review', *Proceedings of the Institution of Mechanical Engineers, Part B: Journal of Engineering Manufacture*, 231(1), pp. 96–117.

Schröder, M., Falk, B. and Schmitt, R. (2015) 'Evaluation of cost structures of additive manufacturing processes using a new business model', *Procedia CIRP*, 30, pp. 311–316. Available at: http://dx.doi.org/10.1016/j.procir.2015.02.144.

Shahzad, K., Deckers, J., Kruth, J.-P. and Vleugels, J. (2013) 'Additive manufacturing of alumina parts by indirect selective laser sintering and post processing', *Journal of Materials Processing Technology*, 213, pp. 1484–1494. Available at: http://dx.doi.org/10.1016/j.jmatprotec.2013.03.014.

Shiomi, M., Osakada, K., Nakamura, K., Yamashita, T. and Abe, F. (2004) 'Residual stress within metallic model made by selective laser melting process', *CIRP Annals*, 53(1), pp. 195–198. Available at: http://linkinghub.elsevier.com/retrieve/pii/S0007850607606775.

Siddique, S., Imran, M., Rauer, M., Kaloudis, M., Wycisk, E., Emmelmann, C. and Walther, F. (2015) 'Computed tomography for characterization of fatigue performance of selective laser melted parts', *Materials & Design*, 83, pp. 661–669. Available at: https://linkinghub.elsevier.com/retrieve/pii/S026412751500413X.

Simonelli, M., Tse, Y. Y. and Tuck, C. (2012) 'Microstructure of Ti-6Al-4V produced by selective laser melting', *Journal of Physics: Conference Series*, 371, p. 012084.

Singh, S., Sachdeva, A. and Sharma, V. (2012) 'Investigation of dimensional accuracy/mechanical properties of part produced by selective laser sintering', *International Journal of Applied Science and Engineering*, 10(1), pp. 59–68.

Slotwinski, J. A., Garboczi, E. J. and Hebenstreit, K. M. (2014) 'Porosity measurements and

analysis for metal additive manufacturing process control', *Journal of Research of the National Institute of Standards and Technology*, 119, p. 494. Available at: https://nvlpubs.nist.gov/nistpubs/jres/119/jres.119.019.pdf.

Song, B., Dong, S., Liao, H. and Coddet, C. (2012) 'Process parameter selection for selective laser melting of Ti6Al4V based on temperature distribution simulation and experimental sintering', *The International Journal of Advanced Manufacturing Technology*, 61(9-12), pp. 967–974. Available at: http://link.springer.com/10.1007/s00170-011-3776-6.

Spierings, A. B., Schneider, M. and Eggenberger, R. (2011) 'Comparison of density measurement techniques for additive manufactured metallic parts', *Rapid Prototyping Journal*, 17(5), pp. 380–386. Available at: http://www.emeraldinsight.com/doi/10.1108/13552541111156504.

Stamp, R., Fox, P., O'Neill, W., Jones, E. and Sutcliffe, C. (2009) 'The development of a scanning strategy for the manufacture of porous biomaterials by selective laser melting', *Journal of Materials Science: Materials in Medicine*, 20(9), pp. 1839–1848.

Strano, G., Hao, L., Everson, R. M. and Evans, K. E. (2013) 'Surface roughness analysis, modelling and prediction in selective laser melting', *Journal of Materials Processing Technology*, 213(4), pp. 589–597. Available at: http://dx.doi.org/10.1016/j.jmatprotec.2012.11.011.

Suzuki, T., Oikawa, H., Imafuku, M., Suzuki, H., Sugiyama, M., Nose, T., Tomota, Y. and Moriai, A. (2011) 'Residual stress measurement of welding area by neutron diffraction method', *Nippon Steel Technical Report*, (100), pp. 47–50.

Tang, Y., Loh, H. T., Fuh, J. Y. H., Wong, Y. S., Lu, L., Ning, Y. and Wang, X. (2004) 'Accuracy analysis and improvement for direct laser sintering', *Innovation in Manufacturing Systems and Technology (IMST)*, 119260.

Thijs, L., Verhaeghe, F., Craeghs, T., Humbeeck, J. Van and Kruth, J. P. (2010) 'A study of the microstructural evolution during selective laser melting of Ti-6Al-4V', *Acta Materialia*, 58(9), pp. 3303–3312. Available at: http://dx.doi.org/10.1016/j.actamat.2010.02.004.

Thompson, M. K., Moroni, G., Vaneker, T., Fadel, G., Campbell, R. I., Gibson, I., Bernard, A., Schulz, J., Graf, P., Ahuja, B. and Martina, F. (2016) 'Design for additive manufacturing: Trends, opportunities, considerations, and constraints', *CIRP Annals*, 65(2), pp. 737–760. Available at: https://linkinghub.elsevier.com/retrieve/pii/S0007850616301913.

Töppel, T., Müller, B., Hoeren, K. P. J. and Witt, G. (2016) 'Eigenspannungen und verzug bei der additiven fertigung durch laserstrahlschmelzen', *Schweissen und Schneiden*, 68(4), pp. 176–186.

Toth-Tascau, M. and Stoia, D. I. (2011) 'Analysis of dimensional accuracy of two models of customized hip prostheses made of Polyamide powder by Selective Laser Melting Technology', *Optoelectronics and Advanced Materials - Rapid Communications*, 5(12), pp. 1356–1363.

Verhaeghe, F., Craeghs, T., Heulens, J. and Pandelaers, L. (2009) 'A pragmatic model for selective laser melting with evaporation', *Acta Materialia*, 57(20), pp. 6006–6012. Available at: http://dx.doi.org/10.1016/j.actamat.2009.08.027.

Vrancken, B. (2016) *Study of residual stresses in selective laser melting*. PhD Thesis, Katholieke Universiteit Leuven.

Vrancken, B., Cain, V., Knutsen, R. and Van Humbeeck, J. (2014) 'Residual stress via the contour method in compact tension specimens produced via selective laser melting', *Scripta Materialia*, 87, pp. 29–32.

Vrancken, B., Thijs, L., Kruth, J. and Van Humbeeck, J. (2012) 'Heat treatment of Ti6Al4V produced by selective laser melting : Microstructure and mechanical properties', *Journal of Alloy and Compounds*, 541, pp. 177–185. Available at: http://linkinghub.elsevier.com/retrieve/pii/S0925838812011826.

Vrancken, B., Wauthle, R., Kruth, J. and Van Humbeeck, J. (2013) 'Study of the influence of material properties on residual stress in selective laser melting', in *Solid Freeform Fabrication Symposium*. Austin, pp. 393–407.

Wang, L., Jiang, X., Zhu, Y., Ding, Z., Zhu, X., Sun, J. and Yan, B. (2018) 'Investigation of performance and residual stress generation of AlSi10Mg processed by selective laser melting', *Advances in Materials Science and Engineering*, 2018, pp. 1–12.

Wang, Z., Palmer, T. A. and Beese, A. M. (2016) 'Effect of processing parameters on microstructure and tensile properties of austenitic stainless steel 304L made by directed energy deposition additive manufacturing', *Acta Materialia*, 110, pp. 226–235. Available at: https://linkinghub.elsevier.com/retrieve/pii/S1359645416301744.

Wohlers, T. (2018) *Wohlers Report 2018*.

Wohlers, T. and Gornet, T. (2014) 'History of additive manufacaturing', in *Wohlers Report 2014*, pp. 1–34.

Wong, K. V. and Hernandez, A. (2012) 'A review of additive manufacturing', *ISRN Mechanical Engineering*, 2012, pp. 1–10.

Wu, A. S., Brown, D. W., Kumar, M., Gallegos, G. F. and King, W. E. (2014) 'An experimental investigation into additive manufacturing-induced residual stresses in 316L stainless steel', *Metallurgical and Materials Transactions A: Physical Metallurgy and Materials Science*, 45(13), pp. 6260–6270.

Yadollahi, A., Shamsaei, N., Thompson, S. M., Elwany, A. and Bian, L. (2017) 'Effects of building orientation and heat treatment on fatigue behavior of selective laser melted 17-4 PH stainless steel', *International Journal of Fatigue*, 94, pp. 218–235.

Yadroitsava, I. and Yadroitsev, I. (2015) 'Residual stress in metal specimens produced by direct metal laser sintering', in *Solid Freeform Fabrication Symposium*. Austin, pp. 614–625.

Yadroitsev, I. and Smurov, I. (2011) 'Surface morphology in selective laser melting of metal powders', *Physics Procedia*, 12(PART 1), pp. 264–270.

Yadroitsev, I., Yadroitsava, I., Bertrand, P. and Smurov, I. (2012) 'Factor analysis of selective laser melting process parameters and geometrical characteristics of synthesized single tracks', *Rapid Prototyping Journal*, 18(3), pp. 201–208.

Yakout, M., Elbestawi, M. A. and Veldhuis, S. C. (2018) 'On the characterization of stainless steel 316L parts produced by selective laser melting', *International Journal of Advanced Manufacturing Technology*, 95, pp. 1953–1974.

Yan, J. J., Zheng, D. L., Li, H. X., Jia, X., Sun, J. F., Li, Y. L., Qian, M. and Yan, M. (2017) 'Selective laser melting of H13: microstructure and residual stress', *Journal of Materials Science*, pp. 12476–12485. Available at: http://link.springer.com/10.1007/s10853-017-1380-3.

Yang, L., Smith, L., Gothekar, A. and Chen, X. (2010) *Measure strain distribution using digital image correlation (DIC) for tensile tests*. Rochester.

Yang, Y., Lu, J., Luo, Z.-Y. and Wang, D. (2012) 'Accuracy and density optimization in directly fabricating customized orthodontic production by selective laser melting', *Rapid Prototyping Journal*, 18(6), pp. 482–489.

Yasa, E., Deckers, J., Craeghs, T., Badrossamay, M. and Kruth, J.-P. (2009) 'Investigation on occurrence of elevated edges in selective laser melting', in *Solid Freeform Fabrication Symposium*. Austin.

Yasa, E., Kempen, K. and Kruth, J. (2010) 'Microstructure and mechanical properties of Maraging Steel 300 after selective laser melting', in *Solid Freeform Fabrication Symposium*. Austin, pp. 383–396.

Yasa, E. and Kruth, J. (2011) 'Application of laser re-melting on selective laser melting parts', *Advances in Production Engineering & Management*, 6(4), pp. 259–270.

Yu, J., Lin, X., Ma, L., Wang, J., Fu, X., Chen, J. and Huang, W. (2011) 'Influence of laser deposition patterns on part distortion, interior quality and mechanical properties by laser solid forming (LSF)', *Materials Science and Engineering A*, 528, pp. 1094–1104.

Yusuf, S., Chen, Y., Boardman, R., Yang, S. and Gao, N. (2017) 'Investigation on porosity and microhardness of 316L stainless steel fabricated by selective laser melting', *Metals*, 7(2), p. 64. Available at: http://www.mdpi.com/2075-4701/7/2/64.

Zaeh, M. F. and Branner, G. (2010) 'Investigations on residual stresses and deformations in selective laser melting', *Production Engineering*, 4(1), pp. 35–45. Available at: http://link.springer.com/10.1007/s11740-009-0192-y.

Zeng, K., Pal, D. and Stucker, B. (2012) 'A review of thermal analysis methods in laser sintering and selective laser melting', in *Solid Freeform Fabrication Symposium*. Austin, pp. 796–814.

Zhang, B., Dembinski, L. and Coddet, C. (2013) 'The study of the laser parameters and environment variables effect on mechanical properties of high compact parts elaborated by selective laser melting 316L powder', *Materials Science and Engineering A*, 584, pp. 21–31. Available at: http://dx.doi.org/10.1016/j.msea.2013.06.055.

Zhang, W., Shi, Y., Liu, B., Xu, L. and Jiang, W. (2009) 'Consecutive sub-sector scan mode with adjustable scan lengths for selective laser melting technology', *The International Journal of Advanced Manufacturing Technology*, 41(7-8), pp. 706–713. Available at: http://link.springer.com/10.1007/s00170-008-1527-0.

Zhu, J. G., Xie, H. M., Li, Y. J., Hu, Z. X., Luo, Q. and Gu, C. Z. (2014) 'Interfacial residual stress analysis of thermal spray coatings by miniature ring-core cutting combined with DIC method', *Experimental Mechanics*, 54, pp. 127–136.

Ziółkowski, G., Chlebus, E., Szymczyk, P. and Kurzac, J. (2014) 'Application of X-ray CT method for discontinuity and porosity detection in 316L stainless steel parts produced with SLM technology', *Archives of Civil and Mechanical Engineering*, 14(4), pp. 608–614.

ADDENDUM A: POWDER MATERIAL DATA

A1: CL50WS material data – Concept Laser

.material data

CONCEPTLASER
hofmann innovation group

CL 50WS Hot-work steel

Hot-work steel 1.2709 (powder)

CL 50WS is a powder material for the production of components for tool inserts with conformal cooling. These tool inserts can be used for series injection moulding as well as for die-casting. Furthermore the material can also be used for functional components.

26
Fe
55,847

Source: Werkzeugbau Siegfried Hofmann GmbH

CHEMICAL COMPOSITION

Component	Indicative value (%)
Fe	Balance
C	≤ 0,03
Si	≤ 0,10
Mn	≤ 0,15
P	≤ 0,010
S	≤ 0,010
Cr	≤ 0,25
Mo	4,50 - 5,20
Ni	17,0 - 19,0
Ti	0,80 - 1,20
Co	8,50 - 10,0

www.concept-laser.de

160

A2: FE-339 material data – PRAXAIR

Certificate of Analysis & Certificate of Conformity

PRAXAIR
SURFACE TECHNOLOGIES

1555 Main Street, Indianapolis, IN 46224

Product Name: FE-339	**Customer:** WEARTECH		**Ship Date:** 25.10.16
Praxair Spec: 034040-BK	**Shipping Order #:** .		**Printed Date:**
Item Number 034040-10	**Customer PO #:** Sample		
Lot Number: 9	**Quantity:** 20	**UM:** LBS	

All elements measured in weight percent unless otherwise specified. Sampling Method per ASTM B215.

Chemistry	Test Method	Test Lab	Min	Max	Result	OK
Aluminum	XRF	Praxair		0.15	0.10	Yes
Carbon (total)	Leco	Praxair		0.030	0.004	Yes
Cobalt	XRF	Praxair	8.50	10.00	9.08	Yes
Chromium	XRF	Praxair		0.3	0.2	Yes
Iron	By Diff	Praxair		Balance	Balance	Yes
Manganese	XRF	Praxair		0.15	0.03	Yes
Molybdenum	XRF	Praxair	4.50	5.20	4.78	Yes
Nitrogen	Leco	Praxair		Report	0.0	Yes
Nickel	XRF	Praxair	17.0	19.0	18	Yes
Oxygen	Leco	Praxair		Report	0.0	Yes
Phosphorus	XRF	Praxair		0.010	<0.005	Yes
Sulfur		Praxair		0.010	0.003	Yes
Silicon	XRF	Praxair		0.10	0.04	Yes
Titanium	XRF	Praxair	0.80	1.20	1	Yes
Total All Other	Calculation	Praxair		0.50	0.00	Yes

Microtrac	Test Method	Test Lab	Min	Max	Result	OK
-5.5	Microtrac	Praxair		1	0.5	Yes
d50	Microtrac	Praxair		Report	24.4	Yes

Sieve per ASTM B214	Test Method	Test Lab	Min	Max	Result	OK
-325		Praxair	98		99.8	Yes

PST: 166772   C-77508

Spec ranges shown above in italics are target or nominal specifications only.

* indicates test is not required for routine acceptance.

Nadcap Accredited

(317) 240-2650
Telefax (317) 240-2225
Toll-Free Telefax 1-800-234-6738 U.S.A

AS9100 Registered
Quality System

Materials Testing Laboratory

This report is confidential and proprietary, and intended for the recipient of the product. If you receive in error you are prohibited from disclosing, copying, distributing, or using any of the information. The test report shall not be reproduced except in full, without the written approval of the laboratory. Please contact our office for instructions. The recording of false, fictitious, fraudulent statements or entries on the certificate may be punished as a felony under federal law. All elements measured in percent unless otherwise specified.

Estimated uncertainty of measurement is available upon request.   1   of   2

ADDENDUM B: NEUTRON DIFFRACTRION STRESS DATA

B1: Stress data for influence of part thickness on residual stresses (reported in 5.2)

B1-1: 9 mm thick specimen

NORMAL COMPONENT										
	Width [mm]	1.60	2.39	3.17	3.96	6.32	8.68	11.04	11.83	12.61	13.40
Depth [mm]	1.60	-47	-40	60	70	62	164	53	29	-38	-35
	2.47	-106	-72	-66	38	91	117	24	-43	-92	-42
	3.33	-58	-78	-27	-17	96	141	-8	-16	-87	-18
	4.20	-86	-60	-13	35	68	119	28	-46	-134	41
	5.07	-46	-62	3	66	92	95	14	-18	-89	-22
	5.93	-37	-38	39	25	83	74	7	6	-45	-16
	6.80	-26	-14	12	29	31	54	-8	-28	-26	-31
					ERROR						
	Width [mm]	1.60	2.39	3.17	3.96	6.32	8.68	11.04	11.83	12.61	13.40
Depth [mm]	1.60	16	17	17	18	19	20	17	16	15	15
	2.47	16	15	16	17	17	17	16	15	15	15
	3.33	15	15	16	16	16	17	17	15	15	15
	4.20	15	16	15	16	15	16	16	15	15	29
	5.07	15	16	15	15	15	15	15	15	15	19
	5.93	14	15	14	15	14	15	14	15	14	14
	6.80	15	15	15	15	15	14	14	14	14	14
LONGITUDINAL COMPONENT										
	Width [mm]	1.60	2.39	3.17	3.96	6.32	8.68	11.04	11.83	12.61	13.40
Depth [mm]	1.60	10	4	89	53	9	61	-36	-41	-39	-30
	2.47	-37	-51	-79	-51	10	-4	-64	-102	-100	-89
	3.33	26	-40	-37	-87	-27	32	-69	9	-14	4
	4.20	-21	2	-5	-22	6	55	24	-14	-114	198
	5.07	34	-5	38	27	41	39	-27	-11	-10	44
	5.93	33	19	78	-13	108	89	-9	39	31	74
	6.80	49	39	27	57	28	83	6	-33	18	23
					ERROR						

	Width [mm]	1.60	2.39	3.17	3.96	6.32	8.68	11.04	11.83	12.61	13.40
Depth [mm]	1.60	25	26	25	26	26	24	25	24	23	22
	2.47	26	24	24	24	23	24	25	23	23	23
	3.33	24	23	26	25	24	25	26	24	24	23
	4.20	26	26	25	25	23	25	25	25	26	67
	5.07	24	26	25	24	24	26	24	24	24	41
	5.93	23	24	24	23	24	25	23	24	22	24
	6.80	25	26	25	25	26	24	23	23	23	22

TRANSVERSE COMPONENT

	Width [mm]	1.60	2.39	3.17	3.96	6.32	8.68	11.04	11.83	12.61	13.40
Depth [mm]	1.60	-30	18	99	66	23	81	13	14	0	-15
	2.47	-76	1	-72	-22	-54	-22	-70	-97	-84	-58
	3.33	-23	-17	-32	-96	-68	-36	-110	-89	-87	-42
	4.20	-51	-3	-30	-25	-72	-29	-87	-98	-120	41
	5.07	-9	-42	17	25	-13	-19	-59	-64	-69	-21
	5.93	0	44	99	57	105	82	24	49	10	15
	6.80	89	137	163	174	163	138	108	98	109	82
	Error										
	Width [mm]	1.60	2.39	3.17	3.96	6.32	8.68	11.04	11.83	12.61	13.40
Depth [mm]	1.60	16	16	17	17	16	16	16	15	15	15
	2.47	17	16	17	17	16	16	16	15	15	15
	3.33	15	16	19	16	15	16	16	15	15	15
	4.20	16	18	17	17	15	15	15	15	15	29
	5.07	16	17	16	16	15	15	15	15	15	20
	5.93	15	15	16	16	15	15	15	15	14	15
	6.80	16	16	15	16	15	15	15	14	14	14

B1-2: 12 mm thick specimen

Normal											
	Width [mm]	1.60	2.39	3.17	3.96	6.32	8.68	11.04	11.83	12.61	13.40
Depth [mm]	1.60	-73	-39	-24	3	-39	144	34	39	34	-2
	2.38	-46	-48	-15	28	60	118	33	-43	-56	18
	3.17	-39	-71	-55	-35	49	147	44	-38	-61	68
	3.95	-92	-82	-53	-31	72	109	-45	-95	-44	114
	6.30	-85	-37	27	45	71	63	-3	-23	-23	21
	8.65	-66	8	53	49	46	37	-2	-8	-15	3
	11.00	-24	14	11	28	19	4	-28	-62	-58	-52
								Average	0		
	Error										
	Width [mm]	1.60	2.39	3.17	3.96	6.32	8.68	11.04	11.83	12.61	13.40
Depth [mm]	1.60	18	19	20	20	22	21	21	19	18	17
	2.38	18	18	17	19	21	23	20	18	17	17
	3.17	17	18	18	18	21	22	18	18	17	17
	3.95	16	17	16	17	17	19	18	17	16	16
	6.30	16	16	16	16	16	16	16	15	15	15
	8.65	16	15	16	15	16	16	16	15	15	15
	11.00	16	16	16	16	16	16	15	15	15	15
Longitudinal											
	Width [mm]	1.60	2.39	3.17	3.96	6.32	8.68	11.04	11.83	12.61	13.40
Depth [mm]	1.60	-37	4	-8	-5	-51	114	1	41	19	-42
	2.38	0	-40	-76	14	-30	26	-6	-79	-81	-56
	3.17	-30	-50	-55	-53	-34	25	58	-37	-102	-19
	3.95	-51	-72	-47	-46	-58	-51	-26	-76	-8	61
	6.30	-21	-6	37	51	48	-2	-23	-11	39	19
	8.65	-19	39	72	106	58	64	77	75	41	48
	11.00	77	77	23	105	40	44	11	-50	-32	-24
								Average	0		
	Error										
	Width [mm]	1.60	2.39	3.17	3.96	6.32	8.68	11.04	11.83	12.61	13.40
Depth [mm]	1.60	24	26	24	26	25	25	24	23	22	22
	2.38	24	25	24	25	25	25	24	23	22	23
	3.17	24	23	23	24	25	25	25	23	23	23

164

	3.95	24	24	23	24	23	25	24	23	23	24
	6.30	24	23	25	25	24	23	25	23	23	22
	8.65	26	24	23	24	23	24	25	24	22	24
	11.00	24	24	24	25	24	25	23	23	23	22
Transverse											
	Width [mm]	1.60	2.39	3.17	3.96	6.32	8.68	11.04	11.83	12.61	13.40
Depth [mm]	1.60	-92	-18	23	20	-7	205	115	125	93	-17
	2.38	-84	-59	-35	-34	-39	90	38	-27	-41	-75
	3.17	-96	-64	-76	-66	-100	9	-13	-6	-52	-62
	3.95	-148	-86	-58	-89	-150	-134	-91	-58	-36	-40
	6.30	-122	-22	10	57	76	-54	-46	-18	6	-76
	8.65	-64	54	125	130	133	47	15	5	-6	-54
	11.00	47	146	174	212	199	122	84	38	43	-25
									Average	0	
Error											
	Width [mm]	1.60	2.39	3.17	3.96	6.32	8.68	11.04	11.83	12.61	13.40
Depth [mm]	1.60	18	19	19	19	20	18	18	17	17	17
	2.38	17	19	19	20	20	18	18	17	17	17
	3.17	17	18	19	19	19	19	19	18	17	16
	3.95	17	18	19	20	20	20	19	18	18	17
	6.30	18	17	18	19	17	18	19	18	17	17
	8.65	17	17	18	18	18	18	18	17	17	16
	11.00	17	18	17	18	17	18	18	18	18	16

165

B1-3: 15 mm thick specimen

Normal										
	Width [mm]	1.60	2.39	3.17	3.96	6.32	8.68	11.04	11.83	12.61	13.40
Depth [mm]	1.60	-46	-53	-42	8	1	56	34	20	53	95
	2.40	-67	-56	-103	-6	-6	66	-16	-10	30	133
	3.20	-79	-95	-51	-25	-25	20	-50	-62	-15	147
	5.90	-57	-93	-180	-93	-70	-63	-78	-29	36	268
	8.60	-29	-148	-118	-59	41	6	-39	-4	63	201
	11.30	-9	56	46	28	67	55	56	33	57	117
	12.10	-13	25	9	42	31	29	1	35	28	31
	12.90	-80	-39	-45	-20	-25	-57	-42	-36	-24	-52
										Average	-4
	Error										
	Width [mm]	1.60	2.39	3.17	3.96	6.32	8.68	11.04	11.83	12.61	13.40
Depth [mm]	1.60	20	21	21	20	22	21	22	21	20	20
	2.40	20	21	20	19	23	21	21	21	21	19
	3.20	19	22	20	22	22	22	21	20	19	18
	5.90	19	20	23	19	22	23	20	18	18	17
	8.60	17	21	21	17	19	19	18	17	17	16
	11.30	16	21	18	16	17	17	17	22	16	15
	12.10	16	16	16	17	17	17	16	20	16	15
	12.90	16	17	17	17	17	17	16	21	16	16
Longitudinal											
	Width [mm]	1.60	2.39	3.17	3.96	6.32	8.68	11.04	11.83	12.61	13.40
Depth [mm]	1.60	-55	-37	-14	73	14	107	35	36	50	40
	2.40	-58	-82	-51	-4	8	5	27	2	-13	0
	3.20	-107	-98	-63	-33	-94	1	-54	-75	-67	-32
	5.90	-125	-124	-196	-47	-102	-76	-62	-50	-43	36
	8.60	-47	-181	-91	-8	13	-35	12	22	9	18
	11.30	59	152	68	94	68	93	103	94	102	99
	12.10	57	53	75	111	74	77	54	82	83	26
	12.90	-61	-11	-17	69	18	-36	13	29	14	-34
										Average	0
	Error										
	Width [mm]	1.60	2.39	3.17	3.96	6.32	8.68	11.04	11.83	12.61	13.40

Depth [mm]	1.60	18	18	18	19	22	21	20	18	19	17
	2.40	18	18	18	19	23	22	19	20	19	17
	3.20	18	19	18	20	21	21	20	19	19	17
	5.90	20	31	42	19	22	22	19	18	18	17
	8.60	18	35	35	19	22	21	19	18	18	17
	11.30	18	38	20	19	22	20	18	21	17	16
	12.10	19	19	20	21	23	22	19	21	18	17
	12.90	20	22	22	23	26	22	21	22	19	18
Transverse											
	Width [mm]	1.60	2.39	3.17	3.96	6.32	8.68	11.04	11.83	12.61	13.40
Depth [mm]	1.60	-58	22	60	112	112	222	170	127	119	57
	2.40	-87	-42	-19	27	21	107	62	64	23	4
	3.20	-114	-36	17	23	-68	41	-5	1	1	1
	5.90	-168	-43	-62	7	-151	-103	-21	5	33	30
	8.60	-79	-84	-30	-3	-24	-74	5	62	32	9
	11.30	-21	83	111	74	75	48	62	32	77	36
	12.10	-14	64	67	123	129	83	48	51	65	-17
	12.90	-35	77	124	172	195	111	106	67	55	-37
										Average	29
	Error										
	Width [mm]	1.60	2.39	3.17	3.96	6.32	8.68	11.04	11.83	12.61	13.40
Depth [mm]	1.60	18	18	18	17	18	18	18	17	24	17
	2.40	17	17	18	18	19	18	18	19	26	18
	3.20	17	18	17	18	18	19	19	18	18	17
	5.90	24	20	23	19	19	21	20	18	18	18
	8.60	16	21	22	19	19	20	19	18	17	16
	11.30	16	22	24	18	17	18	18	32	17	16
	12.10	16	17	17	19	18	18	18	27	18	16
	12.90	16	17	18	17	18	18	18	28	17	17

B1-4: 18 mm thick specimen

Normal											
	Width [mm]	1.60	2.39	3.17	3.96	6.32	8.68	11.04	11.83	12.61	13.40
Depth [mm]	1.60	29	22	45	51	35	58	105	119	86	58
	2.38	9	-54	2	28	2	32	19	22	17	2
	3.17	45	-29	-1	-60	-39	34	22	-1	-9	71
	3.95	26	26	-32	6	6	30	-6	-28	-55	178
	6.30	74	-40	26	-35	-47	-66	-24	-134	48	342
	8.65	129	7	-39	-82	-110	-81	-58	-40	54	327
	11.00	17	11	-31	-54	-32	-43	-18	-41	62	257
	13.35	1	5	11	35	12	28	44	21	17	102
	14.13	7	27	78	65	52	71	34	61	12	111
	14.92	13	48	73	108	56	18	25	5	8	58
	15.70	11	38	87	93	63	0	-17	-26	-1	-33
										Average	10
	Error										
	Width [mm]	1.60	2.39	3.17	3.96	6.32	8.68	11.04	11.83	12.61	13.40
Depth [mm]	1.60	23	24	23	21	21	24	21	39	22	21
	2.38	22	22	22	24	22	22	20	21	21	21
	3.17	23	24	25	22	22	22	23	21	23	22
	3.95	22	22	23	21	23	21	23	58	22	21
	6.30	21	22	21	21	21	22	22	44	20	20
	8.65	19	18	20	20	23	23	20	32	19	18
	11.00	18	18	18	18	20	21	18	28	18	17
	13.35	17	17	17	18	18	18	18	18	17	17
	14.13	17	18	18	17	17	18	17	17	17	16
	14.92	17	17	16	17	17	17	17	17	17	16
	15.70	17	16	17	16	16	17	17	16	16	16
Longitudinal											
	Width [mm]	1.60	2.39	3.17	3.96	6.32	8.68	11.04	11.83	12.61	13.40
Depth [mm]	1.60	85	56	58	35	40	80	121	55	46	40
	2.38	33	-15	-4	18	-26	81	-32	2	12	-6
	3.17	-2	-71	-2	-76	-54	28	41	-47	-7	-29
	3.95	-80	33	-45	-55	-69	1	-33	-26	-92	45

		1.60	2.39	3.17	3.96	6.32	8.68	11.04	11.83	12.61	13.40
	6.30	0	-98	-11	-77	-100	-90	-64	-77	-18	122
	8.65	8	-32	-46	-85	-108	-23	-73	-102	-21	69
	11.00	-41	9	-3	-76	-68	-49	-21	-31	35	68
	13.35	20	10	0	11	-61	48	81	7	73	8
	14.13	25	22	85	80	52	93	-7	90	42	84
	14.92	63	92	107	129	95	76	24	21	49	34
	15.70	65	77	125	119	140	77	-35	-67	1	-28
										Average	10
Error											
	Width [mm]	1.60	2.39	3.17	3.96	6.32	8.68	11.04	11.83	12.61	13.40
Depth [mm]	1.60	21	21	20	21	20	20	19	23	18	16
	2.38	19	19	20	20	18	18	15	18	18	16
	3.17	19	18	22	20	21	18	21	19	18	20
	3.95	20	20	20	19	18	20	20	29	20	19
	6.30	18	20	19	21	19	21	20	26	17	19
	8.65	19	18	19	20	20	20	20	20	19	18
	11.00	19	19	18	19	19	22	18	21	19	17
	13.35	19	17	18	20	18	20	20	19	20	20
	14.13	20	21	21	18	18	18	19	19	17	19
	14.92	18	20	17	17	21	18	17	18	20	18
	15.70	18	17	19	18	17	19	16	16	14	16
Transverse											
	Width [mm]	1.60	2.39	3.17	3.96	6.32	8.68	11.04	11.83	12.61	13.40
Depth [mm]	1.60	-6	56	92	116	189	257	247	149	135	4
	2.38	-57	-15	25	47	49	172	106	104	37	-65
	3.17	-84	-42	-5	-38	-40	93	48	-12	-33	-94
	3.95	-122	-15	-46	8	-57	11	-14	-28	-72	-61
	6.30	-153	-85	7	-45	-115	-105	-26	-94	-43	-23
	8.65	-106	-69	-28	-78	-142	-70	-61	-62	-66	-65
	11.00	-160	-31	-26	-65	-95	-96	-22	-59	-26	-76
	13.35	-82	-2	-11	-9	-10	-28	36	-19	-23	-99
	14.13	-45	16	79	37	92	64	14	51	-3	-66
	14.92	-32	114	133	199	211	114	47	20	12	-41
	15.70	66	144	245	253	294	188	95	49	48	-50
										Average	10
Error											
	Width [mm]	1.60	2.39	3.17	3.96	6.32	8.68	11.04	11.83	12.61	13.40

Depth [mm]	1.60	18	19	18	18	17	17	17	21	25	17
	2.38	18	17	18	19	19	17	17	18	17	16
	3.17	18	18	18	18	18	18	19	18	18	17
	3.95	17	17	18	18	20	18	19	28	19	17
	6.30	17	17	18	18	20	20	19	24	17	18
	8.65	17	16	18	19	22	20	18	20	17	16
	11.00	16	18	18	18	21	21	19	19	17	16
	13.35	17	17	18	18	18	18	18	18	17	16
	14.13	16	17	18	17	18	17	17	18	16	16
	14.92	16	16	17	17	17	17	16	17	17	16
	15.70	16	16	17	16	16	17	17	16	16	16

B1-5: 21 mm thick specimen

Normal						
	Width [mm]	1.60	3.96	6.32	8.68	11.04	13.40
Depth [mm]	1.60	-19	43	23	102	37	66
	3.75	-51	-69	-65	30	-23	103
	5.90	68	-109	-78	-95	22	253
	8.05	96	-95	-105	-101	-50	344
	10.20	50	-64	-104	-71	-31	304
	12.35	-34	-111	-36	-52	-24	210
	14.50	-36	-43	-9	30	20	71
	16.65	-68	11	62	-22	34	-12
	18.80	-87	-18	23	-65	-92	-165
	Error						
	Width [mm]	1.60	3.96	6.32	8.68	11.04	13.40
Depth [mm]	1.60	22	22	21	22	21	20
	3.75	23	22	21	22	22	21
	5.90	22	22	22	22	22	21
	8.05	20	22	22	24	22	20
	10.20	19	21	22	22	20	19
	12.35	18	19	20	20	19	18
	14.50	17	18	19	19	18	17
	16.65	17	17	17	17	17	17
	18.80	17	17	17	17	17	16
Longitudinal						
	Width [mm]	1.60	3.96	6.32	8.68	11.04	13.40
Depth [mm]	1.60	40	82	93	132	111	-1
	3.75	-66	-53	-22	54	10	7
	5.90	-32	-99	23	-21	26	56
	8.05	-58	-33	-70	-58	-37	28
	10.20	-62	-78	-56	-46	-68	-37
	12.35	-106	-70	-37	-47	-18	-21
	14.50	-34	4	9	43	7	-88
	16.65	17	83	123	35	84	7
	18.80	25	137	146	76	-29	-105

	Error					
	Width [mm]	1.60	3.96	6.32	8.68	11.04	13.40
Depth [mm]	1.60	25	26	25	22	23	21
	3.75	23	24	23	24	24	24
	5.90	24	25	25	23	26	25
	8.05	23	24	24	25	23	23
	10.20	23	23	23	22	23	24
	12.35	23	25	24	24	22	25
	14.50	22	24	23	24	24	23
	16.65	22	23	23	23	24	23
	18.80	25	24	25	24	23	21
Transverse							
	Width [mm]	1.60	3.96	6.32	8.68	11.04	13.40
Depth [mm]	1.60	-94	158	241	394	273	-67
	3.75	-245	43	29	153	86	-161
	5.90	-235	-10	64	47	77	-215
	8.05	-299	55	45	17	72	-186
	10.20	-313	34	36	60	77	-259
	12.35	-343	18	41	46	41	-323
	14.50	-231	45	53	91	94	-334
	16.65	-129	126	197	61	81	-244
	18.80	17	291	394	223	105	-197
	Error						
	Width [mm]	1.60	3.96	6.32	8.68	11.04	13.40
Depth [mm]	1.60	18	18	18	18	18	18
	3.75	17	18	18	19	19	18
	5.90	18	18	19	19	19	19
	8.05	17	18	19	20	19	17
	10.20	17	18	20	18	18	18
	12.35	17	18	19	19	18	18
	14.50	17	18	19	20	18	18
	16.65	17	17	17	17	18	17
	18.80	17	17	17	18	18	17

172

B2: Stress data for scan vector length on residual stresses (reported in 5.3.2 and 5.3.5)

B2-1: 3 mm × 3 mm islands

Normal											
	Width [mm]	1.60	2.39	3.17	3.96	6.32	8.68	11.04	11.83	12.61	13.40
Depth [mm]	1.60	58	71	74	22	15	46	-19	0	-45	69
	2.40	63	116	63	-26	50	50	-36	-10	33	89
	3.20	93	117	89	110	2	42	-12	-97	-31	138
	5.90	32	121	7	21	-17	-65	-145	-172	-73	133
	8.59	61	21	52	58	16	-35	-144	-139	-82	124
	11.30	35	31	51	52	50	13	-20	-88	-37	28
	12.10	7	16	57	32	47	13	-26	-44	-36	-3
	12.90	-20	-4	18	0	7	-13	-40	-76	-65	-45
	Error										
	Width [mm]	1.60	2.39	3.17	3.96	6.32	8.68	11.04	11.83	12.61	13.40
Depth [mm]	1.60	21	21	21	21	22	24	21	22	22	20
	2.40	20	20	20	22	23	22	22	20	20	19
	3.20	19	20	22	21	22	23	21	19	20	19
	5.90	18	21	18	19	21	21	20	19	18	17
	8.59	16	17	18	18	20	20	17	17	17	16
	11.30	16	16	16	16	16	17	16	20	15	15
	12.10	16	15	15	16	16	16	16	15	15	15
	12.90	15	15	15	16	16	16	15	15	15	14
Longitudinal											
	Width [mm]	1.60	2.39	3.17	3.96	6.32	8.68	11.04	11.83	12.61	13.40
Depth [mm]	1.60	136	136	176	103	143	195	140	159	126	172
	2.40	55	83	71	-4	70	98	59	62	87	92
	3.20	22	5	-2	18	-54	-30	-7	-48	-18	37
	5.90	-162	-11	-151	-186	-194	-143	-184	-215	-171	-113
	8.59	-136	-139	-99	-149	-162	-162	-186	-160	-155	-86
	11.30	-33	-45	-11	-32	23	14	-13	-35	-33	-44
	12.10	36	29	87	41	89	64	68	23	52	17
	12.90	77	83	84	84	115	127	131	68	105	48

	Error									
	Width [mm]	1.60	2.39	3.17	3.96	6.32	8.68	11.04	11.83	12.61	13.40
Depth [mm]	1.60	17	17	18	18	20	21	18	18	17	16
	2.40	17	16	17	18	21	19	18	17	17	16
	3.20	16	17	18	17	19	20	17	17	17	16
	5.90	16	31	17	18	20	21	18	18	16	15
	8.59	16	16	17	18	19	20	17	17	16	16
	11.30	17	16	17	17	19	21	17	18	16	16
	12.10	16	16	17	18	19	20	17	17	16	15
	12.90	17	16	17	17	19	19	17	17	16	15
Transverse											
	Width [mm]	1.60	2.39	3.17	3.96	6.32	8.68	11.04	11.83	12.61	13.40
Depth [mm]	1.60	-2	22	53	9	65	161	117	94	31	-15
	2.40	-4	59	48	-14	31	98	24	22	28	-41
	3.20	-3	44	29	72	-26	8	-5	-40	-23	-43
	5.90	-62	49	-36	-58	-104	-81	-48	-67	-57	-99
	8.59	-21	-12	19	10	-59	-112	-80	-63	-40	-97
	11.30	-12	12	17	28	51	-29	-30	-11	-11	-101
	12.10	-26	-2	68	71	117	52	31	-21	12	-96
	12.90	-20	11	62	46	146	123	101	29	5	-69
	Error										
	Width [mm]	1.60	2.39	3.17	3.96	6.32	8.68	11.04	11.83	12.61	13.40
Depth [mm]	1.60	16	17	17	17	16	17	16	16	16	16
	2.40	16	16	16	17	17	17	17	16	16	15
	3.20	15	16	18	16	16	18	17	16	15	15
	5.90	16	19	17	17	17	19	19	17	15	15
	8.59	15	15	16	18	17	20	16	16	15	14
	11.30	15	16	17	16	16	16	16	17	15	15
	12.10	15	15	16	17	15	17	16	16	15	15
	12.90	15	15	15	16	14	16	15	16	15	14

174

B2-2: 5 mm × 5 mm islands (single exposure)

Stress											
Normal											
	Width [mm]	1.60	2.39	3.17	3.96	6.32	8.68	11.04	11.83	12.61	13.40
Depth [mm]	1.60	-46	-53	-42	8	1	56	34	20	53	95
	2.40	-67	-56	-103	-6	-6	66	-16	-10	30	133
	3.20	-79	-95	-51	-25	-25	20	-50	-62	-15	147
	5.90	-57	-93	-180	-93	-70	-63	-78	-29	36	268
	8.60	-29	-148	-118	-59	41	6	-39	-4	63	201
	11.30	-9	56	46	28	67	55	56	33	57	117
	12.10	-13	25	9	42	31	29	1	35	28	31
	12.90	-80	-39	-45	-20	-25	-57	-42	-36	-24	-52
	Error										
	Width [mm]	1.60	2.39	3.17	3.96	6.32	8.68	11.04	11.83	12.61	13.40
Depth [mm]	1.60	20	21	21	20	22	21	22	21	20	20
	2.40	20	21	20	19	23	21	21	21	21	19
	3.20	19	22	20	22	22	22	21	20	19	18
	5.90	19	20	23	19	22	23	20	18	18	17
	8.60	17	21	21	17	19	19	18	17	17	16
	11.30	16	21	18	16	17	17	17	22	16	15
	12.10	16	16	16	17	17	17	16	20	16	15
	12.90	16	17	17	17	17	17	16	21	16	16
Longitudinal											
	Width [mm]	1.60	2.39	3.17	3.96	6.32	8.68	11.04	11.83	12.61	13.40
Depth [mm]	1.60	-55	-37	-14	73	14	107	35	36	50	40
	2.40	-58	-82	-51	-4	8	5	27	2	-13	0
	3.20	-107	-98	-63	-33	-94	1	-54	-75	-67	-32
	5.90	-125	-124	-196	-47	-102	-76	-62	-50	-43	36
	8.60	-47	-181	-91	-8	13	-35	12	22	9	18
	11.30	59	152	68	94	68	93	103	94	102	99
	12.10	57	53	75	111	74	77	54	82	83	26
	12.90	-61	-11	-17	69	18	-36	13	29	14	-34

	Error									
	Width [mm]	1.60	2.39	3.17	3.96	6.32	8.68	11.04	11.83	12.61	13.40
Depth [mm]	1.60	18	18	18	19	22	21	20	18	19	17
	2.40	18	18	18	19	23	22	19	20	19	17
	3.20	18	19	18	20	21	21	20	19	19	17
	5.90	20	31	42	19	22	22	19	18	18	17
	8.60	18	35	35	19	22	21	19	18	18	17
	11.30	18	38	20	19	22	20	18	21	17	16
	12.10	19	19	20	21	23	22	19	21	18	17
	12.90	20	22	22	23	26	22	21	22	19	18
Transverse										
	Width [mm]	1.60	2.39	3.17	3.96	6.32	8.68	11.04	11.83	12.61	13.40
Depth [mm]	1.60	-58	22	60	112	112	222	170	127	119	57
	2.40	-87	-42	-19	27	21	107	62	64	23	4
	3.20	-114	-36	17	23	-68	41	-5	1	1	1
	5.90	-168	-43	-62	7	-151	-103	-21	5	33	30
	8.60	-79	-84	-30	-3	-24	-74	5	62	32	9
	11.30	-21	83	111	74	75	48	62	32	77	36
	12.10	-14	64	67	123	129	83	48	51	65	-17
	12.90	-35	77	124	172	195	111	106	67	55	-37
	Error									
	Width [mm]	1.60	2.39	3.17	3.96	6.32	8.68	11.04	11.83	12.61	13.40
Depth [mm]	1.60	18	18	18	17	18	18	18	17	24	17
	2.40	17	17	18	18	19	18	18	19	26	18
	3.20	17	18	17	18	18	19	19	18	18	17
	5.90	24	20	23	19	19	21	20	18	18	18
	8.60	16	21	22	19	19	20	19	18	17	16
	11.30	16	22	24	18	17	18	18	32	17	16
	12.10	16	17	17	19	18	18	18	27	18	16
	12.90	16	17	18	17	18	18	18	28	17	17

176

B2-3: 7 mm × 7 mm islands

Stress											
Normal											
	Width [mm]	1.60	2.39	3.17	3.96	6.32	8.68	11.04	11.83	12.61	13.40
Depth [mm]	1.60	-54	-84	-4	11	-73	1	10	86	4	85
	2.40	-62	-70	-92	-60	48	-44	-53	-58	-28	77
	3.20	3	-137	-35	-43	-43	11	28	-15	-5	125
	5.90	-75	-130	-72	-84	-60	-30	-52	-61	25	280
	8.60	-27	-101	-96	-20	3	-6	-70	-59	52	243
	11.30	-8	-3	33	75	116	66	31	28	46	148
	12.10	-6	7	50	58	73	87	56	36	13	92
	12.90	-22	-14	6	-4	15	62	53	35	-9	-24
	Error										
	Width [mm]	1.60	2.39	3.17	3.96	6.32	8.68	11.04	11.83	12.61	13.40
Depth [mm]	1.60	20	20	22	21	24	21	22	20	20	19
	2.40	20	23	20	22	21	22	21	19	20	18
	3.20	21	20	20	20	22	19	22	19	18	17
	5.90	28	18	19	22	20	21	21	18	17	16
	8.60	16	16	17	20	20	18	17	16	16	16
	11.30	16	16	16	17	17	17	17	16	16	15
	12.10	16	16	16	16	17	18	16	16	16	15
	12.90	16	16	17	17	18	17	17	16	16	16
Longitudinal											
	Width [mm]	1.60	2.39	3.17	3.96	6.32	8.68	11.04	11.83	12.61	13.40
Depth [mm]	1.60	-44	-72	-21	16	-69	54	13	67	17	52
	2.40	-116	-61	-93	-38	-9	-84	-108	-90	-45	3
	3.20	-43	-155	-48	-55	-134	-16	-65	-56	-35	-2
	5.90	-105	-166	-124	-102	-165	-109	-132	-91	-30	47
	8.60	-58	-93	-77	-4	-78	-63	-101	-69	-28	75
	11.30	44	69	93	113	131	100	33	80	120	143
	12.10	72	88	110	126	120	138	111	93	100	128
	12.90	27	64	61	50	44	144	119	95	58	3

	Error										
	Width [mm]	1.60	2.39	3.17	3.96	6.32	8.68	11.04	11.83	12.61	13.40
Depth [mm]	1.60	18	18	19	19	22	21	20	18	18	18
	2.40	18	19	19	20	24	23	19	19	18	17
	3.20	19	18	20	20	23	21	22	18	18	16
	5.90	21	18	19	22	22	22	22	18	18	17
	8.60	18	17	18	22	22	21	19	18	18	16
	11.30	18	19	19	21	22	20	19	19	18	16
	12.10	18	20	21	20	24	22	20	18	18	18
	12.90	20	20	26	25	28	24	22	21	19	19
Transverse											
	Width [mm]	1.60	2.39	3.17	3.96	6.32	8.68	11.04	11.83	12.61	13.40
Depth [mm]	1.60	-38	0	49	57	56	173	108	156	49	75
	2.40	-104	-14	-49	-40	36	-33	-38	-43	13	8
	3.20	-49	-84	-9	-63	-99	-6	55	-15	-10	-15
	5.90	-78	-73	-14	-53	-165	-128	-1	-28	29	61
	8.60	-68	-44	-54	2	-124	-147	-129	-91	46	40
	11.30	-29	49	46	74	93	40	16	-2	61	49
	12.10	15	59	93	108	172	175	68	52	36	37
	12.90	54	102	153	152	198	250	232	193	50	-29
	Error										
	Width [mm]	1.60	2.39	3.17	3.96	6.32	8.68	11.04	11.83	12.61	13.40
Depth [mm]	1.60	17	18	18	18	18	17	26	17	18	22
	2.40	17	18	18	19	18	30	19	18	17	17
	3.20	17	17	18	18	18	17	28	18	17	17
	5.90	27	18	18	33	19	21	29	17	17	17
	8.60	16	17	18	31	20	19	19	17	17	16
	11.30	16	18	18	18	18	18	19	18	16	16
	12.10	17	17	17	18	18	28	18	17	17	17
	12.90	17	17	19	18	18	18	18	18	17	17

B2-4: 5 mm × 5 mm islands (double exposure)

Stress											
Normal											
	Width [mm]	1.60	2.39	3.17	3.96	6.32	8.68	11.04	11.83	12.61	13.40
Depth [mm]	1.60	-12	32	25	52	69	79	28	43	76	54
	2.40	-26	2	-51	-22	74	61	-36	3	80	122
	3.20	-57	-42	-24	-72	1	38	-62	5	84	137
	5.90	-50	-57	-126	-127	-76	-47	-96	-25	80	198
	8.60	-63	-45	-52	-81	-7	0	-107	-15	95	159
	11.30	-15	20	-2	0	19	8	-43	24	67	26
	12.10	9	7	-15	-5	17	7	-39	-18	34	-38
	12.90	-39	-13	-10	8	1	-17	-71	-52	-12	-98
	Error										
	Width [mm]	1.60	2.39	3.17	3.96	6.32	8.68	11.04	11.83	12.61	13.40
Depth [mm]	1.60	16	16	17	16	18	16	17	16	15	15
	2.40	15	17	19	17	19	15	16	15	15	14
	3.20	14	15	17	17	18	17	16	16	14	14
	5.90	13	14	15	15	16	17	15	14	13	13
	8.60	13	14	14	15	15	15	14	13	13	12
	11.30	15	16	13	18	18	13	13	13	12	12
	12.10	14	15	13	18	22	13	13	13	13	12
	12.90	17	15	13	18	14	13	13	13	13	13
Longitudinal											
	Width [mm]	1.60	2.39	3.17	3.96	6.32	8.68	11.04	11.83	12.61	13.40
Depth [mm]	1.60	61	85	25	24	132	147	94	101	115	26
	2.40	-3	-28	-62	-68	29	56	-59	-10	36	43
	3.20	-62	-86	-110	-142	-59	-7	-68	-55	-7	-12
	5.90	-121	-144	-216	-173	-173	-114	-161	-154	-59	-42
	8.60	-139	-116	-147	-198	-108	-119	-198	-127	-45	-79
	11.30	37	2	-42	-23	-19	14	-12	15	63	-15
	12.10	126	77	17	33	70	104	38	17	74	-16
	12.90	82	83	72	121	104	92	33	9	80	-37

	Error										
	Width [mm]	1.60	2.39	3.17	3.96	6.32	8.68	11.04	11.83	12.61	13.40
Depth [mm]	1.60	15	15	15	17	19	18	14	16	14	14
	2.40	14	15	15	16	20	18	15	15	14	13
	3.20	15	14	15	17	21	18	16	15	14	13
	5.90	14	15	16	16	18	18	16	14	14	13
	8.60	14	15	15	16	19	19	16	15	14	13
	11.30	24	15	15	34	34	17	15	15	14	14
	12.10	22	15	15	34	48	17	15	15	14	13
	12.90	30	15	15	33	18	17	15	15	14	14
Transverse											
	Width [mm]	1.60	2.39	3.17	3.96	6.32	8.68	11.04	11.83	12.61	13.40
Depth [mm]	1.60	-10	40	31	60	142	189	137	73	57	-53
	2.40	-33	-8	-61	-9	9	89	12	-3	17	-8
	3.20	-50	-29	-34	-75	-67	11	-13	-17	1	-46
	5.90	-72	-44	-105	-58	-172	-133	-68	-53	-16	-75
	8.60	-97	-47	-31	-104	-132	-99	-65	-18	-3	-88
	11.30	-34	-5	1	35	44	-38	-25	3	1	-108
	12.10	6	48	56	128	127	35	15	-23	-15	-117
	12.90	9	96	130	179	183	98	44	4	1	-115
	Error										
	Width [mm]	1.60	2.39	3.17	3.96	6.32	8.68	11.04	11.83	12.61	13.40
Depth [mm]	1.60	14	15	15	15	18	14	14	14	13	14
	2.40	14	14	15	15	15	14	14	14	14	13
	3.20	14	14	15	15	15	15	15	14	14	13
	5.90	14	14	15	15	15	16	15	14	14	13
	8.60	14	14	15	16	15	17	15	14	13	13
	11.30	15	14	14	19	18	14	14	14	14	13
	12.10	15	14	14	19	22	14	15	14	14	13
	12.90	17	14	14	18	14	14	14	15	14	14

ADDENDUM C: - XRD Sin²ψ curves

C1: Sin²ψ curves for different island sizes (reported in 5.3.3and 5.3.5)
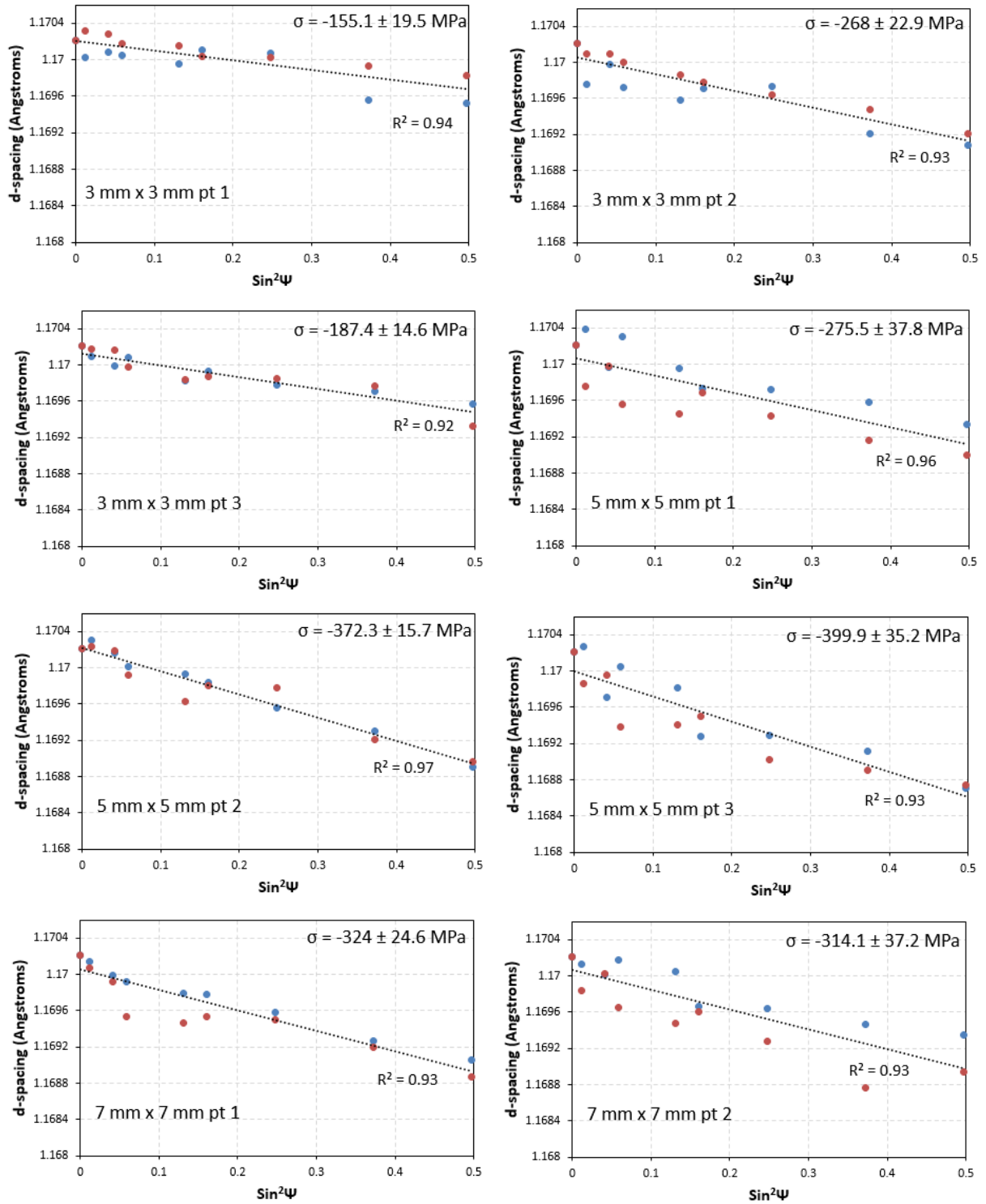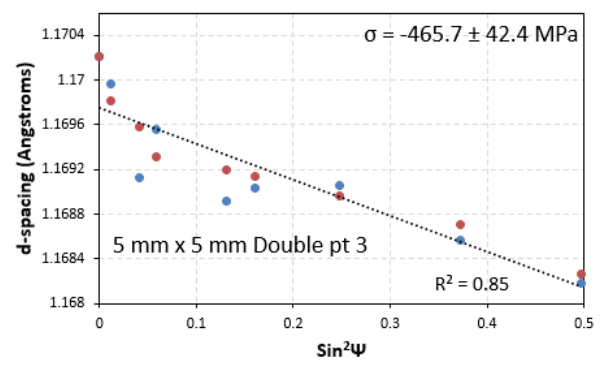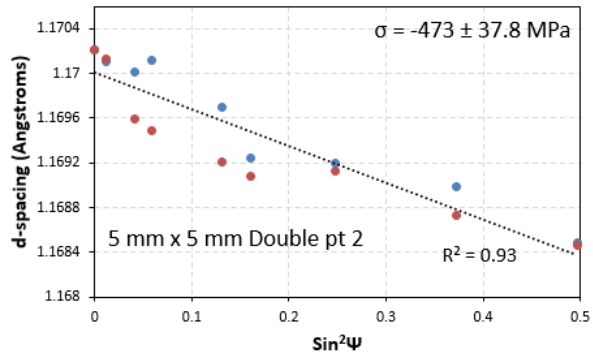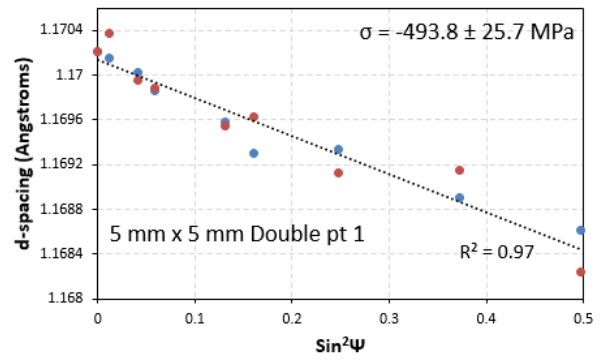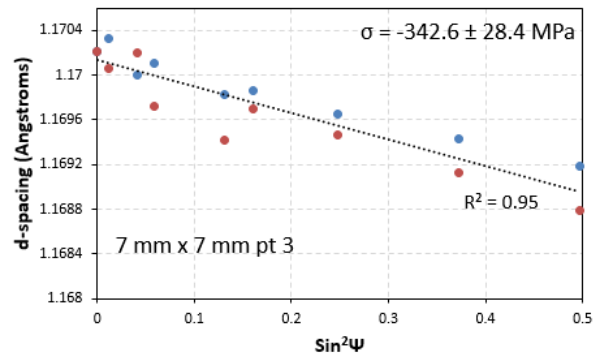
C2: Sin²ψ curves for different scanning sequences (reported in 5.3.6)
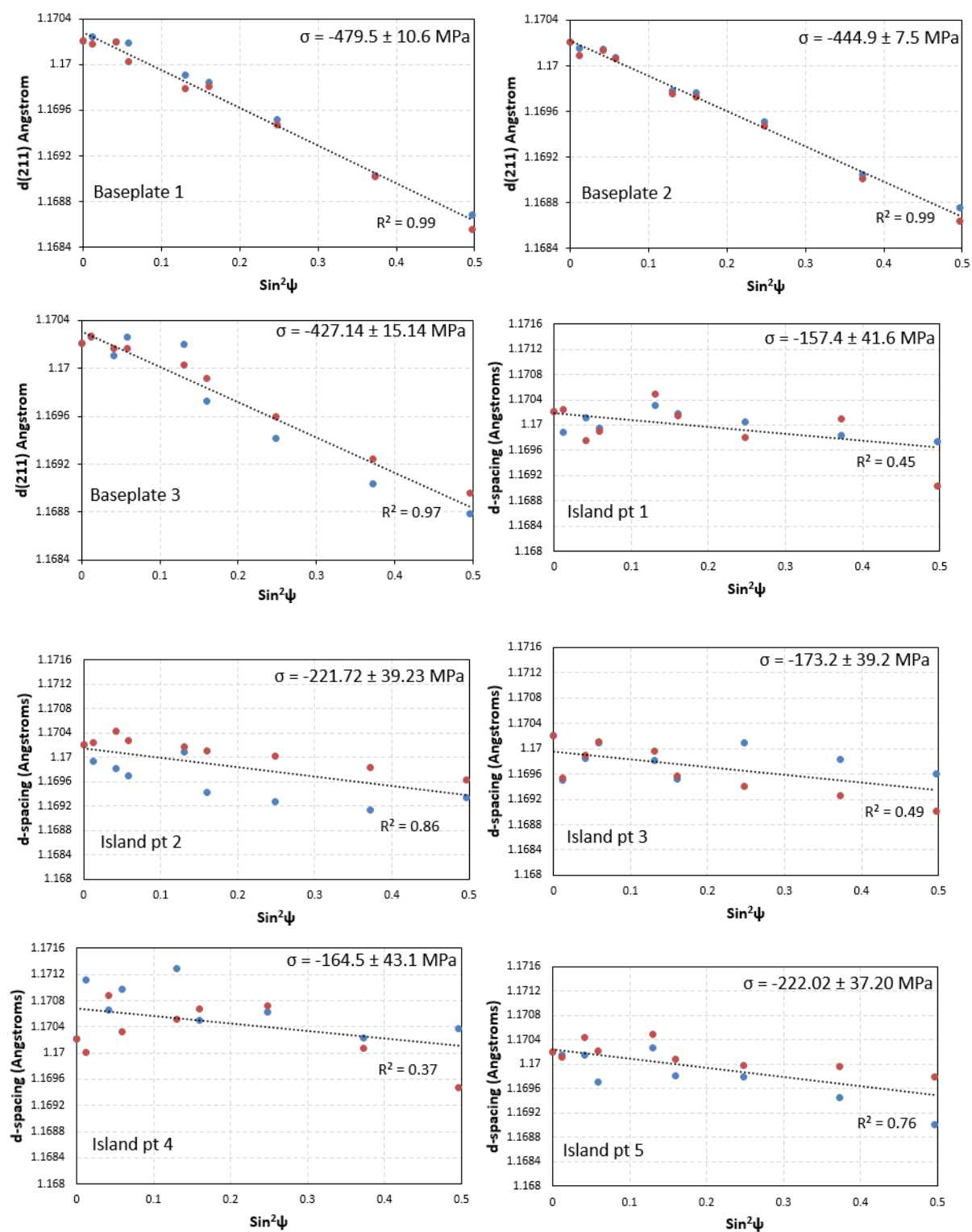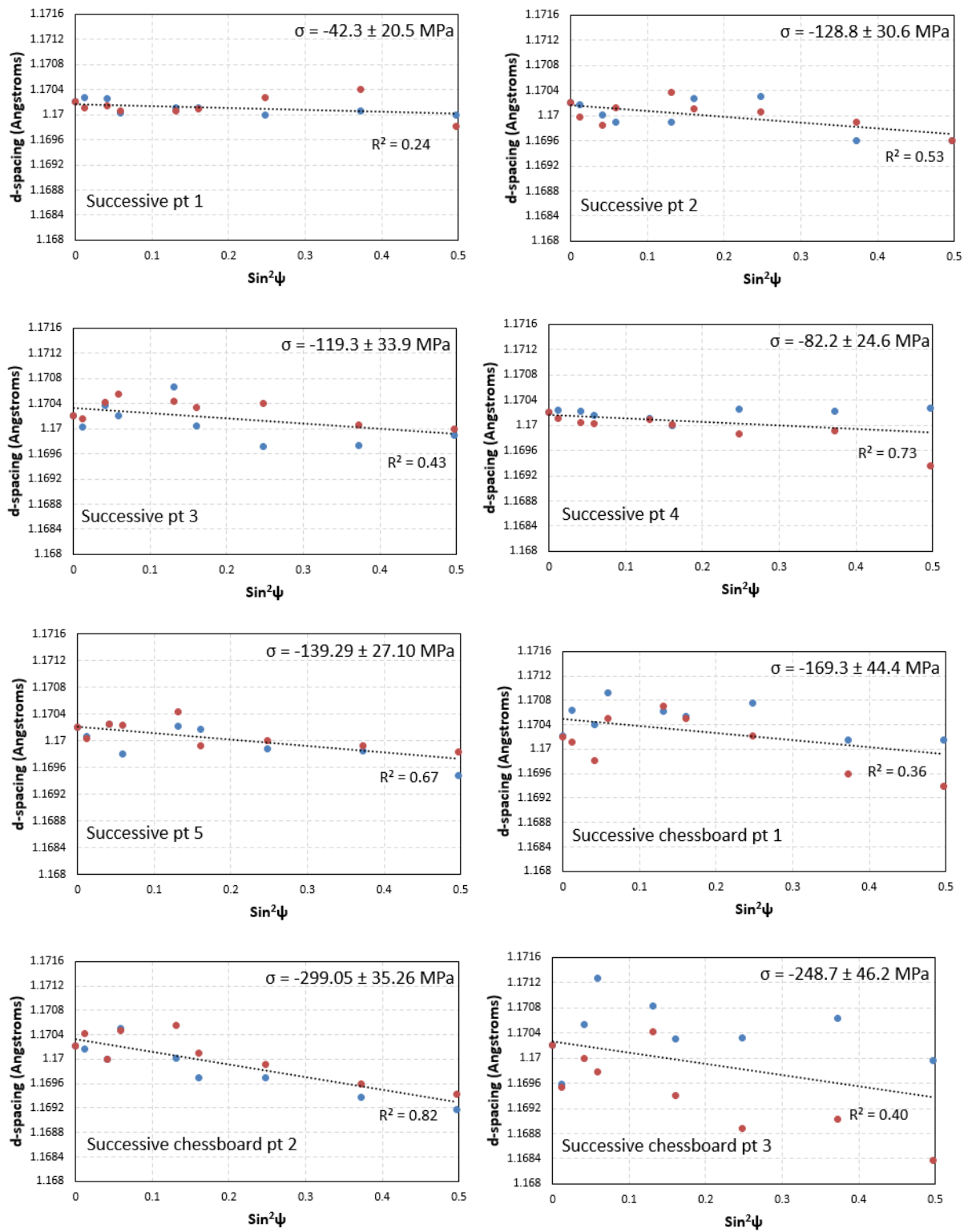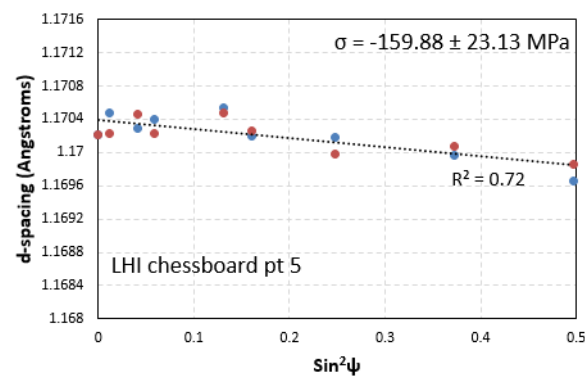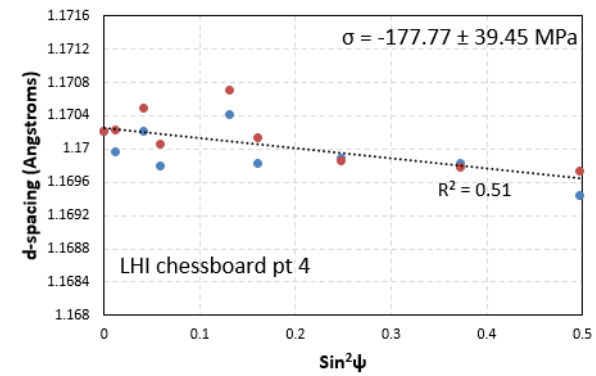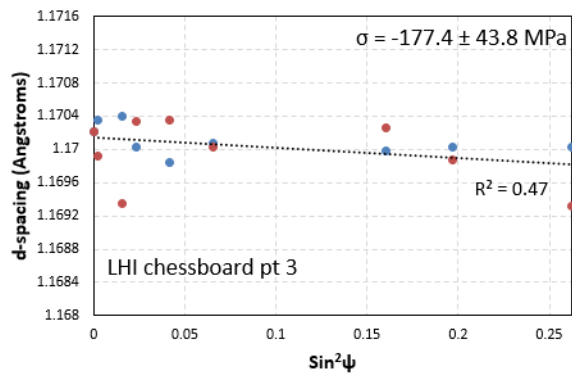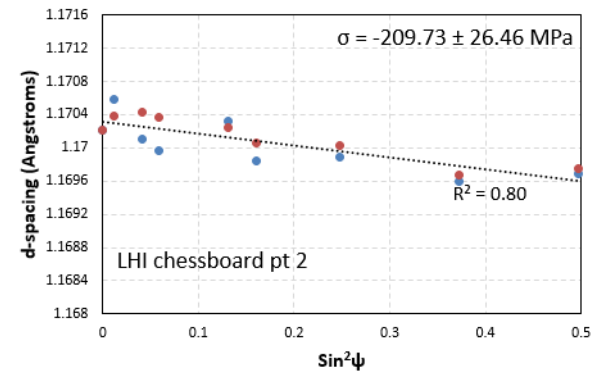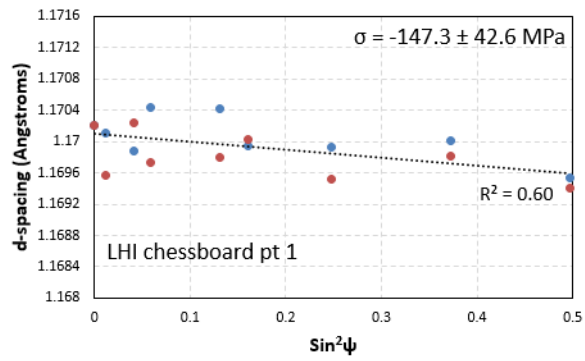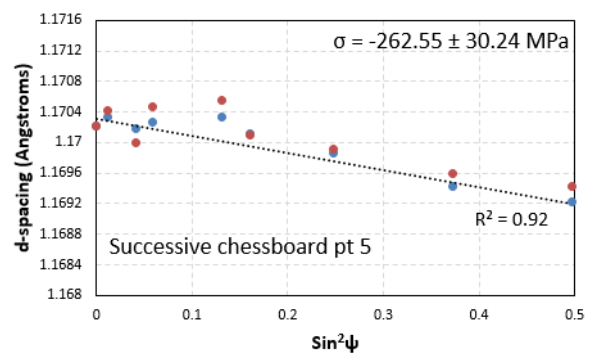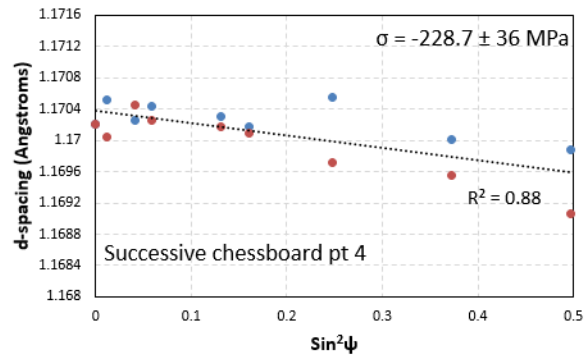
C3: Sin²ψ curves for process parameters (power, speed, layer thickness)

C3-1: Sin²ψ curves from M2 LaserCUSING experiments (reported in 5.4.2)
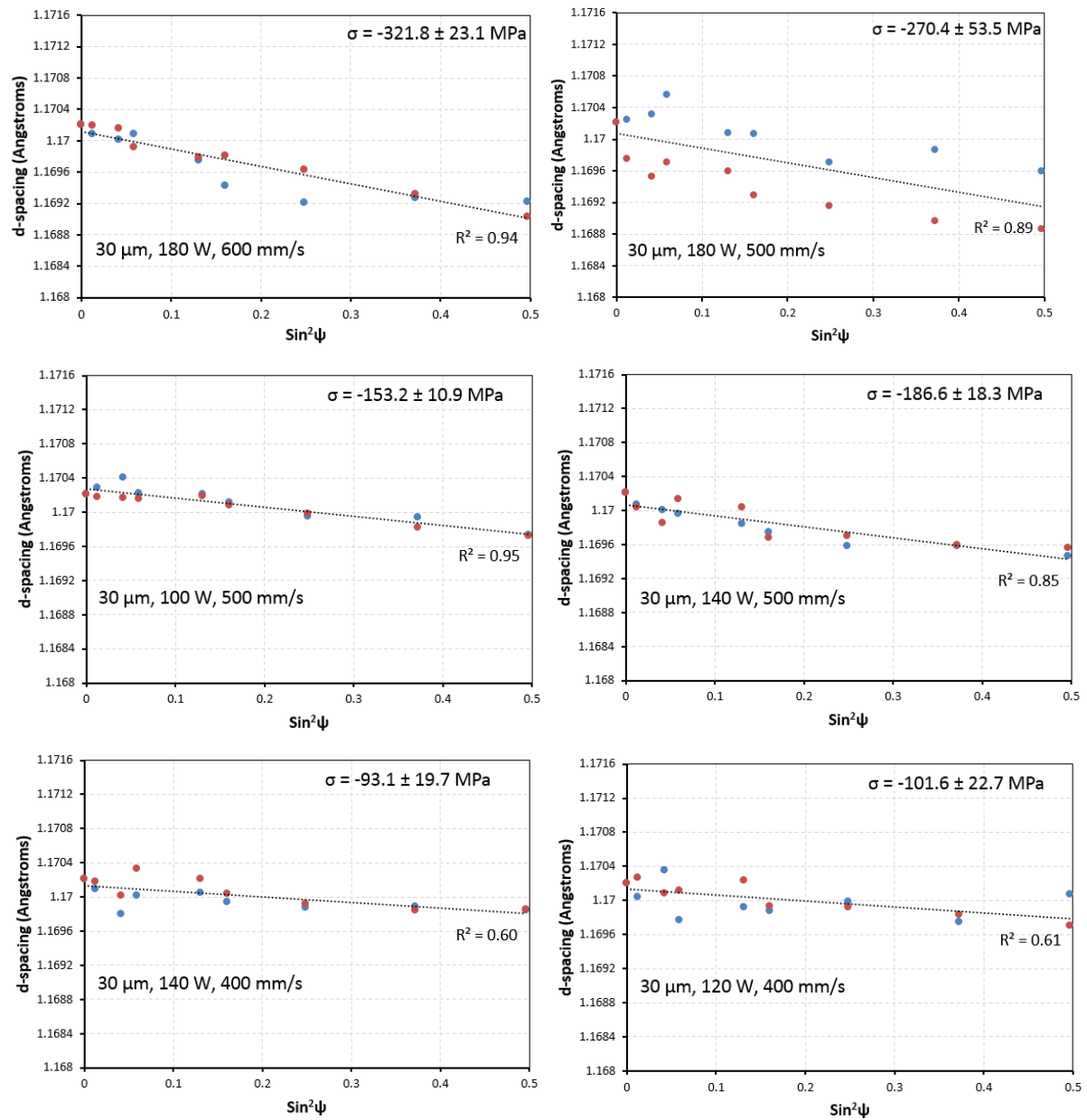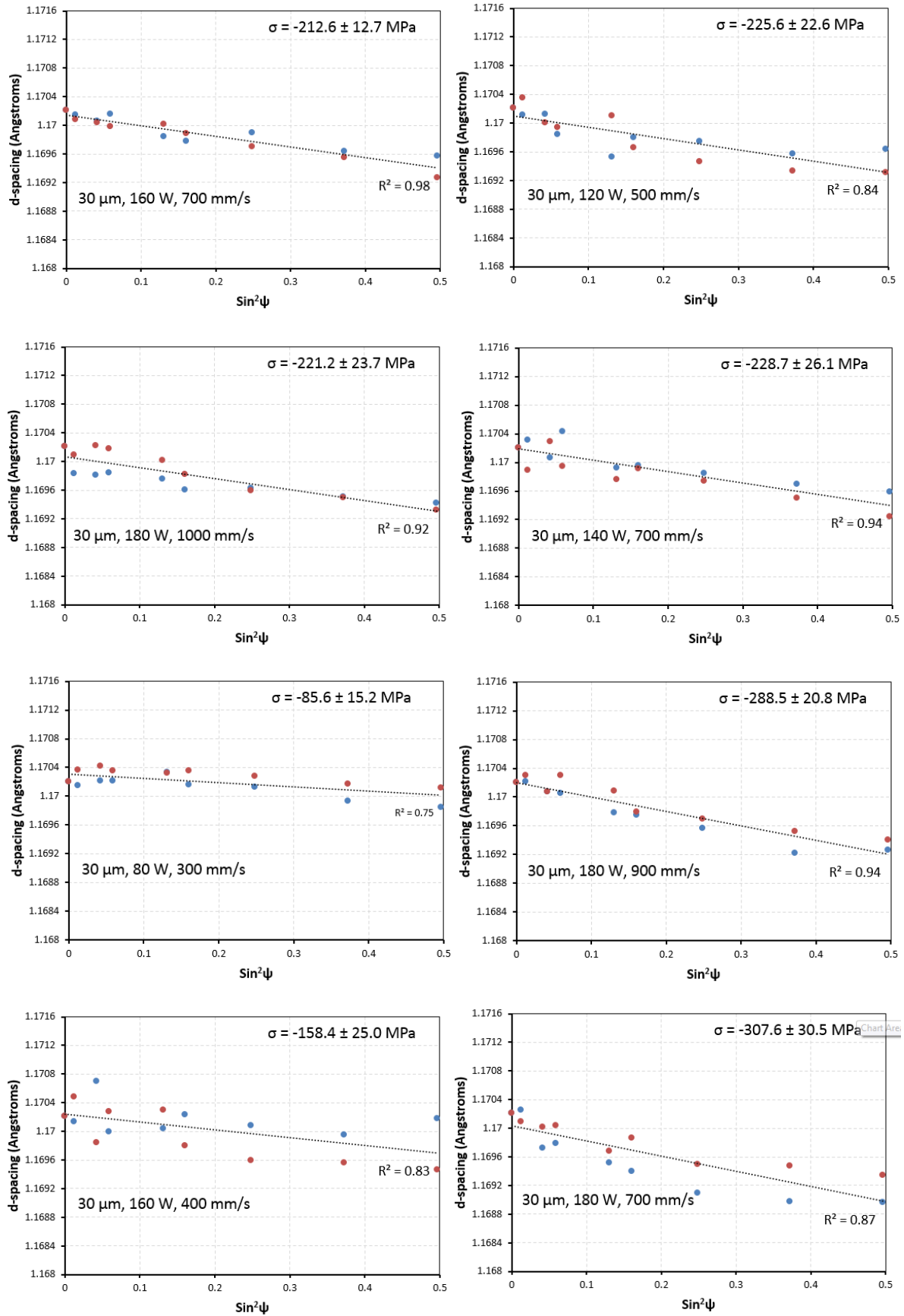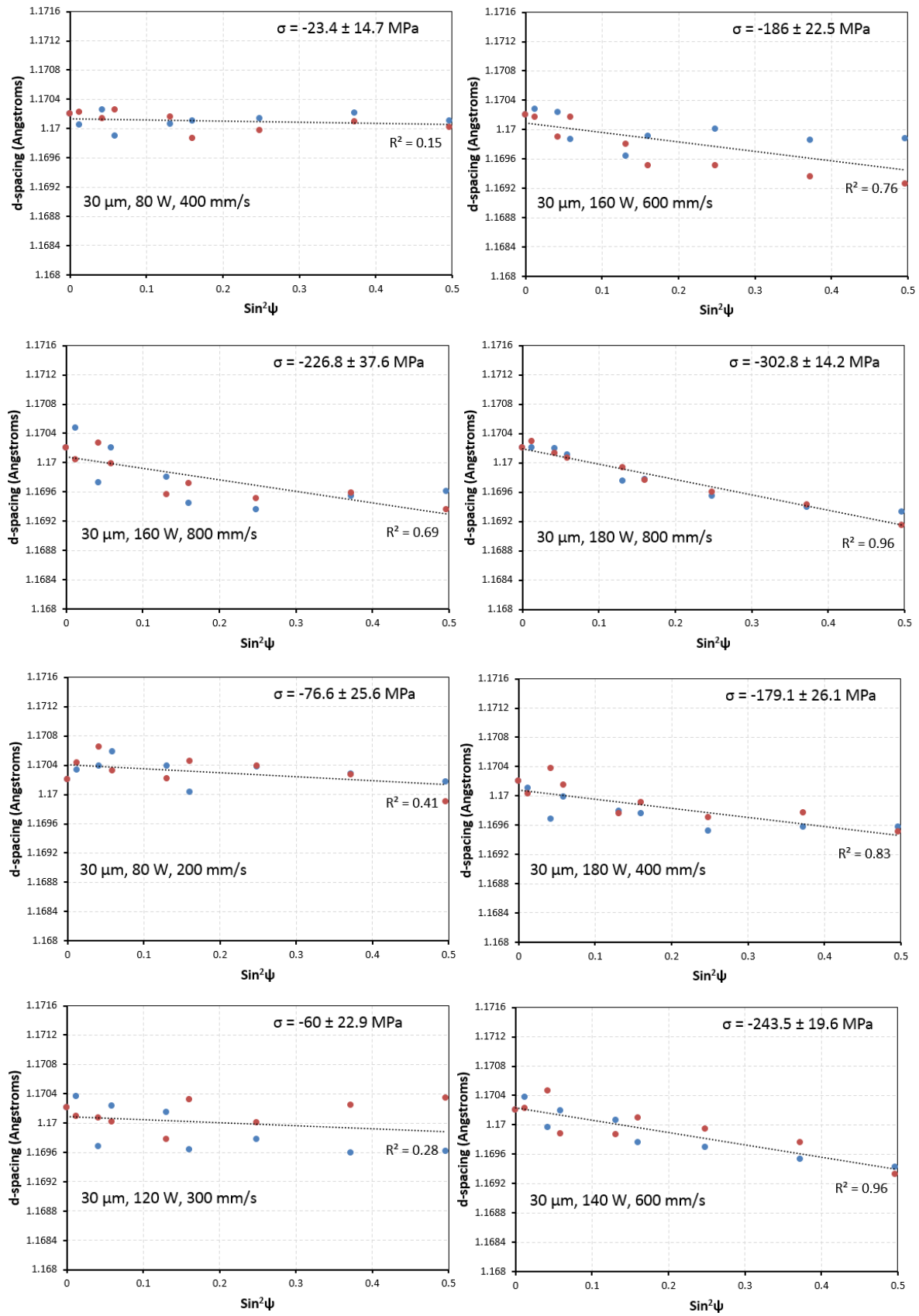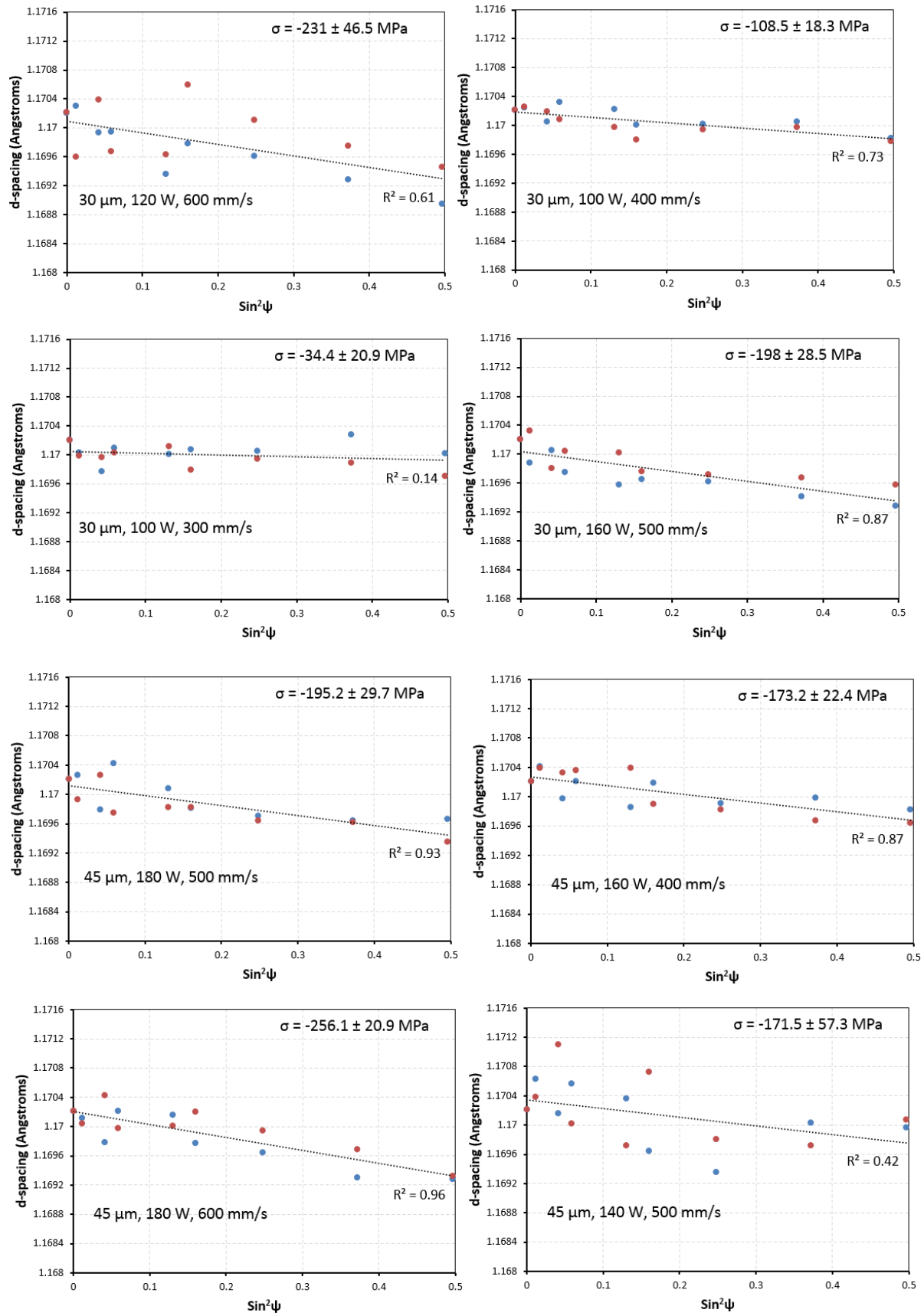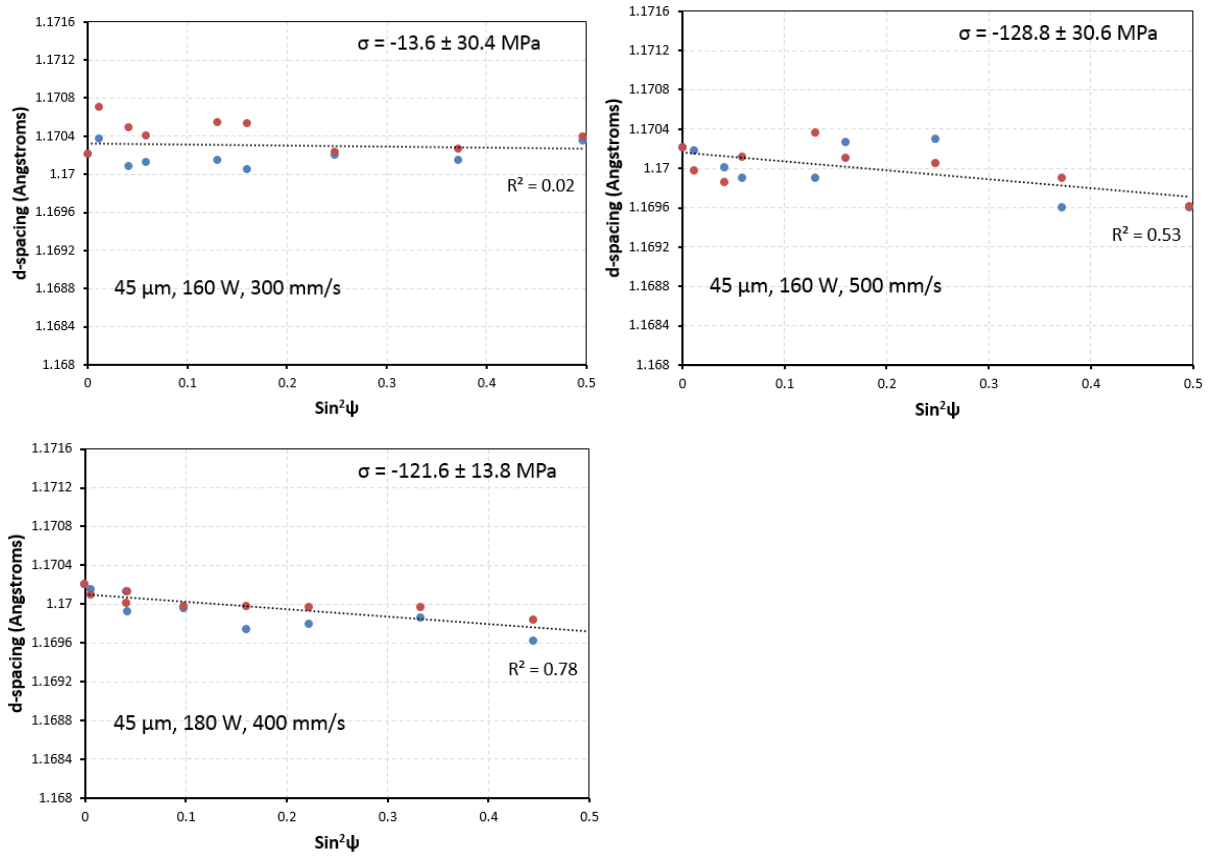
C3-2: Sin²ψ curves from EOSINT M280 verification experiments (reported in 6.3.1)

190
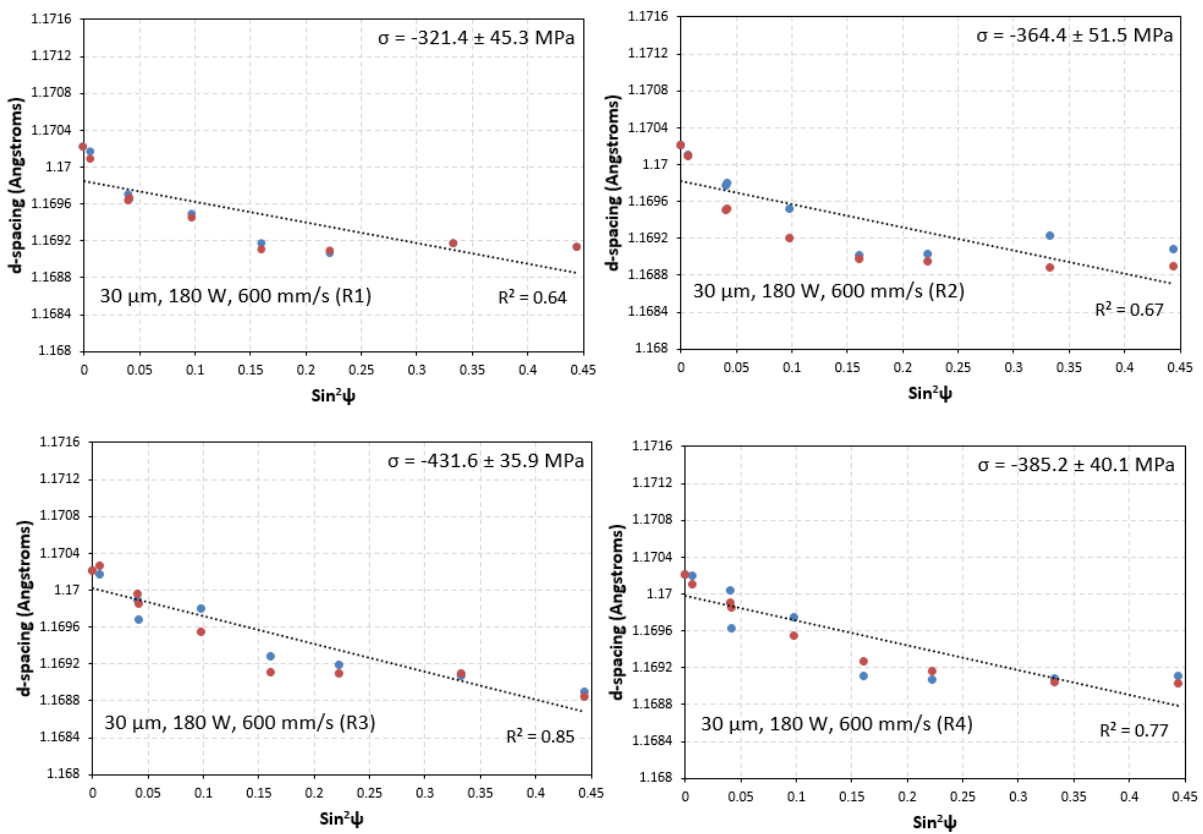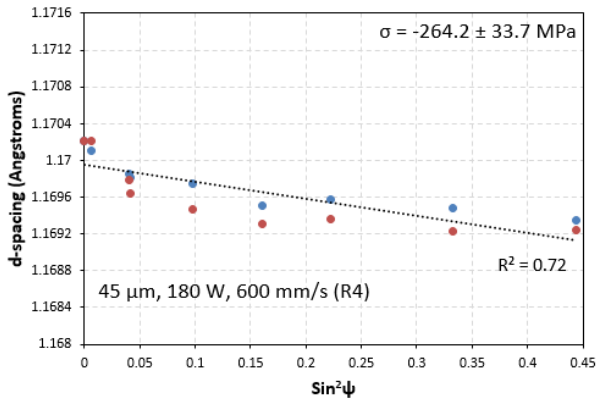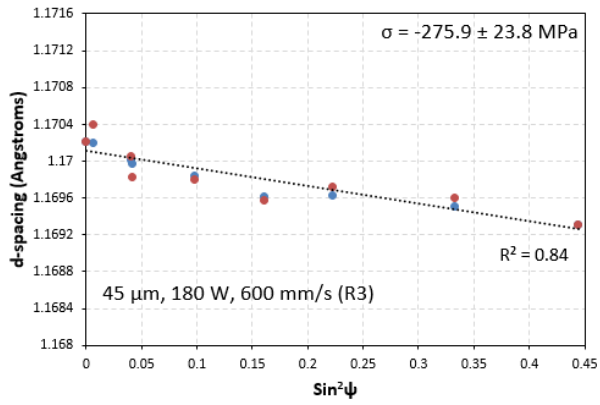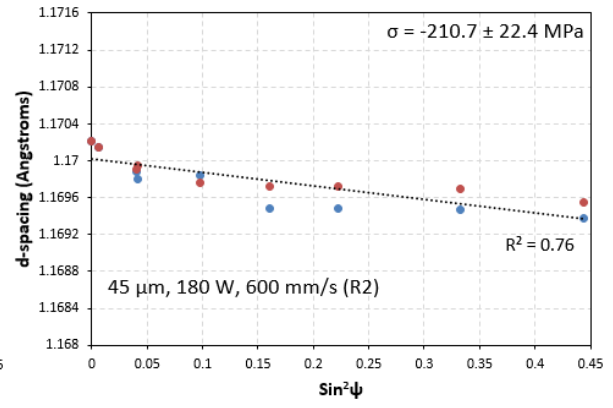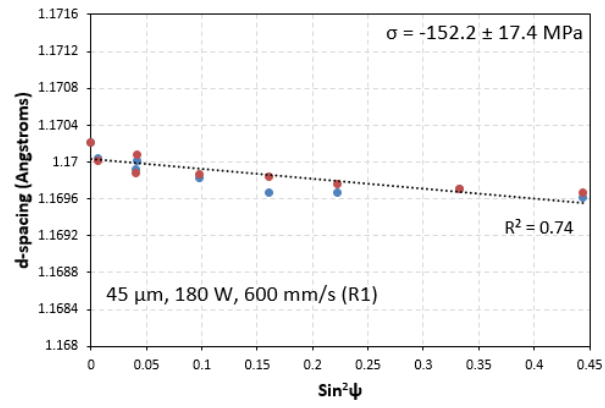
ADDENDUM D: Influence of process parameters

D1 – Porosity results (reported in 5.4.1)

Layer thickness [µm]	Laser power [W]	Scanning speed [mm/s]	Run 1 porosity [%]	Run 2 porosity [%]	Average porosity
30	80	200	5.25	4.21	4.73
30	80	300	9.02	8.58	8.80
30	80	400	10.83	10.01	10.41
30	100	300	8.97	7.86	8.41
30	100	400	4.03	4.43	4.23
30	100	500	3.96	4.50	4.23
30	120	300	6.11	6.50	6.31
30	120	400	3.47	3.17	3.32
30	120	500	1.58	1.09	1.33
30	120	600	3.24	3.51	3.37
30	140	400	3.73	3.85	3.79
30	140	500	3.10	3.79	3.44
30	140	600	1.24	1.82	1.53
30	140	700	1.96	1.81	1.88
30	160	400	3.81	3.59	3.70
30	160	500	3.41	3.22	3.32
30	160	600	1.09	1.53	1.31
30	160	700	0.94	1.09	1.02
30	160	800	1.27	1.52	1.40
30	180	400	3.12	3.68	3.40
30	180	500	1.38	1.72	1.55
30	180	600	0.42	0.36	0.39
30	180	700	0.52	0.34	0.43
30	180	800	0.79	0.65	0.72
30	180	900	1.24	0.80	1.02
30	180	1000	1.26	0.78	1.02
45	80	200	11.18	10.45	10.81
45	100	200	15.41	15.59	15.50
45	100	300	10.42	9.72	10.07
45	120	200	8.11	7.81	7.96
45	120	300	11.67	11.55	11.61
45	120	400	8.73	9.51	9.12
45	140	300	8.13	8.64	8.38

45	140	400	9.01	9.80	9.41
45	140	500	2.70	3.44	3.07
45	160	300	7.26	6.81	7.03
45	160	400	4.46	5.07	4.76
45	160	500	4.88	4.50	4.69
45	180	300	6.40	7.33	6.87
45	180	400	7.62	6.02	6.82
45	180	500	1.52	1.52	1.52
45	180	600	0.80	0.51	0.65

D2 – Residual stresses results (reported in 5.4.2)

Layer thickness (µm)	Laser power (W)	Scanning speed (mm/s)	Residual stress magnitude (MPa)
30	80	200	76.6
30	80	300	85.6
30	80	400	23.4
30	100	300	34.4
30	100	400	108.5
30	100	500	153.2
30	120	300	60
30	120	400	101.6
30	120	500	225.6
30	120	600	231
30	140	400	93.1
30	140	500	186.6
30	140	600	243.5
30	140	700	228.7
30	160	400	158.4
30	160	500	198
30	160	600	186
30	160	700	212.6
30	160	800	226.8
30	180	400	179.1
30	180	500	270.4
30	180	600	321.8
30	180	700	307.6
30	180	800	302.8
30	180	900	288.5
30	180	1000	221.2
45	140	500	171.5
45	160	300	13.6
45	160	400	173.2
45	160	500	128.8
45	180	400	121.6
45	180	500	195.2
45	180	600	256

D3 – Cantilever distortion results (reported in 6.4)

Layer thickness (µm)	Laser power (W)	Scanning speed (mm/s)	Run 1 distortion (mm)	Run 2 distortion (mm)	Average distortion (mm)
30	80	200	0.23	0.17	0.20
30	80	300	0.24	0.20	0.22
30	80	400	0.15	0.09	0.12
30	100	300	0.28	0.18	0.23
30	100	400	0.57	0.50	0.54
30	100	500	0.83	0.60	0.72
30	120	300	0.38	0.38	0.38
30	120	400	0.65	0.45	0.55
30	120	500	0.96	1.03	0.99
30	120	600	0.89	0.82	0.85
30	140	400	0.43	0.32	0.38
30	140	500	0.99	0.86	0.92
30	140	600	1.08	0.92	1.00
30	140	700	0.98	0.92	0.95
30	160	400	0.71	0.59	0.65
30	160	500	0.89	0.84	0.86
30	160	600	1.06	1.00	1.03
30	160	700	1.21	1.03	1.12
30	160	800	1.23	0.97	1.10
30	180	400	0.50	0.36	0.43
30	180	500	0.99	0.94	0.96
30	180	600	1.14	1.01	1.07
30	180	700	1.26	1.09	1.18
30	180	800	1.29	1.12	1.21
30	180	900	1.22	1.10	1.16
30	180	1000	1.31	1.05	1.18
45	80	200	0.03	0.04	0.04
45	100	200	0.03	0.12	0.08
45	100	300	0.11	0.01	0.06
45	120	200	0.25	0.26	0.25
45	120	300	0.14	0.03	0.09
45	120	400	0.12	0.06	0.09
45	140	300	0.14	0.18	0.16
45	140	400	0.15	0.28	0.22

45	140	500	0.27	0.23	0.25
45	160	300	0.01	0.16	0.09
45	160	400	0.10	0.025	0.06
45	160	500	0.14	0.25	0.19
45	180	300	0.07	0.10	0.08
45	180	400	0.09	0.14	0.07
45	180	500	0.34	0.40	0.37
45	180	600	0.56	0.61	0.58

ADDENDUM E – Distortion results for titanium plates (reported in 6.2)

E1: Stripe hatch (1)

X	Y	Z	X	Y	Z	X	Y	Z
0	0	0.216	25	15	0.012	40	30	0.094
5	0	0.172	20	15	0.015	45	30	0.151
10	0	0.14	15	15	0.028	45	35	0.166
15	0	0.119	10	15	0.058	40	35	0.109
20	0	0.098	5	15	0.1	35	35	0.072
25	0	0.106	0	15	0.149	30	35	0.05
30	0	0.119	0	20	0.144	25	35	0.038
35	0	0.139	5	20	0.091	20	35	0.039
40	0	0.174	10	20	0.051	15	35	0.055
45	0	0.225	15	20	0.021	10	35	0.076
45	5	0.198	20	20	0.007	5	35	0.117
40	5	0.135	25	20	0	0	35	0.169
35	5	0.106	30	20	0.013	0	40	0.178
30	5	0.079	35	20	0.046	5	40	0.13
25	5	0.063	40	20	0.086	10	40	0.106
20	5	0.058	45	20	0.145	15	40	0.084
15	5	0.083	45	25	0.144	20	40	0.072
10	5	0.106	40	25	0.085	25	40	0.068
5	5	0.133	35	25	0.048	30	40	0.079
0	5	0.19	30	25	0.022	35	40	0.101
0	10	0.165	25	25	0.006	40	40	0.136
5	10	0.113	20	25	0.007	45	40	0.185
10	10	0.074	15	25	0.021	45	45	0.212
15	10	0.051	10	25	0.054	40	45	0.171
20	10	0.037	5	25	0.09	35	45	0.141
25	10	0.03	0	25	0.148	30	45	0.119
30	10	0.044	0	30	0.159	25	45	0.114
35	10	0.071	5	30	0.107	20	45	0.115
40	10	0.115	10	30	0.061	15	45	0.127
45	10	0.173	15	30	0.032	10	45	0.146
45	15	0.152	20	30	0.019	5	45	0.162
40	15	0.097	25	30	0.017	0	45	0.186
35	15	0.056	30	30	0.029			
30	15	0.025	35	30	0.056			

E2: Stripe hatch (2)

X	Y	Z	X	Y	Z	X	Y	Z
0	0	0.225	25	15	0.019	40	30	0.148
5	0	0.163	20	15	0.007	45	30	0.219
10	0	0.112	15	15	0.024	45	35	0.219
15	0	0.079	10	15	0.065	40	35	0.149
20	0	0.061	5	15	0.132	35	35	0.092
25	0	0.062	0	15	0.286	30	35	0.048
30	0	0.085	0	20	0.196	25	35	0.029
35	0	0.122	5	20	0.114	20	35	0.011
40	0	0.173	10	20	0.053	15	35	0.023
45	0	0.236	15	20	0.014	10	35	0.055
45	5	0.226	20	20	0	5	35	0.113
40	5	0.159	25	20	0.012	0	35	0.262
35	5	0.104	30	20	0.032	0	40	0.254
30	5	0.065	35	20	0.081	5	40	0.169
25	5	0.041	40	20	0.142	10	40	0.109
20	5	0.037	45	20	0.216	15	40	0.072
15	5	0.052	45	25	0.218	20	40	0.058
10	5	0.091	40	25	0.146	25	40	0.034
5	5	0.146	35	25	0.083	30	40	0.059
0	5	0.215	30	25	0.033	35	40	0.097
0	10	0.216	25	25	0.011	40	40	0.153
5	10	0.139	20	25	0.001	45	40	0.215
10	10	0.073	15	25	0.012	45	45	0.211
15	10	0.035	10	25	0.046	40	45	0.152
20	10	0.019	5	25	0.108	35	45	0.101
25	10	0.021	0	25	0.191	30	45	0.062
30	10	0.048	0	30	0.25	25	45	0.037
35	10	0.085	5	30	0.148	20	45	0.033
40	10	0.148	10	30	0.087	15	45	0.043
45	10	0.219	15	30	0.056	10	45	0.073
45	15	0.218	20	30	0.005	5	45	0.337
40	15	0.141	25	30	0.018	0	45	0.193
35	15	0.084	30	30	0.042			
30	15	0.04	35	30	0.084			

E3: Random (island) strategy (1)

X	Y	Z	X	Y	Z	X	Y	Z
0	0	0.178	25	15	0.02	40	30	0.062
5	0	0.149	20	15	0.02	45	30	0.094
10	0	0.136	15	15	0.026	45	35	0.119
15	0	0.128	10	15	0.04	40	35	0.088
20	0	0.115	5	15	0.067	35	35	0.062
25	0	0.114	0	15	0.101	30	35	0.049
30	0	0.118	0	20	0.09	25	35	0.037
35	0	0.122	5	20	0.054	20	35	0.034
40	0	0.129	10	20	0.028	15	35	0.032
45	0	0.141	15	20	0.012	10	35	0.05
45	5	0.115	20	20	0.006	5	35	0.077
40	5	0.094	25	20	0.008	0	35	0.102
35	5	0.085	30	20	0.016	0	40	0.128
30	5	0.074	35	20	0.029	5	40	0.098
25	5	0.072	40	20	0.048	10	40	0.086
20	5	0.072	45	20	0.08	15	40	0.072
15	5	0.082	45	25	0.082	20	40	0.067
10	5	0.097	40	25	0.05	25	40	0.072
5	5	0.11	35	25	0.026	30	40	0.082
0	5	0.142	30	25	0.011	35	40	0.099
0	10	0.119	25	25	0.002	40	40	0.125
5	10	0.084	20	25	0	45	40	0.146
10	10	0.063	15	25	0.008	45	45	0.185
15	10	0.051	10	25	0.028	40	45	0.164
20	10	0.041	5	25	0.049	35	45	0.141
25	10	0.041	0	25	0.083	30	45	0.124
30	10	0.046	0	30	0.085	25	45	0.111
35	10	0.054	5	30	0.055	20	45	0.105
40	10	0.07	10	30	0.028	15	45	0.106
45	10	0.095	15	30	0.013	10	45	0.113
45	15	0.084	20	30	0.01	5	45	0.132
40	15	0.063	25	30	0.011	0	45	0.156
35	15	0.036	30	30	0.02			
30	15	0.023	35	30	0.036			

E4: Random (island) strategy (2)

X	Y	Z	X	Y	Z	X	Y	Z
0	0	0.209	25	15	0.003	40	30	0.117
5	0	0.151	20	15	0.004	45	30	0.189
10	0	0.1	15	15	0.021	45	35	0.19
15	0	0.064	10	15	0.06	40	35	0.12
20	0	0.038	5	15	0.106	35	35	0.065
25	0	0.026	0	15	0.171	30	35	0.032
30	0	0.034	0	20	0.168	25	35	0.016
35	0	0.06	5	20	0.106	20	35	0.018
40	0	0.102	10	20	0.06	15	35	0.03
45	0	0.149	15	20	0.021	10	35	0.059
45	5	0.152	20	20	0	5	35	0.101
40	5	0.1	25	20	0.006	0	35	0.16
35	5	0.054	30	20	0.021	0	40	0.159
30	5	0.025	35	20	0.049	5	40	0.099
25	5	0.015	40	20	0.103	10	40	0.059
20	5	0.027	45	20	0.174	15	40	0.034
15	5	0.044	45	25	0.181	20	40	0.025
10	5	0.078	40	25	0.107	25	40	0.023
5	5	0.136	35	25	0.057	30	40	0.04
0	5	0.195	30	25	0.021	35	40	0.074
0	10	0.181	25	25	0.004	40	40	0.127
5	10	0.113	20	25	0.005	45	40	0.196
10	10	0.062	15	25	0.021	45	45	0.198
15	10	0.031	10	25	0.06	40	45	0.131
20	10	0.011	5	25	0.103	35	45	0.079
25	10	0.005	0	25	0.165	30	45	0.081
30	10	0.019	0	30	0.163	25	45	0.022
35	10	0.047	5	30	0.102	20	45	0.022
40	10	0.108	10	30	0.061	15	45	0.031
45	10	0.174	15	30	0.024	10	45	0.06
45	15	0.167	20	30	0.013	5	45	0.1
40	15	0.097	25	30	0.007	0	45	0.152
35	15	0.048	30	30	0.025			
30	15	0.015	35	30	0.06			

E5: Successive chessboard strategy (1)

X	Y	Z	X	Y	Z	X	Y	Z
0	0	0.143	25	15	0.011	40	30	0.08
5	0	0.105	20	15	0.012	45	30	0.135
10	0	0.073	15	15	0.022	45	35	0.129
15	0	0.057	10	15	0.05	40	35	0.082
20	0	0.048	5	15	0.081	35	35	0.043
25	0	0.045	0	15	0.128	30	35	0.023
30	0	0.054	0	20	0.13	25	35	0.015
35	0	0.073	5	20	0.082	20	35	0.019
40	0	0.111	10	20	0.045	15	35	0.066
45	0	0.155	15	20	0.017	10	35	0.06
45	5	0.159	20	20	0.002	5	35	0.093
40	5	0.106	25	20	0.003	0	35	0.138
35	5	0.075	30	20	0.016	0	40	0.146
30	5	0.047	35	20	0.051	5	40	0.103
25	5	0.035	40	20	0.086	10	40	0.068
20	5	0.037	45	20	0.143	15	40	0.051
15	5	0.047	45	25	0.139	20	40	0.038
10	5	0.069	40	25	0.08	25	40	0.034
5	5	0.098	35	25	0.045	30	40	0.04
0	5	0.143	30	25	0.014	35	40	0.061
0	10	0.135	25	25	0.002	40	40	0.091
5	10	0.089	20	25	0	45	40	0.134
10	10	0.058	15	25	0.017	45	45	0.145
15	10	0.033	10	25	0.046	40	45	0.104
20	10	0.022	5	25	0.085	35	45	0.076
25	10	0.02	0	25	0.132	30	45	0.061
30	10	0.036	0	30	0.136	25	45	0.057
35	10	0.068	5	30	0.092	20	45	0.06
40	10	0.095	10	30	0.048	15	45	0.071
45	10	0.156	15	30	0.024	10	45	0.09
45	15	0.148	20	30	0.013	5	45	0.118
40	15	0.095	25	30	0.004	0	45	0.156
35	15	0.048	30	30	0.013			
30	15	0.021	35	30	0.04			

E6: Successive chessboard strategy (2)

X	Y	Z	X	Y	Z	X	Y	Z
0	0	0.157	25	15	0.024	40	30	0.066
5	0	0.145	20	15	0.022	45	30	0.1
10	0	0.133	15	15	0.025	45	35	0.119
15	0	0.124	10	15	0.04	40	35	0.092
20	0	0.12	5	15	0.055	35	35	0.07
25	0	0.12	0	15	0.085	30	35	0.044
30	0	0.118	0	20	0.074	25	35	0.052
35	0	0.132	5	20	0.047	20	35	0.059
40	0	0.149	10	20	0.023	15	35	0.055
45	0	0.172	15	20	0.009	10	35	0.066
45	5	0.142	20	20	0	5	35	0.093
40	5	0.115	25	20	0.004	0	35	0.114
35	5	0.095	30	20	0.01	0	40	0.145
30	5	0.084	35	20	0.025	5	40	0.118
25	5	0.085	40	20	0.055	10	40	0.102
20	5	0.083	45	20	0.081	15	40	0.09
15	5	0.091	45	25	0.089	20	40	0.082
10	5	0.094	40	25	0.053	25	40	0.077
5	5	0.107	35	25	0.024	30	40	0.077
0	5	0.129	30	25	0.008	35	40	0.08
0	10	0.104	25	25	0.003	40	40	0.103
5	10	0.079	20	25	0.003	45	40	0.131
10	10	0.061	15	25	0.014	45	45	0.159
15	10	0.053	10	25	0.026	40	45	0.135
20	10	0.053	5	25	0.051	35	45	0.115
25	10	0.052	0	25	0.079	30	45	0.107
30	10	0.056	0	30	0.093	25	45	0.115
35	10	0.071	5	30	0.064	20	45	0.122
40	10	0.088	10	30	0.044	15	45	0.13
45	10	0.115	15	30	0.025	10	45	0.141
45	15	0.095	20	30	0.022	5	45	0.156
40	15	0.062	25	30	0.019	0	45	0.179
35	15	0.04	30	30	0.02			
30	15	0.023	35	30	0.039			